Universidad Autónoma de Madrid

Facultad de Ciencias

Departamento de Física Teórica

Description of odd-mass nuclei in Beyond Mean Field approaches with the Gogny energy density functional

Memoria de Tesis
Presentada en la Facultad de Ciencias
de la Universidad Autónoma de Madrid
para optar al grado de Doctor en Ciencias Físicas

Trabajo dirigido por
Cat. Jose Luis Egido de los Ríos

Description of odd-mass nuclei in Beyond Mean Field approaches with the Gogny energy density functional

Abstract

Mean field theories are one of the most successful methods used to describe nuclear structure. Part of its success emerges from the introduction of correlations thanks to the rupture of symmetries of the system. However, in order to give a correct description of the system we must recover these symmetries using beyond mean field methods (BMF). Moreover, these methods enable to incorporate another kind of correlations. BMF methods are developed in two directions in our calculations: the recovery of the symmetries broken at MF approach and the incorporation of fluctuations around the most sensitive states in the frame of the generator coordinate method (GCM).

The other ingredient needed to describe the nuclear structure is the interaction used. In our case we use a "universal" effective interaction, in particular the Gogny energy density functional, which can be used throughout the whole nuclear chart.

Our calculations involve GCM calculations using states with particle number and angular momentum projection usinsg the nuclear deformations as degrees of freedom. We develop these techniques in two main ways in this work.

The first one is the use of time reversal symmetry breaking wave functions by means of the cranking procedure. As an application we calculate the excitation energies of the lowest 2^+ and 4^+ states of the even-A magnesium isotopes. As a result of the introduction of the cranking the theoretical values

obtained coincide with the experimental ones. The cranking procedure also enables to describe aligned states unreachable in previous calculations. In particular we predicted correctly the recently measured 4^+ state in the exotic ^{44}S nucleus. Moreover, the diminution of the collectivity in the resulting wave functions leads to a decrease of the electromagnetic transition probabilities, which were too large in previous calculations. This is illustrated in the exotic ^{44}S, as well as in the titanium isotopes.

The second contribution of this work is the application of this mechanism to odd-A nuclei. Ground states properties such as binding energies, mass radii and odd-even mass differences are obtained in a very good agreement with experimental data. A detailed study is also performed in the ^{31}Mg nucleus at the border of the N=20 island of inversion, where ground states and excited states are correctly described, including their electromagnetic properties. Finally, we apply the configuration mixing method to the ^{25}Mg nucleus and we do a detailed comparison with other theoretical approaches.

Description of odd-mass nuclei in Beyond Mean Field approaches with the Gogny energy density functional

Resumen

Las aproximaciones de campo medio (MF) son uno de los métodos más exitosos para describir la estructura de los núcleos. Parte de su éxito radica en la introducción de correlaciones gracias a la ruptura de algunas de las simetrías del sistema. Sin embargo, para dar una descripción correcta del sistema es necesario recobrar estas simetrías mediante el uso de métodos ms allá de campo medio (BMF). Estos métodos permitirán, además, incorporar otro tipo de correlaciones. Los métodos más allá del campo medio desarrollados en este trabajo van en dos direcciones: La restauración de las simetrías rotas a nivel de campo medio y la introducción de fluctuaciones en torno a las configuraciones más probables mediante el método de la coordenada generadora (GCM).

El otro ingrediente fundamental para la descripción del núcleo es la interacción usada. En nuestro caso utilizaremos una interacción efectiva "universal", en particular la interacciń de Gogny, que puede ser utilizada sin modificación en cualquier región de la tabla de núcleos.

Los cálculos realizados hacen uso del método de la coordenada generadora usando funciones de onda proyectadas a buen número de partículas y momento angular usando las deformaciones nucleares β, γ como coordenadas generadoras. En este trabajo se ampliarán los métodos más allá de campo medio utilizados hasta el momento en dos formas:

La primera es la ruptura de la simetría de inversión temporal mediante el uso de funciones de onda de cranking. Como aplicación se calcula la energía de excitación de los estados 2^+ and 4^+ de los núcleos pares de la cadena isotópica de magnesio. La incorporación del procedimiento de cranking nos permite una excelente coincidencia con las medidas experimentales. Este procedimiento nos permite también describir estados alineados no presentes in cálculos previos. En particular predijimos correctamente el recién medido estado 4^+ del núcleo exótico ^{44}S. Es más, la disminución de la colectividad en las funciones de onda resultantes nos lleva a una reducción de los valores de las probabilidades de transición, que eran demasiado altas en cálculos previos. Esto se ilustra en el núcleo ^{44}S así como en la cadena isotópica de titanios.

La segunda aportación de este trabajo es la aplicación de este mecanismo a núcleos con un número impar de partículas. Las propiedades de los estados fundamentales así como las energías de ligadura, radios de masa y diferencia de energía de núcleos par e impar se obtienen con una coincidencia muy buena con el experimento. También se realiza un estudio detallado del ^{31}Mg en el borde de la isla de inversión N=20, donde tanto los estados fundamentales como los excitados se describen correctamente, así como las probabilidades de transición electromagnéticas. Por último, se realiza un cálculo con mezcla de configuraciones en el núcleo ^{25}Mg y se hace una comparación detallada con otros modelos teóricos.

Dedication

A mis padres,

Contents

List of Tables

List of Figures

Chapter 1

Introduction

1.1 Motivation and Objectives

With the development of new experimental techniques in Nuclear Physics, properties of exotic nuclei have been recently measured. The term "exotic" alludes to those nuclei far from the nuclear valley of stability, covers isotopes with an excess of protons and neutrons, and super-heavy nuclei. Theoretical approaches must be improved in order to explain the recent results. Moreover, the development of theoretical tools is of great importance to predict new states which cannot be measured (or have not been measured yet) but are believed to exist in other parts of the universe.

Among the main important approaches there are the ab initio ones, the shell model approaches and self consistent mean field (and beyond) based ones. This work belongs to the latter.

In self-consistent mean field (SCMF) approaches we consider the nucleus as a non-interacting system of particles (or quasi-particles) in an external potential. This potential is obtained with effective interactions and making use of methods such as the Hartree-Fock (HF) or Hartree-Fock-Bogoliubov (HFB). This basic mean field approach is a powerful tool to describe global properties of atomic nuclei such as masses, radii... One of the key points that makes this approach so powerful is the incorporation of correlations through the symmetry breaking mechanism; i.e. we increase the variational space to allow solutions which break some symmetries of the Hamiltonian. This has some disadvantages like the increasing of the computational effort and the fact that the solution do not posses the good quantum numbers. In addition we cannot describe some phenomena observed like shape coexistence with a HF-type solution (product-like solution). To solve these issues Beyond Mean Field Methods (BMF) are used. Their two main ingredients are the recovery of the symmetries broken at mean field level and the incorporation of fluctuations around the most probable values by means of the Generator Coordinate Method (GCM).

We use these methods to study different nuclear systems. The intrinsic wave functions are found by the Particle Number Variation After Projection (PNVAP) using the Gogny Density Functional with the D1S parametrization. This depend on several parameters, which are the generator coordinates, and form the basis used in the GCM.

In this work we develop these tools in two main ways.

1. The first one is to allow time reversal symmetry breaking at mean field level thanks to the cranking procedure. This provides an additional degree of freedom which is used in the configuration mixing. The two main important consequences are the achievement of an accurate description of the nuclear spectra and the possibility to describe single-particle character states, not present in previous calculations.

2. Application of this mechanism to systems with and odd number of protons or neutrons, which have not done before with an exact blocking PN-VAP wave function. Apart form an accurate description of the nuclear spectra, we carry out systematic studies in isotopic chains, obtaining fascinating results on properties such as odd-even mass differences, binding energies per nucleon, magnetic and quadrupole moments...

1.2 Organization of contents

This thesis is organized as follows: On the second chapter we introduce the different theoretical approximations used to solve the nuclear many-body problem, and the different interactions used. Our type of approximation will be studied with detail in chapter 3 (Mean Field and Beyond Mean Field approximations). Chapter 4 is devoted to the symmetries imposed in our system, which is a key part of our work, and allows to reduce the complexity of the calculations. On chapter 5 we introduce the concept of blocking and how is employed in our calculations to solve systems with an odd number of particles, which is one of the most important developments of this work.

Chapter 6 is used to specify which elements of the theory seen in chapter 3 are used in these work, giving details and expressions which are necessary to follow the results of our calculations.

The following chapters are devoted to the results. We divide them in two main parts. First part shows the effect of time reversal symmetry breaking in systems with an even number of particles. This time reversal breaking is done with the inclusion of the cranking term. The second part is devoted to odd nuclei.

We also include several appendix. There are two main ingredients to be calculated in our theory; the expression of the norm overlap and a general operator expected value between particle and angular momentum projected GCM-type states. Both expressions are given with great detail (for even and odd systems) in Appendices A and B. Appendix C applies the results in A and B to calculate de Hamiltonian expected value;i.e. the energy of the system.

Chapter 2

Nuclear Models and interactions

In this work we consider the nucleus as a system of protons and neutrons. To solve the nuclear problem we need two main ingredients. The first one is to know the interaction between its constituents, and the other is the theoretical method to solve the problem. However, both are connected.

Several approaches have been proposed, and are more or less suitable depending on the mass region and the properties described. Among the most important we find ab initio methods [1], shell model ones, and self consistent mean field approaches. In the light mass region, the former are the most widely applied. They use bare nuclear interactions , although these can be previously regularized. For the rest of the regions shell model and mean field approaches are the most used, and are performed with effective interactions.

In the first section we give a brief overview of these methods. In the last section we discuss the different effective interactions which can be used in the mean field based ones.

2.1 Other nuclear models

2.1.1 Ab initio methods

The relevant degrees of freedom for nuclei are protons and neutrons, which are not fundamental particles but complex objects made of quarks, anti-quarks and gluons. In this way, the strong interaction among nucleons is only an effective interaction which emerges non-perturbatively from QCD. These potentials include spin, isospin, tensor, spin-orbit, quadratic moment-dependent, and charge-independence-breaking terms. They depend on certain parameters which are fitted using the huge amount of NN scattering data collected such as phase shifts, and the deuteron binding energy.

The most advanced models rely on low-energy effective fields theory (EFT) of the QCD, chiral EFT [2]. This theory has an infinite number of terms and cannot be renormalized. Ab initio calculations can be done exactly for the lightest nuclei (A=3,4) [3–6]. However in last years there has been much progress and have been apply also to other nuclei. For example for nuclei up to $A \leq 12$ the Green's Function Monte Carlo Method (GFMC) [7–9] has been applied. The No-Core Shell Model (NCSM) with its importance-truncate extension has been used in oxygen isotopes [10]. Now, a big effort

is being done in other extensions such as the symmetry-adapted NCSM and no-core shell model [11] and the no-core Monte-Carlo [12].

Also in the calcium region methods as Coupled Cluster (CCM) [13–17] , the Self-Consistent Green's Function (SCGF) [18] and the In-Medium Similarity Renormalization Group (IM-SRG) [10, 19, 20] have been applied with high accuracy.

Not only bound-state properties of nuclei are properly described, but also methods such as Faddeev [21] , Faddeev-Yakubobsky [22,23], Alt-Grassberger and Sandhas (AGS) [24] and Hyperspherical Harmonics (HH) [25] have included continuum degrees of freedom in A=3,4 systems.

In other mass regions other approaches have to be used at the moment.

2.1.2 Interacting shell model

Both mean field approaches and shell model approaches, describe the nucleus as a system of fermions moving in an external potential generated by the rest of the nucleons. Bare realistic interactions cannot be used in methods such as HF because of the nearly divergent repulsive behavior at short distances.

Nuclear shell model [26] is based on the experimental evidence of extra binding energies in some precise values of the neutron a proton numbers. These numbers are known as magic numbers. To explain this fact, a model of independent nucleons moving in an harmonic oscillator potential plus a strong attractive spin-orbit term is proposed. We construct the wave function solution

(which is a Slater determinant) by filling the lowest orbits of the potential. However new effective nucleon-nucleon interactions have been constructed that contain both two and three-body contributions. The two-body terms are derived from realistic potentials (are consistent with two nucleon data), and the three-body contribution incorporate the monopole terms necessary to correct the bad saturation properties of the realistic interactions. As the number of nucleons grows the Hilbert space becomes intractable and it has to be reduced in some way. The system is divided into a core (completely full) and a valence space; where the problem is solved. In each of valence space an effective interaction is used which is fitted using experimental data. Some examples [27] are the TBME,POT,PWBT in the "p" valence space, the USD, USDA, USDB,SDPOTA in the "sd" shell, the FPMG,GCFP in the "pf" shell, or in heavy region interactions such as GCN28-50 in the $r_3 - g_{9/2}(d_{5/2})$ and GCN50-82 in the $r_4 - h_{11/2}$. This model provides a very precise description of the nuclear spectra. However the need of experimental data to refine the different interactions in each valence space reduces its predictive power. In addition, the applicability regions are limited to those close to magic numbers, where the valence space is small enough to be tractable. However, it is now possible to diagonalize matrices in determinantal spaces of dimensionality up 10^9, which makes more regions accessible to these approaches. In addition many new approximation methods have been developed in order to overcome the dimensionality limitations.

2.2 Phenomenological effective interactions

As we said, due to the repulsive divergent character at short distances, bare nucleon-nucleon interactions cannot be used directly in many-body theories. Effective interactions must be used instead. We can obtain these interactions by a more fundamental point of view; with the renormalization of the bare nucleon-nucleon interaction, or in a phenomenological way, proposing a functional dependent of several parameters and fitting them to describe global properties of selected nuclei or nuclear matter. The latter, on contrast to those used on shell model calculations, are independent of the mass region, which provides them more predictive power. The most widely used are Skyrme, Gogny and/or Relativistic ones.

2.2.1 Skyrme interaction

The Skyrme interaction has been widely used [28] to study masses, radii, quadrupole deformations, fission barriers ...etc. It is a very short range interaction (with a radial delta dependence $\delta(\vec{r}_i - \vec{r}_j)$). This reduces the computational effort substantially. The interaction was first proposed with two and three body terms [29–31]:

$$V = \sum_{i<j} v^2_{ij} + \sum_{i<j<k} v^3_{ijk} \tag{2.1}$$

In the momentum space:

$$\langle \vec{k}|v_{12}|\vec{k}\,'\rangle = t_0(1+x_0P_\sigma)+\frac{1}{2}t_1(\vec{k}+\vec{k}\,')+t_2\vec{k}\cdot\vec{k}\,'+iW_0(\vec{\sigma}_1+\vec{\sigma}_2)\cdot\vec{k}\cdot\vec{k}\,' \quad (2.2)$$

where $\vec{k}=\frac{\nabla_1-\nabla_2}{2i}$ acting to the right and $\vec{k}\,'=-\vec{k}$ but acting on the left. P_σ in the spin exchange operator and $\vec{\sigma}$ are the Pauli matrices. In the coordinate space;

$$\begin{aligned} v_{12} &= t_0(1+x_0P_\sigma)\delta(\vec{r_1}-\vec{r_2})+ \\ &+ \frac{1}{2}t_1[\delta(\vec{r_1}-\vec{r_2})\vec{k}^2+\vec{k}\,'^2\delta(\vec{r_1}-\vec{r_2})]+ \\ &+ \vec{k}\,'\cdot\delta(\vec{r_1}-\vec{r_2})\cdot\vec{k}+iW_0(\vec{\sigma}_1+\vec{\sigma}_2)\cdot\vec{k}\,'\times\delta(\vec{r_1}-\vec{r_2})\cdot\vec{k} \end{aligned} \quad (2.3)$$

The three body term has the form;

$$v(1,2,3)=t_3\delta(\vec{r_1}-\vec{r_2})\delta(\vec{r_2}-\vec{r_3}) \quad (2.4)$$

For a Hartree-Fock calculation with even nuclei this last term is equivalent to;

$$v(1,2)_{dens}=\frac{1}{6}t_3(1+P_\sigma)\delta(\vec{r_1}-\vec{r_2})\rho^\alpha(\frac{\vec{r_1}+\vec{r_2}}{2}) \quad (2.5)$$

where α is usually $\frac{1}{3}$ or $\frac{1}{6}$. The different parameters of the Skyrme interaction are fitted using experimental data. Depending which data we want to reproduce a different parametrization can be used:

1. SI-SVI,SKV,SKa,SKb [31–34]

2. SKM,SKM*,SKP [35]

3. SLy1-SLy10 [36]

4. SkI1-5 [37]

5. BSk1,MSk1-7 [38]

6. SLyMR0 [39] For multi reference calculations

One of the main disadvantages of the Skyrme interaction, which comes from the short range of the force, is the inability to describe pairing interactions. Therefore in mean field calculations it has to be incorporated ad hoc. Usually for the p-p chaannel a contact term is used;

$$v(1,2)_{pai} = G\delta(\vec{r}_1 - \vec{r}_2) \tag{2.6}$$

This gives rise to a pairing field that has a volume character [40]. By adding a density-dependent component, the pairing field becomes surface peaked [41]:

$$v(1,2)_{pai} = G\delta(\vec{r}_1 - \vec{r}_2)[1 - \frac{\rho(\vec{r}_1)^{\gamma}}{\rho_c}] \tag{2.7}$$

where G, ρ_c, γ are also fitting terms. If ρ_c is chosen such that it is close to the saturation density $\rho_c \sim \rho_0(\vec{r}_1 = 0)$, the pairing potential is small in the nuclear interior, and the pairing field becomes surface-peaked. By varying the magnitude of the density-dependent term, the transition from volume pairing to surface pairing can be probed. In addition, as a consequence of the zero range of the force the elements with high moments are very big and a divergent behavior appears in this channel. To solve this a cut-off is included

in this channel, so the only accessible space for the pairing is the one near the Fermi level.

As we mentioned the HF part and the pairing parts are taken from different functionals. This leads to problems when extending this approach beyond mean field [42]. For example, in order to avoid divergences in the particle number restoration, all terms (Hartree, Fock and pairing) of every term of the interaction must be taken into account, which is not possible with the Skyrme functionals.

2.2.2 Gogny energy density functional

Daniel Gogny proposed this interaction in 1973 [43] This is a finite range density dependent force and has widely used in mean field and beyond bean field with excellent results in the description of nuclear radii, binding energies, nuclear spectra ... The form of the functional is the following [44, 45];

$$\begin{aligned} V_{12} &= \sum_{ij} e^{-(\vec{r}_1-\vec{r}_2)^2/\mu_i^2}(W_i + B_i P_\sigma - H_i P_\tau - M_i P_\sigma P_\tau) \\ &+ iW_{LS}(\vec{\sigma}_1 + \vec{\sigma}_2)\cdot\vec{k}\times\delta(\vec{r}_1-\vec{r}_2)\vec{k} \\ &+ (1+x_0 P_\sigma)\delta(\vec{r}_1-\vec{r}_2)\rho^\alpha(\frac{\vec{r}_1+\vec{r}_2}{2}) \end{aligned} \tag{2.8}$$

where $\mu_i, W_i, B_i, H_i, M_i, W_{LS}, t_3, x_0$ are parameters that have to be fitted using experimental data and where $\vec{k} = \frac{\nabla_1-\nabla_2}{2i}$, $P_{\sigma(\tau)}$ in the spin(isospin) exchange operators. Spin orbit terms and density dependent terms coincide in Skyrme and Gogny. However the central term (Brink Boeker) is of a finite

range composed by two Gaussians and posses all possible spin and isospin exchanges. This is the reason why the pairing terms appear naturally in this functional. Therefore all terms (Hartree, Fock and pairing) can be extracted from the same functional, avoiding divergence problems when restoring particle number. There are not many parameterizations of the Gogny density functional (D1,D1',D1S) and more recently D1M [46] and D1N [47]. D1N was built so as to reproduce, at low densities, the neutron matter EOS provided by more fundamental approaches based on the bare nucleon-nucleon force. D1M was fitted to accurately estimate nuclear masses, and for the first time, the mass formula takes an explicit and self-consistent account of all quadrupole correlations affecting the binding energy. More recently a Gogny force with a finite-range density dependence (D2 parametrization) has also been proposed [48]. The parameters of the different parameterizations are listed on table 2.2.2. D1S parametrization is the most extended and is the one used in this work. The fitting of the different parameters was done taking into account [45, 49]:

1. W_{LS} with the splitting of levels $\epsilon_{p3/2} - \epsilon_{p1/2}$ in ^{16}O

2. The density dependent term with the energy difference of $\epsilon_{d3/2} - \epsilon_{p1/2}$ in ^{16}O

3. Symmetry term with the energy difference of $\epsilon_{2s1/2}(neutron) - \epsilon_{p1/2}(proton)$ in ^{48}Ca and with nuclear matter properties.

4. Brink Boeker term using saturation properties of ^{16}O and ^{90}Zr,the spectra of the former, the binding energy per nucleon and the saturation

D1	μ_i	W_i	B_i	H_i	M_i	W_{LS}	t_3
i=1	0.7	-402.4	-100	-496.2	-23.56	-115	1350
i=2	1.2	-21.30	-11.77	37.27	-68.82		
D1'	μ_i	W_i	B_i	H_i	M_i	W_{LS}	t_3
i=1	0.7	-402.4	-100	-496.2	-23.56	-130	1350
i=2	1.2	-21.30	-11.77	37.27	-68.82		
D1S	μ_i	W_i	B_i	H_i	M_i	W_{LS}	t_3
i=1	0.7	-1720.30	-1300	-1813.53	1397.90	-130	1390.60
i=2	1.2	103.64	-163.48	162.81	-223.93		
D1N	μ_i	W_i	B_i	H_i	M_i	W_{LS}	t_3
i=1	0.8	-2133.488	-1800.000	-2537.205	1582.953	-115	1631.0
i=2	1.2	308.451	-316.444	437.075	-325.445		
D1M	μ_i	W_i	B_i	H_i	M_i	W_{LS}	t_3
i=1	0.5	-12797.57	14048.85	-15144.43	11963.89	-115.36	1562.22
i=2	1.0	90.95	-752.27	675.12	-693.572		

Table 2.1: Parameters of the different Gogny parameterizations. The index "i" refers to each of the gaussians on expression 2.8. μ in fm, $W_i, B_i, H_i, M_i, W_{LS}$ in MeV and t_3 in MeVfm . For all parameterizations $\alpha = 1/3$ and $x_0 = 1.0$.

Fermi moment in nuclear matter.

5. Pairing term using the Sn isotopic chain properties.

6. The height of the fission barrier for the second minima in ^{240}Pu.

2.2.3 Relativistic Mean-Field

Finally relativistic mean field aproaches (RMF) [50, 51] have also been used to perform systematic nuclear studies [52] The many-body state is built up as an independent particle or quasi-particle state from single-particle wave

functions. Now these are four-component Dirac spinors. Instead of the non relativistic Schrdinger equation we now have an effective Lagrangian density. From that the equations of movement are deduced. The interaction can be point like or through meson fields. The Lagrange density of the latter is of the form:

$$\begin{aligned}\mathcal{L} &= \bar{\psi}(\gamma(i\partial - g_\omega\omega - g_\rho\vec{\rho}\vec{\tau} - eA) - m - g_\sigma\sigma)\psi \\ &+ \frac{1}{2}(\partial\sigma)^2 - U(\sigma) - \frac{1}{4}\Omega_{\mu\nu}\Omega^{\mu\nu} + \frac{1}{2}m_\omega^2\omega^2 \\ &- \frac{1}{4}\vec{R}_{\mu\nu}\vec{R}^{\mu\nu} + \frac{1}{2}m_\rho^2\vec{\rho}^2 - \frac{1}{4}F_{\mu\nu}F^{\mu\nu} \end{aligned} \tag{2.9}$$

with

$$U(\sigma) = \frac{1}{2}m_\sigma^2\sigma^2 + \frac{1}{3}g_2\sigma^3 + \frac{1}{4}g_3\sigma^4 \tag{2.10}$$

where ψ is the Dirac spinor. This expression contains the Lagrangian of the free nucleons of mass m, the Lagrangian of the free messons (σ, ω, ρ) with masses $(m_\sigma, m_\omega, m_\rho)$, the electromagnetic field and non-linear self-interactions of the σ field. The Lagrangian parameters are obtained by a fitting procedure to some bulk properties of spherical nuclei. The most frequently used are NL1 [21], NL-SH [53] and PL-40 [54]. The latter gives good results in fission barriers. NL1 describes accurately regions along the beta stability line (binding energies, radii, and even superdeformed bands), but is worse far from this region. The NL-SH improve this situation, and also describes deformation properties in a better way. However it produces a slight over-binding along the line of beta-stability and fails to reproduce the superdeformed minima in Hg-isotopes. Another parametrization, NL3 [55], has produced an excellent

agreement with the experimental nuclear masses, as well as the deformation properties, reproducing for the first time the isoscalar monopole energies of Pb and Zr nuclei. More recently a modification of this parameter set (the NL3* [56]) was proposed, which improves the description of ground state properties of many nuclei and simultaneously provides an excellent description of excite states with collective character in spherical as well as deformed nuclei.

Bibliography

[1] Petr Navrtil, Sofia Quaglioni, Guillaume Hupin, Carolina Romero-Redondo, and Angelo Calci. *Physica Scripta*, 91(5):053002, 2016.

[2] Steven Weinberg. *Nuclear Physics B*, 363(1):3 – 18, 1991.

[3] Nir Barnea, Winfried Leidemann, and Giuseppina Orlandini. *Nuclear Physics A*, 693(3-4):565–578, oct 2001.

[4] A. Nogga, D. Hüber, H. Kamada, and W. Glöckle. *Physics Letters B*, 409(1-4):19–25, sep 1997.

[5] J.L. Friar, G.L. Payne, V.G.J. Stoks, and J.J. de Swart. *Physics Letters B*, 311(1-4):4–8, jul 1993.

[6] H. Kamada, A. Nogga, W. Glöckle, E. Hiyama, M. Kamimura, K. Varga, Y. Suzuki, M. Viviani, A. Kievsky, S. Rosati, J. Carlson, Steven C. Pieper, R. B. Wiringa, P. Navrátil, B. R. Barrett, N. Barnea, W. Leidemann, and G. Orlandini. *Phys. Rev. C*, 64:044001, Aug 2001.

[7] R. B. Wiringa and Steven C. Pieper. *Phys. Rev. Lett.*, 89:182501, Oct 2002.

[8] B. S. Pudliner, V. R. Pandharipande, J. Carlson, and R. B. Wiringa. *Phys. Rev. Lett.*, 74:4396–4399, May 1995.

[9] Steven C. Pieper and R. B. Wiringa. *Annual Review of Nuclear and Particle Science*, 51, December 2001.

[10] H. Hergert, S. Binder, A. Calci, J. Langhammer, and R. Roth. *Phys. Rev. Lett.*, 110:242501, Jun 2013.

[11] T. Dytrych, K. D. Launey, J. P. Draayer, P. Maris, J. P. Vary, E. Saule, U. Catalyurek, M. Sosonkina, D. Langr, and M. A. Caprio. *Phys. Rev. Lett.*, 111:252501, Dec 2013.

[12] T. Abe, P. Maris, T. Otsuka, N. Shimizu, Y. Utsuno, and J. P. Vary. *Phys. Rev. C*, 86:054301, Nov 2012.

[13] G. Hagen et al. *Nature Physics*, 12:186190, 2016.

[14] M. Włoch, D. J. Dean, J. R. Gour, M. Hjorth-Jensen, K. Kowalski, T. Papenbrock, and P. Piecuch. *Phys. Rev. Lett.*, 94:212501, Jun 2005.

[15] G. Hagen, T. Papenbrock, and M. Hjorth-Jensen. *Phys. Rev. Lett.*, 104:182501, May 2010.

[16] G. Hagen, M. Hjorth-Jensen, G. R. Jansen, R. Machleidt, and T. Papenbrock. *Phys. Rev. Lett.*, 109:032502, Jul 2012.

[17] S. Bacca, N. Barnea, G. Hagen, G. Orlandini, and T. Papenbrock. *Phys. Rev. Lett.*, 111:122502, Sep 2013.

[18] A. Cipollone, C. Barbieri, and P. Navrátil. *Phys. Rev. Lett.*, 111:062501, Aug 2013.

[19] K. Tsukiyama, S. K. Bogner, and A. Schwenk. *Phys. Rev. Lett.*, 106:222502, Jun 2011.

[20] S. K. Bogner, H. Hergert, J. D. Holt, A. Schwenk, S. Binder, A. Calci, J. Langhammer, and R. Roth. *Phys. Rev. Lett.*, 113:142501, Oct 2014.

[21] P. G. Reinhard, M. Rufa, J. Maruhn, W. Greiner, and J. Friedrich. *Zeitschrift für Physik A Atomic Nuclei*, 323(1):13–25, 1986.

[22] Rimantas Lazauskas. *Phys. Rev. C*, 79:054007, May 2009.

[23] Rimantas Lazauskas and Jaume Carbonell. *Phys. Rev. C*, 70:044002, 2004.

[24] A. Deltuva and A. C. Fonseca. *Phys. Rev. Lett.*, 98:162502, Apr 2007.

[25] L. E. Marcucci, A. Kievsky, L. Girlanda, S. Rosati, and M. Viviani. *Phys. Rev. C*, 80:034003, Sep 2009.

[26] E. Caurier, G. Martínez-Pinedo, F. Nowacki, A. Poves, and A. P. Zuker. *Rev. Mod. Phys.*, 77:427–488, Jun 2005.

[27] B.A. Brown. *Progress in Particle and Nuclear Physics*, 47(2):517 – 599, 2001.

[28] Michael Bender, Paul-Henri Heenen, and Paul-Gerhard Reinhard. *Rev. Mod. Phys.*, 75:121–180, Jan 2003.

[29] T.H.R. Skyrme. *Phil.Mag*, 1:1043, 1956.

[30] T.H.R. Skyrme J.S. Bell. *Phil.Mag*, 1:1055, 1956.

[31] D. Vautherin and D. M. Brink. *Phys. Rev. C*, 5:626–647, Mar 1972.

[32] W. Satuła, J. Dobaczewski, W. Nazarewicz, and M. Rafalski. *Phys. Rev. C*, 81:054310, May 2010.

[33] W. Satuła, J. Dobaczewski, W. Nazarewicz, and T. R. Werner. *Phys. Rev. C*, 86:054316, Nov 2012.

[34] M. Beiner, H. Flocard, Nguyen Van Giai, and P. Quentin. *Nuclear Physics A*, 238(1):29 – 69, 1975.

[35] J. Dobaczewski, H. Flocard, and J. Treiner. *Nuclear Physics A*, 422(1):103 – 139, 1984.

[36] E. Chabanat, P. Bonche, P. Haensel, J. Meyer, and R. Schaeffer. *Nuclear Physics A*, 635(1):231 – 256, 1998.

[37] P.-G. Reinhard and H. Flocard. *Nuclear Physics A*, 584(3):467 – 488, 1995.

[38] S. Goriely, F. Tondeur, and J.M. Pearson. *Atomic Data and Nuclear Data Tables*, 77(2):311 – 381, 2001.

[39] J Sadoudi, M Bender, K Bennaceur, D Davesne, R Jodon, and T Duguet. *Physica Scripta*, (T154):014013, 2013.

[40] E. E. Saperstein and M. A. Troitskil. *Sov. J. Nucl. Phys*, 1(284), 1965.

[41] R. R. Chasman. *Phys. Rev. C*, 14:1935–1945, Nov 1976.

[42] M. Anguiano, J.L. Egido, and L.M. Robledo. *Nuclear Physics A*, 696(3):467 – 493, 2001.

[43] D. Gogny. *Nuclear selfconsistent fields*, Eds. G. Ripka, M. Porneuf. North Holland, 1975.

[44] D. Gogny. *Nuclear Physics A*, 237(3):399 – 418, 1975.

[45] J. Dechargé and D. Gogny. *Phys. Rev. C*, 21:1568–1593, Apr 1980.

[46] S. Goriely, S. Hilaire, M. Girod, and S. Péru. *Phys. Rev. Lett.*, 102:242501, Jun 2009.

[47] F. Chappert, M. Girod, and S. Hilaire. *Physics Letters B*, 668(5):420 – 424, 2008.

[48] F. Chappert, N. Pillet, M. Girod, and J.-F. Berger. *Phys. Rev. C*, 91:034312, Mar 2015.

[49] J.F. Berger, M. Girod, and D. Gogny. *Computer Physics Communications*, 63(1):365 – 374, 1991.

[50] Brian D. Serot and John Dirk Walecka. *Adv. Nucl. Phys.*, 16:1–327, 1986.

[51] D. Vretenar, A.V. Afanasjev, G.A. Lalazissis, and P. Ring. *Physics Reports*, 409(34):101 – 259, 2005.

[52] A Shukla, Sven berg, and Awanish Bajpeyi. *Journal of Physics G: Nuclear and Particle Physics*, 44(2):025104, 2017.

[53] M. M. Sharma, M. A. Nagarajan, and P. Ring. *Phys. Lett.*, B312:377–381, 1993.

[54] P. G. Reinhard. *Zeitschrift für Physik A Atomic Nuclei*, 329(3):257–266, 1988.

[55] G. A. Lalazissis, J. Konig, and P. Ring. *Phys. Rev.*, C55:540–543, 1997.

[56] G.A. Lalazissis, S. Karatzikos, R. Fossion, D. Pena Arteaga, A.V. Afanasjev, and P. Ring. *Physics Letters B*, 671(1):36 – 41, 2009.

Chapter 3

Mean Field and Beyond Mean Field Methods

In the first section of this chapter we study in the first section the most general mean field approximation; the Hartree-Fock-Bogoliubov Method (HFB). In the second section we describe the general concepts of the Beyond Mean Field approximations (BMF) used in our work; the Generator Coordinate Method (GCM) and the projection methods.

3.1 Hartree-Fock-Bogoliubov Method

As we have seen, to solve the nuclear many-body problem we have to do some approximations. In this chapter we will study the HFB method which is the starting point of our calculation. In this theory we propose a trial

wave function which is as a product of quasi-particles, and using the Ritz variational principle we look for the best solution among them. Note that the Ritz theorem guarantees obtaining the exact solution as long as it is in the trial variational space.

3.1.1 HFB transformation

The simplest wave function we can propose to describe a fermion system is a Slater determinant; i.e. an antisymmetrized product of one particle states. The variational method applied to this system leads to the HF equations. The solution corresponds to a system of non-interacting particles moving in an external potential. In this approach only long range correlation (p-h correlations) are included. If we want to include short range correlation (p-p correlations) , without loosing this non-interacting picture, we can propose a solution which is an antisymmetrized product of *quasi-particles*, obtaining the HFB equations. The quasiparticles β_μ are obtained by the general Bogoliubov transformation [1]:

$$\begin{pmatrix} \beta \\ \beta^\dagger \end{pmatrix} = \mathcal{W}^\dagger \begin{pmatrix} c \\ c^\dagger \end{pmatrix} = \begin{pmatrix} U^\dagger & V^\dagger \\ V^T & U^T \end{pmatrix} \begin{pmatrix} c \\ c^\dagger \end{pmatrix} \tag{3.1}$$

where $\{c_\rho^\dagger, c_\rho\}$ is the set of particle creation and annihilation operators of an arbitrary basis of the Hilbert space. The index ρ label the set of quantum numbers of this basis (for example n_x, n_y, n_z of a three dimensional harmonic oscillator). In order to maintain the anticommutation relations for

$\{\beta^\dagger_\rho, \beta_\rho\}$ the U, V transformation matrices must fulfill the following properties: $\mathcal{W}^\dagger\mathcal{W} = \mathbb{I} \rightarrow$

$$\begin{aligned} U^\dagger U + V^\dagger V &= \mathbb{I}\,, \qquad UU^\dagger + V^\star V^T = \mathbb{I}, \\ U^\dagger V + V^\dagger U &= 0\,, \qquad UV^\dagger + V^\star U^T = 0 \end{aligned} \tag{3.2}$$

The Bloch-Messiah theorem [2] ensures that the previous transformation can be written as three successive transformations:

1. A unitary D transformation between particle operators:

$$a^\dagger_\rho = \sum_\mu D_{\mu\rho} c^\dagger_\mu \tag{3.3}$$

2. A BCS type transformation:

$$\begin{aligned} \alpha^\dagger_k &= u_k a^\dagger_k - v_k a_{\bar{k}}\,, \qquad \alpha_k = u_k a_k - v_k a^\dagger_{\bar{k}} \\ \alpha^\dagger_{\bar{k}} &= u_k a^\dagger_{\bar{k}} + v_k a_k\,, \qquad \alpha_{\bar{k}} = u_k a_{\bar{k}} + v_k a^\dagger_k \end{aligned} \tag{3.4}$$

   where $k, \bar{k}$ label canonical conjugate states.

3. A unitary transformation C between quasi-particles;

$$\beta^\dagger_\rho = \sum_\mu C_{\mu\rho} \alpha^\dagger_\mu \tag{3.5}$$

These three transformations can be written

$$\mathcal{W} = \begin{pmatrix} D & 0 \\ 0 & D^\star \end{pmatrix} \begin{pmatrix} \bar{U} & \bar{V} \\ \bar{V} & \bar{U} \end{pmatrix} \begin{pmatrix} C & 0 \\ 0 & C^\star \end{pmatrix} \tag{3.6}$$

or

$$U = D\bar{U}C \qquad V = D^\star \bar{V} C^\star \tag{3.7}$$

These matrices $\bar{U}, \bar{V}$ are of the special form;

$$\bar{U} = \left[\begin{array}{ccccc|c} 0 & & & & & \\ & \ddots & & & & \\ & & 0 & & & \\ \hline & & u_1 \quad 0 & & & \\ & & 0 \quad u_1 & & & \\ \hline & & & \ddots & & \\ \hline & & & & u_n \quad 0 & \\ & & & & 0 \quad u_n & \\ \hline & & & & & 1 \\ & & & & & \ddots \\ & & & & & 1 \end{array}\right] \tag{3.8}$$

$$\bar{V} = \left[\begin{array}{ccc|cc|cc} 1 & & & & & & \\ & \ddots & & & & & \\ & & 1 & & & & \\ \hline & & & 0 & v_1 & & \\ & & & -v_1 & 0 & & \\ \hline & & & & & \ddots & \\ \hline & & & & & 0 & v_n \\ & & & & & -v_n & 0 \\ \hline & & & & & & 0 \\ & & & & & & \ddots \\ & & & & & & 0 \end{array}\right] \tag{3.9}$$

where each small box contains the u, v amplitudes for both signatures $u_i = u_{\bar{i}}, v_i = -v_{\bar{i}}$. The states with $u_i = 0, v_i = 1$ are occupied states, while the states with $u_i = 1, v_i = 0$ are empty states.

3.1.2 HFB equations

The most general (non relativistic) Hamiltonian $\hat{H}$ with one and two body interactions [3];

$$\hat{H} = \sum_{\mu_1\mu_2} t_{\mu_1\mu_2} c^\dagger_{\mu_1} c_{\mu_2} + \frac{1}{4} \sum_{\mu_1\mu_2\mu_3\mu_4} \bar{v}_{\mu_1\mu_2\mu_3\mu_4} c^\dagger_{\mu_1} c^\dagger_{\mu_2} c_{\mu_4} c_{\mu_3} \tag{3.10}$$

with $\bar{v}_{\mu_1\mu_2\mu_3\mu_4} = v_{\mu_1\mu_2\mu_3\mu_4} - v_{\mu_1\mu_2\mu_4\mu_3}$ is written in the quasi-particle basis:

$$\hat{H} = H_0 + \sum_{\mu_1\mu_2} H^{11}_{\mu_1\mu_2}\beta^\dagger_{\mu_2}\beta_{\mu_2^\dagger+\sum_{\mu_1<\mu_2}}(H^{20}_{\mu_1\mu_2}\beta^\dagger_{\mu_2}\beta^\dagger_{\mu_2} + h.c) + H_{int} \tag{3.11}$$

The indexes $i,(j)$ in $H^{i,j}_{\mu_1\mu_2}$ matrices refer to the number of creation (annihilation) operators $\beta^\dagger(\beta)$. H^{int} is the contribution of the rest of possible terms; $H^{31}, H^{13}, H^{40}, H^{04}, H^{22}$.

The matrices H^{20} and H^{11} are related to the amplitudes U, V of the Bogoliubov transformation 3.1 and 3.10 by:

$$\begin{aligned} H^{20} = U^\dagger(t+\Gamma+\delta\Gamma)V^\star - V^\dagger(t+\Gamma+\delta\Gamma)^T U^\star \\ +U^\dagger\Delta U^\star - V^\dagger\Delta^\star V^\star \end{aligned} \tag{3.12}$$

$$\begin{aligned} H^{11} = U^\dagger(t+\Gamma+\delta\Gamma)U - V^\dagger(t+\Gamma+\delta\Gamma)^T V \\ +U^\dagger\Delta V - V^\dagger\Delta^\star U \end{aligned} \tag{3.13}$$

where we defined the fields:

$$\Gamma_{\mu\mu'} = \sum_{\gamma\gamma'} \bar{v}_{\mu\gamma\mu'\gamma'}\rho_{\gamma'\gamma} \tag{3.14}$$

$$\Delta_{\mu\mu'} = \sum_{\gamma\gamma'} \bar{v}_{\mu\mu'\gamma\gamma'}\kappa_{\gamma\gamma'} \tag{3.15}$$

and the density matrix ρ and the pairing tensor κ as:

$$\rho_{\mu\mu'} = \langle\Phi|c^\dagger_{\mu'}c_\mu|\Phi\rangle = (V^\star V^T)_{\mu\mu'} \tag{3.16}$$

$$\kappa_{\mu\mu'} = \langle\Phi|c_{\mu'}c_\mu|\Phi\rangle = (V^\star U^T)_{\mu\mu'} \tag{3.17}$$

$$\tag{3.18}$$

The terms $\delta\Gamma$ are called rearrangement terms and are a consequence of the explicit density-dependence of the Hamiltonian. Now we apply the variational principle to

$$E[U,V] = \frac{\langle\Phi[U,V]|\hat{H}|\Phi[U,V]\rangle}{\langle\Phi[U,V]|\Phi[U,V]\rangle} \tag{3.19}$$

to obtain the best U, V. However, thanks to Thouless theorem [4] we can express any wave function $|\Phi'(\mathbb{Z})\rangle$ non orthogonal to $|\Phi\rangle$ using

$$|\Phi'(\mathbb{Z})\rangle = \langle\phi|\phi'(\mathbb{Z})\rangle e^{\sum_{k<k'}\mathbb{Z}_{kk'}\beta^\dagger_k\beta^\dagger_{k'}}|\Phi\rangle \tag{3.20}$$

where $\mathbb{Z}$ is a skew symmetric matrix and depends on the amplitudes U, V. Applying the variational principle $\mathbb{Z}$ is found (an therefore the best U, V) [3]:

$$\frac{\partial}{\partial\mathbb{Z}^\star}\frac{\langle\Phi'(\mathbb{Z})|\hat{H}|\Phi'(\mathbb{Z})\rangle}{\langle\Phi'(\mathbb{Z})|\Phi'(\mathbb{Z})\rangle}\bigg|_{\mathbb{Z}=0} \delta(\mathbb{Z}) = 0 \rightarrow H^{20} = 0 \tag{3.21}$$

where H^{20} was given in 3.13. As a consequence of the use of the HFB transformation, which mixes creation and annihilation operators, the particle number is not longer a good quantum number. If we want to conserve this

number at least in average, we must use a modified Hamiltonian;

$$\hat{H}' = \hat{H} - \lambda_N \hat{N} - \lambda_Z \hat{Z} \tag{3.22}$$

and instead of $\hat{H}$ minimize $\hat{H}'$ obtaining;

$$(H^{20} - \lambda_N \hat{N}^{20} - \lambda_Z \hat{Z}^{20}) = 0 \tag{3.23}$$

where λ_Z and λ_N are Lagrange multipliers and are found by the condition:

$$\langle \Phi | \hat{Z} | \Phi \rangle = Z \ , \qquad \langle \Phi | \hat{N} | \Phi \rangle = N \tag{3.24}$$

and $Z^{20}(N^{20}) = \langle \Phi | [\beta_{k'}\beta_k, \hat{Z}(\hat{N})] | \Phi \rangle$. This is solved using the conjugate gradient method [5]. We can extend this procedure to any desired operator $\hat{Q}$, using as many Lagrange multipliers as we need, and solve the general constrained HFB equation:

$$H^{20} - \lambda_N \hat{N}^{20} - \lambda_Z \hat{Z}^{20} - \sum_i \lambda_i Q_i^{20} = 0 \tag{3.25}$$

where in general, $Q_i^{20} = \langle \Phi | [\beta_{k'}\beta_k, \hat{Q}] | \Phi \rangle$.

It is believed that the largest energy dependence of the nuclear interaction is related to the deformation parameters (β, γ), so the quadrupole moment operators $\hat{Q}_{20}, \hat{Q}_{22}$ will be considered throughout this work. Their mean

values q_{20}, q_{22} are related to the deformation parameters by:

$$q_{20} = \frac{\beta_2 \cos\gamma}{C}; q_{22} = \frac{\beta_2 \sin\gamma}{\sqrt{2}C}; C = \frac{4\pi}{3r_0^2 A^{5/3}}\sqrt{\frac{5}{4\pi}} \tag{3.26}$$

with $r_0 = 1.2fm$. As in 3.24, the Lagrange multipliers $\lambda_{q_0}, \lambda_{q_2}$ are found by the condition

$$\langle \hat{Q}_{20} \rangle = q_{20}\ ; \quad \langle \hat{Q}_{22} \rangle = q_{22} \tag{3.27}$$

Pairing fluctuations can be self-consistently incorporated as well as the quadrupole deformations. The best operator to constrain in this case is [6–8] $\Delta\hat{N}^2 = (\hat{N} - \langle \hat{N} \rangle^2)$ operator, being $\hat{N}$ the number of particles, protons or neutrons, as is closely connected with the pairing gap Δ.

3.1.3 Cranking approximation

Apart from a constraint in the quadrupole deformations, we can also add the term $-\omega \hat{J}_x$ on the Hamiltonian, where ω is called the cranking frequency and $\hat{J}_x$ is the x-component of the total angular momentum $\hat{J}$. The addition of this term breaks explicitly the time reversal symmetry. This term is important for two main reasons:

1. Introduction of angular content on the wave function

   Consider an even-even system. The absence of the cranking term in the Hamiltonian H' is equivalent to use $\langle \hat{J}_x \rangle = 0$, and therefore all states with no angular content are favored at mean field level. As a consequence, when we recover rotational invariance (see next section),states

with $J \neq 0$ are disfavored and the spectra is stretched. In odd nuclei the absence of cranking also favors the wave functions with smaller angular momentum and therefore the spectra is also stretched. We will see that the inclusion of this term results in an improvement on this matter.

2. Inclusion of aligned states

   Single-particle effects through pair alignment are also included with the cranking procedure. We will see that the inclusion of the cranking term opens the possibility of including np-nh excitations coupled to angular momentum different from zero, providing the possibility of studying new states.

We can include angular momentum content in two different ways:

1. Constraining the expected value of $\hat{J}_x$

   Lets call the intrinsic angular momentum which is included in the wave function J_c. Using the Kamlah expansion [9, 10] this angular momentum content is given :

$$\langle J_x \rangle = \sqrt{J_c(J_c+1) - \langle \hat{J}_z^2 \rangle} \tag{3.28}$$

   so the cranking frequency ω acts as a lagrange multiplier.

2. Fixing the cranking frequency . In this case we do not set a particular angular momentum content.

Both ways are studied in the present work.

3.2 Beyond Mean Field Methods

Product-type wave functions are easy to work with. However more complex solutions must be proposed if we want to recover the symmetries broken and include other type of correlations.

3.2.1 Generator Coordinate Method

In this method the solution is a superposition of product-type wave functions [3] $|\Phi(\vec{q})\rangle$ labeled by a set of parameters $\{\vec{q}\} = q_1, q_2 ...$:

$$|\Psi\rangle = \int f(\vec{q})|\Phi(\vec{q})\rangle d\vec{q} \tag{3.29}$$

The weights $f(\vec{q})$ are determined variationally by minimizing:

$$E[|\Psi\rangle] = \frac{\langle\Psi|\hat{H}|\Psi\rangle}{\langle\Psi|\Psi\rangle} \tag{3.30}$$

This leads to the Hill-Wheeler-Griffin (HWG) equation [11, 12]:

$$\int (\mathcal{H}(\vec{q},\vec{q'}) - E^{\sigma}\mathcal{H}(\vec{q},\vec{q'}))f(\vec{q})d\vec{q} = 0 \tag{3.31}$$

with the energy $\mathcal{H}$ and norm $\mathcal{N}$ overlaps:

$$\mathcal{H}(\vec{q},\vec{q'}) = \langle\Psi(\vec{q})|\hat{H}|\Psi(\vec{q}\,')\rangle \tag{3.32}$$

$$\mathcal{N}(\vec{q},\vec{q'}) = \langle\Psi(\vec{q})|\Psi(\vec{q}\,')\rangle \tag{3.33}$$

and $\sigma = 1, 2, ...$ labels all possible solutions of the eigenvalue problem 3.31 . This equation is solved in the following way:

1. Diagonalization of the norm overlap $\mathcal{N}$:

   In this step we obtain the eigenvalues n_μ and eigenvectors $u_\mu(\vec{q})$.

2. Take the $u_\mu(\vec{q})$ ϵ $n_\mu \neq 0$. This conforms the natural basis $\{\mu\}$

$$|\mu\rangle = \frac{1}{\sqrt{n_\mu}} \int u_\mu(\vec{q})|\Psi(\vec{q})\rangle d\vec{q} \tag{3.34}$$

3. Express the wave function $|\Psi\rangle$ in the natural basis.

$$|\Psi\rangle = \sum_{\mu, n_\mu \neq 0} g_\mu |\mu\rangle \tag{3.35}$$

4. Diagonalize the Hamiltonian $\mathcal{H}$ in the natural basis:

$$\sum_{\mu', n_{\mu'} \neq 0} \langle\mu|\hat{H}|\mu'\rangle g^\sigma_{\mu'} = E^\sigma |\mu\rangle \tag{3.36}$$

   In this last step we obtain the final eigenvalues E^σ. The relation be-

tween these g_μ and the $f(\vec{q})$ on eq 3.29 is:

$$f_\mu = \sum_{n_\mu \neq 0} \frac{g_\mu}{\sqrt{n_\mu}} u_\mu(\vec{q}) \tag{3.37}$$

3.2.2 Projection Methods

Lets suppose our Hamiltonian has a certain symmetry $\hat{S}$: i.e. $[\hat{H}, S] = 0$. If we propose as trial wave functions $|\Phi\rangle$ that are not eigenstates of this symmetry, we will arrive at a solution which is also not an eigenstate of $\hat{S}$, this means;

$$\hat{S}|\Phi\rangle \neq S_i|\Phi\rangle \tag{3.38}$$

Although this has served to include important correlations in the system, the final solution must be an eigenstate of all symmetries of the Hamiltonian. One way of recovering the broken symmetries is by the projection technique [3]. This consists on:

1. Apply the elements of the symmetry group $T(\alpha)$ onto the HFB w.f.:

$$|\Phi(\alpha)\rangle = T(\alpha)|\Phi\rangle \tag{3.39}$$

2. The weights $f(\alpha)$ that convert the wave function into an eigenstate of the desired symmetry and minimizes the energy are determined by the corresponding symmetry [13]:

$$\int f(\alpha)|\Phi(\alpha)\rangle d\alpha = |\Psi^S\rangle \rightarrow \hat{S}|\Psi^S\rangle = S_i|\Phi\rangle \tag{3.40}$$

This defines the operator P^S;

$$P^S = \int f(\alpha)T(\alpha)d\alpha \tag{3.41}$$

An example is the particle number projector operator. In this case $\alpha = \varphi$ is the gauge angle, $T(\alpha) = e^{i\varphi\hat{N}}$, $f(\alpha) = \frac{e^{-i\varphi N}}{2\pi}$, so the projected function is;

$$|\Psi^N\rangle = \frac{1}{2\pi}\int_0^{2\pi} e^{i\varphi(\hat{N}-N)}|\Phi\rangle d\varphi \tag{3.42}$$

The projection can be done after the minimization procedure in the so called Projection After Variation (PAV) or before the minimization in a Variation After Projection (VAP). The first approach is computationally less expensive. We solve equation 3.23 obtaining the HFB solution and after we apply the projection operator to recover the broken symmetry. If we call $|\Phi_{HFB}\rangle$ the solution found by solving 3.23 , the PAV solution is

$$|\Phi^s_{PAV}\rangle = P^S|\Phi_{HFB}\rangle$$

. The PAV energy is given by;

$$\begin{aligned} E^S_{PAV}(\vec{r}) &= \frac{\langle\Phi_{HFB}|(P^S)^\dagger\hat{H}P^S|\Phi_{HFB}\rangle}{\langle\Phi_{HFB}|(P^S)^\dagger P^S|\Phi_{HFB}\rangle} \\ &= \frac{\langle\Phi_{PAV}|\hat{H}|\Phi_{PAV}\rangle}{\langle\Phi_{PAV}|\Phi_{PAV}\rangle} \end{aligned} \tag{3.43}$$

We can calculate the mean value of any operator $\hat{O}$ by:

$$O^S_{PAV}(\vec{r}) = \frac{\langle\Phi_{HFB}|(P^S)^\dagger\hat{O}P^S|\Phi_{HFB}\rangle}{\langle\Phi_{HFB}|(P^S)^\dagger P^S|\Phi_{HFB}\rangle} \tag{3.44}$$

On the other hand, on the VAP approach, the projection is done before the minimization procedure, so we solve:

$$\delta\left(\frac{\langle\Phi(\vec{q})|(P^S)^\dagger\hat{H}P^S|\Phi(\vec{q})\rangle}{\langle\Phi(\vec{q})|(P^S)^\dagger P^S|\Phi(\vec{q})\rangle}-\lambda_{\vec{q}}\langle\Phi(\vec{q})|\hat{\vec{Q}}|\Phi(\vec{q})\rangle\right)=0\rightarrow|\Phi^S_{VAP}(\vec{q})\rangle \quad (3.45)$$

We can calculate the mean value of any operator in this approach;

$$O^S_{VAP}(\vec{r})=\frac{\langle\Phi^S_{VAP}(\vec{q})|\hat{O}|\Phi^S_{VAP}(\vec{q})\rangle}{\langle\Phi^S_{VAP}(\vec{q})|\Phi^S_{VAP}(\vec{q})\rangle} \quad (3.46)$$

Bibliography

[1] N. N. Bogolyubov. *Sov. Phys. JETP*, 7:41–46, 1958. [Front. Phys.6,399(1961)].

[2] Claude Bloch and Albert Messiah. *Nuclear Physics*, 39:95 – 106, 1962.

[3] P. Ring and P. Schuck. *The Nuclear Many-Body Problem*. Physics and astronomy online library. Springer, 2004.

[4] D.J. Thouless. *Nuclear Physics*, 21:225 – 232, 1960.

[5] J.L. Egido, J. Lessing, V. Martin, and L.M. Robledo. *Nuclear Physics A*, 594(1):70 – 86, 1995.

[6] Nuria López Vaquero, Tomás R. Rodríguez, and J. Luis Egido. *Physics Letters B*, 704(5):520 – 526, 2011.

[7] Nuria López Vaquero, Tomás R. Rodríguez, and J. Luis Egido. *Physics Letters B*, 705(5):543 –, 2011.

[8] Nuria López Vaquero, J. Luis Egido, and Tomás R. Rodrguez. *Phys. Rev.*, C88(6):064311, 2013.

[9] Kamlah.A. *Phys. Rev.*, 216:52, 1968.

[10] A. Kamlah. *Nucl. Phys.*, A163:166–192, 1971.

[11] David Lawrence Hill and John Archibald Wheeler. *Phys. Rev.*, 89:1102–1145, Mar 1953.

[12] James J. Griffin and John A. Wheeler. *Phys. Rev.*, 108:311–327, Oct 1957.

[13] H. D. Zeh. *Z. Phys*, 202:38, 1967.

Chapter 4

Symmetries of the wave functions

As we saw, the use of wave functions which are not eigenvectors of one or more operators that commute with the Hamiltonian (symmetry violation) allow to introduce important correlations. However the conservation of some of these symmetries allow us to reduce the computational effort substantially. Therefore it is useful to use a basis which conserves different symmetries of the Hamiltonian. These symmetries are: third component of the isospin, parity, simplex and the $\Pi_2\hat{T}$ symmetry.

4.1 Goodman Basis

On the first place we define the basis used. This is the so-called Goodman basis [1]. The state $|k\rangle$ is the result of the creation of a particle in the vacuum $|-\rangle$:

$$|k\rangle = c_k^\dagger|-\rangle \tag{4.1}$$

The state $|\bar{k}\rangle$ is obtained by the action of $c_{\bar{k}}^\dagger$:

$$|\bar{k}\rangle = c_{\bar{k}}^\dagger|-\rangle \tag{4.2}$$

These operators follow the fermionic anticommutation relations. The states $|k\rangle(|\bar{k}\rangle)$ can be divided into the spatial an spin parts as:

$$|k\rangle = |n_x n_y n_z\rangle|S_k\rangle \ , \qquad |\bar{k}\rangle = |n_x n_y n_z\rangle|S_{\bar{k}}\rangle \tag{4.3}$$

The spatial part is the solution of the three dimensional harmonic oscillator expressed in the Cartesian basis:

$$\langle\vec{r}|n_x n_y n_z\rangle = \phi_{n_x}(x)\phi_{n_y}(y)\phi_{n_z}(z) \tag{4.4}$$

with $\phi_{n_i} = \frac{e^{-\frac{x_i^2}{2b_i^2}}}{\sqrt{(2^{n_i} n_i! b_i\sqrt{\pi})}} H_{n_i}(\frac{x_i}{b_i})$, where H_{n_i} are the Hermite polynomials [2]. The spin part;

$$\begin{aligned} |S_k\rangle &= \frac{i^{n_y}}{\sqrt{2}}(|\uparrow\rangle - (-1)^{n_x}|\downarrow\rangle) \\ |S_{\bar{k}}\rangle &= \frac{i^{n_y}}{\sqrt{2}}(-1)^{n_x+n_y+1}(|\uparrow\rangle + (-1)^{n_x}|\downarrow\rangle) \end{aligned}$$

where $|\uparrow\rangle$ and $|\downarrow\rangle$ represent the two possible values $\pm\frac{\hbar}{2}$ of the third component of the spin $\hat{S}_z$. The operators defined above have the following properties:

The action of the third component of the isospin $\hat{T}_3$:

$$\begin{aligned} e^{-i\hat{T}_3} c_\mu^\dagger e^{i\hat{T}_3} &= e^{it_{3_\mu}} c_\mu^\dagger \,, \qquad e^{-i\hat{T}_3} c_\mu e^{i\hat{T}_3} = e^{it_{3_\mu}} c_\mu \\ e^{-i\hat{T}_3} c_{\bar{\mu}}^\dagger e^{i\hat{T}_3} &= e^{it_{3_\mu}} c_{\bar{\mu}}^\dagger \,, \qquad e^{-i\hat{T}_3} c_{\bar{\mu}} e^{i\hat{T}_3} = e^{it_{3_\mu}} c_{\bar{\mu}} \end{aligned} \tag{4.5}$$

with

$$t_3 \begin{cases} +1/2 \rightarrow \text{proton} \\ -1/2 \rightarrow \text{neutron} \end{cases}$$

The spatial parity $\hat{P}$:

$$\begin{aligned} \hat{P} c_\mu^\dagger \hat{P}^\dagger &= \pi_\mu c_\mu^\dagger \,, \qquad \hat{P} c_\mu \hat{P}^\dagger = \pi_\mu c_\mu \\ \hat{P} c_{\bar{\mu}}^\dagger \hat{P}^\dagger &= \pi_\mu c_{\bar{\mu}}^\dagger \,, \qquad \hat{P} c_{\bar{\mu}} \hat{P}^\dagger = \pi_\mu c_{\bar{\mu}} \end{aligned} \tag{4.6}$$

$$\pi_\mu \begin{cases} +1 \rightarrow \text{positive parity} \\ -1 \rightarrow \text{negative parity} \end{cases}$$

The $\Pi_2 \hat{\mathcal{T}}$ with $\Pi_2 = \hat{P} e^{-i\pi J_y}$, being $\hat{\mathcal{T}} = \hat{K}_0 e^{i\pi \hat{S}_y}$ the time reversal operator,

being $\hat{K}_0$ the complex conjugate operator: $\hat{\mathcal{T}} c_k^\dagger \hat{\mathcal{T}}^\dagger = c_{\bar{k}}^\dagger$

$$\begin{aligned} \Pi_2 \hat{\mathcal{T}} c_\mu^\dagger (\Pi_2 \hat{\mathcal{T}})^\dagger &= c_\mu^\dagger \ , \qquad \Pi_2 \hat{\mathcal{T}} c_\mu (\Pi_2 \hat{\mathcal{T}})^\dagger = c_\mu \\ \Pi_2 \hat{\mathcal{T}} c_{\bar{\mu}}^\dagger (\Pi_2 \hat{\mathcal{T}})^\dagger &= c_{\bar{\mu}}^\dagger \ , \qquad \Pi_2 \hat{\mathcal{T}} c_{\bar{\mu}} (\Pi_2 \hat{\mathcal{T}})^\dagger = c_{\bar{\mu}} \end{aligned} \tag{4.7}$$

The last is the simplex $\Pi_1 = \hat{P} e^{-i\pi J_x}$ with eigenvalue s_μ (which can be $+i$ or $-i$) .

$$\begin{aligned} \Pi_1 c_m^\dagger \Pi_1^\dagger &= i c_m^\dagger \ , \qquad \Pi_1 c_m \Pi_1^\dagger = -i c_m \\ \Pi_1 c_{\bar{m}}^\dagger \Pi_1^\dagger &= -i c_{\bar{m}}^\dagger \ , \qquad \Pi_1 c_{\bar{m}} \Pi_1^\dagger = i c_{\bar{m}} \end{aligned} \tag{4.8}$$

From now on we will use latin indeces to distinguish levels according to their signature $\{k, l, m\}$ (positive) and $\{\bar{k}, \bar{l}, \bar{m}\}$ (negative). We will use greek indeces $\{\rho, \mu\}$ if we do not need to distinguish.

4.2 Imposed symmetries on quasi-particle operators

We now impose these symmetries of the particle operators on the quasi-particle ones.

The $\Pi_2 \hat{\mathcal{T}}$ operator is antilineal. If $\beta, \beta^\dagger$ fulfill 4.7 the amplitudes U, V implies the amplitudes U, V are real quantities.

Now we turn to the implications of the rest of the operators seen in last

sections; $\hat{P}, \Pi_1, e^{-i\hat{T}_3}$. We divide them into two groups, whether they have the same or different actuation on creation and annihilation operators. We start with those operators $\hat{O}$ which have the same actuation on creation and annihilation operators c_μ and $c_\mu^\dagger$ (these are $\hat{P}$ and $e^{-i\hat{T}_3}$). If we impose this symmetry also in the quasi-particle operators:

$$\begin{aligned} \hat{O}\beta_\rho\hat{O}^\dagger &= \hat{O}(\sum_{\mu=1} U_{\mu\rho}c_\mu^\dagger + V_{\mu\rho}c_\mu)\hat{O}^\dagger \\ &= \sum_{\mu=1} o_\mu(U_{\mu\rho}c_\mu^\dagger + V_{\mu\rho}c_\mu) \overset{impose}{\equiv} o_\rho\beta_\rho \end{aligned} \tag{4.9}$$

o_μ must be equal for all μ and we call its value o_ρ.

$$o_\mu = o_\rho \tag{4.10}$$

This means that the transformation **does not mix quasi-particle with different values of this operator** $\hat{O}$, and therefore matrices U and V can be divided in blocks. The third component of the isospin is one example. The possible eigenvalues are $o_\rho = e^{it_3} = \pm 1$ (+ for protons (Z) and - for neutrons (N)). The block structure of U and V is:

$$U = \begin{pmatrix} U^Z & 0 \\ 0 & U^N \end{pmatrix} \quad ; \quad \begin{pmatrix} V^Z & 0 \\ 0 & V^N \end{pmatrix} \tag{4.11}$$

Another example in the spatial parity. In this case $o_\mu = \pi_\mu = \pm 1$

$$U = \begin{pmatrix} U^+ & 0 \\ 0 & U^- \end{pmatrix} \quad ; \quad \begin{pmatrix} V^+ & 0 \\ 0 & V^- \end{pmatrix} \tag{4.12}$$

Finally, the simplex operator has a different actuation on the $c_k^\dagger$ and c_k. We impose the same relation 4.8 on the quasi-particle operators:

$$\Pi_1 \beta_k^\dagger \Pi_1^\dagger = i\beta_k^\dagger \qquad \Pi_1 \beta_{\bar{k}}^\dagger \Pi_1^\dagger = -i\beta_{\bar{k}}^\dagger \tag{4.13}$$

Expanding relation 3.1;

$$\begin{aligned} \beta_k^\dagger &= \sum_{m>0}^{M} U_{mk} c_m^\dagger + V_{mk} c_m + U_{\bar{m}k} c_{\bar{m}}^\dagger + V_{\bar{m}k} c_{\bar{m}} \quad k > 0 \\ \beta_{\bar{k}}^\dagger &= \sum_{m>0}^{M} U_{m\bar{k}} c_m^\dagger + V_{m\bar{k}} c_m + U_{\bar{m}\bar{k}} c_{\bar{m}}^\dagger + V_{\bar{m}\bar{k}} c_{\bar{m}} \quad k < 0 \end{aligned} \tag{4.14}$$

Using 4.8 on 4.14;

$$\begin{aligned} \Pi_1 \beta_k^\dagger \Pi_1^\dagger &= i \sum_{k>0}^{M} \{ U_{mk} c_m^\dagger - V_{mk} c_m - U_{\bar{m}k} c_{\bar{m}}^\dagger + V_{\bar{m}k} c_{\bar{m}} \} \\ \Pi_1 \beta_{\bar{k}}^\dagger \Pi_1^\dagger &= i \sum_{k>0}^{M} \{ U_{m\bar{k}} c_m^\dagger - V_{m\bar{k}} c_m + U_{\bar{m}\bar{k}} c_{\bar{m}}^\dagger + V_{\bar{m}\bar{k}} c_{\bar{m}} \} \end{aligned} \tag{4.15}$$

Finally imposing now condition 4.13

$$U_{\bar{m}k} = V_{mk} = 0 \quad U_{m\bar{k}} = V_{\bar{m}\bar{k}} = 0 \tag{4.16}$$

and we can write;

$$\begin{aligned}\beta_k^\dagger &= \sum_{m>0}^{M} U_{mk}^1 c_m^\dagger + V_{mk}^1 c_{\bar{m}} \quad m = 1, .., M \\ \beta_{\bar{k}}^\dagger &= \sum_{m>0}^{M} U_{mk}^2 c_{\bar{m}}^\dagger + V_{mk}^2 c_m \quad m = 1, .., M \end{aligned} \tag{4.17}$$

where we defined;

$$\begin{aligned} U_{mk} = U_{mk}^1 \quad U_{\bar{m}\bar{k}} = U_{mk}^2 \\ V_{\bar{m}k} = V_{mk}^1 \quad V_{m\bar{k}} = V_{mk}^2 \end{aligned} \tag{4.18}$$

So the block structure of these matrices is;

$$U = \begin{pmatrix} U^1 & 0 \\ 0 & U^2 \end{pmatrix} \quad V = \begin{pmatrix} 0 & V^2 \\ V^1 & 0 \end{pmatrix} \tag{4.19}$$

4.3 Final block structure of U and V amplitudes

To sum up, using the four symmetries described above, the matrices U and V are real and can be separated in different blocks;

$$U = \begin{pmatrix} U^{Z,+} & 0 & 0 & 0 \\ 0 & U^{Z,-} & 0 & 0 \\ 0 & 0 & U^{N,+} & 0 \\ 0 & 0 & 0 & U^{N,-} \end{pmatrix}; \quad V = \begin{pmatrix} V^{Z,+} & 0 & 0 & 0 \\ 0 & V^{Z,-} & 0 & 0 \\ 0 & 0 & V^{N,+} & 0 \\ 0 & 0 & 0 & V^{N,-} \end{pmatrix}$$

with

$$U^{\tau,\pi} = \begin{pmatrix} U^{\tau,\pi,1} & 0 \\ 0 & U^{\tau,\pi,2} \end{pmatrix} \quad V^{\tau,\pi} = \begin{pmatrix} 0 & V^{\tau,\pi,2} \\ V^{\tau,\pi,1} & 0 \end{pmatrix} \tag{4.20}$$

$\tau = Z, N$ and the parity $\pi = +, -$.

4.4 About time reversal symmetry

As we said, in this work, apart from the isospin, we have imposed the parity conservation, the simplex and the $\Pi_2\hat{\mathcal{T}}$ as self-consistent symmetries. The set of operators $\{\hat{P}, \hat{\Pi}_1, \hat{\Pi}_2\}$ are the three generators of a subgroup D_{2h} of the more general point group D_{2h}^T [3–5]. The latter has an additional generator, e.g., the time-reversal operator.

The choice of coordinates (β, γ) divides the quadrupole deformations in six sextants for the different γ ranges [6]. Values of γ equal to $(0°, 120°, 240°)$ correspond to prolate axial deformations with (z, x, y) as symmetry axis, while $(60°, 180°, 300°)$ correspond to oblate axial deformations with (z, x, y) as symmetry axis.

In even-even nuclei and absence of cranking, the Hamiltonian commutes with the time reversal operator; $[\hat{H}, \hat{\mathcal{T}}] = 0$. If the initial wave function proposed in the self-consistent process preserves this symmetry, the final wave function will preserve it. This means the states are invariant under the group D_{2h}^{T} and the three different orientations of the symmetry axis can be related to the z-axis and the calculation can be reduced to one sextant. This is not true in case of time reversal symmetry breaking as the states are only invariant under the subgroup D_{2h}. As a consequence the sextants are now only symmetric with respect to the $\gamma = (120°, 300°)$ direction, and three sextants must be used. We check this in 7.

Bibliography

[1] A.L. Goodman. *Advances in Nuclear Physics*, 11:263, 1979.

[2] Frank Laloe Claude Cohen-Tannoudji, Bernard Diu. *Quantum Mechanics*. A Wiley-Interscience Publication, 1991.

[3] J. Dobaczewski, J. Dudek, S. G. Rohoziński, and T. R. Werner. *Phys.Rev. C*, 62:014310, 2000.

[4] J. Dobaczewski, J. Dudek, S. G. Rohoziński, and T. R. Werner. *Phys.Rev. C*, 62:014310, 2000.

[5] S. Frauendorf. *Rev.Mod. Phys*, 73:463, 2001.

[6] P. Ring and P. Schuck. *The Nuclear Many-Body Problem*. Physics and astronomy online library. Springer, 2004.

Chapter 5

Odd nuclei description

5.1 Construction of and odd system from an even system: Blocking procedure

The ground state of an even-even nucleus is written [1]:

$$|\phi\rangle = \prod_{\substack{\tau=N,Z \\ \pi=+,-}} |\phi\rangle^{\tau\pi} = |\phi\rangle^{Z+}|\phi\rangle^{Z-}|\phi\rangle^{N+}|\phi\rangle^{N-} \tag{5.1}$$

$$|\phi\rangle^{\tau\pi} = \prod_{k=1}^{M} \beta_k^{\tau\pi}\beta_{\bar{k}}^{\tau\pi}|-\rangle = \prod_{\mu=1}^{2M} \beta_\mu^{\tau\pi}|-\rangle \tag{5.2}$$

where τ, π are the isospin and parity and $|-\rangle$ is the particle vacuum.$|\Phi\rangle$ is the vacuum of the quasi-particle operators:

$$\beta_\mu^{\tau\pi}|\phi\rangle = 0 \quad \mu = 1, ...2M \quad \tau = Z, N \quad p = +- \tag{5.3}$$

From 5.2 we see that the parity and simplex of the ground state is +1; i.e.

$$\hat{P}|\phi\rangle^{\tau\pi} = \hat{P}\prod_{k=1}^{M}\beta_k^{\tau\pi}\beta_{\bar{k}}^{\tau\pi}|-\rangle = \prod_{k=1}^{M}\pi_k\pi_{\bar{k}}|\phi\rangle^{\tau\pi} = \prod_{k=1}^{M}\pi_k^2|\phi\rangle^{\tau\pi} = |\phi\rangle^{\tau\pi} \tag{5.4}$$

so

$$\hat{P}|\phi\rangle = \hat{P}|\phi\rangle^{Z+}|\phi\rangle^{Z-}|\phi\rangle^{N+}|\phi\rangle^{N-} = |\phi\rangle \tag{5.5}$$

For the simplex;

$$\Pi_1|\phi\rangle^{\tau\pi} = \Pi_1\prod_{k=1}^{M}\beta_k^{\tau\pi}\beta_{\bar{k}}^{\tau\pi}|-\rangle = \prod_{k=1}^{M}s_k s_{\bar{k}}|\phi\rangle^{\tau\pi} = -i^2|\phi\rangle^{\tau\pi} = |\phi\rangle^{\tau\pi} \tag{5.6}$$

so

$$\Pi_1|\phi\rangle = \Pi_1|\phi\rangle^{Z+}|\phi\rangle^{Z-}|\phi\rangle^{N+}|\phi\rangle^{N-} = |\phi\rangle \tag{5.7}$$

An odd-even nucleus with τ isospin and π parity can be written as [2–4]

$$|\tilde{\phi}\rangle = \beta_{\rho_i}^{\dagger,\tau\pi}|\phi\rangle \tag{5.8}$$

where ρ_i can be any of the possible $2M^\pi$ levels of the configuration space for that parity. The wave function 5.8 is a vacuum of a different set of quasi-particle operators $\tilde{\beta}_\mu^{\dagger,\tau\pi}$;

$$\tilde{\beta}_\mu^{\tau\pi}|\tilde{\phi}\rangle = 0 \quad \mu = 1,...2M^\pi \tag{5.9}$$

The 2M operators $\{\tilde{\beta}^{\tau\pi}\}$ can be obtained from those $\{\beta^{\tau\pi}\}$ by replacing the annihilator operator $\beta_{\rho_i}^{\tau\pi}$ by the corresponding creation operator $\beta_{\rho_i}^{\pi\tau\dagger}$ and leaving the rest unchanged. This is called the blocking procedure. The

blocked level can have positive or negative simplex. As creation and annihilator operators have opposite simplex, is clear that the number of operators of each simplex will be different. For example if we block one level with positive simplex we will have $M^\pi - 1$ creation operators with positive simplex and $M^\pi + 1$ with negative simplex, and eq. 4.17 :

$$\begin{aligned}\tilde{\beta}^{\dagger,\tau\pi}_k &= \sum_{m>0}^{M} U^1_{mk} c^\dagger_m + V^1_{mk} c_{\bar{m}} \quad k = 1, .., M^\pi - 1 \\ \tilde{\beta}^{\dagger,\tau\pi}_{\bar{k}} &= \sum_{m>0}^{M} U^2_{mk} c^\dagger_{\bar{m}} + V^2_{mk} c_m \quad k = 1, .., M^\pi + 1 \end{aligned} \tag{5.10}$$

This can be extended to any number of blocked levels;

$$\begin{aligned}\tilde{\beta}^{\dagger,\tau\pi}_k &= \sum_{m>0}^{M} U^{\tau\pi,1}_{mk} c^\dagger_m + V^{\tau\pi,1}_{mk} c_{\bar{m}} \quad k = 1, .., M^{\tau\pi}_1 \\ \tilde{\beta}^{\dagger,\tau\pi}_{\bar{k}} &= \sum_{m>0}^{M} U^{\tau\pi,2}_{mk} c^\dagger_{\bar{m}} + V^{\tau\pi,2}_{mk} c_m \quad k = 1, .., M^{\tau\pi}_2 \end{aligned} \tag{5.11}$$

with $M^{\tau\pi}_1 = M^\pi - n^{\tau\pi}_b$, $M^{\tau\pi}_2 = M^\pi + n^{\tau\pi}_b$, where we defined the blocking number $n^{\tau\pi}_b$ as the difference between the number of blocked levels with positive and negative simplex for each isospin τ and parity π. Note that the number can be positive (if there are more blocked states with positive simplex) or negative (otherwise).

5.2 U,V amplitudes

The matrices $U^{\tau\pi,1(2)}, V^{\tau\pi,1(2)}$ are now rectangular matrices with M rows and $M^{\tau\pi}_{+(-)}$ columns:

$$U^{\tau\pi} = \begin{matrix} \\ M^{\pi}\{ \\ M^{\pi}\{ \end{matrix} \begin{pmatrix} \overbrace{\quad}^{M^{\tau\pi}_{+}} & \overbrace{\quad}^{M^{\tau\pi}_{-}} \\ U^{\tau\pi,1} & 0 \\ 0 & U^{\tau\pi,2} \end{pmatrix} \quad ; \quad V^{\tau\pi} = \begin{matrix} \\ M^{\pi}\{ \\ M^{\pi}\{ \end{matrix} \begin{pmatrix} \overbrace{\quad}^{M^{\tau\pi}_{+}} & \overbrace{\quad}^{M^{\tau\pi}_{-}} \\ 0 & V^{\tau\pi,2} \\ V^{\tau\pi,1} & 0 \end{pmatrix} \tag{5.12}$$

5.3 Blocking channels

As we have seen there are, in principle, eight possible blocking channels, obtained by changing isospin, parity and simplex. The simplex is important if we break time-reversal symmetry explicitly; i.e. by adding the cranking term. Otherwise blocked levels with positive and negative simplex are degenerated [5]. We have therefore four blocking channels (protons or neutrons, with positive or negative parity). In this work we concentrate in odd-A nuclei and we only block one quasi-particle state. For and odd-A nuclei the blocked isospin channel is the one with an odd number of particles; i.e. for an odd-Z nuclei we must block the proton channel and for an odd-N nuclei the neutron channel. This reduces the possibilities to two, corresponding to the different parities. Note that the parity of the wave function is determined by the

parity of the blocked particle;

$$\begin{aligned} \hat{P}|\tilde{\phi}\rangle &= \hat{P}\beta^{\dagger,\tau\pi}_{\rho_i}|\phi\rangle = \pi_{\rho_i}\beta^{\dagger,\tau\pi}_{\rho_i}\hat{P}|\phi\rangle \\ &\overset{5.5}{=} \pi_{\rho_i}\beta^{\dagger,\tau\pi}_{\rho_i}|\phi\rangle = \pi_{\rho_i}|\tilde{\phi}\rangle \end{aligned} \tag{5.13}$$

Bibliography

[1] P. Ring and P. Schuck. *The Nuclear Many-Body Problem*. Physics and astronomy online library. Springer, 2004.

[2] P. Ring, R. Beck, and H. J. Mang. *Zeitschrift für Physik A Hadrons and nuclei*, 231(1):10–25, 1970.

[3] P. Ring, H.J. Mang, and B. Banerjee. *Nuclear Physics A*, 225(1):141 – 156, 1974.

[4] J.L. Egido, H.-J. Mang, and P. Ring. *Nuclear Physics A*, 334(1):1 – 20, 1980.

[5] M. Borrajo and J. L. Egido. *The European Physical Journal A*, 52(9):277, 2016.

Chapter 6

Particle Number VAP + Angular Momentum PAV calculation

We have explained the general concepts of mean field and beyond mean field methods in chapter 3. In this chapter we describe the details and particular approaches used in our calculations. There are three main steps.

The fist two steps consist on the self-consistent calculation and the restoration of the particle number and the rotational invariance. The third step consist on the configuration mixing of the different states obtained in the first two steps. The two first steps are performed in all of our calculations. The final step (the configuration mixing approach) is not always performed.

The particle number restoration is perform before the variational procedure

(PN-VAP) [1]. All terms [2] of the Hamiltonian are taken into account to avoid divergence problems. This guarantees that we obtain the self-consistent minimum. However, the restoration of the rotational invariance requires the calculation of a three dimensional integral. In this case the only affordable calculation is to perform a PAV approach.

The approach of solving the PN-VAP variational equation to find the self-consistent minimum and afterwards to perform an AM-PAV is not the optimal because the AMP is not able to exploit any degree of freedom of the HFB transformation and self-consistency with respect to the AMP is not guarantied. An intermediate way is to perform an approximate AM-VAP approach by solving the variational PN-VAP equation for a large set of relevant physical situations as to cover the sensitive degrees of freedom. Afterwards an AM-PAV to this set of wave functions will determine the absolute minimum among these states for different angular momenta. This method guarantees, at least, AM-VAP self-consistency with respect to these relevant quantities. For example, in the limit of strong rotational symmetry breaking, the cranking model -which breaks the time-reversal symmetry- is an accurate approximation for the variation after angular momentum projection equations [3, 4]

So the first step is the construction of a set of intrinsic many-body states for a set of parameters $\{q_i\}$;$|\Phi(\vec{q})\rangle$. These parameters can be the quadrupole moment, cranking frequency...The states are found by minimizing the particle number projected energy;i.e. a PN-VAP approach (eq (3.23) with P^S the neutron and proton number projectors). In this step we can study the VAP

potential energy surfaces.

In the second step, we apply the projection technique to the angular momentum in a PAV approach. At this point we can study the angular momentum projected surfaces.

If we want to include fluctuations around the most probable values we can do a final step. We use the states found in step 2, which already have the correct quantum numbers and use them in a generator coordinate method, being the parameters $\vec{q}$ the generating coordinate. We can study the collective wave functions and energies.

6.1 PN-VAP calculation

6.1.1 Particle number projector

The particle number projection operator P^N is [4]:

$$P^N = \frac{1}{2\pi} \int_0^{2\pi} e^{i\varphi(\hat{N}-N)} d\varphi \tag{6.1}$$

where φ is the Gauge angle. Lets prove that the application of this operator to a HFB-type wave function is an eigenstate of the particle number operator $\hat{N}$ with eigenvalue N. First notice that we can decompose the wave function in a complete orthogonal set of wave functions $|\alpha N_i\rangle$ being N_i the particle

number and α the rest of necessary parameters to form a complete basis.

$$|\phi\rangle = \sum_{\alpha,N_i} |\alpha N_i\rangle\langle\alpha N_i|\phi\rangle = \sum_{\alpha,N_i} C_{\alpha N_i}|\alpha N_i\rangle \tag{6.2}$$

Applying the projection operator;

$$\begin{aligned} P^N|\phi\rangle &= \frac{1}{2\pi}\int_0^{2\pi} e^{i\varphi(\hat{N}-N)} \sum_{\alpha,N_i} C_{\alpha,N_i}|\alpha,N_i\rangle d\varphi \\ &= \frac{1}{2\pi}\sum_{\alpha,N_i} C_{\alpha,N_i}|\alpha,N_i\rangle \int_0^{2\pi} e^{i\varphi(N_i-N)} d\varphi \\ &= \sum_{\alpha,N_i} C_{\alpha,N_i}|\alpha,N_i\rangle\delta_{N_i,N} = C_{\alpha,N}|\alpha,N\rangle \end{aligned} \tag{6.3}$$

So it is clear that $P^N|\phi\rangle$ is an eigenstate of $\hat{N}$ operator with eigenvalue N;

$$\hat{N}P^N|\phi\rangle = \hat{N}C_{\alpha,N}|\alpha,N\rangle = NC_{\alpha,N}|\alpha,N\rangle = NP^N|\phi\rangle \tag{6.4}$$

As a projector, this operator fulfills;

$$(P^N)^2 = P^N \tag{6.5}$$

$$(P^N)^\dagger = P^N \tag{6.6}$$

6.1.2 Particle number projected wave function

In the VAP approach we have to minimize the projected energy functional to find the best solution among the trial ones. This is done for every value of

the parameters q_i. We solve equation (3.23) to obtain the best wave function:

$$\begin{aligned}
\delta \quad & E'^{NZ}[U,V] = \\
\delta \quad & \left[\frac{\langle\Phi(\vec{q})|(P^N P^Z)^\dagger \hat{H} P^N P^Z|\Phi(\vec{q})\rangle}{\langle\Phi(\vec{q})|(P^N P^Z)^\dagger P^N P^Z|\Phi(\vec{q})\rangle} - \lambda_{\vec{q}}\langle\Phi(\vec{q})|\hat{\vec{Q}}|\Phi(\vec{q})\rangle\right] = \\
\delta \quad & \left[\frac{\langle\Phi^{NZ}(\vec{q})|\hat{H}|\Phi^{NZ}(\vec{q})\rangle}{\langle\Phi^{NZ}(\vec{q})|\Phi^{NZ}(\vec{q})\rangle} - \lambda_{\vec{q}}\langle\Phi(\vec{q})|\hat{\vec{Q}}|\Phi(\vec{q})\rangle\right] \rightarrow |\Phi^{NZ}_{VAP}(\vec{q})\rangle
\end{aligned} \tag{6.7}$$

The Lagrange multipliers are determined by the constraints;

$$\langle\Phi(\vec{q})|\hat{Q}_i|\Phi(\vec{q})\rangle = q_i \qquad \forall i \tag{6.8}$$

6.1.3 Particle number projected surfaces

The potential energy surfaces are given by:

$$E^{NZ}_{VAP}(\vec{q}) \;=\; \frac{\langle\Phi^{NZ}_{VAP}(\vec{q})|\hat{H}|\Phi^{NZ}_{VAP}(\vec{q})\rangle}{\langle\Phi^{NZ}_{VAP}(\vec{q})|\Phi^{NZ}_{VAP}(\vec{q})\rangle} \tag{6.9}$$

These surfaces provide information such as the optimal values for $\vec{q}$, and the hardness or softness of the energy on the different $\vec{q}$ directions. As the intrinsic HFB wave functions fulfill $e^{i\pi(\hat{N}-N)}|\Phi(\vec{q})\rangle = |\Phi(\vec{q})\rangle$ the interval can be reduced to $[0,\pi]$. In practice the integral is substituted by a discrete sum (Fomenko expansion [5]):

$$\frac{1}{\pi}\int_0^\pi e^{i\varphi(\hat{N}-N_\tau)}d\varphi \;\rightarrow\; \frac{1}{L}\sum_{l=1}^{L} e^{i\varphi(\hat{N}-N_\tau)},\; \varphi = \frac{\pi}{L}l \tag{6.10}$$

We use $L = 11$ in our calculations. If we insert the expression of the particle number projection operators P^N, P^Z in the functional 6.7, and we take into account that the state $|\Phi(\vec{q})\rangle = |\Phi_Z(\vec{q})\rangle|\Phi_N(\vec{q})\rangle$;

$$\begin{aligned} E^{NZ}(\vec{q}) &= \frac{\sum_{l_Z=1}^{L}\sum_{l_N=1}^{L}\langle\Phi_Z|\langle\Phi_N|\hat{H}'e^{i\varphi_{l_Z}(\hat{Z}-Z)}e^{i\varphi_{l_N}(\hat{N}-N)}|\Phi_N\rangle|\Phi_Z\rangle}{\sum_{l_Z=1}^{L}\sum_{l_N=1}^{L}\langle\Phi_Z|\langle\Phi_N|e^{i\varphi_{l_Z}(\hat{Z}-Z)}e^{i\varphi_{l_N}(\hat{N}-N)}|\Phi_N\rangle|\Phi_Z\rangle} \\ &= \sum_{l_Z=1}^{L}\sum_{l_N=1}^{L} y_{l_\pi} y_{l_N} \frac{\langle\Phi_Z|\langle\Phi_N|\hat{H}'e^{i\varphi_{l_Z}\hat{Z}}e^{i\varphi_{l_N}\hat{N}}|\Phi_N\rangle|\Phi_Z\rangle}{\langle\Phi_Z|\langle\Phi_N|e^{i\varphi_{l_Z}\hat{Z}}e^{i\varphi_{l_N}\hat{N}}|\Phi_N\rangle|\Phi_Z\rangle} \end{aligned} \tag{6.11}$$

with

$$y_{l_\tau} = \frac{\langle\Phi_\tau|e^{i\varphi_{l_\tau}(\hat{\tau}-\tau)}|\Phi_\tau\rangle}{\sum_{l_\tau=1}^{L}\langle\Phi_\tau|e^{i\varphi_{l_\tau}(\hat{\tau}-\tau)}|\Phi_\tau\rangle} = \frac{e^{-i\varphi_{l_\tau}\tau}n^\tau(\vec{q},\varphi_{l_\tau})}{\sum_{l_\tau=1}^{L}e^{-i\varphi_{l_\tau}\tau}n^\tau(\vec{q},\varphi_{l_\tau})} \tag{6.12}$$

with

$$n^\tau(\vec{q},\varphi_{l_\tau}) = \langle\Phi_\tau|e^{i\varphi_{l_\tau}\hat{\tau}}|\Phi_\tau\rangle \tag{6.13}$$

and the hamiltonian overlap;

$$e(\vec{q},\varphi_{l_Z},\varphi_{l_\nu}) = \frac{\langle\Phi_Z|\langle\Phi_N|\hat{H}'e^{i\varphi_{l_Z}\hat{Z}}e^{i\varphi_{l_N}\hat{N}}|\Phi_N\rangle|\Phi_Z\rangle}{\langle\Phi_Z|\langle\Phi_N|e^{i\varphi_{l_Z}\hat{Z}}e^{i\varphi_{l_N}\hat{N}}|\Phi_N\rangle|\Phi_Z\rangle} \tag{6.14}$$

Note that the two ingredients to be calculated are 6.13 and 6.14. Once we get 6.13 is easy to obtain 6.12. Finally we use the latter together with 6.14 to obtain 6.11. In Appendices A,B,C we see how to calculate both in the most general case (particle and angular momentum projection) between states with different values of the constraints q_i, q_i'. However in case of only particle number projection and $q_i = q_i'$ the Onishi formula can be use to calculate the norm overlap.

Norm overlap

When there is only particle number projection the norm overlap can be calculated using the Onishi formula [6–8]

$$n^{\tau}(\vec{q},\varphi_{l_\tau}) = |T_{22}^{1,\tau}(\varphi_{l_\tau})|^{1/2}|T_{22}^{2,\tau}(\varphi_{l_\tau})|^{1/2}e^{i\varphi_{l_\tau}D_\tau} \tag{6.15}$$

where matrices T_{22} are defined in appendix B and $D^{\tau} = \frac{1}{2}(D_i^{\tau} + D_i^{\tau})$, with $D_{1(2)}^{\tau}$ being the dimension of each of the block with signatures 1(2). In Appendix B we show that these in turn are divided into two blocks with positive and negative parity. Therefore, if $M_i^{\tau,\pi=+(-)}$ is the dimension of the configuration space used for positive (negative) parity;

$$D_i^{\tau} = M_i^{\tau+} + M_i^{\tau-}$$

In the case of even-even nuclei $M_1^{\tau+} = M_2^{\tau+}$ so is clear that $D^{\tau} = M^{\tau,+}+M^{\tau,-}$. However, this is also true for blocked wave functions;

$$\begin{aligned} D^{\tau} &= \frac{1}{2}(M^{\tau,+} - n_b^{\tau+} + M^{\tau,+} + n_b^{\tau+} + M^{\tau,-} - n_b^{\tau-} + M^{\tau,-} + n_b^{\tau-}) \\ &= M^{\tau,+} + M^{\tau,-} \end{aligned} \tag{6.16}$$

Because there is an square root in expression 6.15 we may think there is an indetermination with the sign. However in Appendix A we show that $|T_{22}^1| = |T_{22}^2|$. In particular in case of only PN projection, $|T_{22}^1| = e^{i\varphi}V^TV + e^{-i\varphi}U^TU = \cos\varphi - i\sin\varphi(U^TU - V^TV)$ for an even system *and* also for an odd system. So the sign is not relevant.

In case of particle and angular momentum projection the norm overlap will be calculated using the Pffafian [9, 10].

Hamiltonian overlap

The Hamiltonian overlap 6.14 is obtained in detail in appendices B C for the most general case: with particle and angular momentum projection and between states with different constraints $\vec{q}, \vec{q}\,'$. The overlap in the present case (only particle number projection between equal states) is obtained by using $\hat{R}(\Omega) = \mathbb{I}$ and $\vec{q} = \vec{q}\,'$ in those expressions. We give here the final expression;

$$\begin{aligned} e(\vec{q}, \varphi_{l_Z}, \varphi_{l_\nu}) &= Tr\{t\Big(\rho^{10,Z}(\vec{q}, \varphi_{l_Z}) + \rho^{10,N}(\vec{q}, \varphi_{l_Z})\Big) \\ &+ \frac{1}{2}\Big(\Gamma^{10,ZZ}(\vec{q}, \varphi_{l_Z})\rho^{10,Z}(\vec{q}, \varphi_{l_Z}) + \Gamma^{10,ZN}(\vec{q}, \varphi_{l_N})\rho^{10,N}(\vec{q}, \varphi_{l_Z}) \\ &+ \frac{1}{2}\Big(\Gamma^{10,NZ}(\vec{q}, \varphi_{l_Z})\rho^{10,N}(\vec{q}, \varphi_{l_N}) + \Gamma^{10,NN}(\vec{q}, \varphi_{l_N})\rho^{10,N}(\vec{q}, \varphi_{l_N}) \\ &- \Delta^{10,Z}(\vec{q}, \varphi_{l_Z})\kappa^{01,Z}(\vec{q}, \varphi_{l_Z}) - \Delta^{10,N}(\vec{q}, \varphi_{l_N})\kappa^{01,N}(\vec{q}, \varphi_{l_N})\Big)\} \end{aligned} \tag{6.17}$$

with the density matrix and pairing tensors:;

$$\rho^{10,\tau}_{\mu\mu'}(\vec{q}, \varphi_{l_\tau}) = \Big(e^{i\varphi_{l_\tau}} V^\star(\vec{q}) T^{-1}_{22}(\vec{q}, \varphi_{l_\tau}) V^T(\vec{q})\Big)_{\mu\mu'} \tag{6.18}$$

$$\kappa^{10,\tau}_{\mu\mu'}(\vec{q}, \varphi_{l_\tau}) = \Big(e^{i\varphi_{l_\tau}} V^\star(\vec{q}) T^{-1}_{22}(\vec{q}, \varphi_{l_\tau}) U^T(\vec{q})\Big)_{\mu\mu'} \tag{6.19}$$

$$\kappa^{01,\tau}_{\mu\mu'}(\vec{q}, \varphi_{l_\tau}) = -\Big(e^{-i\varphi_{l_\tau}} U^\star(\vec{q}) T^{-1}_{22}(\vec{q}, \varphi_{l_\tau}) V^T(\vec{q})\Big)_{\mu\mu'} \tag{6.20}$$

where we defined the fields;

$$\Gamma^{10,\tau,\tau'}_{\mu,\mu'}(\vec{q},\varphi_{l_\tau}) = \sum_{\gamma,\gamma'} \bar{v}_{\mu\gamma\mu'\gamma'}\rho^{10,\tau}_{\gamma'\gamma}(\vec{q},\varphi_{l_\tau}) \tag{6.21}$$

$$\Delta^{10,\tau,\tau'}_{\mu,\mu'}(\vec{q},\varphi_{l_\tau}) = \frac{1}{2}\sum_{\gamma,\gamma'} \bar{v}_{\mu\mu'\gamma\gamma'}\kappa^{10,\tau}_{\gamma\gamma'}(\vec{q},\varphi_{l_\tau}) \tag{6.22}$$

With 6.15 and 6.17 we are now ready to compute the particle number projected energy $E^{NZ}(\vec{q})$.

Density dependent term

Gogny force includes a density dependent term;

$$V_{dd} = \frac{1}{2}t_3(1+x_0\hat{P}_\sigma)\delta(\vec{r}_1-\vec{r}_2)\rho^{1/3}(\vec{r}_1+\vec{r}_2) \tag{6.23}$$

At mean field level the density is uniquely defined [2, 11–14]. However in projected theories we have to choose some prescription, which must fulfill several requirements. For example the energy must be a scalar quantity and remain real. There are two main prescriptions:

1. Projected density prescription

   This prescription is inspired by the following: In the MFA, the energy is given by $\frac{\langle\Phi(\vec{q})|\hat{H}|\Phi(\vec{q})\rangle}{\langle\Phi(\vec{q})|\Phi(\vec{q})\rangle}$ and V_{DD} depends on the density $\frac{\langle\Phi(\vec{q})|\hat{\rho}|\Phi(\vec{q})\rangle}{\langle\Phi(\vec{q})|\Phi(\vec{q})\rangle}$. If the wave function which describes the nuclear system is the projected wave function $\Phi^{NZ}(\vec{q})$, we must calculate the element $\frac{\langle\Phi^{NZ}(\vec{q})|\hat{V}_{DD}|\Phi^{NZ}(\vec{q})\rangle}{\langle\Phi^{NZ}(\vec{q})|\Phi^{NZ}(\vec{q})\rangle}$ so

it is reasonable to use the projected density;

$$\rho^{N,Z}_{\vec{q}}(\vec{r}) = \frac{\langle \Phi^{NZ}(\vec{q})|\hat{\rho}(\vec{r})|\Phi^{NZ}(\vec{q})\rangle}{\langle \Phi^{NZ}(\vec{q})|\Phi^{NZ}(\vec{q})\rangle} \tag{6.24}$$

2. Mixed density prescription

   To evaluate the density dependent part of the energy we have to evaluate elements between the different product wave functions $|\Phi(\vec{q})\rangle$ and $|\tilde{\Phi}(\vec{q})\rangle = e^{i\varphi\hat{N}}|\Phi(\vec{q})\rangle$, i.e; calculate elements of the type; $\frac{\langle\Phi(\vec{q})|\vec{V}_{DD}|\tilde{\Phi}\vec{q}\rangle}{\langle\Phi(\vec{q})|\tilde{\Phi}\vec{q}\rangle}$, and therefore the mixed density can be chosen;

$$\rho^{\varphi}_{\vec{q}}(\vec{r}) = \frac{\langle \Phi(\vec{q})|\hat{\rho}(\vec{r})|\tilde{\Phi}(\vec{q})\rangle}{\langle \Phi(\vec{q})|\tilde{\Phi}(\vec{q})\rangle} \tag{6.25}$$

In case os spatial parity and rotational invariance restoration the most appropriate prescription is the mixed one, which fulfills the mentioned requirements [13]. The projected prescription cannot be used when recovering spatial symmetries [15]. However in the case of particle number projection we choose the projected prescription.

This prescription has the advantage that does not have divergence problems, which is not true for the mixed prescription (although those divergences are integrable) [1] . In addition the problem is computationally cheaper, and differences between both prescription are small. The projected energy of the density dependent term E^{NZ}_{DD} is obtained evaluating the contribution of 6.23 using the density **??** . In the Gogny force $x_0 = 1$, which cancels the contribution of this $\hat{V}_{DD}$ to the pairing field Δ and to the Hartree-Fock field

of the type $\Gamma^{\tau\tau}$. We find;

$$E_{DD}^{NZ} = \frac{1}{2}\sum_{\tau\neq\tau'} Tr(\Gamma^{\tau\tau'}\rho^{\tau}) \tag{6.26}$$

where

$$\Gamma^{\tau\tau'}_{\mu_1\mu_3} = \sum_{\mu_2\mu_4}(\bar{v}_{dd}[\rho^{NZ}])_{\mu_1\mu_2\mu_3\mu_4}\rho^{\tau'}_{\mu_4\mu_2} \tag{6.27}$$

6.2 PNAMP-PAV calculation

Now we proceed to derive the expressions needed in the angular momentum restoration. By applying the angular momentum projector we create eigenstates of the total angular momentum $\hat{I}^2$ (with eigenvalue I) and the third component $\hat{I}_z$ (with eigenvalue M). This operator is given by [4]:

$$\begin{aligned} P^{IM} &= \sum_K f^I_K P^I_{MK} \rightarrow P^I_{MK} = \frac{2I+1}{8\pi^2}\int D^{I\star}_{MK}(\Omega)\hat{R}(\Omega)d\Omega \\ \hat{R}(\Omega) &= e^{-i\alpha\hat{I}_z}e^{-i\beta\hat{I}_y}e^{-i\gamma\hat{I}_z} \end{aligned} \tag{6.28}$$

with $\Omega = (\alpha, \beta, \gamma)$ the Euler angles and $D^I_{MK}(\Omega)$ the Wigner functions. The angular momentum projection has been done with the set of integration points in the Euler angles ($N_{\boldsymbol{\alpha}} = N_{\boldsymbol{\beta}} = N_{\boldsymbol{\gamma}} = 32$) in the intervals $\boldsymbol{\alpha} \in [0, 2\pi], \boldsymbol{\beta} \in [0, \pi], \boldsymbol{\gamma} \in [0, 2\pi]$.

The following property is useful:

$$\int d\Omega D^{I_1\star}_{M_1M_1'}(\Omega)D^{I_2}_{M_2M_2'}(\Omega) = \frac{8\pi^2}{2I_1+1}\delta_{I_1I_2}\delta_{M_1M_2}\delta_{M_1'M_2'} \tag{6.29}$$

The actuation of this operator on an eigenstate of I y and M is :

$$\hat{R}(\Omega)|IM\rangle = \sum_{M'} D^{I}_{M'M}(\Omega)|IM'\rangle \tag{6.30}$$

Now is easy to see that $P^{IM}|\Phi\rangle$ is an eigenstate of I y M .

$$\begin{aligned}
P^{IM}|\Phi\rangle &\overset{1}{=} P^{IM}\sum_{I'M'\alpha}|I'M'\alpha\rangle\langle I'M'\alpha|\Phi\rangle = P^{IM}\sum_{I'M'\alpha} b_{I'M'\alpha}|I'M'\alpha\rangle \\
&= \frac{2I+1}{8\pi^2}\sum_{\substack{I'M'\\K\alpha}} f^{I}_{K} b_{I'M'\alpha}\int d\Omega D^{I\star}_{MK}(\Omega)\hat{R}(\Omega)|I'M'\alpha\rangle \\
&\overset{(6.30)}{=} \frac{2I+1}{8\pi^2}\sum_{\substack{I'M'\\KM''\alpha}} f^{I}_{K} b_{I'M'\alpha}\int d\Omega D^{I\star}_{MK}(\Omega) D^{I'}_{M''M'}(\Omega)|I'M''\alpha\rangle \\
&\overset{(6.29)}{=} \sum_{K\alpha} a^{I}_{K} b_{IK\alpha}|IM\alpha\rangle
\end{aligned} \tag{6.31}$$

In Dirac notation P^{I}_{MK} :

$$\begin{aligned}
P^{I}_{MK} &= \frac{2I+1}{8\pi^2}\sum_{\substack{I'K'\\I''M''}}|I'K'\rangle\langle I'K'|\int d\Omega D^{I\star}_{MK}(\Omega)\hat{R}(\Omega)|I''M''\rangle\langle I''M''| \\
&\overset{(6.30)}{=} \frac{2I+1}{8\pi^2}\sum_{\substack{I'K'\\I''M''M'}}|I'K'\rangle\langle I'K'|\int d\Omega D^{I\star}_{MK}(\Omega) D^{I''}_{M'M''}(\Omega)|I''M'\rangle\langle I''M''| \\
&\overset{(6.29)}{=} \sum_{I'K'}|I'K'\rangle\langle I'K'|IM\rangle\langle IK| \\
&= |IM\rangle\langle IK|
\end{aligned} \tag{6.32}$$

Using the above equations is now easy to prove the following properies:

$$(P^{I}_{MK})^{\dagger} = (|IK\rangle\langle IM|)^{\dagger} = |IK\rangle\langle IM| = P^{I}_{KM} \tag{6.33}$$

$$\begin{aligned} P^{I_1}_{M_1K_1}P^{I_2}_{M_2K_2} &= |I_1M_1\rangle\langle I_1K_1|I_2M_2\rangle\langle I_2K_2| \\ &= \delta_{I_1I_2}\delta_{K_1M_2}|I_1M_1\rangle\langle I_1K_2| \\ &= \delta_{I_1I_2}\delta_{K_1M_2}P^{I_1}_{M_1K_2} \end{aligned} \tag{6.34}$$

The wave function obtained after the angular momentum projection does not have the correct particle number anymore. Therefore we do a simultaneous projection to particle number:

$$\begin{aligned} |\Psi^{NZ;IM}(\vec{q})\rangle &= P^{IM}P^NP^Z|\Phi(\vec{q})\rangle \\ &= \sum_K f^I_{K\sigma}(\vec{q})P^I_{MK}P^NP^Z|\Phi(\vec{q})\rangle \\ &= \sum_K f^I_{K\sigma}(\vec{q})|\Phi(\vec{q})^{NZ;IMK}\rangle \end{aligned} \tag{6.35}$$

The $f^I_K(\vec{q})$ are variational parameters. As we saw in chapter 3, this is an example of the generator coordinate method, being the generator coordinate K. Therefore we have to solve the Hill-Wheeler-Griffin equation [16, 17]:

$$\sum_{K'}\left(\mathcal{H}^{NZ,I}_{KK'}(\vec{q}) - E^{NZ,I}_\sigma(\vec{q})\mathcal{N}^{NZ,I}_{K,K'}\right)f^I_{K'\sigma}(\vec{q}) = 0 \tag{6.36}$$

with

$$\mathcal{H}^{NZ,I}_{KK'}(\vec{q}) = \langle\Phi(\vec{q})^{NZ,IMK}|\hat{H}_{KK'}|\Phi(\vec{q})^{NZ,IMK'}\rangle \tag{6.37}$$

$$\mathcal{N}^{NZ,I}_{KK'}(\vec{q}) = \langle\Phi(\vec{q})^{NZ,IMK}|\Phi(\vec{q})^{NZ,IMK'}\rangle \tag{6.38}$$

The subscript σ labels the different eigenvalues and eigenvectors obtained solving eq (6.36). The ground state corresponds $\sigma = 1$, the first excited state to $\sigma = 2$ ...etc. Note that for each I value a different diagonalization is performed. The presence of the norm matrix 6.38 is a consequence of the linear dependence of the basis states $|\Phi(\vec{q})^{NZ,IMK}\rangle$.

We define the probability distribution of finding an eigenstate of the angular momentum $|IK\rangle$;

$$W_K^{NZ,I}(\vec{q}) = \frac{\mathcal{N}_{KK}^{NZ,I}(\vec{q})}{\langle\Phi(\vec{q})|P^N P^Z|\Phi(\vec{q})\rangle} \tag{6.39}$$

and the total probability distribution,

$$W^{NZ,I}(\vec{q}) = \sum_K W_{K\sigma}^{NZ,I}(\vec{q}) \tag{6.40}$$

which represents the probability of finding a value of the angular momentum I. Both quantities represent the distribution of the wave function $|\Phi(\vec{q})^{NZ;IMK}\rangle$ on the subspaces $|IK\rangle$ and $|I\rangle$ respectively. Also we define the IK-projected energy as;

$$E_K^{NZ,I}(\vec{q}) = \frac{\mathcal{H}_{KK}^{NZ,I}(\vec{q})}{\mathcal{N}_{KK}^{NZ,I}(\vec{q})} \tag{6.41}$$

The techniques to solve equation (6.36) were explained in chapter 3. Applied to this case:

1. Diagonalizaion of the norm overlap

$$\sum_{K'} \mathcal{N}^{NZ,I}_{KK'}(\vec{q}) u^{NZ,I}_{\mu}(\vec{q}\, K') = n^{NZ,I}_{\mu} u^{NZ,I}_{\mu}(\vec{q}\, K) \tag{6.42}$$

where the index μ labels the different eigenvalues $n^{N,I}_{\mu}$ of the norm. Those which are zero or close to zero correspond to linearly dependent states and are elimianted. The criterium to set a cutoff is that we leave those which are $n^{N,I}_{\mu}/n^{N,I}_{max} > \epsilon$. Typically $\epsilon = 10^{-6}$ in our calculations.

2. Construction of the natural basis

Now we can define the orthonormal natural basis;

$$|\mu^{NZ,I}\rangle = \sum_{K} \frac{u^{NZ,I}_{\mu}}{\sqrt{n^{NZ,I}_{\mu}}} |\Phi(\vec{q})^{NZ;IMK}\rangle \tag{6.43}$$

3. Diagonalizaion of the Hamiltonian in the natural basis

$$\sum_{\mu'} \langle \mu^{NZ,I} | \hat{H} | \mu^{,NZ,I} \rangle g^{I}_{\mu'\sigma} = E^{NZ,I}_{\sigma}(\vec{q}) g^{I}_{\mu\sigma} \tag{6.44}$$

This provides the eigenvalues $E^{N,I}_{\sigma}$ and the eigenvectors $g^{I}_{\mu\sigma}$. The weights $f^{I}_{K'\sigma}(\vec{q})$ are given by:

$$f^{I}_{K\sigma}(\vec{q}) = \sum_{\mu} \frac{g^{I}_{\mu\sigma}}{\sqrt{n^{N,I}_{\mu}}} u^{NZ,I}_{\mu}(\vec{q}\, K) \tag{6.45}$$

The coefficients $\sum_K |f^{I}_{K\sigma}(\vec{q})|^2 \neq 1$ as the states $|\Phi(\vec{q})^{NZ;IMK}\rangle$ are not orthonormal. From coefficients $g^{I}_{\mu\sigma}$ we can define the so-called collective wave

function $F^I_\sigma(\vec{q})$ that account for the probability density, normalized to 1, of finding the state (I,σ) with a given $\vec{q}$;

$$F^I_\sigma(\vec{q}) = \sum_K F^I_{K,\sigma}(\vec{q}) \tag{6.46}$$

with

$$F^I_{K\sigma}(\vec{q}) = \sum_\mu g^I_{\mu\sigma} u^{NZ,I}_\mu(\vec{q}\,K) \tag{6.47}$$

which accounts for the probability density of finding the state (I,σ) with a given K value in $\vec{q}$. Therefore the probability of finding a value K is;

$$P^I_{K\sigma}(\vec{q}) = |F^I_{K\sigma}(\vec{q})|^2 \tag{6.48}$$

It is easy to show that effectively $\sum_K |F^I_{K\sigma}(\vec{q})|^2 = 1$;

$$\begin{aligned} \sum_K |F^I_{K\sigma}(\vec{q})|^2 &= \sum_K \sum_{\mu\mu'} (g^I_{\mu\sigma})^\star (u^{NZ,I}_{\mu'}(\vec{q}\,K'))^\star g^I_{\mu'\sigma} u^{NZ,I}_{\mu'}(\vec{q}\,K) \\ &= \sum_\mu |g^I_{\mu\sigma}|^2 = 1 \end{aligned} \tag{6.49}$$

where we used $\sum_K u^{NZ,I}_\mu(\vec{q}\,K)(u^{NZ,I}_{\mu'}(\vec{q}\,K'))^\star = \delta_{\mu\mu'}$.

At this point we can also study the particle number and angular momentum projected energy surfaces AMP-PES, this is, for each value of the constraints $\vec{q}$ and angular momentum I we plot the $E^{NZ,I}_\sigma(\vec{q})$.

6.2.1 Norm overlap

The norm overlap 6.38 is:

$$\begin{aligned}
\mathcal{N}^{NZ,I}_{KK'}(\vec{q}) &= \langle\Phi(\vec{q})^{NZ,IMK}|\Phi(\vec{q})^{NZ,IMK'}\rangle \\
&= \langle\Phi(\vec{q})^{NZ}|(P^I_{MK})^\dagger P^I_{MK'}|\Phi(\vec{q})^{NZ}\rangle \\
&= \langle\Phi^{NZ}(\vec{q})|P^I_{KM}P^I_{MK'}|\Phi^{NZ}(\vec{q})\rangle \\
&\overset{(6.34)}{=} \langle\Phi^{NZ}(\vec{q})|P^I_{KK'}|\Phi^{NZ}(\vec{q})\rangle \\
&= \frac{2I+1}{8\pi^2}\int d\Omega D^{I\star}_{KK'}(\Omega)\langle\Phi^{NZ}(\vec{q})|\hat{R}(\Omega)|\Phi^{NZ}(\vec{q})\rangle \\
&= \frac{2I+1}{8\pi^2}\int d\Omega D^{I\star}_{KK'}(\Omega) n^{NZ}(\vec{q},\Omega) \qquad (6.50)
\end{aligned}$$

where we defined

$$\begin{aligned}
n^{NZ}(\vec{q},\Omega) &= \langle\Phi^{NZ}(\vec{q})|\hat{R}(\Omega)|\Phi^{NZ}(\vec{q})\rangle \\
&= \langle\Phi(\vec{q})|(P^N)^\dagger(P^Z)^\dagger\hat{R}(\Omega)P^ZP^N|\Phi(\vec{q})\rangle \\
&\overset{[P^\tau,\hat{R}(\Omega)]}{=} \langle\Phi(\vec{q})|\hat{R}(\Omega)(P^N)^\dagger(P^Z)^\dagger P^ZP^N|\Phi(\vec{q})\rangle \\
&\overset{(P^\tau)^\dagger=(P^\tau)^2=P^\tau}{=} \langle\Phi(\vec{q})|\hat{R}(\Omega)P^ZP^N|\Phi(\vec{q})\rangle \qquad (6.51)
\end{aligned}$$

As $\hat{R} \neq \hat{R}(N,\,Z)$

$$\begin{aligned}
n^{NZ}(\vec{q},\Omega) &= \langle\Phi_Z(\vec{q})|\hat{R}(\Omega)P^Z|\Phi_Z(\vec{q})\rangle\langle\Phi_N(\vec{q})|\hat{R}(\Omega)P^N|\Phi_N(\vec{q})\rangle \\
&= n^Z(\vec{q},\Omega)n^N(\vec{q},\Omega) \qquad (6.52)
\end{aligned}$$

Using the explicit expression for P^τ we can write;

$$\begin{aligned} n^\tau(\vec{q},\Omega) &= \frac{1}{L}\sum_{l_\tau=1}^{L} e^{-i\varphi_{l_\tau}N_\tau}\langle\Phi_\tau(\vec{q})|\hat{R}(\Omega)e^{i\varphi_{l_\tau}\hat{N}_\tau}|\Phi_\tau(\vec{q})\rangle \\ &= \frac{1}{L}\sum_{l_\tau=1}^{L} e^{-i\varphi_{l_\tau}N_\tau} n(\vec{q},\Omega,\varphi_{l_\tau}) \qquad (6.53) \\ n(\vec{q},\Omega,\varphi_{l_\tau}) &= \langle\Phi_\tau(\vec{q})|\hat{R}(\Omega)e^{i\varphi_{l_\tau}\hat{N}_\tau}|\Phi_\tau(\vec{q})\rangle \qquad (6.54) \end{aligned}$$

To sum up, the main ingredient to calculate the norm overlap 6.50 is 6.54. Once this is done, we just sum over the euler angle to obtain 6.53 , and finally perform the integral 6.50, as shown in the following sequence:

$$n(\vec{q},\Omega,\varphi_{l_\tau}) \overset{\sum_{l_\tau=1}^{L} e^{-i\varphi_{l_\tau}N_\tau}}{\rightarrow} n^\tau(\vec{q},\Omega) \overset{\Pi_{\tau=Z,N}}{\rightarrow} n^{NZ}(\vec{q}) \overset{\int d\Omega D^{I\star}_{KK'}(\Omega)}{\rightarrow} \mathcal{N}^{NZ,I}_{KK'}(\vec{q}) \qquad (6.55)$$

This main ingredient (blue) is obtained in detail in Appendix A for the general case in which the states on left and right are different $\vec{q} \neq \vec{q}\,'$. Therefore the expression in this particular case is obtained by using $\vec{q} = \vec{q}\,$.

6.2.2 Hamiltonian overlap

The terms of the Hamiltonian which commute with the rotation operator $\hat{R}$ can be expressed as:

$$\begin{aligned}
\mathcal{H}^{INZ}(\vec{q},\Omega) &= \langle\Phi(\vec{q})^{NZ}|(P^I_{MK})^\dagger \hat{H} P^I_{MK'}|\Phi(\vec{q})^{NZ}\rangle \\
&\overset{[\hat{H},\hat{R}]=0}{=} \langle\Phi(\vec{q})^{NZ}|\hat{H}(P^I_{MK})^\dagger P^I_{MK'}|\Phi(\vec{q})^{NZ}\rangle \\
&\overset{(6.33)}{=} \langle\Phi^{NZ}(\vec{q})|\hat{H} P^I_{KM} P^I_{MK'}|\Phi^{NZ}(\vec{q})\rangle \\
&\overset{(6.34)}{=} \langle\Phi^{NZ}(\vec{q})|\hat{H} P^I_{KK'}|\Phi^{NZ}(\vec{q})\rangle \\
&= \frac{2I+1}{8\pi^2}\int d\Omega D^{I\star}_{KK'}(\Omega)\langle\Phi^{NZ}(\vec{q})|\hat{H}\hat{R}(\Omega)|\Phi^{NZ}(\vec{q})\rangle \\
&= \frac{2I+1}{8\pi^2}\int d\Omega D^{I\star}_{KK'}(\Omega) h^{NZ}(\vec{q},\Omega) \qquad (6.56)
\end{aligned}$$

where we defined

$$\begin{aligned}
h^{NZ}(\vec{q},\Omega) &= \langle\Phi^{NZ}(\vec{q})|\hat{H}\hat{R}(\Omega)|\Phi^{NZ}(\vec{q})\rangle \\
&= \langle\Phi(\vec{q})|(P^N)^\dagger(P^Z)^\dagger\hat{H}\hat{R}(\Omega)P^Z P^N|\Phi(\vec{q})\rangle \\
&[P^\tau,\ \hat{R}(\Omega)] = 0 \\
&[P^\tau,\ \hat{H}(\Omega)] = 0 \\
&= \langle\Phi(\vec{q})|\hat{H}\hat{R}(\Omega)(P^N)^\dagger(P^Z)^\dagger P^Z P^N|\Phi(\vec{q})\rangle \\
&\overset{(P^\tau)^\dagger=(P^\tau)^2=P^\tau}{=} \langle\Phi(\vec{q})|\hat{H}\hat{R}(\Omega)P^Z P^N|\Phi(\vec{q})\rangle \qquad (6.57)
\end{aligned}$$

Moreover, using the mixed density prescription the density dependent term can also be expressed as in eq 6.57 [13]. In order to use the Wick theorem [6] and the generalized density and pairing tensors (See Appendix B); we derive

the expression for

$$e^{NZ}(\vec{q},\Omega) = \frac{h^{NZ}(\vec{q},\Omega)}{n^{NZ}(\vec{q},\Omega)} \tag{6.58}$$

$$= \frac{\langle\Phi(\vec{q})|\hat{H}\hat{R}(\Omega)P^Z P^N|\Phi(\vec{q})\rangle}{\langle\Phi(\vec{q})|\hat{R}(\Omega)P^Z P^N|\Phi(\vec{q})\rangle} \tag{6.59}$$

and after calculate $h^{NZ}(\vec{q},\Omega)$ as;

$$h^{NZ}(\vec{q},\Omega) = \frac{h^{NZ}(\vec{q},\Omega)}{n^{NZ}(\vec{q},\Omega)} n^{NZ}(\vec{q},\Omega)$$

$$= e^{NZ}(\vec{q},\Omega) n^{NZ}(\vec{q},\Omega) \tag{6.60}$$

With (6.51) y (6.57) we can write in a compact way :

$$\frac{\langle\Phi(\vec{q})|\hat{H}\hat{R}(\Omega)\hat{P}^Z\hat{P}^N|\Phi(\vec{q})\rangle}{\langle\Phi(\vec{q})|\hat{R}(\Omega)\hat{P}^Z\hat{P}^N|\Phi(\vec{q})\rangle} = \sum_{l_Z=1}^{L}\sum_{l_Z=1}^{L} y_{l_Z} y_{l_N} e(\vec{q},\Omega,\varphi_{l_Z},\varphi_{l_N}) \tag{6.61}$$

where

$$y_{l_\tau}(\vec{q},\Omega,\varphi_{l_\tau}) = \frac{\langle\Phi_\tau(\vec{q})|\hat{R}(\Omega)e^{i\varphi_{l_\tau}(\hat{N}_\tau - N_\tau)}|\Phi_\tau(\vec{q})\rangle}{\sum_{l_\tau=1}^{L}\langle\Phi_\tau(\vec{q})|\hat{R}(\Omega)e^{i\varphi_{l_\tau}(\hat{N}_\tau - N_\tau)}|\Phi_\tau(\vec{q})\rangle} \tag{6.62}$$

$$e(\vec{q},\Omega,\varphi_{l_Z},\varphi_{l_N}) = \frac{\langle\Phi(\vec{q})|\hat{H}\hat{R}(\Omega)e^{i\varphi_{l_Z}\hat{N}_Z}e^{i\varphi_{l_Z}\hat{N}_N}|\Phi(\vec{q})\rangle}{\langle\Phi(\vec{q})|\hat{R}(\Omega)e^{i\varphi_{l_Z}\hat{N}_Z}e^{i\varphi_{l_Z}\hat{N}_N}|\Phi(\vec{q})\rangle} \tag{6.63}$$

Again we have to calculate a main ingredient, which in this case is 6.63.

$$e(\vec{q},\Omega,\varphi_{l_Z},\varphi_{l_N}) \overset{\sum_{l_Z=1}^{L}\sum_{l_N=1}^{L} y_{l_Z} y_{l_N}}{\rightarrow} e(\vec{q},\Omega) \overset{\times n^{NZ}(\vec{q})}{\rightarrow} h^{NZ}(\vec{q},\Omega) \overset{\int d\Omega D^{I\star}_{KK'}(\Omega)}{\rightarrow} \mathcal{H}^{NZ,I}_{KK'}(\vec{q}) \tag{6.64}$$

This main ingredient (blue colour) is obtained in detail in appendices B,C. Expressions 6.61-6.66 are valid for the expected value of any operator $\hat{O}$;

$$\frac{\langle\Phi(\vec{q})|\hat{O}\hat{R}(\Omega)\hat{P}^{Z}\hat{P}^{N}|\Phi(\vec{q})\rangle}{\langle\Phi(\vec{q})|\hat{R}(\Omega)\hat{P}^{Z}\hat{P}^{N}|\Phi(\vec{q})\rangle} = \sum_{l_Z=1}^{L}\sum_{l_Z=1}^{L} y_{l_Z}y_{l_N}o(\vec{q},\Omega,\varphi_{l_Z},\varphi_{l_N}) \tag{6.65}$$

$$o(\vec{q},\Omega,\varphi_{l_Z},\varphi_{l_N}) = \frac{\langle\Phi(\vec{q})|\hat{O}\hat{R}(\Omega)e^{i\varphi_{l_Z}\hat{N}_Z}e^{i\varphi_{l_N}\hat{N}_N}|\Phi(\vec{q})\rangle}{\langle\Phi(\vec{q})|\hat{R}(\Omega)e^{i\varphi_{l_Z}\hat{N}_Z}e^{i\varphi_{l_N}\hat{N}_N}|\Phi(\vec{q})\rangle} \tag{6.66}$$

6.3 SCCM

In this final step we use the states with the correct quantum number N, Z, I, K, M and different values of parameters $\vec{q}$ and use them in a complete configuration mixing. The general ansatz is given by;

$$|\Psi_{\sigma}^{NZ;IM}\rangle = \sum_{\vec{q},K} f_{K\sigma}^{I}(\vec{q})|\Phi(\vec{q})^{NZ;IMK}\rangle \tag{6.67}$$

The general Hill-Wheeler-Griffin equation:

$$\sum_{K'\vec{q}'}\left(\mathcal{H}_{KK'}^{NZ,I}(\vec{q},\vec{q}\,') - E_{\sigma}^{NZ,I}\mathcal{N}_{K,K'}^{NZ,I}(\vec{q},\vec{q}\,')\right)f_{K'\sigma}^{I,NZ}(\vec{q}\,') = 0 \tag{6.68}$$

with

$$\mathcal{H}_{KK'}^{NZ,I}(\vec{q},\vec{q}\,') = \langle\Phi^{NZ,IMK}(\vec{q})|\hat{H}_{KK'}|\Phi^{NZ,IMK'}(\vec{q}\,')\rangle \tag{6.69}$$

$$\mathcal{N}^{NZ,I}_{KK'}(\vec{q},\vec{q}\,') \;=\; \langle\Phi(\vec{q})^{NZ,IMK}|\Phi(\vec{q}\,')^{NZ,IMK'}\rangle \tag{6.70}$$

Again, the first step is the diagonalization of the norm overlap:

$$\sum_{\vec{q},\,'\,K'} \mathcal{N}^{NZ,I}_{KK'}(\vec{q},\vec{q}\,')u^{NZ,I}_{\mu}(\vec{q}\,'\;K') = n^{NZ,I}_{\mu}u^{NZ,I}_{\mu}(\vec{q}\;K) \tag{6.71}$$

With the eigenvalues $n^{NZ,I}_{\mu}$ and eigenvectors $u^{NZ,I}_{\mu}(\vec{q}\;K)$ we construct the natural basis;

$$|\mu^{NZ,I}\rangle = \sum_{\vec{q}K} \frac{u^{NZ,I}_{\mu}(\vec{q}\,K)}{\sqrt{n^{NZ,I}_{\mu}}}|\Phi(\vec{q})^{NZ;IMK}\rangle \tag{6.72}$$

The Hamiltonian in this basis is given by;

$$\langle\mu^{NZ,I}|\hat{H}|\mu^{,NZ,I}\rangle = \sum_{K,K',\vec{q},\vec{q}\,'} u^{\star,NZ,I}_{\mu}(\vec{q}\,K)\frac{\mathcal{H}^{NZ,I}_{KK'}(\vec{q},\vec{q}\,')}{\sqrt{n^{NZ,I}_{\mu}n^{NZ,I}_{\mu'}}}u^{NZ,I}_{\mu'}(\vec{q}\,'\;K') \tag{6.73}$$

with

$$\mathcal{H}^{NZ,I}_{KK'}(\vec{q},\vec{q}\,') = \langle\Phi(\vec{q})^{NZ;IMK}|\hat{H}|\Phi(\vec{q}\,')^{NZ;IMK'}\rangle \tag{6.74}$$

We diagonalize the Hamiltonian in this basis;

$$\sum_{\mu'}\langle\mu^{NZ,I}|\hat{H}|\mu^{,NZ,I}\rangle g^{NZ,I}_{\mu'\sigma} = E^{NZ,I}_{\sigma}g^{NZ,I}_{\mu\sigma} \tag{6.75}$$

This provides the eigenvalues $E^{NZ,I}_{\sigma}$ and the eigenvectors $g^{I}_{\mu\sigma}$. The weights $f^{I}_{K'\sigma}(\vec{q})$ are given by:

$$f^{I}_{K\sigma}(\vec{q}) = \sum_{\mu}\frac{g^{I}_{\mu\sigma}}{\sqrt{n^{NZ,I}_{\mu}}}u^{NZ,I}_{\mu}(\vec{q}\,K) \tag{6.76}$$

In analogy to 6.46 the quantity:

$$F^I_{K\sigma}(\vec{q}) = \sum_{\mu} g^I_{\mu\sigma} u^{NZ,I}_{\mu}(\vec{q}\,K) \tag{6.77}$$

represents the probability density of finding a given $I, K, \vec{q}$. The probability density of finding a given $I, \vec{q}$:

$$F^I_{\sigma}(\vec{q}) = \sum_{\mu K} g^I_{\mu\sigma} u^{I}_{\mu}(\vec{q}\,K) \tag{6.78}$$

Again the total probability mus be equal to 1;

$$\begin{aligned} \sum_{K\vec{q}} |F^I_{K\sigma}(\vec{q})|^2 &= \sum_{K(\vec{q})} \sum_{\mu\mu'} (g^I_{\mu\sigma})^{\star} u^{\star NZ,I}_{\mu}(\vec{q}\,K) g^I_{\mu'\sigma} u^{NZ,I}_{\mu'}(\vec{q}\,K) \\ &= \sum_{\mu} |g^I_{\mu\sigma}|^2 = 1 \end{aligned} \tag{6.79}$$

where we now used $\sum_{K\vec{q}} u^{NZ,I}_{\mu}(\vec{q}\,K) u^{\star NZ,I}_{\mu'}(\vec{q}\,K') = \delta_{\mu\mu'}$.

Now we can define two different probabilities. The probability of finding a given K is obtained by summing in all possibles $\vec{q}$;

$$P^I_{K\sigma} = \sum_{\vec{q}} |F^I_{K\sigma}(\vec{q})|^2 \tag{6.80}$$

and the probability of finding a fixed point $\vec{q}$, which is obtained by summing in K.

$$P^I_{\sigma}(\vec{q}) = \sum_{K} |F^I_{K\sigma}(\vec{q})|^2 \tag{6.81}$$

6.3.1 Norm overlap

We will use a similar derivation of expressions and sequence 6.55, but with $\vec{q}, \vec{q}\,'$. The norm;

$$\mathcal{N}^{NZ,I}_{KK'}(\vec{q},\vec{q}\,') = \frac{2I+1}{8\pi^2}\int d\Omega D^{I\star}_{KK'}(\Omega) n^{NZ}(\vec{q},\vec{q}\,',\Omega) \tag{6.82}$$

$$\begin{aligned} n^{NZ}(\vec{q},\Omega) &= \langle \Phi^{NZ}(\vec{q})|\hat{R}(\Omega)|\Phi^{NZ}(\vec{q}\,')\rangle \\ &= \langle \Phi(\vec{q})|\hat{R}(\Omega)P^Z P^N|\Phi(\vec{q}\,')\rangle \end{aligned} \tag{6.83}$$

As $\hat{R} \neq \hat{R}(N,\, Z)$

$$\begin{aligned} n^{NZ}(\vec{q},\vec{q}\,',\Omega) &= \langle \Phi_\pi(\vec{q})|\hat{R}(\Omega)P^Z|\Phi_\pi(\vec{q}\,')\rangle\langle \Phi_N(\vec{q})|\hat{R}(\Omega)P^N|\Phi_N(\vec{q}\,')\rangle \\ &= n^Z(\vec{q},\vec{q}\,',\Omega)n^N(\vec{q},\vec{q}\,',\Omega) \end{aligned} \tag{6.84}$$

and finally;

$$n^\tau(\vec{q},\vec{q}\,',\Omega) = \frac{1}{L}\sum_{l_\tau=1}^{L} e^{-i\varphi_{l_\tau}N_\tau} n(\vec{q},\vec{q}\,',\Omega,\varphi_{l_\tau}) \tag{6.85}$$

Now sequence 6.55 becomes;

$$\begin{array}{lll} n(\vec{q},\vec{q}\,',\Omega,\varphi_{l_\tau}) & \overset{\sum_{l_\tau=1}^{L} e^{-i\varphi_{l_\tau}N_\tau}}{\rightarrow} & n^\tau(\vec{q},\vec{q}\,',\Omega) \quad \overset{\prod_{\tau=Z,N}}{\rightarrow} \\ & & n^{NZ}(\vec{q},\vec{q}\,') \quad \overset{\int d\Omega D^{I\star}_{KK'}(\Omega)}{\rightarrow} \mathcal{N}^{NZ,I}_{KK'}(\vec{q},\vec{q}\,') \end{array} \tag{6.86}$$

6.3.2 Hamiltonian overlap

Similarly for the Hamiltonian;

$$\mathcal{H}^{NZ,I}_{KK'}(\vec{q},\vec{q}\,') = \frac{2I+1}{8\pi^2}\int d\Omega D^{I\star}_{KK'}(\Omega) h^{NZ}(\vec{q},\vec{q}\,',\Omega) \tag{6.87}$$

with

$$\begin{aligned} h^{NZ}(\vec{q},\vec{q}\,',\Omega) &= \langle\Phi^{NZ}(\vec{q})|\hat{H}\hat{R}(\Omega)|\Phi^{NZ}(\vec{q}\,')\rangle \\ &= \langle\Phi(\vec{q})|\hat{H}\hat{R}(\Omega)P^Z P^N|\Phi(\vec{q}\,')\rangle \end{aligned} \tag{6.88}$$

Again we calculate;

$$e^{NZ}(\vec{q},\Omega) = \frac{h^{NZ}(\vec{q},\vec{q'},\Omega)}{n^{NZ}(\vec{q},\vec{q'},\Omega)} \tag{6.89}$$

and after calculate $h^{NZ}(\vec{q},\vec{q}\,',\Omega)$ as;

$$\begin{aligned} h^{NZ}(\vec{q},\vec{q}\,',\Omega) &= \frac{h^{NZ}(\vec{q},\vec{q'},\Omega)}{n^{NZ}(\vec{q},\vec{q}\,',\Omega)} n^{NZ}(\vec{q},\vec{q}\,',\Omega) \\ &= e^{NZ}(\vec{q},\vec{q}\,',\Omega) n^{NZ}(\vec{q},\vec{q}\,',\Omega) \end{aligned} \tag{6.90}$$

So; $\hat{H}$:

$$\frac{\langle\Phi(\vec{q})|\hat{H}\hat{R}(\Omega)\hat{P}^Z\hat{P}^N|\Phi(\vec{q'})\rangle}{\langle\Phi(\vec{q})|\hat{R}(\Omega)\hat{P}^Z\hat{P}^N|\Phi(\vec{q}\,')\rangle} = \sum_{l_\pi=1}^{L}\sum_{l_\pi=1}^{L} y_{l_\pi} y_{l_N} e(\vec{q},\vec{q}\,',\Omega,\varphi_{l_\pi},\varphi_{l_N}) \tag{6.91}$$

where

$$y_{l_\tau}(\vec{q},\vec{q}\,',\Omega,\varphi_{l_\tau}) = \frac{\langle\Phi_\tau(\vec{q})|\hat{R}(\Omega)e^{i\varphi_{l_\tau}(\hat{N}_\tau-N_\tau)}|\Phi_\tau(\vec{q'})\rangle}{\sum_{l_\tau=1}^{L}\langle\Phi_\tau(\vec{q})|\hat{R}(\Omega)e^{i\varphi_{l_\tau}(\hat{N}_\tau-N_\tau)}|\Phi_\tau(\vec{q}\,')\rangle} \quad (6.92)$$

$$e(\vec{q},\vec{q'},\Omega,\varphi_{l_Z},\varphi_{l_N}) = \frac{\langle\Phi(\vec{q})|\hat{H}\hat{R}(\Omega)e^{i\varphi_{l_Z}\hat{N}_Z}e^{i\varphi_{l_N}\hat{N}_N}|\Phi(\vec{q'})\rangle}{\langle\Phi(\vec{q})|\hat{R}(\Omega)e^{i\varphi_{l_Z}\hat{N}_Z}e^{i\varphi_{l_N}\hat{N}_N}|\Phi(\vec{q}\,')\rangle} \quad (6.93)$$

Now the sequence 6.64 becomes;

$$\begin{array}{ccccc} e(\vec{q},\vec{q}\,',\Omega,\varphi_{l_Z},\varphi_{l_N}) & \overset{\sum_{l_Z=1}^{L}\sum_{l_N=1}^{L} y_{l_Z}y_{l_N}}{\rightarrow} & e(\vec{q},\vec{q}\,',\Omega) & \overset{\times n^{NZ}(\vec{q},\vec{q}\,')}{\rightarrow} & \\ & & h^{NZ}(\vec{q},\vec{q}\,',\Omega) & \overset{\int d\Omega D^{I\star}_{KK'}(\Omega)}{\rightarrow} & \mathcal{H}^{NZ,I}_{KK'}(\vec{q},\vec{q}\,') \end{array} \quad (6.94)$$

Again, expressions 6.91-6.93 are valid for the expected value of any operator $\hat{O}$;

$$\frac{\langle\Phi(\vec{q})|\hat{O}\hat{R}(\Omega)\hat{P}^Z\hat{P}^N|\Phi(\vec{q}\,')\rangle}{\langle\Phi(\vec{q})|\hat{R}(\Omega)\hat{P}^Z\hat{P}^N|\Phi(\vec{q}\,')\rangle} = \sum_{l_Z=1}^{L}\sum_{l_Z=1}^{L} y_{l_Z}y_{l_N}o(\vec{q},\vec{q}\,',\Omega,\varphi_{l_Z},\varphi_{l_N}) \quad (6.95)$$

with

$$o(\vec{q},\vec{q}\,',\Omega,\varphi_{l_Z},\varphi_{l_N}) = \frac{\langle\Phi(\vec{q})|\hat{O}\hat{R}(\Omega)e^{i\varphi_{l_Z}\hat{N}_Z}e^{i\varphi_{l_N}\hat{N}_N}|\Phi(\vec{q}\,')\rangle}{\langle\Phi(\vec{q})|\hat{R}(\Omega)e^{i\varphi_{l_Z}\hat{N}_Z}e^{i\varphi_{l_N}\hat{N}_N}|\Phi(\vec{q}\,')\rangle} \quad (6.96)$$

Bibliography

[1] M. Anguiano, J.L. Egido, and L.M. Robledo. *Nuclear Physics A*, 696(3):467 – 493, 2001.

[2] M. Anguiano, J.L. Egido, and L.M. Robledo. *Nuclear Physics A*, 683(1):227 – 254, 2001.

[3] A. Kamlah. 216:52, 1968.

[4] P. Ring and P. Schuck. *The Nuclear Many-Body Problem*. Physics and astronomy online library. Springer, 2004.

[5] V.N.Fomenko. A3:8, 1970.

[6] R. Balian and E. Brezin. *Il Nuovo Cimento B (1965-1970)*, 64(1):37–55, 1969.

[7] K. Hara and S. Iwasaki. *Nuclear Physics A*, 332(1):61 – 68, 1979.

[8] K. Hara, S. Iwasaki, and K. Tanabe. *Nuclear Physics A*, 332(1):69 – 81, 1979.

[9] GF Bertsch and LM Robledo. *Physical review letters*, 108(4):042505, 2012.

[10] C. González-Ballestero, L.M. Robledo, and G.F. Bertsch. *Computer Physics Communications*, 182(10):2213 – 2218, 2011.

[11] A. Valor, J. L. Egido, and L. M. Robledo. *Phys. Rev. C*, 53:172–175, Jan 1996.

[12] A. Valor, J.L. Egido, and L.M. Robledo. *Nuclear Physics A*, 665(12):46 – 70, 2000.

[13] R. Rodríguez-Guzmán, J.L. Egido, and L.M. Robledo. *Nuclear Physics A*, 709(1):201 – 235, 2002.

[14] T. Duguet and P. Bonche. *Phys. Rev. C*, 67:054308, May 2003.

[15] L.M. Robledo. *Conference: Correlations in nuclei: beyond mean-field and shell model*, Trento,2007.

[16] David Lawrence Hill and John Archibald Wheeler. *Phys. Rev.*, 89:1102–1145, Mar 1953.

[17] James J. Griffin and John A. Wheeler. *Phys. Rev.*, 108:311–327, Oct 1957.

RESULTS I

Time reversal symmetry breaking in even nuclei

Chapter 7

Symmetry conserving configuration mixing method with cranked states

We perform the first calculations of a symmetry conserving configuration mixing method (SCCM) using time-reversal symmetry breaking Hartree-Fock-Bogoliubov (HFB) states with the Gogny D1S interaction. The method includes particle number and tridimensional angular momentum symmetry restorations as well as configuration mixing within the generator coordinate method (GCM) framework. The nucleus ^{32}Mg is chosen to show the performance and reliability of the calculations. Additionally, 2_1^+ and 4_1^+ states are computed for the magnesium isotopic chain, where a noticeable stretching of the spectrum is obtained by including cranked states, leading to an almost perfect agreement with the known experimental data. The results are

published in [1].

Up to now our implementations of the SCCM method had assumed that the intrinsic states conserved the time-reversal symmetry. The usual variational calculations assuming time-reversal symmetry conservation and angular momentum projection afterwards (which is our case) tend to favor the ground states with respect to other excited states. The most typical signature of such an effect is the stretching found in the spectra with respect to the experimental values. The addition of time-reversal symmetry breaking intrinsic states would thus increase the variational space for excited states and provide a better description of the spectrum. The cranking model -which breaks the time-reversal symmetry- is an accurate approximation for the variation after angular momentum projection in the limit of strong rotational symmetry breaking. Pioneering angular momentum projection of cranking states have been reported with schematic pairing plus quadrupole interactions [2–4] and with Skyrme energy density functionals [5,6]. However, neither configuration -shape- mixing nor, in the case of Skyrme interactions, pairing correlations, were taking into account. We now present the first results of the extension of the SCCM method including now time-reversal-symmetry breaking intrinsic states introduced through cranking calculations.

We will follow the steps studied in Chapter 6. In 7.1 we show the results of the Particle Number VAP calculation (step one). In 7.2 we recover rotational invariance (step two). Finally in 7.3 we perform the most general configuration mixing; i.e. mixing in the deformation parameters and states with different angular content (step three).

7.1 PN-VAP calculation

The starting point of the method is the construction of a set of intrinsic many-body states having different deformations and intrinsic angular momentum. Such states, $|\Phi(\beta,\gamma,J_c)\rangle \equiv |\rangle$, have the structure of Hartree-Fock-Bogoliubov (HFB) and are found by minimizing the particle number projected HFB energy, i.e. , eq. (6.7) with $\hat{\vec{Q}} = (\hat{Q}_{20}, \hat{Q}_{20}, \hat{J}_x)$.

$$E'_{J_c}(\beta,\gamma) = \frac{\langle \hat{H} P^N P^Z \rangle}{\langle P^N P^Z \rangle} - \omega_{J_c}\langle \hat{J}_x \rangle - \lambda_{q_{20}}\langle \hat{Q}_{20} \rangle - \lambda_{q_{22}}\langle \hat{Q}_{22} \rangle \qquad (7.1)$$

The first term in the r.h.s. of Eq. 7.1 is the particle number projected energy and the last terms correspond to the constraints on the cranking angular momentum J_c and on the quadrupole deformation of the system (β,γ), being ω_{J_c}, $\lambda_{q_{20}}$ and $\lambda_{q_{22}}$ the Lagrange multipliers that ensure the conditions:

$$\langle \hat{J}_x \rangle = \sqrt{J_c(J_c+1)};\ \langle \hat{Q}_{20} \rangle = q_{20};\ \langle \hat{Q}_{22} \rangle = q_{22} \qquad (7.2)$$

where $\hat{J}_x$ is the x-component of the angular momentum operator and $\hat{Q}_{2\mu}$ with $\mu = -2,-1,..,2$ is the μ component of the quadrupole operator. See equation 3.26.

In the chapter devoted to the symmetries we saw that due to the inclusion of the term $\omega_{J_c}\langle \hat{J}_x \rangle$ time reversal symmetry is not preserved, the states are only invariant under the subgroup D_{2h}. This leads to a non-equivalence of the six sextants and therefore three of them must be used in the calculations (there is only symmetry with respect to the $\gamma = 120°, 300°$ direction). However in case

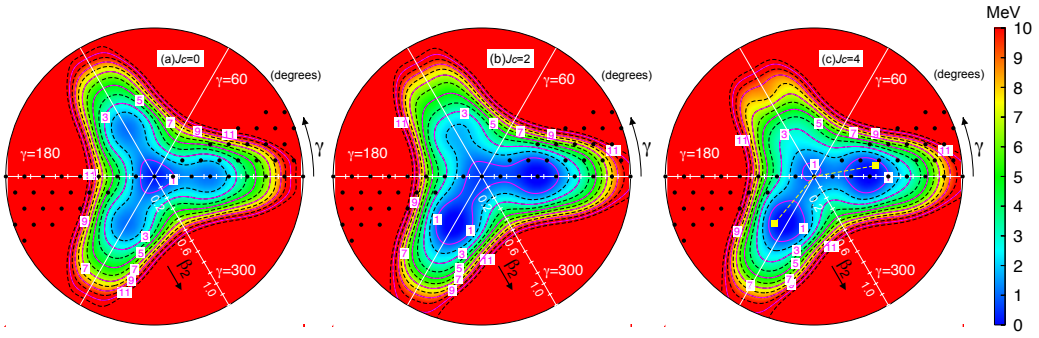

Figure 7.1: PN-VAP potential energy surfaces for different values of the cranking angular momentum J_c for the nucleus ^{32}Mg. Gogny D1S interaction is used here. The contour plots are separated in energy by 1.0 MeV. Each PES is normalized to the energy of their corresponding minima, i.e., (a) -249.902 MeV, (b) -247.910 MeV and (c) -246.789 MeV. The black bullets are the states included in the GCM calculation while the yellow squares are the states analyzed in detail in Figs. 7.2- 7.3.

$J_c = 0$ they must be equivalent. This property is used to test the performance of the method since they provide non-trivial checks that help to identify possible inconsistencies. We check this symmetry by performing PN-VAP calculations in the $(\beta, 0° \leq \gamma \leq 360°)$ plane for three values of the cranking angular momentum $J_c = 0$ (time-reversal symmetry conserving), $J_c = 2$ and $J_c = 4$, selecting the nucleus ^{32}Mg as an example. In Fig. 7.1 we show such potential energy surfaces (PES) -first term in the r.h.s. of Eq. 7.1. Here, the intrinsic states were expanded in nine major spherical harmonic oscillator shells and the number of points included in the mesh of each PES is 502. We notice first the equivalence between all of the sextants in the case where the time-reversal symmetry is preserved ($J_c = 0$, Fig. 7.1(a)). Such a redundancy is reduced to the half of the plane separated by the $\gamma = (120°, 300°)$ axis for $J_c = 2$ and 4 (Figs. 7.1(b)-(c)) as expected. We find the absolute minimum

of the $J_c = 0$ PES in the spherical point as it is presumed from the neutron magic number $N = 20$. The energy grows more rapidly along the oblate directions than in the prolate ones. Additionally, a second minimum -around 1 MeV higher- is obtained at axial prolate configurations with $\beta = 0.45$. For larger values than $\beta \approx 0.7$ the energy increases quickly also along the prolate lines. For $J_c = 2, 4$ the PES resemble the $J_c = 0$ one except for the values along $\gamma = 120°$, where the energy is not as favored as in $\gamma = 0°$ and $\gamma = 240°$. The minima of these surfaces appear at such prolate configurations with $\beta = 0.45$, as in the $J_c = 0$ case but shifted to higher values, around ≈ 2 MeV and ≈ 3 MeV for $J_c = 2$ and 4 respectively.

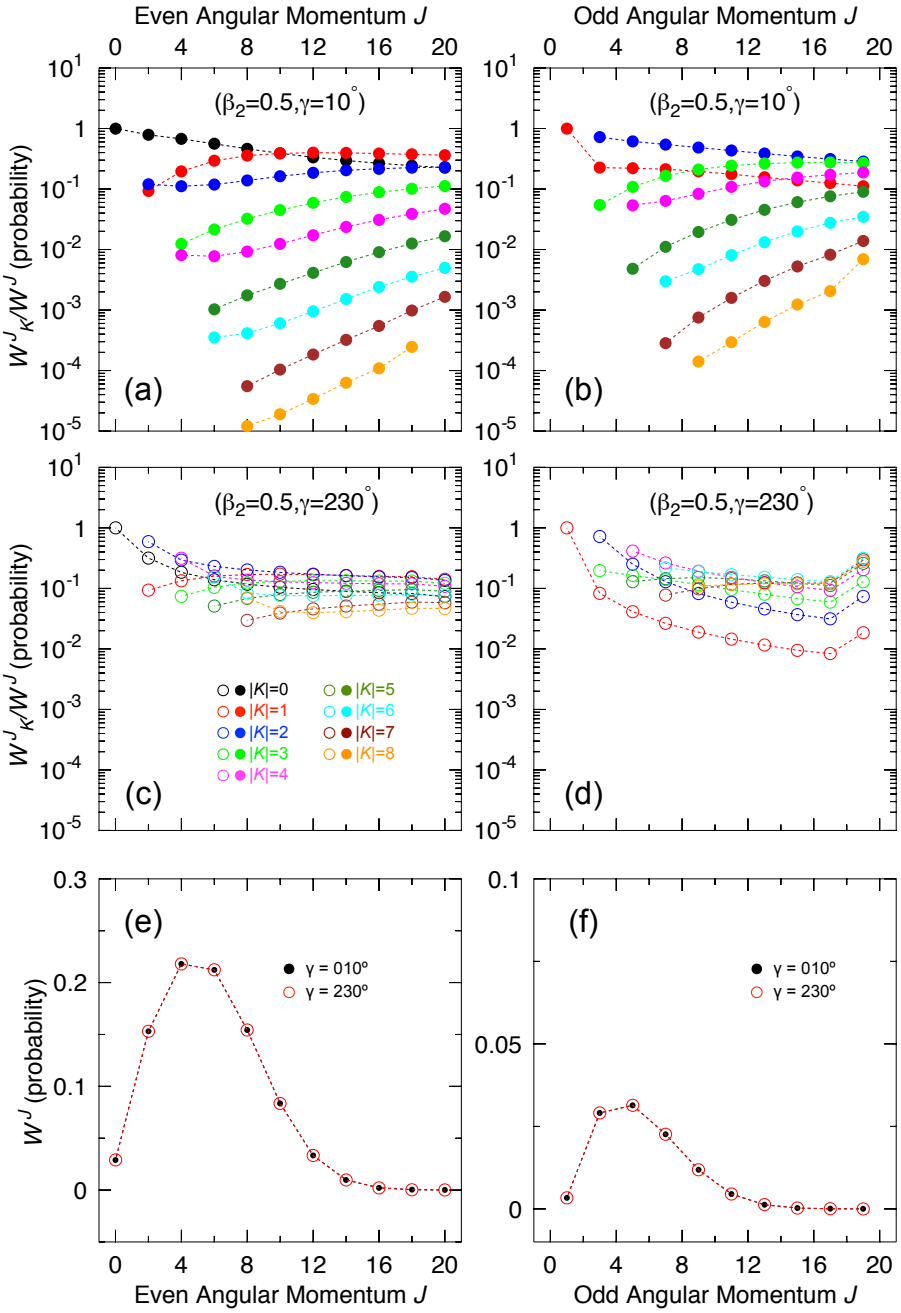

Figure 7.2: Probability distributions of projections K -$W^I_K(\beta,\gamma,J_c)$- for even (left panel) and odd (right panel) values of the angular momentum I for the intrinsic states (a)-(b) $(\beta,\gamma,J_c) = (0.5, 10°, 4)$ and (c)-(d) $(\beta,\gamma,J_c) = (0.5, 230°, 4)$. Distribution of probabilities of (e) even values and (f) odd values of the angular momentum I -$W^I(\beta,\gamma,J_c)$- for the same intrinsic HFB-type wave functions.

7.2 Restoration of rotational invariance

The intrinsic many-body states, $|\rangle$, apart from the particle number symmetry, break the rotational invariance of the hamiltonian. These quantum numbers can be restored by projecting simultaneously onto good number of particles and angular momentum , eq. (6.35) for the special case $\vec{q} = (\beta, \gamma, J_c)$.

$$\begin{aligned} |\Psi_{\sigma}^{NZ;IM}(\beta,\gamma,J_c)\rangle &= \sum_K f_{K\sigma}^I(\beta,\gamma,J_c) P_{MK}^I P^N P^Z |\Phi(\beta,\gamma,J_c)\rangle \\ &= \sum_K f_{K\sigma}^I(\beta,\gamma,J_c) |\Phi^{NZ;IMK}(\beta,\gamma,J_c)\rangle \end{aligned} \tag{7.3}$$

The coefficients $f_{K\sigma}^I(\beta,\gamma,J_c)$ and the energies $E^I_{\sigma,\beta,\gamma,J_c}$ are found variationally by solving the Hill-Wheeler-Griffin (HWG) equations in the subspace (K) eq.(6.36):

$$\sum_{K'} \left(\mathcal{H}_{KK'}^{I;NZ}(\beta,\gamma,J_c) - E_{\sigma}^I(\beta,\gamma,J_c) \mathcal{N}_{KK'}^{I;NZ}(\beta,\gamma,J_c) \right) f_{K\sigma}^I(\beta,\gamma,J_c) = 0 \tag{7.4}$$

where the kernels $\mathcal{H}_{KK'}^{I;NZ}(\beta,\gamma,J_c), \mathcal{N}_{KK'}^{I;NZ}(\beta,\gamma,J_c)$ were defined in 6.37 and 6.38 .

As we saw in chapter 6 we can study the distribution of the wave function $|\Phi^{NZ;IMK}(\beta,\gamma,J_c)\rangle$ in the $|IK\rangle$ subspace;

$$W_K^{NZ,I}(\beta,\gamma,J_c) = \frac{\mathcal{N}_{KK}^{NZ,I}(\beta,\gamma,J_c)}{\langle \Phi(\beta,\gamma,J_c)|P^N P^Z|\Phi(\beta,\gamma,J_c)\rangle} \tag{7.5}$$

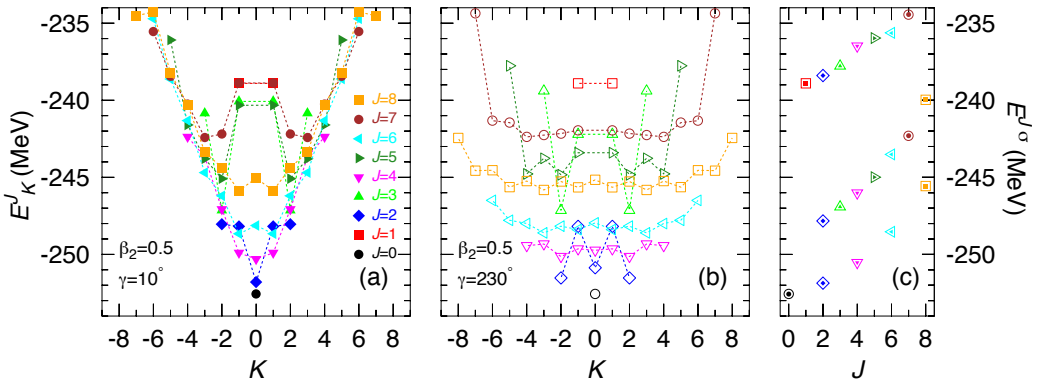

Figure 7.3: Particle number and angular momentum projected energy overlaps $E^I_K(\beta,\gamma,J_c)$ as a function of K for the intrinsic wave functions (a) $(\beta,\gamma,J_c) = (0.5, 10°, 4)$ (filled symbols) and (b) $(\beta,\gamma,J_c) = (0.5, 230°, 4)$ (empty symbols). The last column corresponds to the lowest energies for a given I after $K-$ mixing $E^{J\sigma}_{\beta,\gamma,J_c}$ (Eq. 7.4) for the same intrinsic states as in (a) and (b).

and the total distribution in each I, eq. 6.40:

$$W^{NZ,I}(\beta,\gamma,J_c) = \sum_K W^{NZ,I}_{K\sigma}(\beta,\gamma,J_c) \tag{7.6}$$

Finally the IK-projected energy (6.41);

$$E^{NZ,I}_K(\beta,\gamma,J_c) = \frac{\mathcal{H}^{NZ,I}_{KK}(\beta,\gamma,J_c)}{\mathcal{N}^{NZ,I}_{KK}(\beta,\gamma,J_c)} \tag{7.7}$$

The decomposition $W^{NZ,I}_K(\beta,\gamma,J_c)$ and the energy $E^I_K(\beta,\gamma,J_c)$ are quantities that depend on the orientation of the principle axes of inertia with respect to the (x,y,z)-axes. Nevertheless, the following properties are deduced from the self-consistent symmetries imposed to the intrinsic states: $W^{NZ,I}_K(\beta,\gamma,J_c) = W^{NZ,I}_{-K}(\beta,\gamma,J_c)$, $E^{NZ,I}_K(\beta,\gamma,J_c) = E^{NZ,I}_{-K}(\beta,\gamma,J_c)$, and, if I is odd, the $K=0$ component is forbidden. The dependence on K is re-

moved once the K-mixing is performed since the norm $W^{NZ,I}(\beta,\gamma,J_c)$ and the energy $E^{NZ,I}_{\sigma\beta,\gamma,J_c}$ are scalar quantities [**?**,7,8]. Hence, the same probability distribution $W^{I}(\beta,\gamma,J_c)$ and the same angular momentum projected energy are found in the six sextants of the (β,γ) plane if $J_c = 0$, in a similar way to the PN-VAP energies (Fig. 7.1(a)). However, if the cranking term is non-zero, the (β,γ) plane is again split in two equivalent parts divided by the $(\gamma = 120°, 300°)$ line. We now exploit these symmetries to perform consistency tests of the results and check the implementation of the method. Therefore, we select first two intrinsic states, $|\Phi^{NZ;IMK}(\beta = 0.5, \gamma = 10°, J_c = 4)\rangle$ and $|\Phi^{NZ;IMK}(\beta = 0.5, \gamma = 230°, J_c = 4)\rangle$symmetric with respect to the $(\gamma = 120°, 300°)$ line (see yellow squares in Fig. 7.1(c)). We represent the decomposition of those states in components of the angular momentum I and intrinsic z-projection K in Fig. 7.2(a)-(d), normalized to the total probability of having a given I. The latter is plotted in Fig. 7.2(e)-(f). Here we observe that the decomposition in K is different depending on the value of γ. For $\gamma = 10°$ the probability decreases in general rapidly with increasing K for a fixed value of I. Furthermore, the relative weight of the components with large K tends to increase with larger angular momentum I, while the $K = 0$ component for even I and $K = 1, 2$ components for odd I slightly decrease. These results are consistent with having the intrinsic long inertia axis almost oriented in the z-axis. On the other hand, the probability for a given I is distributed in a larger number of K components for $\gamma = 230°$ and these components are much flatter than in the previous case when the angular momentum I is increased. In this case, the intrinsic long inertia axis is almost oriented perpendicular to the z-axis. In spite of these differences in

the W^I_K distribution, the decomposition in I of both states, summing all of the K components, are identical. We observe two separate distributions for even I (Fig. 7.2(e)) and odd I (Fig. 7.2(f)), being the absolute scale larger for the former. The even (odd) distribution probability increases from $I = 0$ (1) until the maximum at $I = 4$ (5) is reached. Then, W^I decreases, obtaining practically zero probability for even (odd) angular momenta larger than 16 (13). We now analyze the energies obtained after performing the angular momentum projection. In Fig. 7.3(a)-(b) we represent the projected energies computed for different values of the angular momentum I and the intrinsic z-component K. Here, we obtain explicitly the condition $E^I_K = E^I_{-K}$. We see as in the previous case noticeable differences depending on γ. For $\gamma = 10°$ the energies rise rather quickly for large values of K while for $\gamma = 230°$ the energies are flatter. These differences are completely removed when K-mixing is performed through solving the HWG equations (Eq. 7.4) as it is shown in Fig. 7.3(c). There, three bands can be distinguished, namely, a ground state rotational band with $\Delta I = 2$ built on top of $I = 0^+_1$, and two $\Delta I = 1$ bands, being $I = 2^+_1$ (γ-band) and $I = 1^+_1$ the corresponding band-heads. It is important to point out that the results shown in Figs. 7.2- 7.3 constitute a highly non-trivial check of the implementation of the method. However, we can test even further the performance of the angular momentum projection by projecting the whole (β, γ) plane as it is plotted in Fig. 7.4. The same mesh of states as in Fig 7.1 is also used in these calculations. Additionally, the number of integration points in the Euler angles are chosen to ensure that the mean values of the total angular momentum operator, $\hat{J}^2$, calculated with the states $|\Phi^{NZ;IMK}(\beta, \gamma, J_c)\rangle$ differ from $I(I+1)$ less than 10^{-4}. Concerning the

conservation and/or breaking of the D_{2h}^{T} point group symmetry, we represent now the angular momentum projected PES for $(I = J_c, \sigma = 1)$. Similarly to the results obtained in Fig. 7.1 for the PN-VAP approach, for the $J_c = 0$ case, the equivalence between the six sextants is preserved when angular momentum projection is performed. In this case, the intrinsic wave functions do not break the D_{2h}^{T} point group symmetries. In Fig 7.4(a) only the PES for $(I = 0, \sigma = 1)$ is shown although the same equivalence is obtained for other values of (I, σ) [8]. However, the angular momentum projected PES attained by restoring the rotational symmetry of the $J_c \neq 0$ states are symmetric only around the axis $(\gamma = 120°, 300°)$ (Fig 7.4(b)-(c)). Once more, although only the energies $E^{I=2}_{\sigma=1}$ and $E^{I=4}_{\sigma=1}$ from projecting $J_c = 2$ and $J_c = 4$ states are represented in Fig. 7.4(b)-(c) respectively, the PES obtained for other values of (I, σ) present similar symmetries (not shown). Apart from

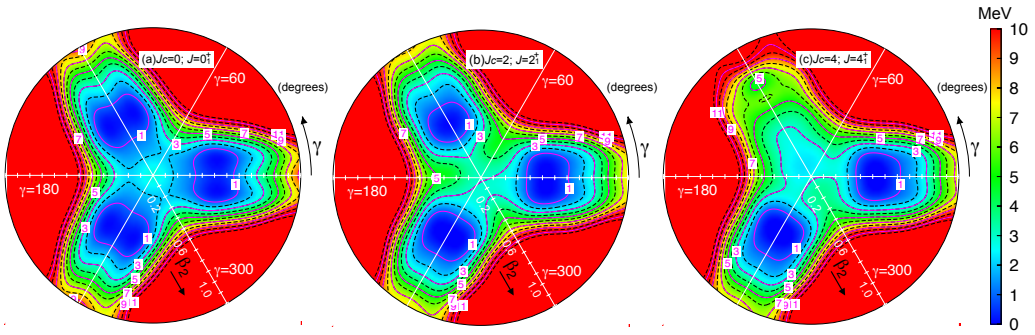

Figure 7.4: Particle number and angular momentum projected potential energy surfaces (Eq. 7.4) for (a) $J_c = 0$ and $(I = 0; \sigma = 1)$; (b) $J_c = 2$ and $(I = 2; \sigma = 1)$; and (c) $J_c = 4$ and $(I = 4; \sigma = 1)$ for the nucleus ^{32}Mg. The contour plots are separated in energy by 1.0 MeV. Each PES is normalized to the energy of their corresponding minima, i.e., (a) -252.924 MeV, (b) -252.021 MeV and (c) -250.463 MeV.

the symmetries discussed above, the angular momentum projection modifies

significantly the surfaces obtained at the PN-VAP approach. In general, the minima found in the PES at the PN-VAP level (Fig. 7.1) are now wider and at slightly larger deformation whenever the angular momentum is restored (Fig. 7.4). As a matter of fact, these beyond mean-field correlations move the ground state from the spherical point to prolate configurations with $\beta \approx 0.5$ (Fig. 7.4(a)), that was formerly a secondary minimum in the PN-VAP calculation (Fig. 7.1(a)). This effect was already obtained with axial calculations [9] and is a self-consistent way to obtain the deformed ground state for the nucleus ^{32}Mg, i.e., as belonging to the 'island of inversion' with an erosion of the $N = 20$ magic number.

7.3 General SCCM

The last step in the SCCM many-body method proposed in this work is the mixing of all of the intrinsic states projected to particle number and angular momentum (third step on Chapter 6). The general wave function 6.67 is given by;

$$|\Psi_{\sigma}^{NZ;I,M;}\rangle = \sum_{\beta,\gamma,J_c,K} f_{K\sigma}^{I}(\beta,\gamma,J_c)|\Phi^{NZ;IMK}(\beta,\gamma,J_c)\rangle \tag{7.8}$$

In this general case, the coefficients $f_{K\sigma}^{I}(\beta,\gamma,J_c)$ in Eq. 7.8, and the final spectrum, $E_{\sigma}^{NZ,I}$, are obtained by solving the corresponding HWG equations

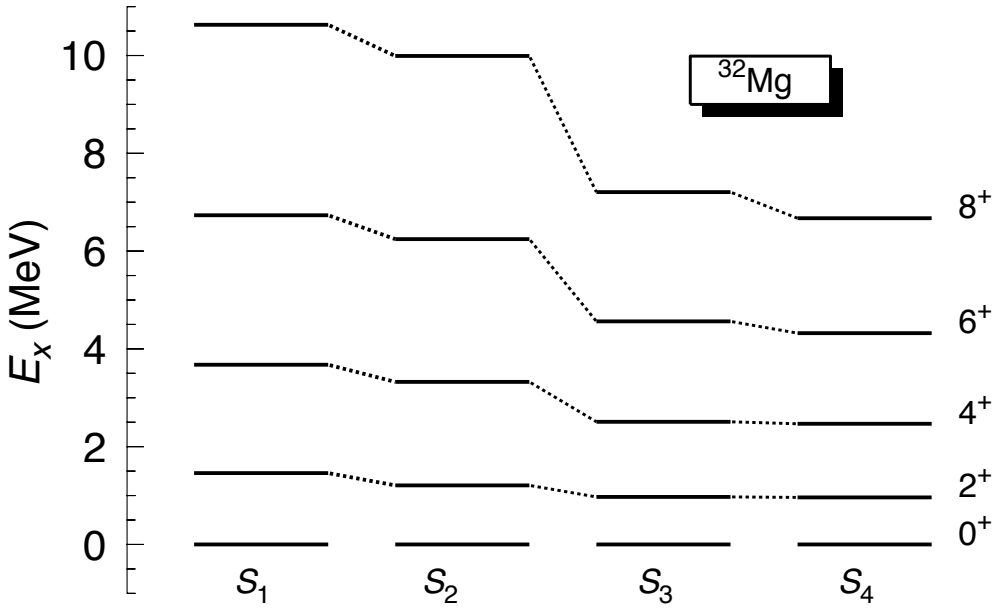

Figure 7.5: Excitation energies of the yrast states calculated for the nucleus ^{32}Mg with the GCM method with 17 axial states and $J_c = 0$ (S_1), 49 axial+triaxial states and $J_c = 0$ (S_2), 81 axial+triaxial states and $J_c = 0, 2$ and 113 axial+triaxial states and $J_c = 0, 2, 4$.

(equation 6.68)

$$\sum_{\{\alpha'\}} \left(\mathcal{H}^{NZ,I}_{\{\alpha\};\{\alpha'\}} - E^{NZ,I}_{\sigma} \mathcal{N}^{NZ,I}_{\{\alpha\};\{\alpha'\}} \right) f^{I}_{\{\alpha'\},\sigma} = 0 \tag{7.9}$$

where $\{\alpha\} \equiv \{\beta, \gamma, K, J_c\}$ now encodes all the constraints in a single index and $\mathcal{H}$ and $\mathcal{N}$ the energy and norm overlaps where defined in 6.69 and 6.70

To shed light on the impact of including time-reversal symmetry breaking states in the spectrum, the nucleus ^{32}Mg has been computed with the GCM method using four sets of intrinsic wave functions. All of them are computed with nine major oscillator shells in the working basis. The simplest one (S_1)

is made of the 17 axial and time-reversal symmetric states. Such states are marked in Fig. 7.1(a) with dots in the ($\gamma = 0°, 180°$) axis. Then, the S_2 set is defined by adding 32 more time-reversal conserving states ($J_c = 0$) in the (β, γ) plane. Finally, two more batches of states, S_3 and S_4, are stablished by adding 32 time-reversal symmetry breaking states with $J_c = 2$, and 32 more with $J_c = 4$ (see the dots in Fig. 7.1). Therefore, $S_1 \subset S_2 \subset S_3 \subset S_4$, being the total number of states in the largest set equal to 113.

The ground state bands obtained with the GCM method implemented with the different choices described above are shown in Fig. 7.5. It is important to point out that the ground state energies obtained for the different calculations, are pretty close except for the pure axial case, where a difference of 0.4 MeV is found. The actual numbers are:

$$E(0_1^+) = -253.056, -253.477, -253.486, -253.498 MeV$$

for S_1, S_2, S_3 and S_4 respectively. That shows that the ground state energy is converged with respect to adding time-reversal symmetry breaking components. However, the excited states are more affected by the inclusion of triaxial and cranking states. Hence, we first observe a moderate compression of the spectrum from the axial ($K = 0$) to triaxial calculations with $J_c = 0$. The decrease in energy is larger with increasing the angular momentum, mainly due to the possibility of having more K-mixing in the GCM states. However, the variational space for the excited states are much better explored if time-reversal symmetry breaking is allowed. Therefore, a significant compression of the spectrum is obtained for the S_3 and S_4 sets and the

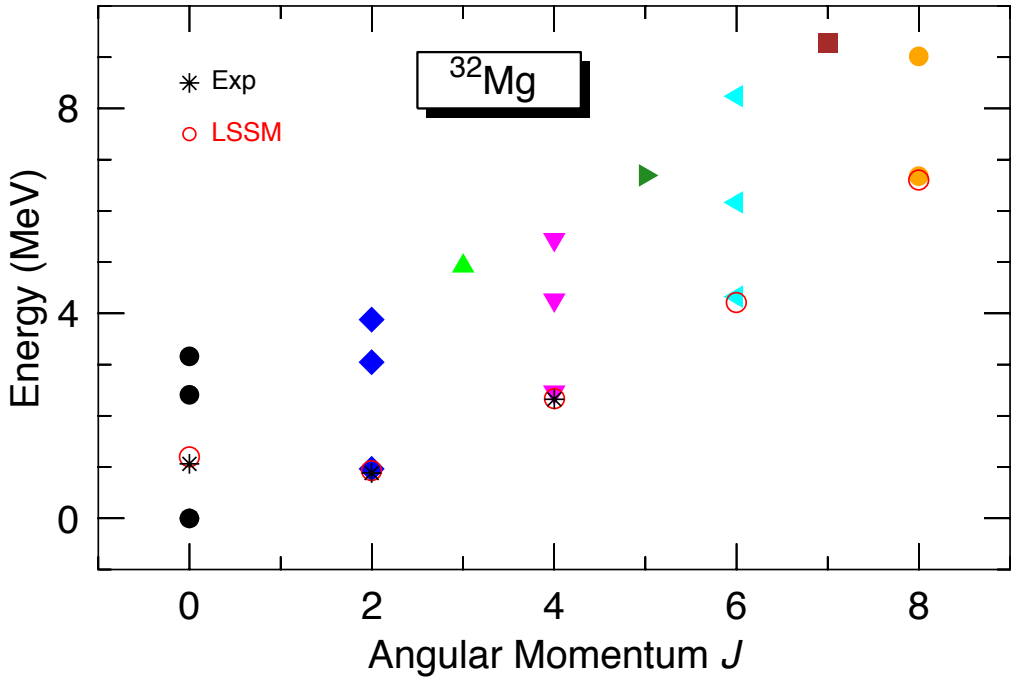

Figure 7.6: Excitation energies for the nucleus ^{32}Mg calculated with the GCM method with 113 axial+triaxial states and $J_c = 0, 2, 4$ (full symbols), large scale shell model calculations (open circles) and experimental data (asterisks).

differences, once again, are bigger for larger angular momentum. In addition, we can infer that the excitation energies for the 2_1^+ and 4_1^+ states are already converged with the S_3 calculation since they do not vary significantly from including $J_c = 4$ states to the $J_c = 0, 2$ ones. This is not the case for larger values of the angular momentum, where probably intrinsic states with $J_c = 6, 8, ...$ should be also included in the GCM.

For the sake of completeness, the full spectrum computed with the S_4 set is represented in Fig. 7.6. Here, the first two bands display a rotational character, with a parabolic trend in the excitation energies, 0^+ band-heads and

$\Delta I = 2$ spacing. A third band starting at 2_3^+ with $\Delta I = 1$ is also obtained, showing a slight odd-even I staggering. In addition, large scale shell model (LSSM) results [10–12] and experimental data [13–17] are also represented in Fig. 7.6. Thanks to the compression of the spectrum produced by the addition of cranking states, a remarkable agreement between the experimental and theoretical values for the 2_1^+ and 4_1^+ energies is obtained. In addition, the present SCCM calculations predict very similar excitation energies to the LSSM values for the g.s. band. However, the low excitation energy of the 0_2^+ state [17] is not reproduced here. LSSM calculations have shown that this state is very sensitive to a subtle mixing of spherical 0p-0h and superdeformed 4p-4h configurations [11]. In the present framework, the inclusion of pairing fluctuations [18,19] and/or explicit quasiparticle excitations could help to solve this puzzle since the excited 0^+ states are mainly affected by such a degree of freedom, lowering the excitation energies of those states.

To explore systematically the effect of the inclusion of time-reversal symmetry breaking states within the GCM framework, we extend the calculations performed in ^{32}Mg to the magnesium isotopic chain $^{24-34}$Mg. The results are obtained with seven major harmonic oscillator shells and the sets of wave functions defined above S_1, S_2, S_3, i.e., axial and triaxial shapes with $J_c = 0$ and 2 are included. In Fig. 7.7 we plot the excitation energies for the 2_1^+ and 4_1^+ calculated with these different approaches compared to the experimental values. We see that the axial calculations describe the trends of the experimental data but the energies are largely overestimated. Including the triaxial degree of freedom without breaking the time-reversal symmetry reduces the

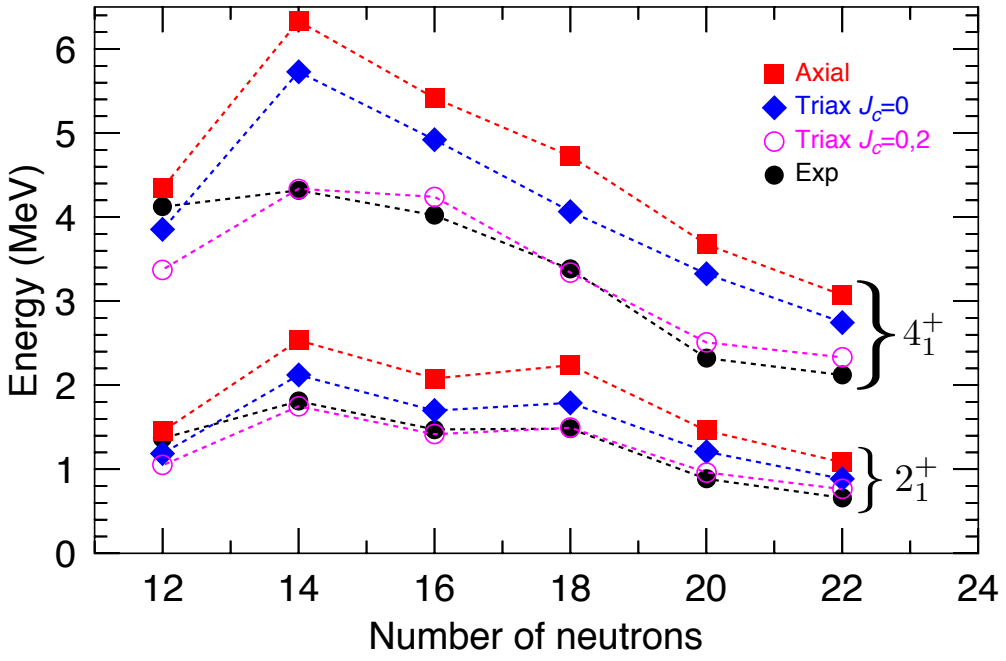

Figure 7.7: 2_1^+ and 4_1^+ excitation energies for the Mg isotopic chain calculated with the GCM method including axial states (red squares), axial+triaxial with $J_c = 0$ states (blue diamonds) and axial+triaxial with $J_c = 0, 2$ states (magenta open dots). Experimental values (black dots) are taken from Ref. [20] and references therein.

excitation energies but the predicted values are still too high with respect to the experiments. Finally, adding $J_c = 2$ states to the GCM set of wave functions compresses further the spectrum and an outstanding agreement with the experimental values is found. The only nucleus where the theoretical values tend to be lower than the experimental ones is the nucleus ^{24}Mg. Two possible explanations for such a disagreement can be addressed. On the one hand, Gogny D1S interaction could slightly overestimate the experimental deformation of this nucleus, producing smaller excitation energies. On the other hand, this is a $N = Z$ nucleus and some alpha clustering and/or proton-

neutron pairing correlations could be missing within the present framework, because the intrinsic states are assumed to be a direct product of protons and neutrons wave functions. The same effect has been also noticed in other proton-rich $N = Z$ nuclei such as ^{72}Kr [21] and ^{80}Zr [22]. However, mixing protons and neutrons to take into account such proton-neutron pairing correlations is beyond the scope of the present study.

In any case, we have to underline that these results constitute the first explicit evidence of the compression of the spectrum when time-reversal symmetry breaking is taken into account in GCM calculations with particle number and angular momentum projection. Global calculations performed with these methods assuming axial symmetry have displayed a systematic overestimation of the 2_1^+ excitation energies around a factor $\sim 1.2 - 1.4$ with respect to the experimental values, both for Skyrme [23] and Gogny [24] functionals. The present results show that such a disagreement can be corrected by including triaxial and $J_c \neq 0$ states in the GCM framework.

7.4 Summary

In summary, we carried out GCM calculations with particle number and angular momentum projection of HFB-like states that have different quadrupole deformations (axial and triaxial) and intrinsic cranking angular momentum. The performance of the method has been checked by taking advantage of the self-consistent symmetries imposed to the intrinsic many-body states. Since such wave functions were chosen to be eigenstates of a D_{2h}^T sub-group

generated by the parity, simplex-x and T-simplex-y symmetry operators ($\{\hat{P}, \hat{\Pi}_1, \hat{\Pi}_2\hat{\mathcal{T}}\}$), the potential energy surfaces (particle number and particle number plus angular momentum projected) must be symmetric in the (β, γ) plane with respect to the $(\gamma = 120°, 300°)$ axis. We have checked such a non-trivial property both in individual states and in the whole (β, γ) plane, taking the nucleus ^{32}Mg as an example. The effect of including incrementally intrinsic states with more symmetries broken in the GCM framework has been also analyzed in ^{32}Mg and in the magnesium isotopic chain $^{24-34}$Mg. The results have shown that adding time-reversal symmetry breaking states ($J_c \neq 0$) squeezes notably the spectra due to a better description of the excited states from a variational point of view. Such a compression puts the theoretical values on top of the experimental ones for the lowest 2^+ and 4^+ states in the chain.

Bibliography

[1] Marta Borrajo, Tomás R. Rodríguez, and J. Luis Egido. Symmetry conserving configuration mixing method with cranked states. *Physics Letters B*, 746:341 – 346, 2015.

[2] K. Hara, A. Hayashi, and P. Ring. *Nucl.Phys. A*, 385:14, 1982.

[3] E. Wüst, A. Ansari, and U. Mosel. *Nucl.Phys. A*, 435:477, 1985.

[4] K. Enami, K. Tanabe, and N. Yoshinaga. *Phys.Rev. C*, 59:135, 1999.

[5] D. Baye and P. h. Heenen. *Phys.Rev. C*, 29:1056, 1984.

[6] J. Dobaczewski H. Zduńczuk, W. Satuł a and M. Kosmulski. *Phys.Rev. C*, 76:044304, 2007.

[7] P. Ring and P. Schuck. *The nuclear many body problem*. Springer-Verlag, Berlin, 1980.

[8] T. R. Rodríguez and J. L. Egido. *Phys.Rev. C*, 81:064323, 2010.

[9] R. Rodríguez-Guzmán, J. L. Egido, and L. M. Robledo. *Nucl.Phys. A*, 709:201, 2002.

[10] E. Caurier, F. Nowacki, and A. Poves. *Nucl.Phys. A*, 693:374, 2001.

[11] E. Caurier, F. Nowacki, and A. Poves. *Phys.Rev. C*, 90:014302, 2014.

[12] A. Poves and F. Nowacki. private communication.

[13] D. Guillemaud et al. *Nucl.Phys. A*, 246:37, 1984.

[14] T. Motobayashi et al. *Phys.Lett. B*, 346:9, 1995.

[15] F. Azaiez et al. and Aip Conf. *Proc.*, 495:171, 1999.

[16] S. Takeuchi et al. *Phys.Rev. C*, 79:054319, 2009.

[17] K. Wimmer et al. *Phys.Rev. Lett.*, 105(25250):1, 2010.

[18] N. L. Vaquero, T. R. Rodríguez, and J. L. Egido. *Phys.Lett. B*, 704:520, 2011.

[19] N. L. Vaquero, J. L. Egido, and T. R. Rodríguez. *Phys.Rev. C*, 88:064311, 2013.

[20] http://www.nndc.bnl.gov.

[21] T. R. Rodríguez. *Phys.Rev. C*, 90:034306, 2014.

[22] T. R. Rodríguez and J. L. Egido. *Phys.Lett. B*, 705:255, 2011.

[23] B. Sabbey, M. Bender, G. F. Bertsch, and P. h. Heenen. *Phys.Rev. C*, 75:044305, 2007.

[24] T. R. Rodríguez, A. Arzhanov, and G. Martínez-Pinedo. *Phys.Rev. C*, 91:044315, 2015.

Chapter 8

Collective and Single-particle Motion in ^{44}S

The SCCM using time-reversal symmetry breaking states is now used to calculate the fascinating structure of the semi-magic ^{44}S nucleus, obtaining an excellent quantitative agreement both with the available experimental data and with state-of-the-art shell model calculations. Moreover, recent experimental results also confirm our predictions [1]. Like before, intrinsic nuclear quadrupole deformations and rotational frequencies are considered simultaneously as the degrees of freedom within the symmetry conserving configuration mixing framework. The results have been published in [2].

We incorporate now two main differences;

1. The angular momentum content is included in the intrinsic wave function by fixing the cranking frequency $\hbar\omega$.

2. We extend the range of triaxial quadrupole deformations to $-60° \leq \gamma \leq 120°$ to the triaxial GCM -see Fig. 8.1(c).

The second point will allow to include single-particle effects through the pair alignment by the cranking procedure. Therefore we study the nuclear states with collective and single-particle character. The success of the present approach can be understood from the shell model point of view if one considers that the wave function of a deformed shape can be expanded as a linear combination of n-particle n-hole (np-nh) excitations of the spherical mean field state [3], see also [4] for odd-nuclei. Previous SCCM calculations were limited by construction to np-nh excitations coupled to AM zero. The consideration of the cranking frequency as coordinate opens the possibility of including np-nh excitations coupled to AM different from zero making the variational space much richer. We now choose the exotic $N = 28$ isotone ^{44}S in which several unconventional properties have been observed. The significant 2_1^+ to 0_1^+ transition probability [5] suggests the erosion of the $N = 28$ shell closure, the presence of a low-lying 0_2^+ state [6, 7] indicates shape coexistence and the very low 4_1^+ to 2_1^+ transition probability suggests a $K = 4$ isomeric state [8]. Recent experimental results also confirm the isomeric character of this state [1]. All these findings have motivated an unusual theoretical activity on this nucleus. There are mean-field calculations with Skyrme and relativistic interactions [9, 10] and BMF studies with density functionals [11–14] supporting the erosion of the $N = 28$ shell closure and the manifestation of possible shape mixing and/or coexistence. Furthermore, large scale SM calculations have been performed [6, 15–18] providing a good

description of the data. In 2015, the Tokyo group [18] proposed a new type of high-K isomerism to explain the long lifetime (of the order of 50 ps [8]) of the 4_1^+ state. This state and its associated band was not found in our earlier calculations [13]. Thus, the calculations we present here are a good benchmark for our new theory.

With the new constraints the general wave function 6.67 is given by;

$$|\Psi_{\sigma}^{NZ;I,M;}\rangle = \sum_{\beta,\gamma,\omega,K} f_{K\sigma}^{I}(\beta,\gamma,\omega)|\Phi^{NZ;IMK}(\beta,\gamma,\omega)\rangle \tag{8.1}$$

In 6.78 we defined the probability density of finding a given I, K and constraints $\vec{q}$;

$$F_{\sigma}^{I}(\beta,\gamma,\omega) = \sum_{\mu K} g_{\mu\sigma}^{I} u_{\mu}^{NZ,I}(\beta,\gamma,\omega,K) \tag{8.2}$$

In the (β,γ) plane the probability amplitude is obtained summing in all possible ω;

$$P_{\sigma}^{I}(\beta,\gamma) = \sum_{\omega} |F_{\sigma}^{I}(\beta,\gamma)|^2 \tag{8.3}$$

As before the HFB w.f.s are determined in the PN variation after projection (VAP) approach. As we have already said the incorporation of ω in the GCM Ansatz of Eq. 8.1 is a generalization of the double projection method of Peierls and Thouless [19, 20] for the case of rotations. This method is known to provide the exact translational mass in the case of translations. We therefore expect that the moments of inertia of our bands will be close to the ones of the AM-VAP providing the sought after spectrum compression. In the numerical applications we use a configuration space of eight harmonic

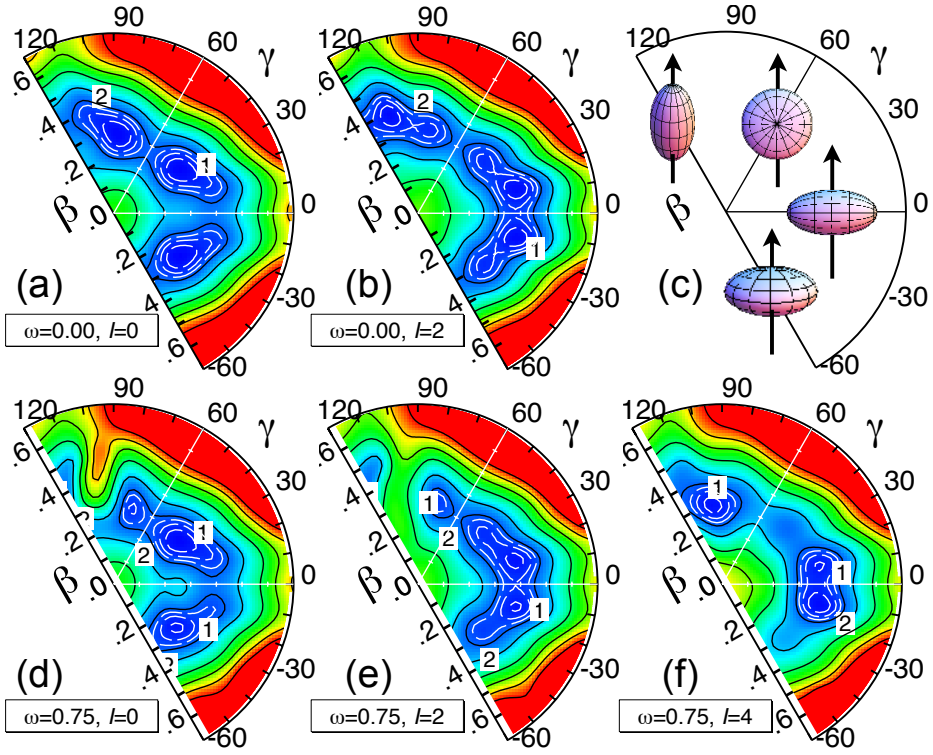

Figure 8.1: Potential energy surfaces in the (β, γ) plane for two angular frequencies and three angular momenta for the nucleus ^{44}S. The energy origin has been set at the energy minimum. The white dashed contours correspond to $0.25, 0.50$ and 0.75 MeV, the unlabeled black contours start at 4 in steps of 2 MeV until 10 MeV. The units are: $\hbar\omega$ in MeV, I in $\hbar$ and γ in degrees.

oscillator shells, large enough for realistic predictions for ^{44}S. Concerning the generator coordinates we take three values of the angular frequency, namely, $\hbar\omega = 0.0, 0.75$ and 1.25 MeV. For each $\hbar\omega$ value we take 70 points in the (β, γ) plane, defined by $0 \leq \beta \leq 0.7$ and $-60° \leq \gamma \leq 120°$ -see Fig. 8.1(c). As we mentioned we consider now this larger γ interval instead of the usual $0° \leq \gamma \leq 60°$ which increase drastically the computational burden, typically at least by two orders of magnitude. We notice that rotations close to $\gamma = -60°$ and $\gamma = 120°$ are non-collective and can excite single particle degrees

of freedom.

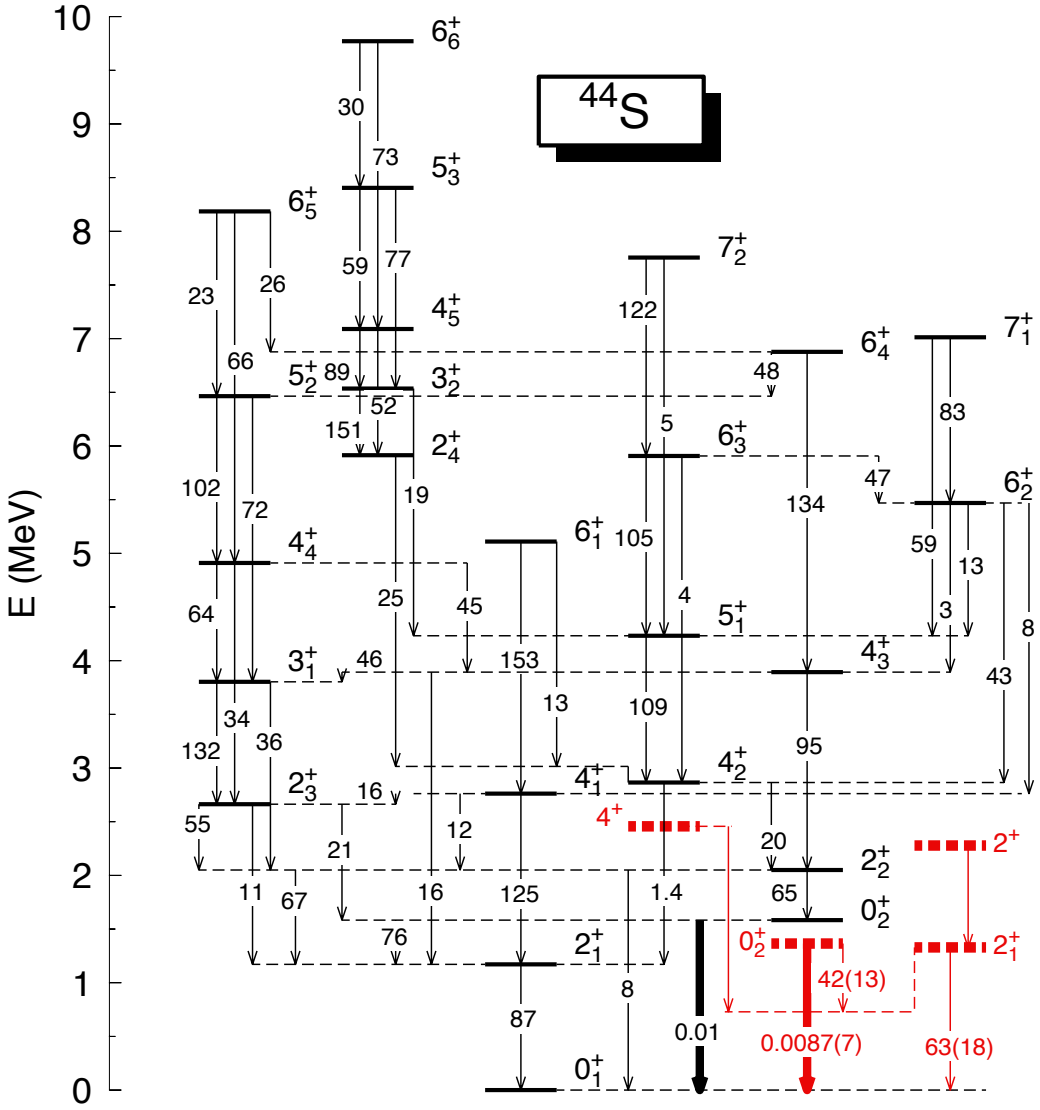

Figure 8.2: Spectrum of ^{44}S, showing the $B(E2)$ transition probabilities in e^2fm^4. The thick arrows represent the E0 transition with its corresponding value for ρ^2. The experimental data [7, 8] are shown as thick dashed lines. Only experimental states with safe spin assignment are included.

8.1 Angular Momentum PES

The GCM states -Eq. 8.1- recover the broken symmetries in the HFB approach and mixes different configurations (β, γ, ω). We can stop in the "step two" studied in chapter 6, which means making a simplified Ansatz just fixing a given (β, γ, ω) value and mixing only in K as to recover the symmetries to calculate the PN-AM projected energy in each point of the (β, γ) plane and plot potential energy surfaces (PESs) for different $\hbar\omega$ values. In Fig. 8.1 we have represented these energies for $\hbar\omega = 0.0$ and 0.75 MeV and for $I = 0, 2$ and 4 $\hbar$. For $\hbar\omega = 0.0$ MeV (Fig. 8.1(a)-(b)) we observe the mentioned symmetry, i.e., the three sextants are equivalent and can be obtained by reflexions around the axis $\gamma = 0°$ and $\gamma = 60°$. For $I = 0$ $\hbar$ we find a nucleus with $\beta \approx 0.30$ and very soft in γ, with a slight minimum at $\gamma \approx 30°$. For $I = 2$ $\hbar$ the lowest contours shifted towards the prolate and oblate shapes and somewhat larger β values, and for $I = 4$ $\hbar$, not shown here, the energy minimum close to the oblate shapes weakens about 1 MeV as compared with the prolate one. The effect of the angular frequency on the PESs can be seen in Fig. 8.1(d)-(f). We first observe that now the three sextants are not equivalent anymore. For $I = 0$ $\hbar$ the PES looks similar to the case $\hbar\omega = 0$ MeV with the exception of the wedge around $\gamma = 90°$. For $I = 2$ $\hbar$ there are two minima at $\gamma \approx \pm 10°$ and at $\gamma \approx \pm 45°$ and the wedge is still present. For $I = 4\hbar$ and larger I-values the wedge disappears. The reason for this behavior is simple: For the (β, γ) values inside the wedge, the HFB w.f. presents a neutron two-quasiparticle state with aligned AM, $\langle\phi|\hat{J}_x|\phi\rangle \approx 4\hbar$, making it costly to project to AM values smaller than $4\hbar$.

However, this is not the case for $I = 4\hbar$, Fig. 8.1(f), and we find three almost degenerated minima, two around $\gamma \approx \pm 10°$ and $\beta = 0.35$ and a third one around $\gamma = 90°$ and $\beta = 0.26$. The minima at $\gamma \approx 90°$ and $\gamma \approx -45°$ will play an important role in the interpretation of the collective w.f.s.

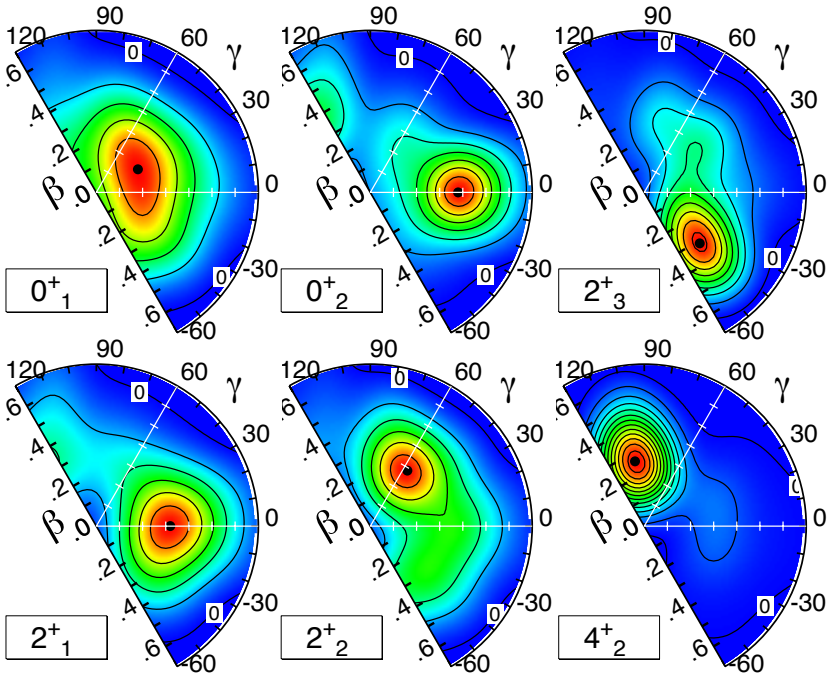

Figure 8.3: Collective w.f.s in the (β, γ) plane for the indicated states. The contour levels are separated by 0.01. The contour labelled 0 sets the scale origin, the maximum is indicated by a black dot.

8.2 SCCM approach

The solution of Eq. 6.68 provides the energy levels and the w.f.s. The transition probabilities [21,22] and the shapes of the w.f.s allow to order the energy levels into bands as shown in Fig. 8.2. The lowest levels provide the ground

band, a band based on the 0_2^+ level, two pseudo-γ-bands based on the 2_3^+ and 2_4^+ states, a band based on the 4_2^+ level and a last one based on the 6_2^+ state. For the physical interpretation of these bands we show in Fig. 8.3 the collective w.f.s, see Eq. 8.3, of representative states. The minima of Fig. 8.1 represent the relevant configurations and play a relevant role in the shape of the collective w.f.s. The high-I members of a band with a w.f. looking similar to the band head are not plotted. The 0_1^+ state presents a very extended w.f. with contributions from many configurations and a maximum in the area $0° \leq \gamma \leq 60°$ and $0.15 \leq \beta \leq 0.3$. It resembles the PES of Fig. 8.1(a)-(b). The higher AM members of the band become prolate as can be seen in the w.f. of the 2_1^+ state. The 0_2^+ state, band head of the first excited band, is soft in the γ direction and peaks at a prolate shape. The higher AM members of the band, however, are oblate, see for example the 2_2^+ state in Fig. 8.3. The second excited band, based on the 2_3^+ state presents a triaxial-oblate shape with the maximum at $\beta = 0.32$ and $\gamma = -45°$. The third, fourth and fifth excited bands, with the 4_2^+, 2_4^+ and 6_2^+ states as band heads, have maxima at $\beta \approx 0.28 - 0.36$ and $\gamma \approx 90° - 100°$, cf. the minimum at this point of Fig. 8.1(f). Since the w.f.s of these three states look rather similar we only display the one of the 4_2^+ state. The w.f. of the 4_2^+ state strongly peaks at the maximum indicating a less collective character. If we analyze the composition of the HFB w.f. at the maximum we find that it corresponds to an aligned state with contributions from the $\nu f_{7/2}$ and $\nu p_{3/2}$ orbitals. The band starting at this level has been assigned in Ref. [18] as a $K = 4$ band. In the present calculations, with explicit breaking of the time reversal symmetry, the K quantum number looses relevance. However, in

some cases, through the cranking mechanism, one has alignment along the $x-$axis which can be used instead to characterize bands. If we express the w.f. in the basis $|IK_X\rangle$, with K_X the projection of the angular momentum along the intrinsic x-axis, we obtain that the w.f. of this state is predominantly $K_X = 4$, in agreement with the interpretation of Ref. [18]. The band based on the 6_2^+ level, is very similar to the one of the 4_2^+ state. In the basis $|IK_X\rangle$ the component with $K_X = 6$ amounts to 76%. We would like to stress the special role played by the sextants $(0°, 60°)$ and $(60°, 120°)$ of the (β, γ) plane. They provide new states, like the 4_2^+, and contribute actively to the configuration mixing of other states. The spherical configurations, not shown here, appear at several MeV of excitation energy, the lowest ones corresponding to the $0_3^+, 2_6^+, 4_8^+$, and 6_8^+ states, a clear indication of the erosion of the $N = 28$ shell closure. The spectroscopic quadrupole moments of the band heads are : $Q_{spec}(2_1^+) = -14.4$ efm^2, $Q_{spec}(2_2^+) = 6.5$ efm^2, $Q_{spec}(4_2^+) = 26.9$ efm^2, $Q_{spec}(2_3^+) = -13.8$ efm^2. For comparison the experimental data have also been plotted in Fig. 8.2 as thick lines. With respect to the energy values we obtain a good agreement.

8.3 Transition probabilities

Concerning the transition probabilities very good agreement is found for the E0 from the 0_2^+ to the 0_1^+ state and the E2 from the 2_1^+ to the 0_1^+ while the $B(E2; 0_2^+ \rightarrow 2_1^+)$ is slightly overestimated. In our calculations the 4_2^+ state decays both to the 2_1^+ (with a $B(E2) = 1.4$ e^{2}fm^4) and 2_2^+ states

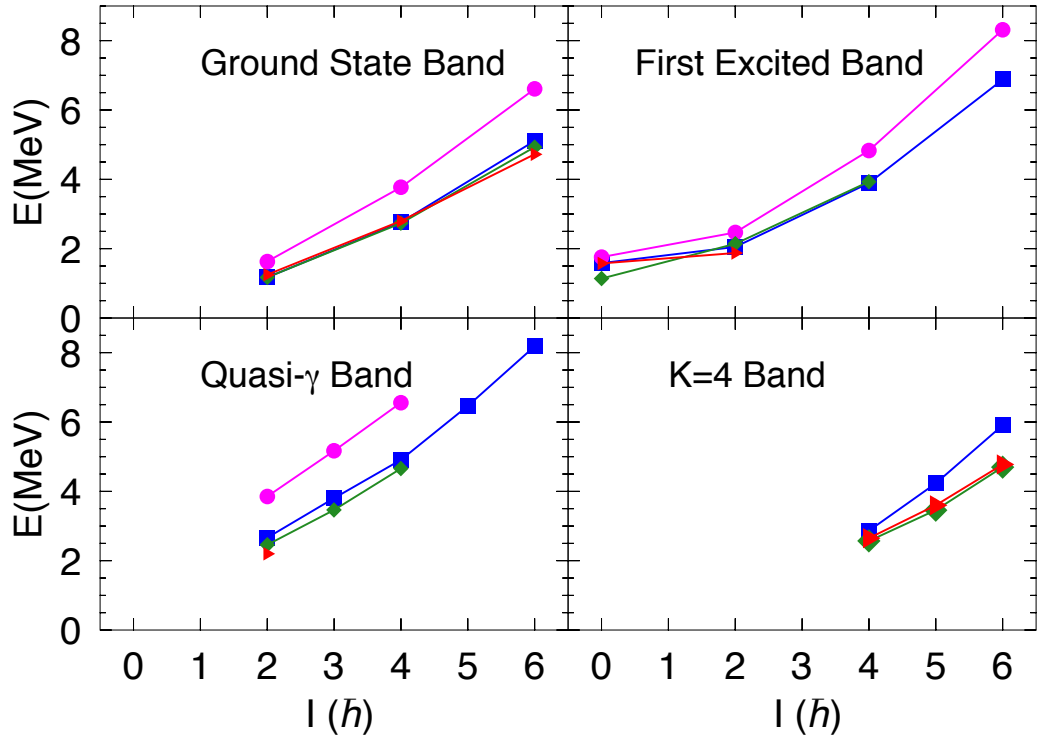

Figure 8.4: Comparison of several theories: Triangles, red lines, Tokyo group [18]; diamonds, green lines, Madrid-Strasbourg collaboration [23]; boxes, blue lines, this work; circles, magenta lines, our former work without angular frequency dependence [13].

(with a $B(E2) = 20$ e^{2}fm^4). The latter decay branch has not been observed experimentally. Considering the theoretical values, we estimate a branching ratio of 74% for the decay branch to the 2_1^+ state and a lifetime of 84 ps to be compared with the experimental value of about 50 ps [8]. Another interesting finding is that the 6_2^+ level, which is similar in structure to the 4_2^+ state, has a much shorter lifetime since it has several decay branches. Furthermore its small excitation energy above Yrast makes it experimentally accessible.

In Fig. 8.4 we now compare the performance of the present method with state-of-the-art SM calculations of the Madrid-Strasbourg collaboration [8] in the

full sd(fp) valence space for protons (neutrons) with the SDPF-U interaction [15, 23] and with those of the Tokyo group [18] in the $\pi(\mathrm{sd})^{(Z-8)}\nu(\mathrm{pf})^{(N-20)}$ and the SDPF-MU. The agreement between the two SM calculations and our present approach for the ground state and first excited bands is extraordinary. Also for the quasi-γ-band we find good agreement between our approach and the one of the Madrid-Strasbourg collaboration. Small deviations are observed for the $I = 5\hbar$ and $6\hbar$ states of the "$K = 4$" band. The transition probabilities are also similar. For example with the SDPF-U interaction one obtains [16] $B(E2; 6_1^+ \rightarrow 4_1^+) = 118$ e^{2}fm^4, $B(E2; 4_1^+ \rightarrow 2_1^+) = 111$ e^{2}fm^4, $B(E2; 2_1^+ \rightarrow 0_1^+) = 75$ e^{2}fm^4, to compare with our values of 153, 125 and 87 e^{2}fm^4, respectively. We note that in our calculations no effective charges are used and that the D1S parametrization was fitted long ago to provide reliable global properties along the nuclide chart, reinforcing the predictive power of our approach. In Fig. 8.4 we can also observe the improvement provided by the present approach as compared to our former results [13] obtained without considering the ω degree of freedom. These calculations gave the right tendency but an stretched spectrum which is corrected in the present framework (see also [24]). Furthermore, we also observe that the aligned structures observed in the present calculations cause a decrease in the collectivity of the w.f.s and consequently a decrease of the transition probabilities which often were found too large in the past. All these facts improve considerably the agreement of the present approach with the experiment.

8.4 Summary

In conclusion, we considered cranked w.f.s together with triaxial deformations (β, γ) in the Symmetry Conserving Configuration Mixing approach. As in the Mg isotopic chain, the cranking procedure introduces an angular momentum dependence in the calculations providing a compression of the otherwise stretched spectrum. Furthermore, through the alignment mechanism, single particle degrees of freedom are introduced, opening a door to a physics unaccessible before in these approaches. The aligned configurations provide a decrease of the collectivity of the w.f.s leading to smaller transition probabilities in agreement with the experiment. These three facts cure the deficiencies of former SCCM approaches providing a very powerful tool in nuclear structure calculations. The exotic nucleus ^{44}S, with a very rich nuclear structure, we have shown that this approach provides high quality nuclear spectroscopy comparable with the state-of-the-art of SM calculations with tailored interactions and experimental data. The advantages of our approach are the added value of the intrinsic system interpretation and that our interaction, the Gogny force, is well known for its predictive power and good performance for bulk properties all over the chart of nuclides. These calculations set a new standard in the state-of-the-art of BMF methods with density dependent interactions. A drawback of our approach in its present form is that the increase from one to tree sextants as well as the consideration of one more coordinate enlarge considerably the CPU time of the calculation. Systematic studies or calculations with a very large number of major shells are not feasible in a small local cluster. In the next chapter we

study a possible approximation to reduce the computational cost.

Bibliography

[1] J. J. et all Parker. *Phys. Rev. Lett.*, 118:052501, Jan 2017.

[2] J. Luis Egido, Marta Borrajo, and Tomás R. Rodríguez. *Phys. Rev. Lett.*, 116:052502, Feb 2016.

[3] J. L. Egido et al. *Phys.Rev. Lett.*, 93:082502, 2004.

[4] B. Bally et al. *Phys.Rev. Lett.*, 113(16250):1, 2014.

[5] T. Glasmacher et al. *Phys.Lett. B*, 395:163, 1997.

[6] S. Grévy et al. *Eur.Phys. J*, 25:111, 2005.

[7] C. Force et al. *Phys.Rev. Lett.*, 105(10250):1, 2010.

[8] D. Santiago-González et al. *Phys.Rev. C*, 83:061305, 2011.

[9] T. R. Werner et al. *Phys.Lett. B*, 333:303, 1994.

[10] G. A. Lalazissis et al. *Phys.Rev. C*, 60:014310, 1999.

[11] S. Peru et al. *Eur.Phys. J*, 9:35, 2000.

[12] J. L. Egido R. Rodríguez-Guzman. *Phys.Rev. C*, 65:024304, 2002.

[13] T. R. Rodríguez and J. L. Egido. *Phys.Rev. C*, 84, 2011.

[14] Z. P. Li et al. *Phys.Rev. C*, 84:054304, 2011.

[15] F. Nowacki and A. Poves. *Phys.Rev. C*, 79:014310, 2009.

[16] R. Chevrier and L. Gaudefroy. *Phys.Rev. C*, 89:05130, 2014.

[17] M. Kimura et al. *Phys.Rev. C*, 87:011301(R), 2013.

[18] Y. Utsuno et al. *Phys.Rev. Lett.*, 114:032501, 2015.

[19] R. E. Peierls and D. T. Thouless. *Nucl.Phys.*, 38:154, 1962.

[20] J. L. Egido. *Phys.Rev. C*, 27:453(R), 1983.

[21] T. R. Rodríguez and J. L. Egido. *Phys.Rev. C*, 81:064323, 2010.

[22] Marta Borrajo, Tomás R. Rodríguez, and J. Luis Egido. *Physics Letters B*, 746:341 – 346, 2015.

[23] L. Cáceres et al. *Phys.Rev. C*, 85:024311, 2012.

[24] M. Borrajo et al. *Phys.Lett. B*, 746:341–346, 2015.

Chapter 9

An approximation in SCCM calculations.

The complexity of the triaxial angular momentum projection and the necessity of considering several generator coordinates has increased the CPU time necessary for these calculations so much that some approximations are needed to study heavy nuclei. In this work we propose an approach that reduces the CPU time considerably and at the same time provides good results. The results have been published in [1]

In the symmetry conserving mean field approximation (SCMFA) the wave function is (see eq 6.67) ;

$$\begin{aligned} |\Psi_{\sigma}^{NZ;IM;}\rangle &= \sum_{\vec{q},K} f_{K\sigma}^{I}(\vec{q}) P_{MK}^{I} P^{N} P^{Z} |\Phi(\vec{q})\rangle \\ &= \sum_{\vec{q},K} f_{K\sigma}^{I}(\vec{q}) |\Phi^{NZ;IMK}(\vec{q})\rangle \end{aligned} \tag{9.1}$$

The present approximation consists on the reduction of this grid by one order of magnitude.

The choice of the coordinates $\vec{q}$ is a very crucial issue. The simplest approach is to consider axially symmetric calculations. In this case there is only one coordinate, namely the β deformation and $K = 0$. There have been calculations of this type with the Skyrme [2], Gogny [3, 4] and relativistic [5] interactions. This approach provides a good qualitative description of nuclei close to axial symmetry. The main drawbacks are obviously the absence of triaxial effects and the prediction of very stretched spectra. A considerably more realistic case is to consider the triaxial deformation. In this case $\vec{q} = (\beta, \gamma, K)$ and again there have been calculations with the three effective interactions mentioned above [6–8]. In these calculations the γ bands are properly described and the spectra are less stretched than in the axial case but still stretched as compared with the experiment. This can be seen in Fig 7.5 of Chapter 7. Also we display in Fig. 9.1 (taken from Ref. [7]) the whole spectrum of ^{24}Mg compared with the experiment In the axial case (left), the experimental ground state band is well reproduced, a well developed β-band is found though at too high excitation energy, but the γ-band is not found. If we now include triaxial effects, i.e., the γ degree of freedom, we obtain the triaxial spectrum shown in the middle panel of Fig. 9.1. Now a well developed γ-band is found and a considerable lowering of the β-band is obtained. To remedy this situation proposed in this work to incorporate the cranking frequency as a generator coordinate. Therefore the use of deformation and cranking frequencies as degrees of freedom can be considered a good ansatz;

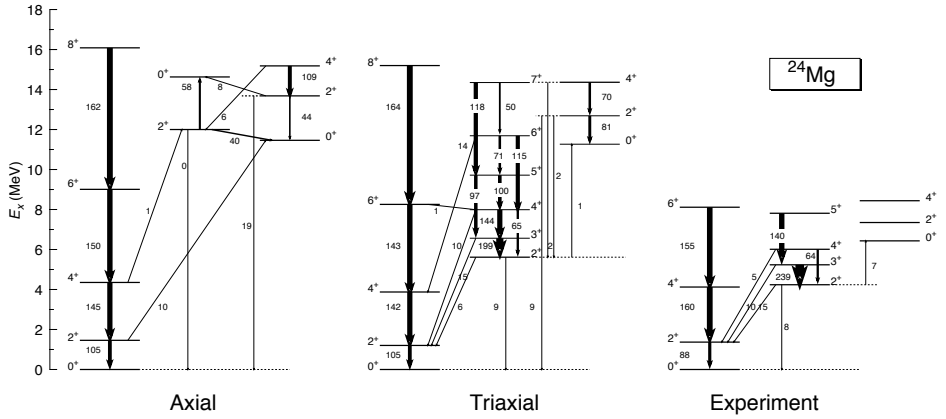

Figure 9.1: Calculated excitation energies and reduced transition probabilities B(E2) (in e^2fm^4) in ^{24}Mg obtained using axially symmetric (left) and triaxial (middle) GCM-PNAMP approaches compared to the experimental values (right). The experimental values are taken from [9].

and Eq. 9.1 looks like

$$|\Psi_\sigma^{NZ,I}\rangle = \sum_{\beta,\gamma,\omega,K} f_\sigma^I(\beta,\gamma,\omega,K)\ P^N P^I_{MK}|\phi(\beta,\gamma,\omega)\rangle. \tag{9.2}$$

As mentioned, the HFB w.f. $|\phi(\beta,\gamma,\omega)\rangle$ are determined by minimizing [10] the energy functional

$$E[\phi] = \frac{\langle\phi|HP^ZP^N|\phi\rangle}{\langle\phi|P^ZP^N|\phi\rangle} - \langle\phi|\omega\hat{J}_x + \lambda_{q_0}\hat{Q}_{20} + \lambda_{q_2}\hat{Q}_{22}|\phi\rangle, \tag{9.3}$$

where $\hat{Q}_{2\mu}$ and $\hat{J}_x$ are quadrupole moment and the x-component of the angular momentum operators respectively, and ω, the cranking frequency, is kept constant in the minimization procedure. (see Ch. 8 for details). With te addition of angular content in the intrinsic wave functions we expect that the moments of inertia of our bands are to the ones of the AM-VAP providing the sought-after spectrum compression, as seen in the Mg isotopic chain and

^{44}S

The consideration of the angular frequency as a generator coordinate has a big impact on the CPU time of the calculations because the cranking term $-\omega\hat{J}_x$ added in Eq. 9.3 causes a time reversal symmetry breaking (TRSB). Besides the obvious fact of adding one more coordinate to the calculations the symmetry breaking has two important consequences: First, one cannot perform axially symmetric calculations even in nuclei where no triaxial effects are expected and second, the usual $0° \leq \gamma \leq 60°$ sextant is not equivalent anymore to all sextants in the $\{\beta, \gamma\}$ plane and the half plane $-60° \leq \gamma \leq 120°$ must be used. In general, the consideration of $\hbar\omega$ as a generator coordinate amounts to an increase of two orders of magnitude in the CPU time.

uncomment the following lines to place a figure

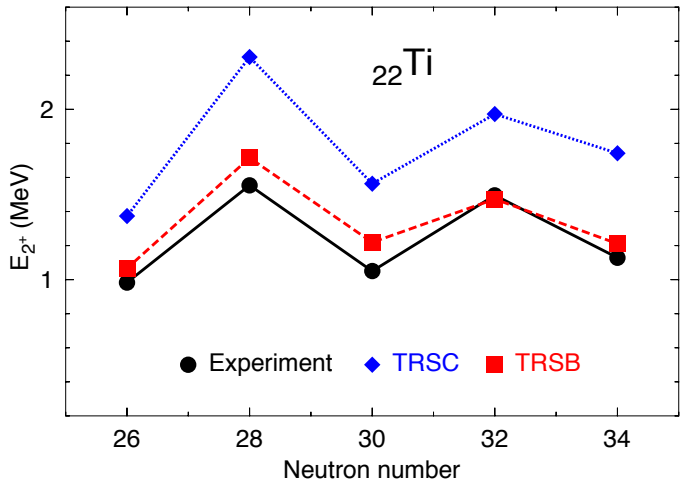

Figure 9.2: Excitation energies of the 2_1^+ states in the Titanium isotopes in two approaches: Time reversal symmetry conserving (filled diamonds, blue color) and time reversal symmetry breaking (filled squares, red color). The experimental values [11–14] (bullets, black color) are also shown.

In the calculations shown in chapters 7 and 8 only light nuclei were studied and a small number of oscillator shells were considered as configuration space. In order to study heavier nuclei some approximations are needed. In the SCCM Ansatz, Eq. 9.1, and for not too large angular momenta, it is sufficient to consider two or three ω values. For β in general about 12 mesh-points are needed and for γ on the average about 18 points. The largest energy dependence is with the β degree of freedom but the coordinate that most increases the CPU time is the γ. The approximation that we investigate is to perform triaxial calculations but without constraining on γ. That means, for fixed ω and β values Eq. 9.3 is solved (obviously without the constraint on $\hat{Q}_{22}$) and the corresponding self-consistent γ value is determined by the variational principle. For a given β and different ω, in general, we obtain different γ values increasing thereby the diversity in the mixing. To test the approach, we have performed calculations for the nucleus $_{22}$Ti, which we already studied in Ref. [4] in an axially symmetric approach. The configuration space has eight oscillator shells. Since we are only interested in the low spin region we consider only two $\hbar\omega$ values, namely $\hbar\omega = 0.0$ MeV and $\hbar\omega = 0.5$ MeV. We use the interval $0 \leq \beta \leq 0.6$ with a step size of 0.05, i.e., 13 points for $\hbar\omega = 0.0$ MeV and 12 points for $\hbar\omega = 0.5$ MeV. That means, we have to solve a Hill-Wheeler Equation with 25 points and triaxial angular projection. In Fig. 9.2 we show the excitation energies of the 2_1^+ states for the Titanium isotopes in two approximations in comparison to the experimental results. The simplest approach is assuming *axial* symmetry, i.e., in the calculations only $\hbar\omega = 0.0$ and 13 β points are considered, these are time reversal symmetry conserving calculations (TRSC). As compared with the

experiment these calculations provide the right behavior of the energy for the different isotopes but with too large values. In the second calculation we add the 12 points corresponding to $\hbar\omega = 0.5$ MeV, these are TRSB calculations and a triaxial angular momentum projection must be performed. As we can observe in Fig. 9.2, the energy lowering is very significant bringing the theoretical results almost in agreement with the experimental ones.

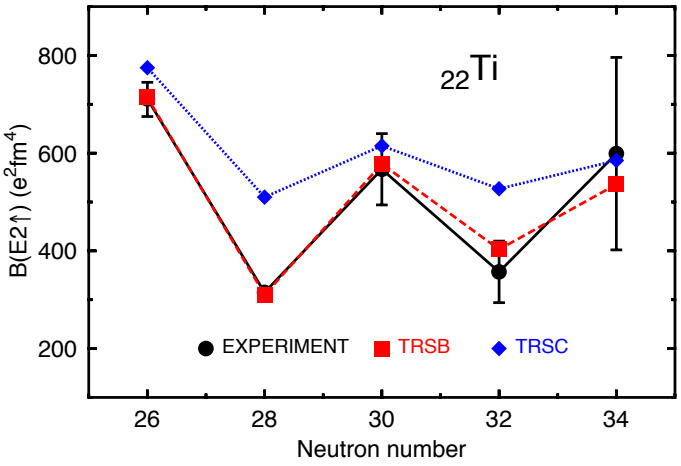

Figure 9.3: $B(E2; 0_1^+ \longrightarrow 2_1^+)$ transition probabilities in the Titanium isotopes in two approaches: Time reversal symmetry conserving (filled diamonds, blue color) and time reversal symmetry breaking (filled squares, red color). The experimental values [15] (bullets, black color) are also shown.

Another aspect of the SCCM calculations, not mentioned yet, which causes some trouble is that it in general they provide larger collectivity than experimentally observed. In Fig. 9.3 we show the $B(E2; 0_1^+ \longrightarrow 2_1^+)$ values for the Titanium isotopes in the same two approximations as before. The TRSC calculations provide $B(E2)$ values that are too high as compared with the experiment. The TRSB, however, decreases these values considerably so a very good agreement in obtained.

In conclusion, we have presented an approach to time reversal symmetry breaking calculations that reduce considerably the computational burden. This approximation will allow to extend the TRSB calculations to medium and heavy nuclei allowing an accurate description of nuclear properties.

Bibliography

[1] M. Borrajo and J. L. Egido. An Approximation in Symmetry Conserving Configuration Mixing Calculations. *Acta Phys. Polon. Supp.*, 8(3):567–574, 2015.

[2] M. Bender, P. h. Heenen, and P. g. Reinhard. *Rev.Mod. Phys*, 75:121, 2003.

[3] R. Rodriguez-Guzmán, J. L. Egido, and L. M. Robledo. *Nucl.Phys. A*, 709:201, 2002.

[4] T. R. Rodríguez and J. L. Egido. *Phys.Rev. Lett.*, 99:062501, 2007.

[5] T. Nikšić, D. Vretenar, and P. Ring. *Phys.Rev. C*, 74:064309, 2006.

[6] M. Bender and P. h. Heenen. *Phys.Rev. C*, 78:024309, 2008.

[7] T. R. Rodríguez and J. L. Egido. *Phys.Rev. C*, 81:064323, 2010.

[8] J. M. Yao et al. *Phys.Rev. C*, 81:044311, 2010.

[9] http://www.nndc.bnl.gov.

[10] J. L. Egido, J. Lessing, V. Martín, and L. M. Robledo. *Nucl.Phys. A*, 594:70, 1995.

[11] S. N. Liddick et al. *Phys.Rev. Lett.*, 92:072502, 2004.

[12] R. V. F. Janssens et al. *Phys.Lett. B*, 546:55, 2002.

[13] S. N. Liddick et al. *Phys.Rev. C*, 70:064303, 2004.

[14] B. Fornal et al. *Phys.Rev. C*, 70:064304, 2004.

[15] D. c. Dinca et al. *Phys.Rev. C*, 71:041302(R, 2005.

RESULTS II

Symmetry conserving configuration methods in odd-A nuclei

Chapter 10

Ground-state properties of even and odd Magnesium isotopes

This is the first systematic description of the odd and even nuclei of an isotopic chain in a symmetry-conserving approach with the Gogny force in a BMFT considering the (β, γ) degrees of freedom explicitly and dealing optimally with the pairing correlations. We consider exact triaxial self-consistent blocking and exact particle number and angular momentum conservation. We apply our theory to the odd an even nuclei of the Magnesium isotopic chain. The results have been published in [1].

In this study we do the first two steps explained of Chapter 6; We solve the PN-VAP equations for a blocked wave function for different triaxial shapes. After, we recover the rotational invariance in each of these points. Basic properties like odd-even mass differences, magnetic and quadrupole moments

as well as mass radii, among others, are investigated. We will see we obtain an outstanding description of the ground-state properties, in particular binding energies, odd-even mass differences, mass radii and electromagnetic moments among others.

10.1 PN-VAP calculation of a blocked wave function

We have already seen this method in even nuclei, so we now concentrate on the solution of the odd ones. We call $|\tilde{\phi}\rangle$ the blocked wave function (see Chapter 5.1). Though the state $|\tilde{\phi}\rangle$ has the right blocking structure, since the Bogoliubov transformation mixes creator and annihilator operators and states with different angular momenta, $|\tilde{\phi}\rangle$ is not an eigenstate of the PN or the AM operators.

The grid of wave functions is obtained as usual, but now for the blocked w.f. $|\tilde{\phi}\rangle$ minimizing;

$$E'[\tilde{\phi}] = \frac{\langle\tilde{\phi}|\hat{H}\hat{P}^N\hat{P}^Z|\tilde{\phi}\rangle}{\langle\tilde{\phi}|\hat{P}^N\hat{P}^Z|\tilde{\phi}\rangle} - \langle\tilde{\phi}|\lambda_{q_0}\hat{Q}_{20} + \lambda_{q_2}\hat{Q}_{22}|\tilde{\phi}\rangle, \tag{10.1}$$

We therefore consider wave functions of the form

$$|\tilde{\phi}^{\tau\pi}\rangle = \beta^{\dagger,\tau\pi}_{\rho_i}|\phi\rangle = \beta^{\dagger,\tau\pi}_{\rho_i}\prod_{\mu=1}^{2M}\beta_\mu|-\rangle. \tag{10.2}$$

According to the isospin and parity we have four blocking channels: protons

(neutrons) of positive or negative parity. Since Magnesium isotopes have $Z = 12$, we restrict ourselves to the neutron channels, so we omit τ index in 10.2 from now on. As we saw in chapter 5.1, equation 5.13 the parity, π, of the state $|\tilde{\phi}^{\pi}\rangle$ is given by the parity of the blocked level $\beta^{\dagger\pi}_{\rho_1}$ (orbitals with the same parity are occupied pairwise). Also, we saw we can block a state with positive or negative simplex, but since we do not break time reversal explicitly both possibilities are degenerated. The minimization of Eq. 10.1 is again performed with the conjugated-gradient method [2]. The blocking structure of the wave function of Eq. (10.2) is a self-consistent symmetry and for a given blocking number we determine the lowest solution in the blocked channel compatible with the imposed constraints. That is, it does not matter which level is initially blocked, at the end of the iteration process the PN-VAP energy and the HFB wave function are independent of this election.

10.2 Rotational invariance restoration

The next step is the simultaneous particle-number and angular-momentum projection (PNAMP) of each state $|\tilde{\phi}^{\pi}(\beta,\gamma)\rangle$ that conforms the (β,γ) grid,

$$\begin{aligned} |\Psi^{NZ;IM,\pi}_{\sigma}(\beta,\gamma)\rangle &= \sum_{K} f^{I,\pi}_{K\sigma} P^{N} P^{Z} P^{I}_{MK} \, |\tilde{\phi}^{\pi}(\beta,\gamma)\rangle \\ &= \sum_{K} f^{I,\pi}_{K\sigma} |\tilde{\phi}^{NZ;IM,\pi}_{\sigma}(\beta,\gamma)\rangle, \end{aligned} \tag{10.3}$$

where the coefficients $f_{K\sigma}^{I,\pi}$ are determined as usual; by the energy minimization which provides a reduced Hill-Wheeler-Griffin equation 6.36 .

We solve this equation in the (β,γ) grid for different angular momenta and now also for different parity, and this provides $E_\sigma^{NZ,I,\pi}(\beta,\gamma)$ as a function of (β,γ), I, π and σ ;

$$E_\sigma^{NZ,I,\pi}(\beta,\gamma) = \frac{\langle\Psi_\sigma^{NZ;IM,\pi}(\beta,\gamma)|\hat{H}|\Psi_\sigma^{NZ;IM,\pi}(\beta,\gamma)\rangle}{\langle\Psi_\sigma^{NZ;IM,\pi}(\beta,\gamma)|\Psi_\sigma^{NZ;IM,\pi}(\beta,\gamma)\rangle}, \tag{10.4}$$

which obviously represents the potential energy surface (PES) of the projected energy in the (β,γ) plane for the given quantum numbers. The minimum value of $E_\sigma^{NZ,I,\pi}(\beta,\gamma)$ in the PES provides the energy and the deformation parameters $(\beta_{\min},\gamma_{\min})$ of the state characterized by the quantum numbers (I,π,σ) in this approximation. Its wave function is given by $|\Psi_\sigma^{NZ;IM,\pi}(\beta_{\min},\gamma_{\min})\rangle$.

We will also study the probability of finding a value K ; see eq. 6.48 .

In the calculations the intrinsic many body wave functions $|\tilde{\phi}^\pi(\beta,\gamma)\rangle$ are expanded in a Cartesian harmonic oscillator basis and the number of spherical shells included in this basis is $N_{shells} = 8$ with an oscillator length of $b = 1.01A^{1/6}$. The (β,γ) grid of equilateral triangles contains 116 points. As in the rest of calculations, we use the Gogny interaction [3] with the D1S parameterization [4]. As with even nuclei, we consider all exchange terms, the Coulomb force and the two-body correction of the kinetic energy to avoid problems with the PNP [5]. Also we adopt the projected density prescription for the PNP and the mixed one for the AMP.

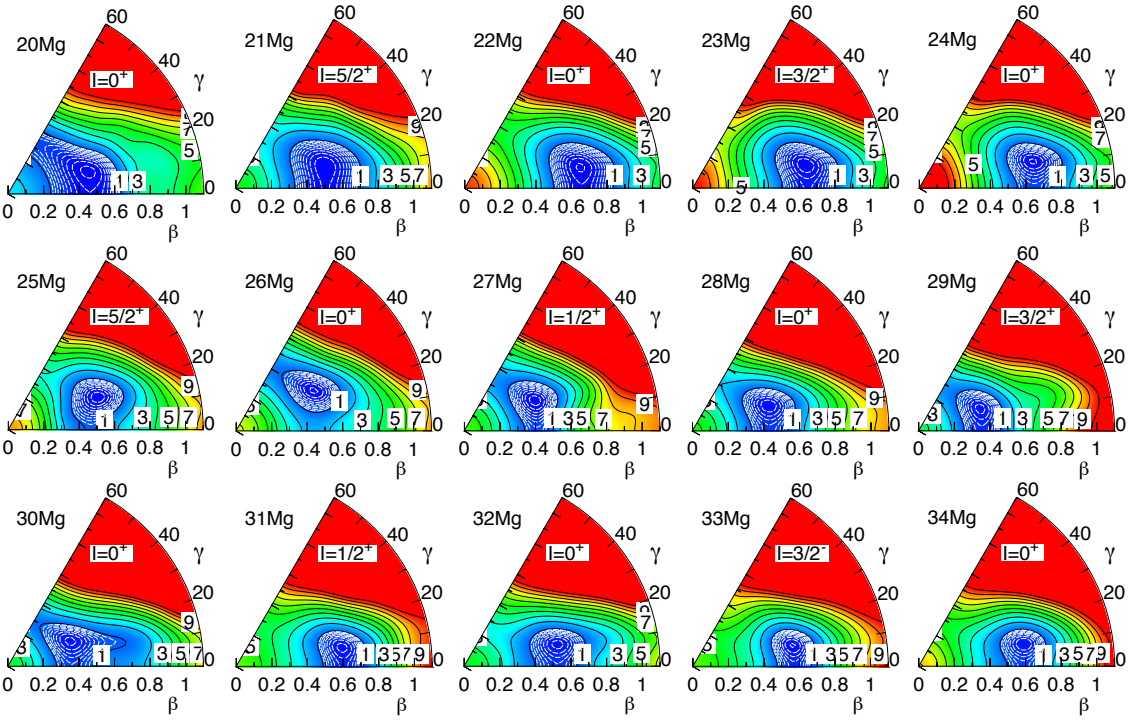

Figure 10.1: Contour plots of $E^{NZ,I,\pi}_{\sigma=0}(\beta,\gamma)$, see Eq. (10.4), as a function of (β,γ) for positive parity and for the angular momentum I providing the lowest energy. The solid black contour lines start at 1MeV and increase 1 MeV. The dashed white lines start at zero and increase 0.1 MeV. The zero contour is only present if the minimum is flat enough. The angle γ units are degrees.

To illustrate the method we have applied the discussed theory to the calculation of the bulk properties of the Magnesium isotopes. Towards this end we have to determine the wave function of the ground state of each isotope. This is done in the following way.

Step 0: We choose a parity (positive for example) for the blocked state in Eq. (10.2). Next we solve the PN-VAP variational equations Eqs. 10.1 for all (β,γ) values of the grid. This step provides a set of wave functions $|\tilde{\phi}^{\pi}(\beta,\gamma)\rangle$

$(P^{NZ}|\tilde{\phi}^{\pi}(\beta,\gamma)\rangle)$ with the right parity (and particle number). However, they are not eigenstates of the angular-momentum operator.

Step 1.0: We choose a value for the angular momentum, 1/2 for example. We now solve Eq. (6.36) for all $|\tilde{\phi}^{\pi}(\beta,\gamma)\rangle$ of the grid determined in step 0 for the given I-value. This provides the PES of Eq. (10.4). The minimum value of $E^{NZ,1/2,+}_{\sigma=0}(\beta,\gamma)$ provides the $(\beta^{1/2,+}_{\rm min},\gamma^{1/2,+}_{\rm min})$ values.

Step 1.1: We repeat step 1.0 for all I-values, and determine the corresponding PESs and the $(\beta^{I,\pi}_{\rm min},\gamma^{I,\pi}_{\rm min})$ values for $I=3/2,5/2,\ldots$. When this step is completed we have found the minima $(\beta^{I,\pi}_{\rm min},\gamma^{I,\pi}_{\rm min})$ for $I=1/2,3/2,5/2,\ldots$ and positive parity. Their corresponding energies are $E^{NZ,1/2,+}_{\sigma=0}(\beta^{1/2,+}_{\rm min},\gamma^{1/2,+}_{\rm min})$, $E^{NZ,3/2,+}_{\sigma=0}(\beta^{3/2,+}_{\rm min},\gamma^{3/2,+}_{\rm min})$, etc. From this set of energies the smallest one provides the angular momentum of the lowest state with positive parity, which we call I_1, and its energy $E^{NZ,I_1,+}_{\sigma=0}(\beta^{I_1,+}_{\rm min},\gamma^{I_1,+}_{\rm min})$.

Step 2: We repeat steps 0, and 1 for the other parity (negative). When this step is completed we have determined the corresponding PESs, the deformation parameters of the minima and the energies $E^{NZ,1/2,-}_{\sigma=0}(\beta^{1/2,-}_{\rm min},\gamma^{1/2,-}_{\rm min})$, $E^{NZ,3/2,-}_{\sigma=0}(\beta^{3/2,-}_{\rm min},\gamma^{3/2,-}_{\rm min})$, etc. As before the smallest energy provides the angular momentum of the lowest state with negative parity. We call it I_2 and its energy $E^{NZ,I_2,-}_{\sigma=0}(\beta^{I_2,-}_{\rm min},\gamma^{I_2,-}_{\rm min})$.

The smallest value of $E^{NZ,I_1,+}_{\sigma=0}(\beta^{I_1,+}_{\rm min},\gamma^{I_1,+}_{\rm min})$ and $E^{NZ,I_2,-}_{\sigma=0}(\beta^{I_2,-}_{\rm min},\gamma^{I_2,-}_{\rm min})$ provides the binding energy, the spin and the parity of the ground state of the given nucleus as well as the deformation parameters $(\beta^{I,\pi}_{\rm min},\gamma^{I,\pi}_{\rm min})$. The wave function $|\Psi^{NZ,I,\pi}_{M,\sigma=0}(\beta^{I,\pi}_{\rm min},\gamma^{I,\pi}_{\rm min})\rangle$ characterized by these quantum numbers determines the

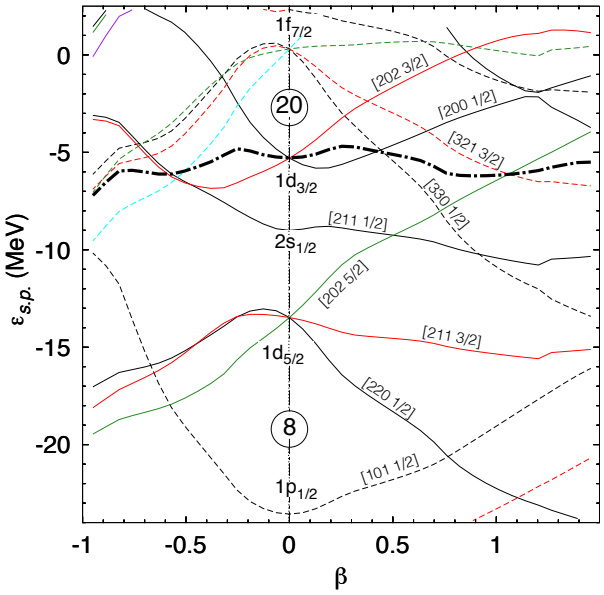

Figure 10.2: Single-particle levels of ^{30}Mg for neutrons obtained from the solution of the axially-symmetric HFB equation. The thick dashed lines represent the corresponding Fermi level.

wave function of the ground state which will be used to calculate electromagnetic properties, radii and so on.

10.2.1 K distribution of the states

Before considering the ground-state properties let us discuss the PESs of the different isotopes since they allow to determine the quality of the approach and in particular if the energy minimum is well defined.

In Fig. 10.1 we present contour lines of the PES $E^{NZ,I,\pi}_{\sigma=0}(\beta,\gamma)$ in the (β,γ) plane for the I^π of the ground state for the Mg isotopes. Let us first mention that the predicted spins and parities coincide with the experimental values

in all cases. Interestingly all nuclei are triaxial with γ values ranging from 10° to 25°, and have large β deformations. Since most minima are very well defined we can conclude that our approach of keeping only one point of the (β, γ) plane works very well for most nuclei. The softest nucleus is ^{20}Mg where a GCM in the (β, γ) could be performed, which, in general, would lead to smaller deformation than the one quoted here. In Table 10.1 the (β, γ) values of the ground states are listed. For a better understanding of our results we use the collective wave function, (see 6.47 or 8.3), to obtain the $|K|$ distribution of the odd neutron. The $|K|$ component with the largest weight is listed in Table 10.1 and it turns out that these wave functions have rather pure $|K|$. This purity, in spite of the, sometimes, large triaxiality has been also observed for even-even nuclei (see Table I of Ref. [6]) for the ground state band. The absence of K-mixing is probably due to the low level density of light nuclei. Furthermore we analyze the intrinsic HFB wave function $|\tilde{\phi}^\pi(\beta, \gamma)\rangle$ in the canonical basis what provides information on the quantum numbers of the blocked state for odd systems. To guide the discussion we will use a Nilsson plot, see Fig. 10.2 for the particular case of ^{30}Mg. We will furthermore use in our analysis the particle plus rotor (PR) model. Let us first discuss the spin values and parities. In the PR model, and according to the deformations of the Mg isotopes, one expects to be in the strong-coupling limit (strong deformations), in which case the lowest possible spin is $I_{\sigma=0} = K$, or in the decoupling limit (intermediate deformations), in which case $I_{\sigma=0} = j$. According to Table 10.1 and Fig. 10.2, the nucleus ^{21}Mg has a very pure $|K| = 1/2$ character and consequently a large component of the wave function of the last neutron is in the orbital [220 1/2] of the $1d_{\frac{5}{2}}$ subshell.

The theoretical value for the spin and parity of ^{21}Mg is $I^{\pi} = \frac{5}{2}^{+}$ which agrees with the decoupling limit prediction of $I = j = \frac{5}{2}$ and with the experimental data. This is a bit surprising since the β value is rather large and in principle one would expect the strong coupling limit. A look at the experimental data reveals that the $I = |K| = \frac{1}{2}$ state is just 200 keV above the $I = j = \frac{5}{2}$ one. As a matter of fact the ^{23,25}Mg isotopes with $|K| = 3/2$ ([211 3/2] orbital) and $|K| = 5/2$ ([202 5/2] orbital), with a larger deformation, see Table 10.1, do have $I = K = \frac{3}{2}$ and $I = |K| = \frac{5}{2}$, respectively, in agreement with the experimental values. The nucleus ^{27}Mg with a neutron with $|K| = \frac{1}{2}$ in the $2s_{1/2}$ sub-shell has obviously $I = \frac{1}{2}$ in agreement with the experimental value. In the case of ^{29}Mg we have $|K| = 1/2$ and the odd neutron sits in the orbital [200 1/2]. Since its deformation is $\beta = 0.37$, smaller than the one of ^{21}Mg, we expect also in this case the decoupling limit value of $I = \frac{3}{2}$, in agreement with our result and the experimental data. In the case of ^{31}Mg, with $|K| = 1/2$, we have two particles in the [330 1/2] and one particle in the [200 1/2], see below, as in ^{29}Mg. However, in this nucleus the deformation is $\beta = 0.60$. We are in the strong-coupling limit, and expect therefore $I = K = \frac{1}{2}$ in coincidence with the theoretical and the experimental values. All these nuclei have the unpaired nucleon in the 2s or the 1d shells and have positive parity. Our last odd nucleus, ^{33}Mg, has $|K| = 3/2$, the last neutron sits in the [321 3/2] orbital and it has a large deformation. We expect therefore $I = |K| = \frac{3}{2}$ and negative parity, in agreement with the theoretical and the experimental values.

A	I^π	β, γ	β_{exp}	$\|K\|(\%)$	Q_{spec}
20	0^+	$0.46, 17.5°$	—	–	—
21	$\frac{5}{2}^+$	$0.54, 14.9°$	—	$\frac{1}{2}(99.1\%)$	-17.80
22	0^+	$0.65, 12.2°$	0.58 (11)	–	—
23	$\frac{3}{2}^+$	$0.64, 10.9°$	—	$\frac{3}{2}(99.9\%)$	13.89
24	0^+	$0.65, 12.2°$	0.605 (8)	–	—
25	$\frac{5}{2}^+$	$0.54, 17.5°$	—	$\frac{5}{2}(99.7\%)$	22.47
26	0^+	$0.49, 25.3°$	0.482 (10)	–	—
27	$\frac{1}{2}^+$	$0.41, 23.4°$	-	$\frac{1}{2}(100\%)$	0
28	0^+	$0.46, 17.5°$	0.491 (35)	–	—
29	$\frac{3}{2}^+$	$0.37, 19.1°$	—	$\frac{1}{2}(96.0\%)$	-10.71
30	0^+	$0.39, 21.1°$	0.431 (19)	–	—
31	$\frac{1}{2}^+$	$0.60, 11.7°$	—	$\frac{1}{2}(100.0\%)$	0
32	0^+	$0.54, 14.9°$	0.473(43)	–	—
33	$\frac{3}{2}^-$	$0.60, 11.7°$	—	$\frac{3}{2}(99.9\%)$	14.17
34	0^+	$0.62, 13.0°$	0.58(6)	–	—

Table 10.1: The 2nd and 3rd columns display the spin and parity and the β, γ deformations of the ground state of the different isotopes. Notice that only ^{33}Mg has a ground state with negative parity. The 4th column shows the experimental β deformation taken from Refs. [7,8]. The 5th column lists the $|K|$ component with the largest weight in the wave function, with the percentage of this $|K|$ value in the total wave function. The 6th column provides the theoretical spectroscopic quadrupole moments, in efm^2.

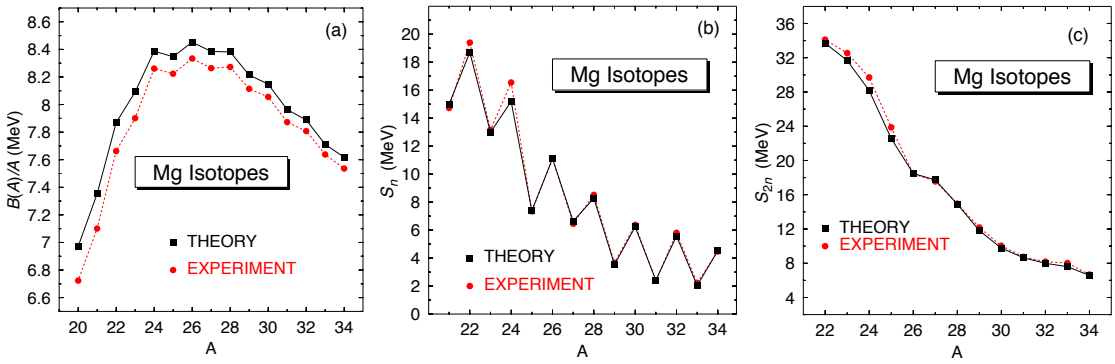

Figure 10.3: (a) Binding energy per particle versus de mass number. (b) One-neutron separation energies versus the mass number. (c) Two-neutron separation energies versus the mass number. The experimental values are taken from Ref. [9]

.

10.2.2 Nuclear shapes

We now discuss the shapes of the nuclei. The nucleus ^{20}Mg has a neutron shell closure at $N = 8$ and therefore one expects a smaller deformation than for the heavier isotopes. The same behaviour is expected for ^{21}Mg with just one neutron outside the closed shell. The isotopes $^{22-24}$Mg have a β-value close to 0.65 and correspond to the filling of the Nilsson orbitals [220 1/2] and [211 3/2] of the $d_{5/2}$ sub-shell, see Fig. 10.2, which are down-sloping. The orbital [202 5/2] of the $d_{5/2}$ sub-shell starts being occupied in ^{25}Mg which causes a decrease of the deformation because of its up-sloping character.

The nuclei $^{26-28}$Mg correspond to the filling up of the $d_{5/2}$ and $s_{1/2}$ sub-shells and the calculated β-value is 0.45 which is close to the crossing of the [202 5/2] and the [211 1/2] Nilsson levels. If we now add more neutrons we populate the orbital [200 1/2] of the $d_{3/2}$ sub-shell which is down-sloping for small

and up-sloping for larger β-values. This explains the moderate deformation of $^{29-30}$Mg. The nearest orbitals available to host the next neutrons are the up-sloping [202 3/2] of the $d_{3/2}$ sub-shell and the strongly down-sloping [330 1/2] of the $f_{7/2}$ sub-shell. In this case it is energetically most convenient to start filling the [202 3/2] orbital at moderate deformation. It should be noticed, however, the softness of the PES of ^{30}Mg in the β degree of freedom corresponding to the population of the [330 1/2] orbital at larger deformation. In the PES of ^{31}Mg we observe an abrupt increment of the deformation parameter as compared with ^{30}Mg. This is because now the orbital [330 1/2] is filled and in the orbital [202 3/2] there is only one neutron, indicating the beginning of the inversion island [10]. For heavier isotopes the up-sloping character of the [202 3/2] orbital at larger deformations will favour the filling of the [321 3/2] orbital of the $f_{7/2}$ shell, driving these isotopes to even larger deformations as we obtain for the $^{32-34}$Mg isotopes.

As mentioned, all analysed Mg isotopes are triaxial and, with the exception of ^{26}Mg, rather soft towards the prolate axis, i.e., contour lines less than 1 MeV cross the prolate axis. These nuclei, because of their large β values, are much harder towards oblate shapes. The softest ones are those with the smallest deformation parameter β, namely ^{26,27}Mg and ^{29,30}Mg for which the contour lines less than 2 MeV cross the oblate axis. Furthermore, the experimental deformations listed in Table 10.1 are in good agreement with the theoretical values. Notice, however, that at variance with our values, the experimental deformations have been extracted from $E2$ transition probabilities, see Refs. [7, 8].

10.3 Ground state relevant properties

10.3.1 Odd evan mass difference and binding energies

We now discuss relevant properties of the ground states. In panel (a) of Fig. 10.3 we present the theoretical binding energies per particle for the Mg isotopes together with the experimental ones versus the mass number. The theoretical binding energies have been obtained from the energy minima of the corresponding ground state PESs. The theory line follows very closely the general behaviour of the experimental one. We obtain overbinding which is due to the fact that we are using the D1S parameterisation of the Gogny force which was fitted to reproduce experimental data with the HFB method. Though the authors of Ref. [3] left some room for eventual BMF effects apparently this was not sufficient, see also Refs. [11, 12]. One should furthermore consider that the 8 harmonic oscillator shells used in the calculations are alright to provide relative but not absolute energies for which a larger number of shells is needed, see Ref. [12, 13]. Based on these references one can estimate that an additional overbinding of 2.3 to 2.7 MeV should be added to the results of the present calculations.

In this plot one can appreciate the odd-even staggering in the two parabolas, one for even-even and another for the odd-even isotopes, obtained both in the experiment and in the theory. The parabola maximum at $A = 26$ corresponds to the neutron half-shell, $N = 14$, which provides maximal binding per particle. In panels (b) and (c) we present the one- and two-neutron sep-

aration energies, respectively. For S_n, with the exception of two isotopes, ^{22,24}Mg, we obtain an extraordinary agreement between the theoretical results and the experimental data. The small disagreement observed for the nuclei ^{22,24}Mg is probably related to the fact that proton-neutron pairing is not included in our calculations. Therefore, we find the largest discrepancy in ^{24}Mg corresponding to the $N = Z = 12$ case. For ^{22}Mg the disagreement is smaller and for ^{26}Mg, with the neutron $1d_{5/2}$ subshell closure, the p-n pairing looses relevance. In the S_{2n} case the excellent agreement is maintained but now with the exception of the isotopes $^{22-25}$Mg for which the agreement is not as good as for the others. The small plateau found at $A = 26, 27$ is due to the behaviour observed at the top of the parabola in panel (a).

In our approach the pairing correlations are treated specially well. First, the finite range density dependent Gogny force used in the calculations is considered to be one of the best to describe pairing correlations and used as benchmark in many calculations. Second, the use of the PN-VAP approach avoids the pairing collapse in the weak pairing regime which is normally observed in the case of odd-even nuclei. And third, the Coulomb anti-pairing effect (CAP) is taken into account since all exchange terms of the force, in particular the Coulomb ones, are considered in our calculations. A quantity which allows to extract information on the pairing energies from the experimental nuclear mass is the odd-even mass difference. In the three point approach this magnitude is given by

$$\Delta_0^3(A) = \frac{1}{2}\left[B(A+1) + B(A-1) - 2B(A)\right], \tag{10.5}$$

with the proton number Z a constant even number and $B(A)$ a positive number. In Fig. 10.4 we plot $\Delta_0^3(A)$ for the Mg isotopes as a function of the mass number. The points above the horizontal line correspond to the odd-even nuclei and those below to the even-even ones. On average the odd-even nuclei have about 0.5 MeV less pairing than the even-even ones. The agreement between the theoretical results and the experimental data is excellent, specially for the heavier isotopes. For the lighter nuclei, in particular ^{21}Mg and $^{23-24}$Mg, the theoretical results are a bit smaller, in absolute value, than the experimental ones. This is again a consequence of the mentioned absence of p-n pairing in our calculations.

10.3.2 Nuclear radii

Another relevant quantity is the nuclear radius. In Fig. 10.5 the experimental mass radii [14] corresponding to point mass nucleons[1] are plotted together with the theoretical results. In the calculation of the mass radius we consider the one-body term of the center-of-mass correction. The theoretical results reproduce very well the overall experimental behaviour. One can distinguish three well differentiated regions. We first observe a rather flat behaviour of the mass radius for $^{24-26}$Mg in which the increase of the neutron radius with filling the neutron $1d_{\frac{5}{2}}$ orbital is compensated by a compression of the charge distribution. This effect has been observed in the Ne [15, 16] and in the Mg isotopes [17]. Though with the filling of the $2s_{\frac{1}{2}}$ orbital one would expect an increase of the mass radius, it seems that the mentioned compensation

[1] Private communication of Dr. Shin Watanabe

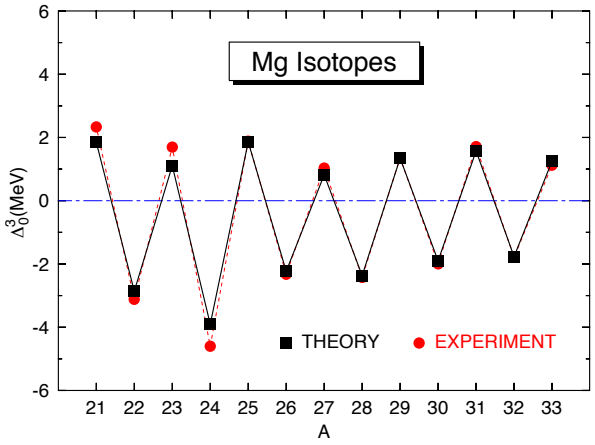

Figure 10.4: Odd-even mass differences according to Eq. (10.5). The experimental data are from Ref. [9]

.

persists also for ^{27}Mg. The second region corresponds to the nuclei $^{28-30}$Mg, where we observe a clear increase of the mass radius associated with two neutrons in the $2s_{\frac{1}{2}}$ or $1d_{\frac{3}{2}}$ orbitals. The third region, for $A \geq 31$ is marked by the beginning of the inversion island in ^{31}Mg [10] and the rise in the mass radius observed for $A \geq 31$ is associated with the increasing occupation of the $1f_{\frac{7}{2}}$ orbital.

10.3.3 Spectroscopic quadrupole moment and magnetic moment

Concerning the spectroscopic quadrupole moments of these nuclei they have been listed in Table 10.1. Experimentally there are only two known values, namely, 11.4 (2) efm^2 in the case of ^{23}Mg [18] and 20.1(3) efm^2 for ^{25}Mg [19]. Both values are somewhat smaller than the theoretical predictions 13.89 efm^2

and 22.47 efm^2, respectively. Concerning the magnetic moments there are more experimental data and these, together with the theoretical values, are plotted in Fig. 10.6. In the calculations we have used the free gyromagnetic factors. We have also plotted the Schmidt values calculated with the occupations determined in the discussion of Fig. 10.1. As expected, due to the large deformations of these nuclei, the Schmidt values provide a poor description. For $^{21-27}$Mg the Schmidt value is $-1.9\mu_N$ and the experimental data are about half of it. The relatively good agreement of the Schmidt with the experimental value for ^{29}Mg is probably due to the fact that this nucleus is the less deformed of all discussed isotopes. According to the occupation of the last nucleon ^{31}Mg should have the same Schmidt magnetic moment as ^{29}Mg. In contrast with the latter the experimental value for ^{31}Mg, however, differs significantly from the Schmidt value. This is probably due to the fact that ^{31}Mg is far more deformed ($\beta = 0.60$) than ^{29}Mg ($\beta = 0.37$) and therefore further away from the spherical limit. For ^{33}Mg, as for the lighter isotopes, the Schmidt value is about twice as large as the experimental data. Concerning our theoretical results we observe that our values not only reproduce the tendency of the experimental data but that they are very close to them providing in some cases quantitative agreement.

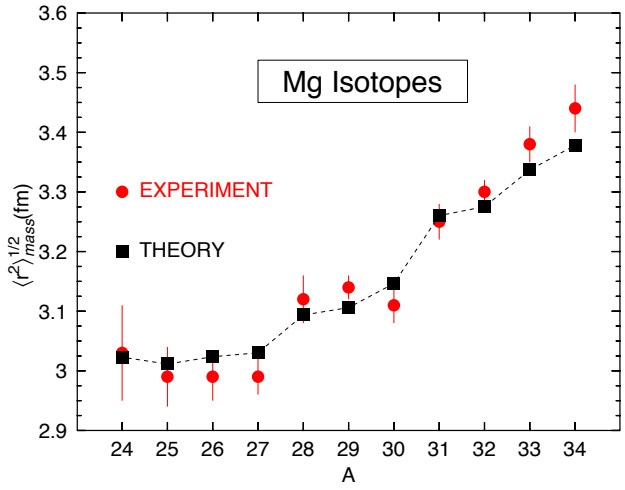

Figure 10.5: Radii of the nuclei $^{27-28}$Mg in the PNVAP+PNAMP approach. The experimental data are from Ref. [14].

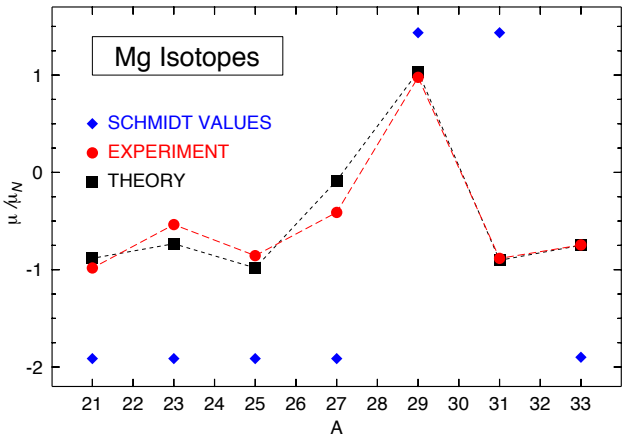

Figure 10.6: Magnetic moments of the ground states of the Magnesium isotopes. The experimental results have been taken from the following references : ^{21}Mg [20] ^{21}Mg, [21, 22], ^{25}Mg [23], $^{27-31}$Mg [24] and ^{33}Mg [25].

10.4 Summary

In conclusion, we have used a novel approach with exact conservation of angular momentum and particle number to describe odd-even nuclei. We have applied this theory to the description of ground-state properties of the Magnesium isotopic chain with the effective Gogny force. The results are in very good agreement with the experimental bulk properties, energy gaps and electromagnetic moments.

Bibliography

[1] Marta Borrajo and J. Luis Egido. *Physics Letters B*, 764:328 – 334, 2017.

[2] J. L. Egido, J. Lessing, V. Martin, and L. M. Robledo. *Nucl.Phys. A*, 594:70, 1995.

[3] J. Dechargé and D. Gogny. *Phys.Rev. C*, 21:1568, 1980.

[4] J. F. Berger, M. Girod, and D. Gogny. *Comp.Phys. Commun.*, 63:365, 1991.

[5] M. Anguiano, J. L. Egido, and L. M. Robledo. *Nucl.Phys.A*, 683:227, 2001.

[6] T. R. Rodríguez and J. L. Egido. *Phys.Rev. C*, 81:064323, 2010.

[7] S. Raman et al., Atomic Data, and 78 Nuclear Data Tables. pages 1–128, 2001.

[8] H. Iwasaki et al. *Phys.Lett. B*, 522:227, 2001.

[9] http://www.nndc.bnl.gov.

[10] M. Borrajo and J. L. Egido. *Eur.Phys. J*, 52:277, 2016.

[11] S. Hilaire and M. Girod. *Proceedings of the International Conference on Nuclear Data for Science and Technology*, 27(2007):107–110, 2008.

[12] T. R. Rodríguez, A. Arzhanov, and G. Martínez-Pinedo. Phys.rev c. 91:044315, 2015.

[13] R. Rodríguez-Guzman, J. L. Egido, and L. M. Robledo. *Nucl.Phys. A*, 709:201, 2002.

[14] S. Watanabe et al. Phys.rev c. 89:044610, 2014.

[15] W. Geithner et al. *Phys.Rev. Lett.*, 101(25250):2, 2008.

[16] K. Marinova et al. *Phys.Rev. C*, 84:034313, 2011.

[17] D. T. Yordanov et al. *Phys Rev Lett.*, 108:042504, 2012.

[18] K. Matsuta et al. *Ann.Rep. Osaka Univ*, 1995, 1996.

[19] R. Weber et al. *Nucl.Phys. A*, 377:361, 1982.

[20] J. Krämer et al. *Phys.Lett. B*, 678:465, 2009.

[21] M. Fukuda et al. *Phys.Lett. B*, 307:278, 1993.

[22] S. M. Perez. *Phys.Rev. C*, 36:1202, 1987.

[23] F. Alder and F. C. Yu. *Phys.Rev.*, 82:105, 1951.

[24] M. Kowalska et al. *Phys.Rev.C*, 77:034307, 2008.

[25] D. T. Yordanov et al. *Phys. Rev. Lett.*, 99(21250):1, 2007.

Chapter 11

Study of ^{31}Mg on the island of inversion

In Chapter 10 we proved the effectiveness of the method to the calculation of ground state properties of odd nuclei. Now we apply our theory to study the energy spectra and the properties of excited states. As an application we choose the nucleus ^{31}Mg at the border of the $N = 20$ inversion island. We evaluate the ground state properties, the excited states and the transition probabilities. In general we obtain a good description of the measured observables. The results have been published in [1].

The procedure is the same as Chapter 10; We choose the desired parity for the blocked state. Next we solve the PN-VAP variational equations Eqs. (10.1) for all (β, γ) values of the grid. This step provides a set of wave functions $\tilde{\phi}^{\pi}(\beta, \gamma)$ with the right parity but without rotational invariance. To find out

$(\beta^I_{\rm min}, \gamma^I_{\rm min})$ we solve Eq. (6.36) for all $\tilde{\phi}^\pi(\beta,\gamma)$ of the grid for a given I-value. The minimum value of $E^{NZ,I,\pi}_{\sigma=1}(\beta,\gamma)$ provides the $(\beta^I_{\rm min}, \gamma^I_{\rm min})$ values. We repeat the previous step for all I-values. The energies $E^{NZ,I,\pi}_{\sigma=1}(\beta^I_{\rm min}, \gamma^I_{\rm min})$ allow to draw the spectrum and the wave functions $|\Psi^{NZ,IM,\pi}_{\sigma}(\beta^I_{\rm min}, \gamma^I_{\rm min})\rangle$ enable the calculation of electromagnetic properties or any other observable.

We would like also to mention the limitations of the present approach: In a symmetry conserving mean field approach one does not consider fluctuations around the most probable values, i.e., we are not considering the large amplitude fluctuations of the GCM. Furthermore in our description we only consider one-quasiparticle states. The nucleus ^{31}Mg has been thoroughly discussed theoretically [2,3] and experimentally [4].

The PN-VAP potential energy surfaces are discussed in Sect. 11.1, the potential energy surfaces (PES) for different angular momenta are displayed in Subsect. 11.2. The spectrum of ^{31}Mg is discussed in Sect. 11.3 together with the electromagnetic properties of this nucleus. Finally, the conclusions and outlook are presented in Sect. 11.4.

11.1 The PN-VAP potential energy surfaces

As in the Mg isotopic chain, the intrinsic many body wave functions $|\tilde{\phi}^\pi(\beta,\gamma)\rangle$ are expanded in a Cartesian harmonic oscillator basis and the number of spherical shells included in this basis is $N_{shells} = 8$ with an oscillator length of $b = 1.01A^{1/6}$. We have compared with calculations with 10 shells and we

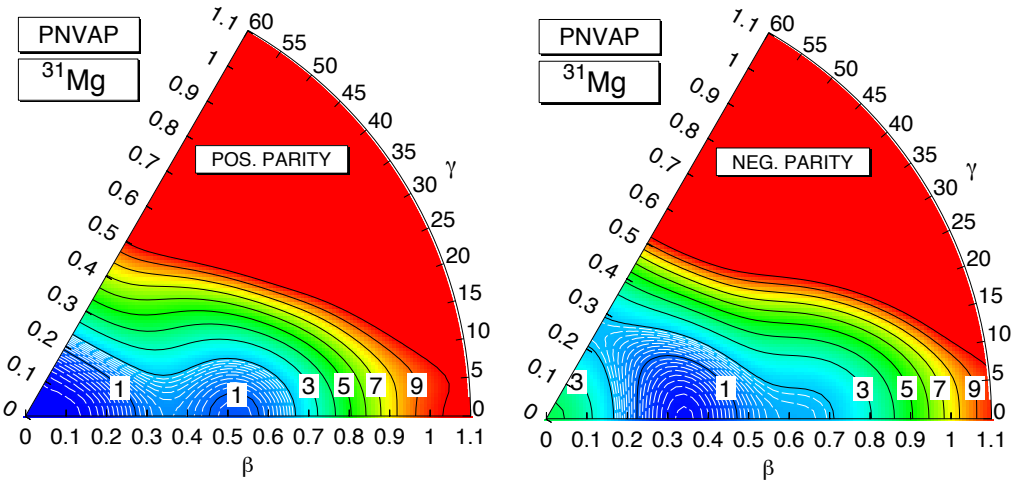

Figure 11.1: Potential energy surfaces (in MeV) of ^{31}Mg in the PNAMP method for positive (left) and negative (right) parity states.The energy origin has been chosen independently for each panel and the energy minimum has been set to zero. The continuous lines represent contours from 1 to 10 MeV in 1 MeV steps. The white dahed contours around the minima are 0.1 MeV apart and extend from 0.1 up to 1.9 MeV. The absolute value of the energy is -243.472 MeV (positive parity) and -243.129 MeV (negative parity)

find a good convergence.

The solution of Eq. (10.1) in the (β, γ) plane for 99 points in a grid of triangles provides PN-VAP wave functions as a function of the deformation parameters. The PN-VAP potential energy surfaces 6.9 are plotted in Fig. 11.1 for the nucleus ^{31}Mg with 12 protons and 19 neutrons for blocked positive (negative) parity neutron states in the left (right) hand panel.

In the positive parity channel we find two minima on the prolate axis, about 300 keV apart, one at $\beta \approx 0.08$ and the other at $\beta \approx 0.5$. Along the prolate axis the surface is softer than along the oblate one. For β values smaller than 0.3 the PES is rather soft in the γ degree of freedom. In the negative

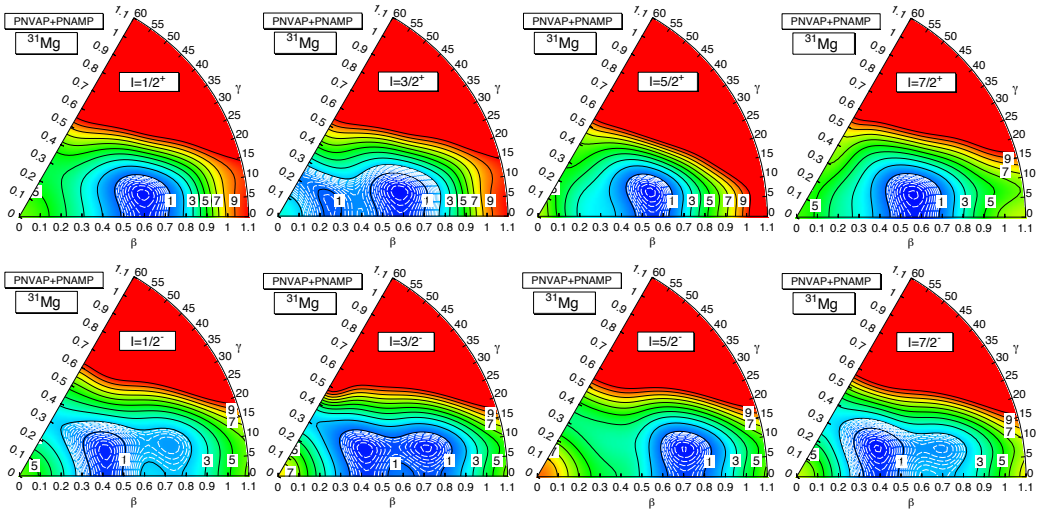

Figure 11.2: Potential energy surfaces (in MeV) of ^{31}Mg in the PNAMP method for positive (top panels) and negative (bottom panels) parity states.The energy origin has been chosen independently for each panel and the energy minimum has been set to zero. The continuous lines represent contours from 1 to 10 MeV in 1 MeV steps. The white dashed contours around the minima are 0.1 MeV apart. The absolute values (in MeV) of the energy minima are $(-246.840, -246.553, -245.791, -245.0127)$ for angular momenta and parity $\frac{1}{2}^+, \frac{3}{2}^+, \frac{5}{2}^+, \frac{7}{2}^+$ and $(-244.282, -246.152, -245.557, -245.990)$ for $\frac{1}{2}^-, \frac{3}{2}^-, \frac{5}{2}^-, \frac{7}{2}^-$ respectively.

parity channel we observe one clear minimum at $\beta \approx 0.34$ on the prolate axis and an incipient secondary minimum at $\beta \approx 0.6$. We also observe a saddle point at $\beta \approx 0.25$ on the oblate axis. The softening of PES in the γ degree of freedom now extends to larger values than for the positive parity. Comparing both parities one observes that the minima of the negative parity channel are shifted to larger deformations as compared to the positive one.

11.2 The PNAMP potential energy surfaces

We now solve the Hill-Wheeler-Griffin equations, Eq. (6.36), for different values of the angular momentum. Each (β, γ) point the Hill-Wheeler-Griffin equation provides several solutions $E_\sigma^{NZ,I,\pi}(\beta,\gamma)$, numbered by the symbol σ (see 6.2 or 10.2). In particular for a given I there are $(2I+1)/2$ linearly independent solutions. In Fig. 11.2 we display the results of such calculations. The PES displayed in Fig. 11.2 have been made taking at each point the lowest solution of Eq. (6.36).

11.2.1 Positive parity states

In the top (bottom) panels the results for positive (negative) parity states are shown. In the top panels we present the PESs for angular momenta $\frac{1}{2}^+, \frac{3}{2}^+, \frac{5}{2}^+, \frac{7}{2}^+$, these values being used to label the corresponding panels. With the exception of the PES for $I = \frac{3}{2}^+$ which has two coexisting minima, the other PESs do have only one minimum. This is somewhat in contrast to the positive parity PES of the PN-VAP approach of Fig. 11.1 which has two. All four PESs present a clear triaxial minimum at $\beta = 0.61$ and $\gamma = 14°$. This common minimum is well localized and much softer in the β than in the γ degree of freedom. The secondary minimum for $I = \frac{3}{2}^+$ is localized at $\beta = 0.31$ and $\gamma = 14°$ and appears at slightly higher energy. This secondary minimum in contrast to the primary one is very soft in the γ degree of freedom. The exact numerical values of the deformations and the excitation energies are given in Table 11.1.

To identify the dominant configuration associated to each minimum it is convenient to consider the single particle levels involved around the Fermi level. In Fig. 11.3 we display the neutron single particle energies in the HF approach for ^{32}Mg, which we will use to provide qualitative arguments. In ^{31}Mg and for positive parity states we must have one particle either in the Nilsson orbital $[200\frac{1}{2}]$ or $[202\frac{3}{2}]$. Furthermore, one can get more insight looking at the K-distribution), see Eq. (6.48), of the wave function in the energy minimum, shown in Table 11.1. As we can see the $I = \frac{3}{2}$ state with $\beta = 0.31$, $\gamma = 14°$ corresponds to $|K| = \frac{3}{2}$ and the $I = \frac{3}{2}$ state with $\beta = 0.61$, $\gamma = 14°$ to $|K| = \frac{1}{2}$. That means in the minimum with smaller deformation the blocked particle sits in the Nilsson orbital with $[202\frac{3}{2}]$ whereas in the minimum with the large deformation the blocked particle sits in the $[200\frac{1}{2}]$. Looking at the single particle energies of these levels it is obvious that in the first case the two additional particles are occupying the $[200\frac{1}{2}]$ level. This is the normal occupation that one expects. In the second case, when the blocked particle is in the $[200\frac{1}{2}]$, the level $[202\frac{3}{2}]$ has crossed the Fermi level, see Fig. 11.3, and the two additional particles sit in the $f_{\frac{7}{2}}$ orbit. This is the intruder occupation that one observes in the inversion island. Since in our calculations the ground state corresponds to this configuration we conclude that in our theory the nucleus ^{31}Mg is inside the inversion region. The large deformation ($\beta = 0.61$) as well as the fact that the particle sits in the $d_{\frac{3}{2}}$ orbital, i.e., small Coriolis interaction, is a clear indication that we are in the strong coupling limit, and that therefore we must have $I = \frac{1}{2}$ [5]. Independently of the Nilsson plot of Fig. 11.3 we can check the occupation of the orbits in the canonical basis of the PN-VAP solution. We find that in the

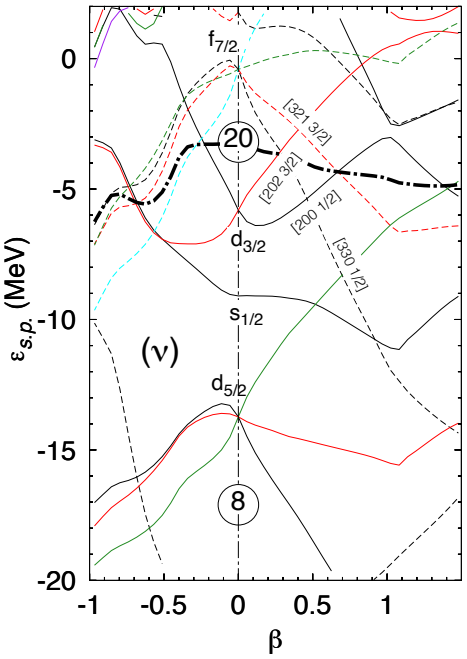

Figure 11.3: Single-particle levels of ^{32}Mg for neutrons in the HFB approach. The thick dashed line represents the Fermi level. The Nilsson quantum numbers $[N, n_z, m_l, \Omega]$ are indicated for the relevant orbitals.

shell model language the minimum at small β value corresponds mostly to $(\mathrm{d}_{\frac{3}{2}})^3(\mathrm{f}_{\frac{7}{2}})^0$, i.e., a 0p1h configuration. The large β value corresponds mostly to $(\mathrm{d}_{\frac{3}{2}})^1(\mathrm{f}_{\frac{7}{2}})^2$, i.e., a 2p3h configuration.

11.2.2 Negative parity states

We now discuss the negative parity channel, i.e., the lower panels of Fig. 11.2. We observe minima with two deformations for the different spins, see also Table 11.1, one at $\beta = 0.45, \gamma = 19°$ (spins $\frac{1}{2}^-$, $\frac{3}{2}^-$, $\frac{7}{2}^-$) and the other at $\beta = 0.69, \gamma = 12°$ (spins $\frac{3}{2}^-$, $\frac{5}{2}^-$). Again as for $I = \frac{3}{2}^+$ we find coexistent shapes. In Table 11.1 we also find that the first one corresponds to $|K| = \frac{1}{2}$

I^π_σ	β, γ	E^+_σ	$\|K\| = \frac{1}{2}$	$\|K\| = \frac{3}{2}$	$\|K\| = \frac{5}{2}$
$1/2^+_1$	$0.61, 13.9°$	0	100	–	–
$3/2^+_1$	$0.61, 13.9°$	0.287	99.4	0.6	–
$3/2^+_2$	$0.31, 13.9°$	0.848	10.6	89.4	–
$5/2^+_1$	$0.61, 13.9°$	1.049	97.7	2.3	0.0
$7/2^+_1$	$0.61, 13.9°$	1.827	98.2	1.7	0.1
$1/2^-_1$	$0.45, 19.1°$	2.558	100	–	–
$3/2^-_1$	$0.45, 19.1°$	0.688	99.6	0.4	–
$3/2^-_2$	$0.69, 12.2°$	0.745	0.1	99.9	–
$5/2^-_1$	$0.69, 12.2°$	1.283	0.1	99.9	0.0
$7/2^-_1$	$0.45, 19.1°$	0.850	97.7	2.0	0.3

Table 11.1: Properties of the minima of the PESs of Fig. 11.2 in the different columns. 1: Spin and parity, 2: (β, γ) coordinates of the minima, 3: Excitation energy (in MeV) with respect to the $I = \frac{1}{2}^+$ state, 4, 5, 6: The weights $P_{K\sigma} = |F^{NZ,I}_{K\sigma}|^2$, in percentage, see Eq. (6.48), for different $|K|$ values.

and the second one to $|K| = \frac{3}{2}$. For negative parity the blocked particle must sit in the $f_{\frac{7}{2}}$ orbit. If we look at Fig. 11.3 we observe that the relevant levels in this orbit are the $[330\frac{1}{2}]$ and the $[321\frac{3}{2}]$. The first level appears at small deformation and will explain the first minimum and the second level at larger deformation the second minimum. In both cases we have two additional particles either in the $d_{\frac{3}{2}}$ (normal occupation, $\beta = 0.45$ minimum) or in the $f_{\frac{7}{2}}$ (intruder occupation, $\beta = 0.69$ minimum). In the shell model language the minimum at small β value corresponds mostly to $(d_{\frac{3}{2}})^2(f_{\frac{7}{2}})^1$, i.e., a 1p2h configuration. The large β value corresponds mostly to $(d_{\frac{3}{2}})^0(f_{\frac{7}{2}})^3$, i.e., a 3p4h configuration.

11.3 Spectrum and other observables

The solution of the Hill-Wheeler-Griffin equation, as a function of (β, γ) provided the PESs displayed in Fig. 11.2 for the different values of the angular momentum. Though in each (β, γ) point there are $(2I + 1)/2$ linearly independent solutions, the energies displayed in the PESs correspond to the the lowest solution at each point. The minima of these surfaces provide the energies of the states corresponding to the spin and parity of the given PES. Since, within a PES, the wave functions of the different (β, γ) points, in general, are not orthogonal to each other, only one point provides a physical state. In Fig. 11.4 we present the excitation energies predicted by the minima of these surfaces. The excited states obtained by considering the solutions $\sigma = 2$ or higher at each point (β, γ) are not considered in this work. The only exception are the states $3/2_2^+$ and $3/2_2^-$ represented by dashed lines in Fig. 11.4 corresponding to the secondary minimum, at $(\beta = 0.31, \gamma = 14.^\circ)$ and $(\beta = 0.69, \gamma = 12.^\circ)$ of Fig. 11.2, respectively. We have exceptionally included them for two reasons: First because these are the levels that should be lowest in the case that inversion has not taken place and second because they are practically orthogonal to the other $I = 3/2_1$ states present in the corresponding PES.

In Fig. 11.4 we have also plotted the experimental spectrum [4,6]. Concerning the positive parity part of the spectrum the ordering of the levels is correctly reproduced by our calculations but rather stretched. As mentioned in the Introduction the approach we are presenting here is the symmetry conserv-

I^π_σ	Q_{spec}	μ	I^π_σ	Q_{spec}	μ
$1/2^+_1$	0	-0.935	$1/2^-_1$	0	1.339
$3/2^+_1$	-15.5	0.690	$3/2^-_1$	-12.16	-1.594
$3/2^+_2$	8.40	1.132	$3/2^-_2$	16.63	-0.695
$5/2^+_1$	-20.00	-0.085	$5/2^-_1$	-6.17	-0.125
$7/2^+_1$	-26.34	1.557	$7/2^-_1$	-21.50	-0.910

Table 11.2: Electromagnetic moments of the positive and the negative parity bands. Q_{spec} is given in units of efm^{2}and μ is in units of μ_N.

ing mean field approach and it is well known from even-even nuclei [7–10] that residual correlations will compress the spectrum. With respect to the negative parity part of the spectrum, experimentally there are two levels clearly identified, the $7/2^-_1$ and the $3/2^-_1$. In the theory they appear again in the right order but too high in energy. One expects again that the residual interactions will compress the spectrum.

Concerning the electromagnetic moments they are quoted in Table 11.2 for the positive and negative bands. Our result for the magnetic moment of the ground state is relatively close to the measured value $-0.88355(15)\mu_N$ [11]. In the calculations we have used the free gyromagnetic values. The electric quadrupole moments correspond to a well deformed nucleus, unfortunately there are no experimental values for this observable. In Table 11.3 we have listed experimental values for dipole and quadrupole electromagnetic transitions and a selection of the theoretical predictions. With the exception of the $M1$ transition from the $\frac{3}{2}^+_1$ level to the $\frac{1}{2}^+_1$ we obtain in general a very reasonable agreement with the experimental values.

I^{π}_{σ}	Experiment	Theory
$B(E2; 5/2^+_1 \longrightarrow 1/2^+_1)$	61(7) [12]	117
$B(M1; 5/2^+_1 \longrightarrow 3/2^+_1)$	0.1-0.5 [12]	0.590
$B(M1; 3/2^+_1 \longrightarrow 1/2^+_1)$	0.019(0.004) [13]	0.093
$B(E2; 7/2^-_1 \longrightarrow 3/2^-_1)$	68(5) [14]	88
$B(E2; 3/2^+_1 \longrightarrow 1/2^+_1)$	–	109
$B(E2; 5/2^+_1 \longrightarrow 3/2^+_1)$	–	38
$B(E2; 7/2^+_1 \longrightarrow 5/2^+_1)$	–	13
$B(E2; 7/2^+_1 \longrightarrow 3/2^+_1)$	–	146
$B(M1; 7/2^+_1 \longrightarrow 5/2^+_1)$	–	0.107

Table 11.3: Transition probabilities in ^{31}Mg, $B(M1)$ in units of μ_N^2 and $B(E2)$ in e^2fm^4

11.4 Conclusions

We have applied our method to the description of the nucleus ^{31}Mg at the border of the inversion island. We find the two coexisting minima corresponding to the normal occupation and the intruder one typical for the inversion island.

In spite of the simplicity of the approximation we obtain a qualitative agreement of the theoretical and the experimental spectrum. As expected due to the lack of correlations we obtain a stretched spectrum. The experimental values of the measured electromagnetic transitions as well as the magnetic moment are also well described.

The results obtained for the nucleus ^{31}Mg with the Gogny force encourage us to improve the present approach by doing a configuration mixing of the different deformations, which is done in the next chapter for the ^{25}Mg nucleus.

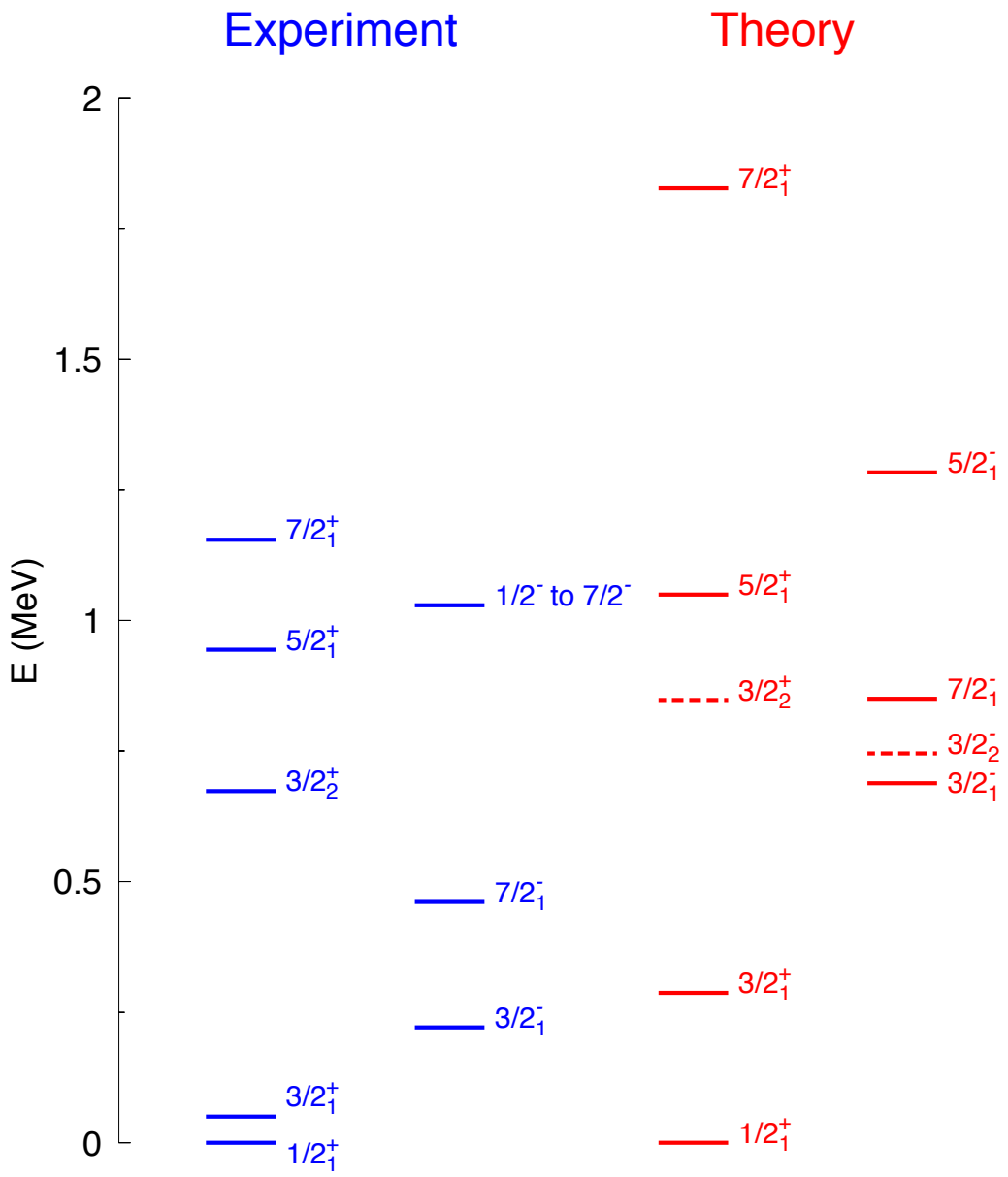

Figure 11.4: Spectrum of the nucleus ^{31}Mg in the symmetry conserving mean field approximation.

Bibliography

[1] M. Borrajo and J. L. Egido. A symmetry-conserving description of odd nuclei with the gogny force. *The European Physical Journal A*, 52(9):277, 2016.

[2] K. Kimura. *Phys. Rev.*, C 75, 2007.

[3] E. Caurier, F. Nowacki, and A. Poves. *Phys. Rev.*, C 90, 2014.

[4] Gerda Neyens. *Phys. Rev.*, C 84, 2011.

[5] P. Ring and P. Schuck. *The nuclear many body problem*. Springer-Verlag, Berlin, 1980.

[6] http://www.nndc.bnl.gov.

[7] N. López Vaquero, T. R. Rodríguez, and J. Luis Egido. *Phys. Lett.*, B704:520–526, 2011.

[8] N. López Vaquero, J. L. Egido, and T. R. Rodríguez. *Phys Rev C*, 88, 2013.

[9] M. Borrajo, T. R. Rodrǵuez, and J. L. Egido. *Phys Lett.*, B 746, 2015.

[10] J. L. Egido, M. Borrajo, and T. R. Rodríguez. *Phys Rev. Lett.*, 11, 2016.

[11] G. Neyens et al. *Phys. Rev. Lett.*, 94, 2005.

[12] M. Seidlitz et al. and B. Physics Letters. 181, 2011.

[13] G. Klotz et al. *Phys. Rev. C*, 47, 1993.

[14] H. et al. Mach. *The 4th International Conference on Exotic Nuclei and Atomic Masses: Refereed and selected contributions.* Springer, Berlin, 2005.

Chapter 12

Configuration mixing in the ^{25}Mg nucleus

We present our first symmetry conserving configuration mixing approach applied to an odd nucleus,i.e. we perform the three steps studied in chapter 6. The β, γ deformation parameters are the generator coordinates. The nucleus ^{25}Mg is chosen to test the reliability of the method in odd-A nuclei. Moreover, the huge amount of experimental data makes this nucleus an ideal benchmark to show the potential of the approach.

12.1 Particle Number restoration

As always we start creating a grid of self-consistently blocked wave functions. The constraints are the quadrupole deformations q_{20}, q_{22} which are related to

β, γ deformation parameters by equation 3.26.

The HFB w.f. is expanded in the Cartesian Harmonic oscillator wit $N = 8$ major spherical shells with an oscillator length $b = 1.01A^{1/6}$.

12.1.1 VAP PES

We solve equation 3.25 in the sextant $0° \leq \gamma \leq 60°$ in the range $\beta \leq 1.1$ ($\beta \leq 1.5$) with 190(216) points for positive(negative) parity.

In Fig 12.1 we display the PN-VAP energy surfaces (eq. 6.9) for both parities. The origin is set independently in each figure, being the energy origin equal at the corresponding energy minimum.

The negative parity one is 4.237 MeV higher. This is consistent with the shell model point of view, as we are in the middle of the $d_{5/2}$ shell and is more economic to fill this positive parity shell with a particle than creating a hole in the $p_{1/2}$ shell or putting a particle in $f_{7/2}$. Both minima sit in $\gamma = 0°$. The positive parity minimum is less deformed $\beta = 0.4231$ than the negative parity one ($\beta = 0.6769$) . This big deformation in the negative parity channel is due to the down-sloping character of the Nilsson [330 1/2] , which crosses the *sd* shells at high deformations. We note also that the positive parity channel is softer in the γ direction because the three sub-shells of the $d_{5/2}$ are down-slopping in the oblate side. Contour lines also open in the negative parity channel for $\beta \sim 0.5$. As we will see, this is due to the possibility of making a hole in the $p_{1/2}$ sub-shell on the oblate side.

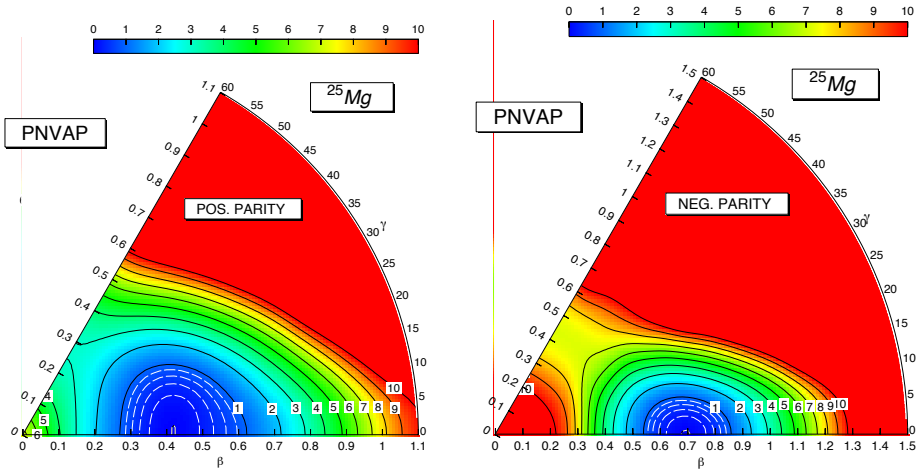

Figure 12.1: PN-VAP potential energy surfaces for positive and negative parity. Black contours are plotted in steps of 1 MeV and white dashed lines in steps of 0.2 MeV

We can also use the canonical basis $\{\tilde{a}_\rho, \tilde{a}^\dagger_\rho\}$ determined by transformation D (eq 3.7) to study some properties of the resulting blocked levels. In this basis the w.f. is written;

$$|\tilde{\phi}\rangle^\pi = \tilde{a}^\dagger_{b_\pi} \prod_{k\neq b} (u_k + v_k \tilde{a}^\dagger_k \tilde{a}^\dagger_{\bar{k}})|-\rangle \tag{12.1}$$

where b_π is the blocked level with parity π. We can study useful properties of the resulting level by calculating different matrix elements; for the third component of the total angular momentum; J_z (which mixes states with different signature):

$$\Omega^{blocked} = \langle -|\tilde{a}_{b_\pi} \hat{J}_z \tilde{a}^\dagger_{\bar{b}_\pi}|-\rangle \tag{12.2}$$

the third component of the total orbital momentum L_Z :

$$\Lambda^{blocked} = \langle -|\tilde{a}_{b_\pi} \hat{L}_z \tilde{a}^\dagger_{\bar{b}_\pi}|-\rangle \tag{12.3}$$

Also we can calculate the mean J value;

$$\langle J^{blocked} \rangle = \sqrt{\langle - | \tilde{a}_{b_\pi} \hat{J}^2 \tilde{a}^\dagger_{b_\pi} | - \rangle} \tag{12.4}$$

We can compare these values with the relevant Nilsson orbitals $\nu = |N n_3 \Lambda \Omega\rangle$ (where N (n_3) are the total(third component) oscillator quanta). Although this analysis is valid in the axial symmetry regions only, mean values on the rest of the γ region can give us valuable information about how triaxiality affects the evolution of the different orbitals and band crossings.

For positive parity there are three relevant Nilsson orbitals namely [202 5/2], [211 1/2] and [200 1/2] . The first one is expected to predominate at smaller deformations. Its $\Omega(\Lambda)$ projections are 2.5 and 2 respectively and its total angular momentum is 2.5. These values are obtained for deformations $0.1 \leq \beta \leq 0.5$. For higher deformations the level [211 1/2] crosses the [202 5/2], and the blocked level corresponds now to this orbit. The Ω value is now pure 1/2. The orbital angular momentum is ~ 1 as expected.

In the negative parity channel we also see two different blocking possibilities. For small deformations it is economically favored to have a hole in the $p_{1/2}$ sub-shell. This leads to a rather small value of the total angular momentum value and a nearly $\Lambda \sim 1$. However, for large deformations a particle in the [330 1/2] orbit is energetically favored due to the down-sloping character of this orbital. As a consequence the orbital angular momentum drops to zero, while the total angular momentum becomes larger. This last assumption is also supported with fig 12.2 where we plot the average number of neutrons

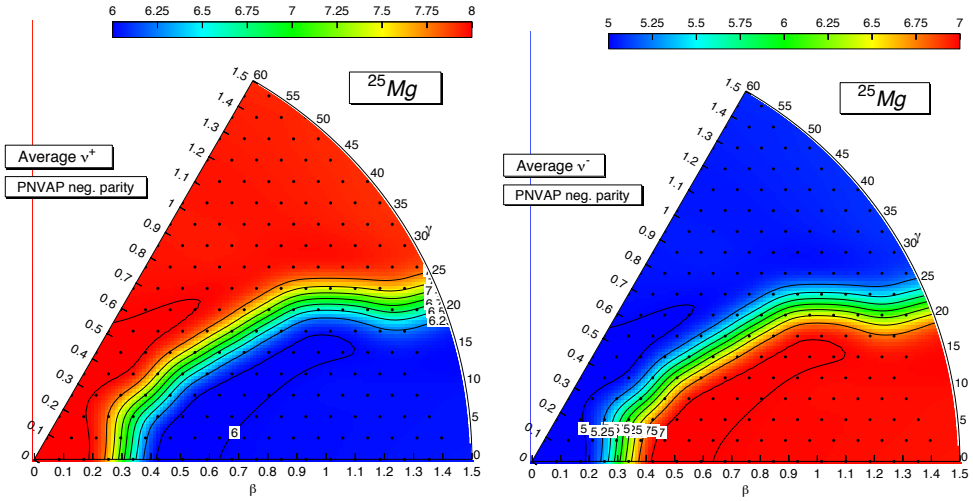

Figure 12.2: Average value of the number of neutrons of positive (left) and negative parity (right) when blocking on the negative parity channel

with positive (negative) parity; i.e. $\langle\tilde{\phi}|\hat{N}_+|\tilde{\phi}\rangle$ ($\langle\tilde{\phi}|\hat{N}_-|\tilde{\phi}\rangle$) . For β near 0 and for big γ (this means near oblate) we have 8 neutrons with positive parity and only 5 with negative parity (4 in the $p_{3/2}$ sub-shell and only one in the $p_{1/2}$ sub-shell). However, for large deformations and γ far from the oblate part the $p_{3/2}$ and $p_{1/2}$ shells are full, and the single neutron sits in the $f_{7/2}$, giving a total number of 7 neutrons in the negative parity channel.

12.1.2 Pairing energy

On Fig 12.3 we show the pairing energies for a PN-projection before variation (PNVAP) approach, which is the one used here, and for a PN-projection after projection. The energies in the latter are drastically lowered, dropping to zero in many β, γ points. The behaviour of the pairing correlations has been studied with the Gogny force [1]. In case of no pairing correlations (for

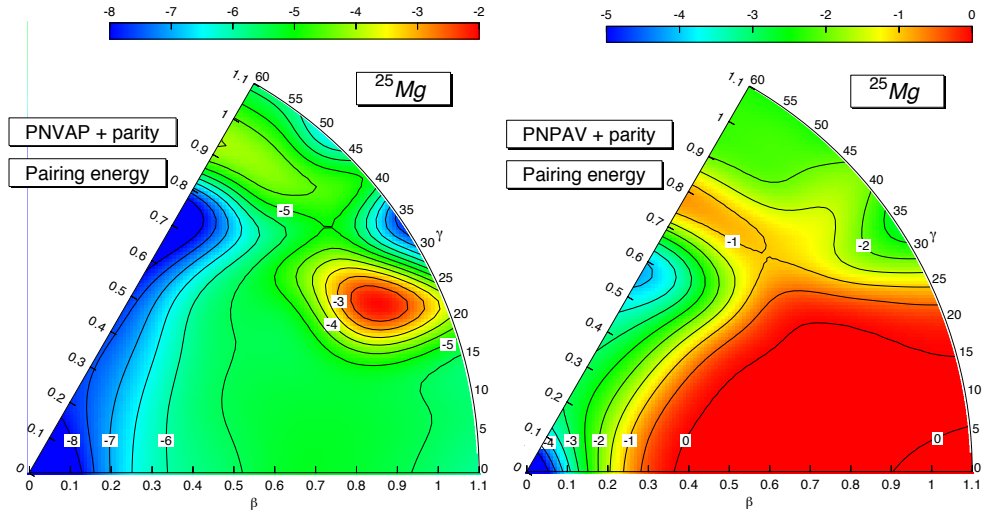

Figure 12.3: Pairing energies on the positive parity channel for two different calculations. On the left the PN-VAP approach and below the ones of a PN-PAV approach. Contours are plotted in steps of 1 MeV.

example in a shell closure) or weak pairing regimen, the HFB w.f. collapses to the HF one, and the subsequent projection does not provide a better approximation. Therefore a VAP calculation in case of particle number is very important.

12.2 Angular Momentum PES

With the β, γ constraints the general wave function 6.67 is given by;

$$|\Psi_{\sigma}^{NZ;I,M;}\rangle = \sum_{\beta,\gamma,K} f_{K\sigma}^{I}(\beta,\gamma)|\Phi^{NZ;IMK}(\beta,\gamma)\rangle \tag{12.5}$$

In 6.78 we defined the probability density of finding a given I, K and con-

straints β, γ, which is the collective wave function;

$$F_{\sigma}^{I\pi}(\beta,\gamma) = \sum_{\mu K} g_{\mu\sigma}^{II\pi} u_{\mu}^{NZ,II\pi}(\beta,\gamma,K) \tag{12.6}$$

The GCM states -Eq. 12.5- recover the broken symmetries in the HFB approach and mixes different configurations (β, γ). Again, we can stop in the "step two" studied in chapter 6, giving a simplified Ansatz just fixing a given (β, γ) value and mixing only in K as to recover the symmetries to calculate the PN-AM projected energy in each point of the (β, γ) plane and plot potential energy surfaces (PESs).

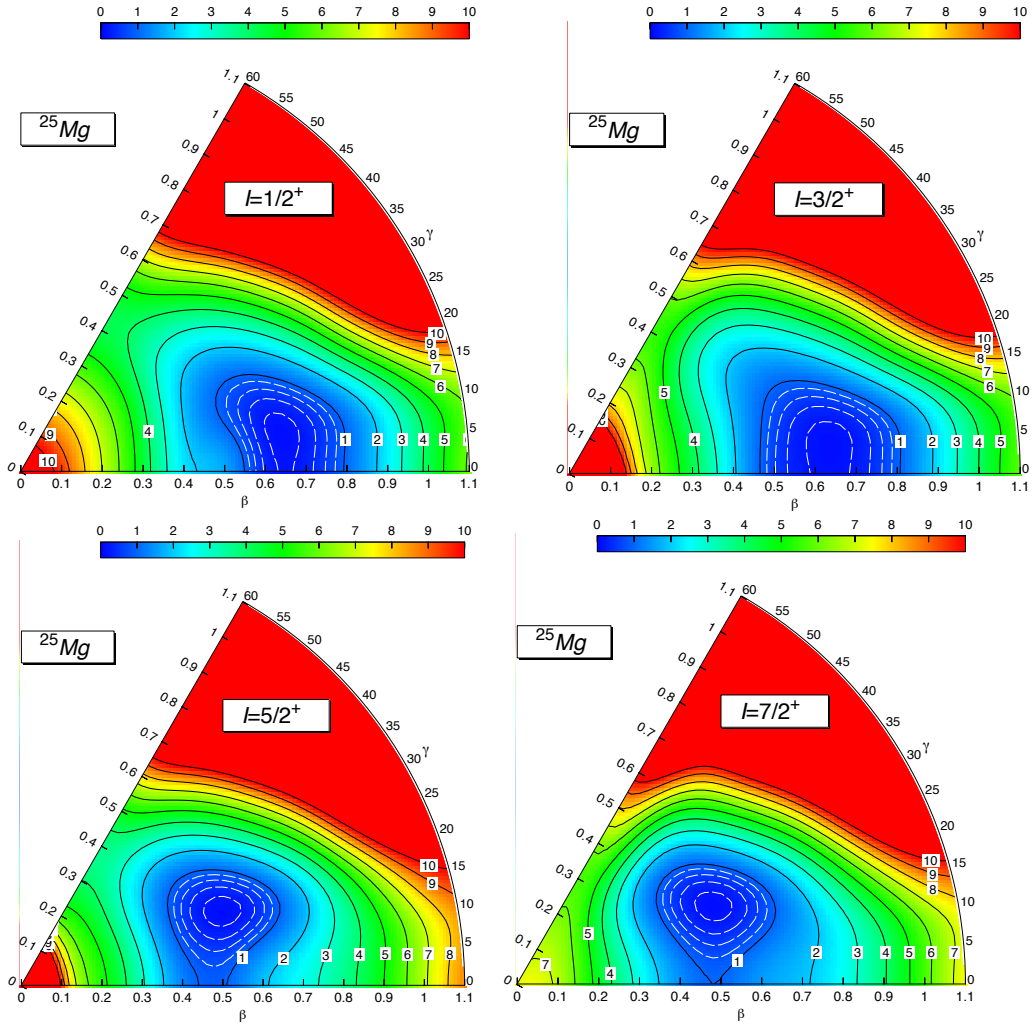

Figure 12.4: Potential energy surfaces of the AMP calculation for low lying I-staets of positive parity. Black contours are plotted in steps on 1 MeV . Dashed white lines are in steps of 0.2 MeV. In each parity the energy origin has been chosen independently and the energy minimum has been set to zero.

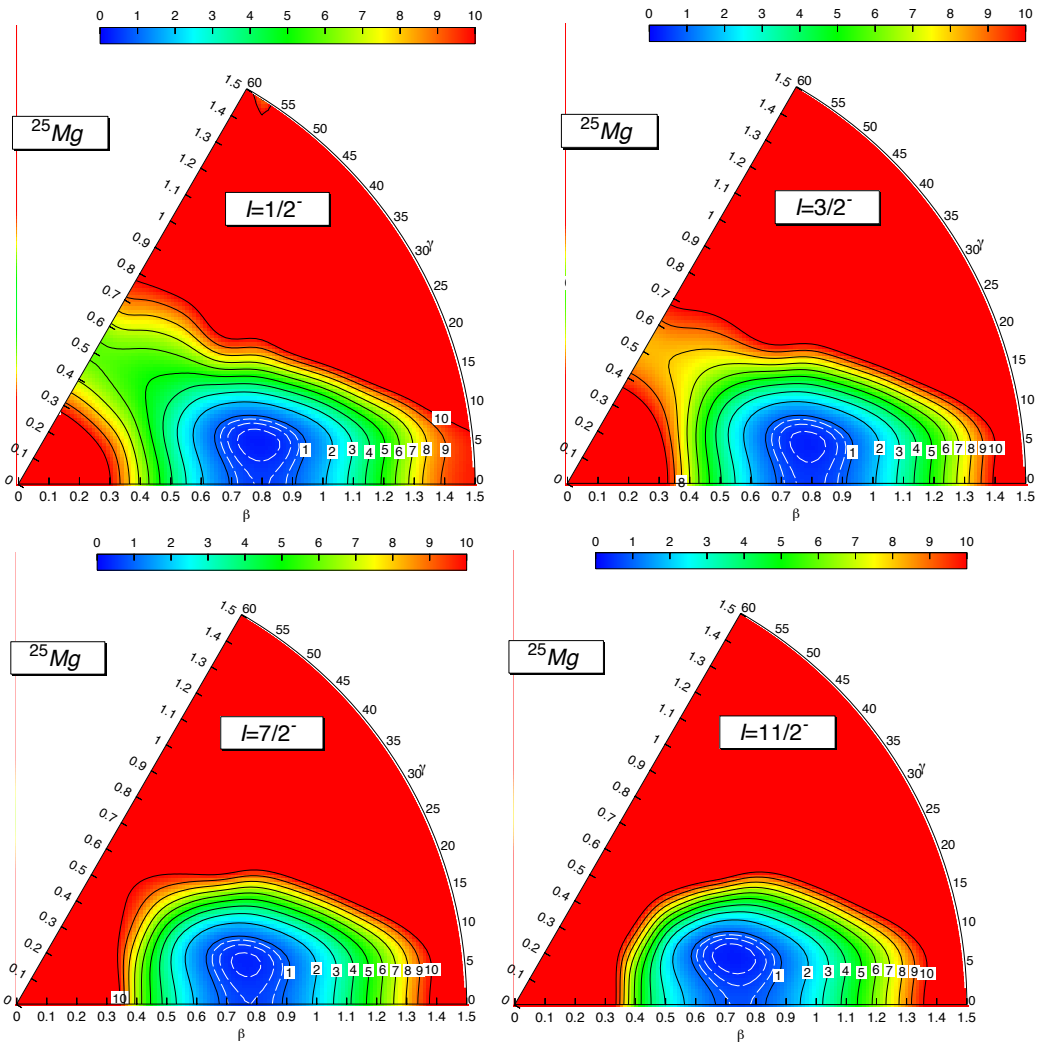

Figure 12.5: Potential energy surfaces of the AMP calculation for low lying I-states of negative parity. Black contours are plotted in steps on 1 MeV. Dashed white lines are in steps of 0.2 MeV. In each parity the energy origin has been chosen independently and the energy minimum has been set to zero.

Figures 12.4 and 12.5 show the Projected Energy Surfaces (PES) for the four low I - states of both parities. The absolute minimum corresponds to $I =$

$5/2^+$, followed by $I = 1/2^+, 3/2^+, 7/2^+$ with energies 0.637MeV,1.023MeV and 1.522MeV respectively. For the negative parity ones the lowest is $I = 3/2^-$ which is at $3.567MeV$, followed by $I = 7/2^-, 1/2^-, 11/2^-$ at 4.228MeV, 4.605MeV, 6.131MeV .

In the positive parity channel we find two clear different behaviours. For $I \geq 5/2$, the minimum is displaced to triaxial shapes and smaller deformations, while for $I < 5/2$ the nucleus is more deformed. This is understood from the Nilsson model. For smaller deformations it is energetically favored to fill the $d_{5/2}$ shell (which is pure $j = 5/2$), but as this orbital is up-sloping, as soon as it crosses the $s_{1/2}$, the latter configuration becomes favoured.

In the negative parity the minimum is also displaced to $\gamma \neq 0$. Contrary to the positive parity channel, the minimum is obtained at the same point for all I . The higher deformation of this channel can also be understood with the Nilsson diagram; i.e. due to the band-cross of the [330 1/2] state at big β. We note that only $1/2^-, 3/2^-$ contour lines open on the oblate side. As we saw in Section 12.1, this corresponds to a hole in the $p_{1/2}$ sub-shell. This sub-shell is a combination of values $j = 1/2, 3/2$, so making a state with $I > 3/2$ is energetically expensive.

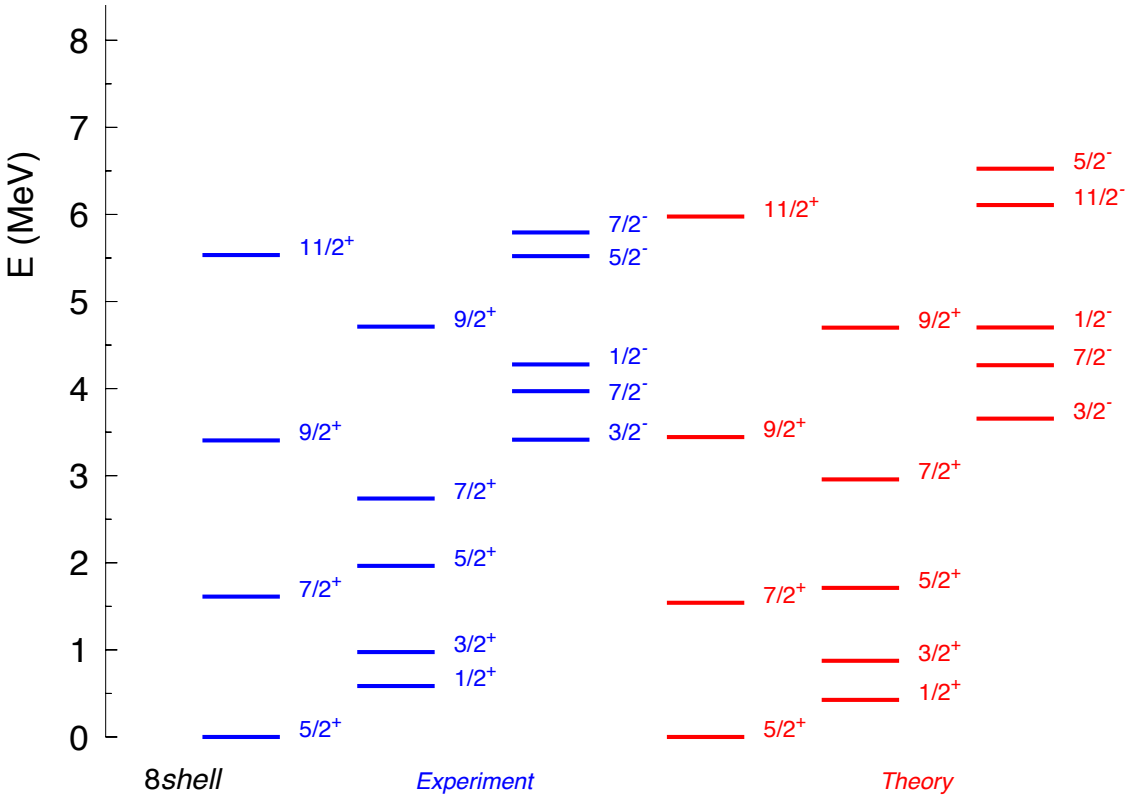

Figure 12.6: Spectrum of ^{25}Mg for positive and negative parity. Experimental data is taken from [2]

12.3 SCCM approach

12.3.1 Configuration mixing

Now we proceed to perform the last step of chapter 6, which consist on mixing the wave functions for different deformations. The solution of Eq. 6.68 provides the energy levels and the w.f.s. The transition probabilities [3, 4] and the shapes of the w.f.s allow to order the energy levels into bands as shown in Fig. 12.6.

From the PESs we can estimate which deformations will play a more important role in the description of the low lying states. As the configuration mixing implies the calculation of $N(N+1)/2$ overlaps (being N the number of w.f. used) it is important to reduce the dimension as much as possible. States with big $y = \beta \sin\gamma$ have high energies so they are expected to mix quite little. Therefore we have chosen a grid of 81 w.f. in the positive channel with $y \leq 0.45$ for the whole β range $0 \leq \beta \leq 1.1$.

In the negative parity channel, projecting to shapes close to sphericity is very expensive, so apart from the condition $y \leq 0.45$ we use a grid $0.4 \leq \beta \leq 1.4$, which gives a total of 95 w.f.

The final spectrum obtained for the first two bands of positive parity and the first of negative parity is shown, together with experimental data, in Figure 12.6 . A more complete spectrum is shown in fig 12.7 .

We have grouped these energy levels into bands with the help of the K-distribution, w.f. shapes and electromagnetic properties. Additionally we show in table 12.2 the average value of the deformation parameters (β, γ):

$$\bar{\beta}^{I\pi\sigma} = \frac{\sum_{\beta,\gamma} \beta \cdot P^{I\pi}_{K\sigma}(\beta,\gamma)}{\sum_{\beta,\gamma} \mathcal{P}^{I\pi\sigma}(\beta,\gamma)} \tag{12.7}$$

$$\bar{\gamma}^{I\pi\sigma} = \frac{\sum_{\beta,\gamma} \gamma \cdot P^{I\pi}_{K\sigma}(\beta,\gamma)}{\sum_{\beta,\gamma} P^{I\pi}_{K\sigma}(\beta,\gamma)} \tag{12.8}$$

where the probability $P^{I\pi}_{K\sigma}(\beta,\gamma)$ was defined in 6.48.

$$P^{I\pi}_{K\sigma}(\vec{q}) = |F^{I\pi}_{K\sigma}(\vec{q})|^2 \tag{12.9}$$

$I^{\pi}_{\sigma} \downarrow, K \rightarrow$	1/2	3/2	5/2	7/2	9/2	11/2
$5/2^+_1$	1.6	1.4	97.0	-	-	-
$7/2^+_1$	0.6	0.2	98.8	0.4	-	-
$9/2^+_1$	1.0	0.5	96.7	0.3	1.5	-
$11/2^+_1$	3.6	0.3	94.8	0.4	0.6	0.3
$1/2^+_1$	100	-	-	-	-	-
$3/2^+_1$	99.6	0.4	-	-	-	-
$5/2^+_2$	99.4	0.1	0.4	-	-	-
$7/2^+_2$	98.8	0.1	0.9	0.2	-	-
$9/2^+_2$	96.5	0.6	2.0	0.2	0.8	-
$11/2^+_2$	95.5	0.3	3.2	0.1	0.6	0.3
$1/2^+_2$	100	-	-	-	-	-
$3/2^+_3$	96.5	3.5	-	-	-	-
$5/2^+_3$	91.3	6.1	2.6	-	-	-
$7/2^+_3$	94.6	1.9	2.9	0.6	-	-
$9/2^+_4$	80.2	8.6	9.8	0.7	0.7	-
$11/2^+_4$	87.6	3.2	8.0	0.3	0.5	0.3
$9/2^+_3$	0.8	0.3	1.0	0.2	97.6	-
$11/2^+_3$	0.7	0.1	1.5	0.1	97.6	0.1
$3/2^+_3$	2.2	97.8	-	-	-	-
$5/2^+_4$	2.9	93.1	4.0	-	-	-
$1/2^-_1$	100	-	-	-	-	-
$3/2^-_1$	98.9	1.1	-	-	-	-
$5/2^-_1$	93.2	6.5	0.2	-	-	-
$7/2^-_1$	96.5	3.5	0.0	0.0	-	-
$11/2^-_1$	94.6	5.3	0.1	0.0	0.0	0.0

Table 12.1: K-distribution of the different states

I^{π}_{σ}	$\bar{\beta}^{I\pi\sigma}$	$\bar{\gamma}^{I\pi\sigma}$
$5/2^{+}_{1}$	0.505	21.16
$7/2^{+}_{1}$	0.523	18.96
$9/2^{+}_{1}$	0.515	18.94
$11/2^{+}_{1}$	0.542	18.73
$1/2^{+}_{1}$	0.669	12.87
$3/2^{+}_{1}$	0.687	12.42
$5/2^{+}_{2}$	0.674	11.92
$7/2^{+}_{2}$	0.708	9.39
$9/2^{+}_{2}$	0.666	11.75
$11/2^{+}_{2}$	0.728	8.28
$1/2^{+}_{2}$	0.639	23.66
$3/2^{+}_{3}$	0.638	22.72
$5/2^{+}_{3}$	0.665	20.39
$7/2^{+}_{3}$	0.630	23.27
$9/2^{+}_{4}$	0.659	19.26
$11/2^{+}_{4}$	0.630	20.83
$9/2^{+}_{3}$	0.592	26.72
$11/2^{+}_{3}$	0.604	24.88
$3/2^{+}_{3}$	0.699	22.65
$5/2^{+}_{4}$	0.684	23.01
$1/2^{-}_{1}$	0.779	8.45
$3/2^{-}_{1}$	0.767	9.04
$5/2^{-}_{1}$	0.779	9.37
$7/2^{-}_{1}$	0.755	9.81
$11/2^{-}_{1}$	0.744	10.51

Table 12.2: $\bar{\beta}^{I\pi\sigma}$ and $\bar{\gamma}^{I\pi\sigma}$ of the different states

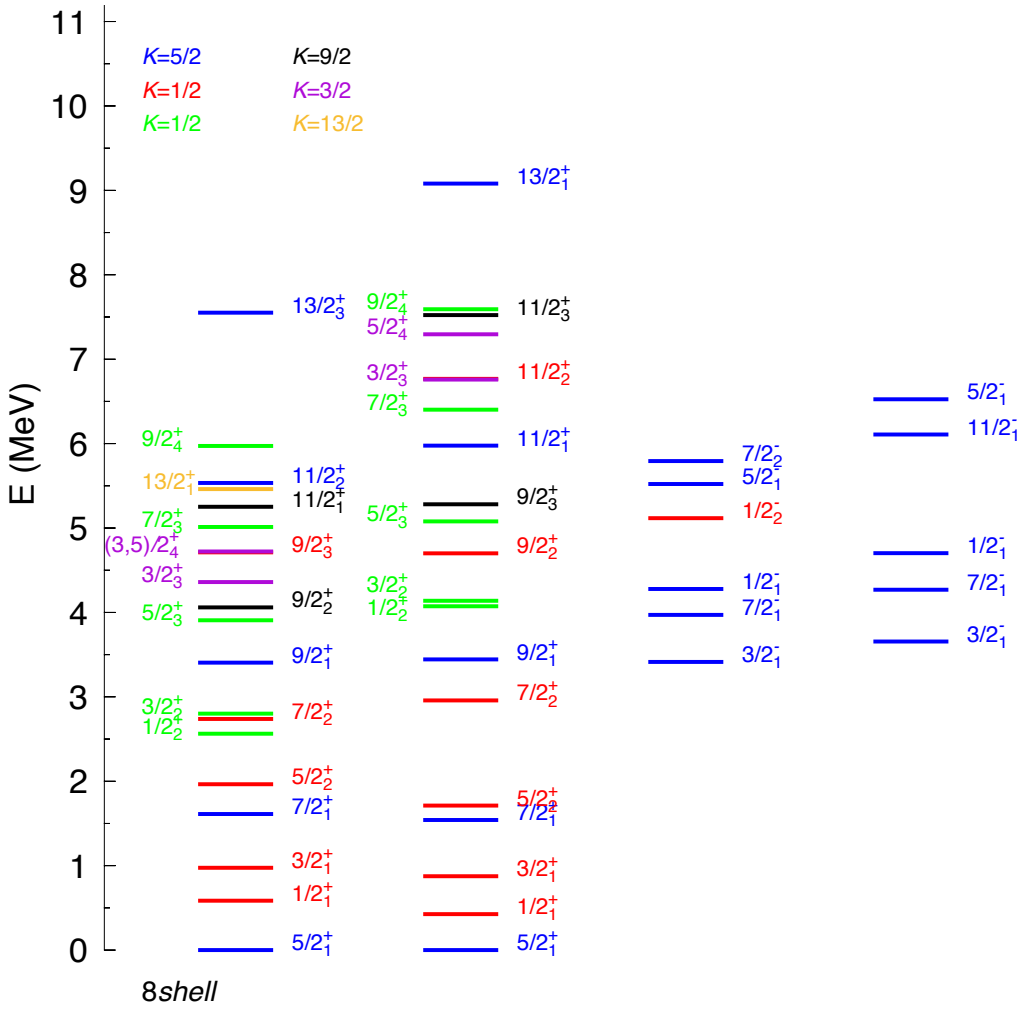

Figure 12.7: Complete spectrum

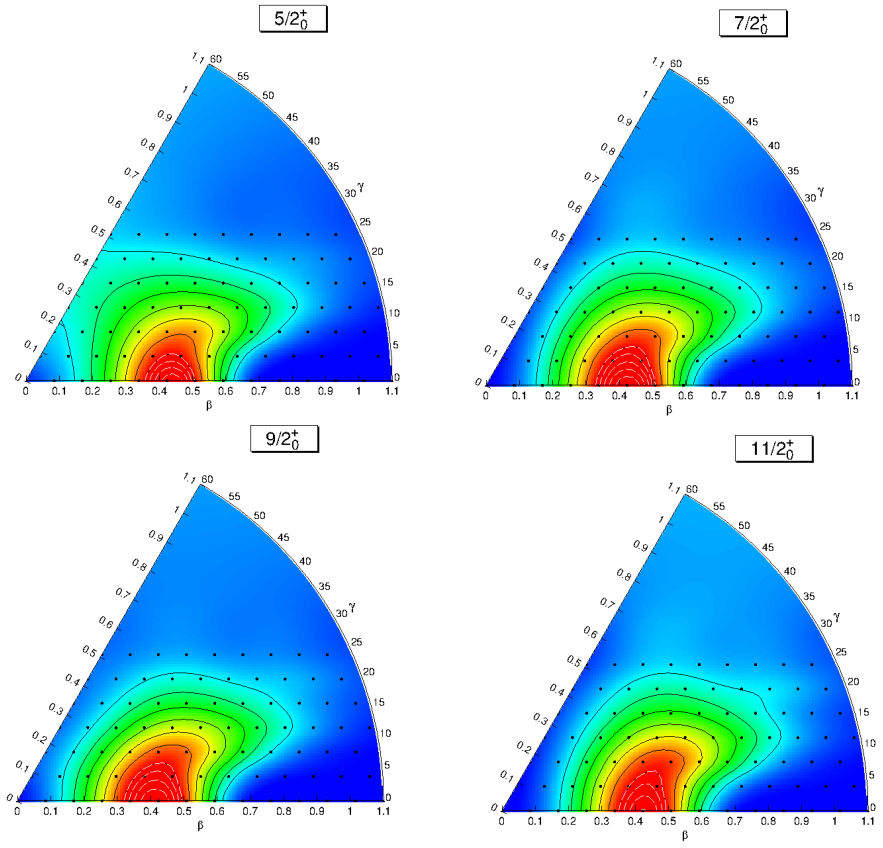

Figure 12.8: Collective w.f.s in the (β, γ) plane for the ground band.

The interpretation is also done with the help of table IV of Ref [5].

For positive parity we find 5 bands.

The ground band corresponds to a particle in the [202 5/2] Nilsson orbit. The interplay between of particles and the collective rotation is described by the Particle-plus-Rotor Model (PR) [6]. We can divide a phenomenological Hamiltonian in a collective part which describes the rotation of the inert

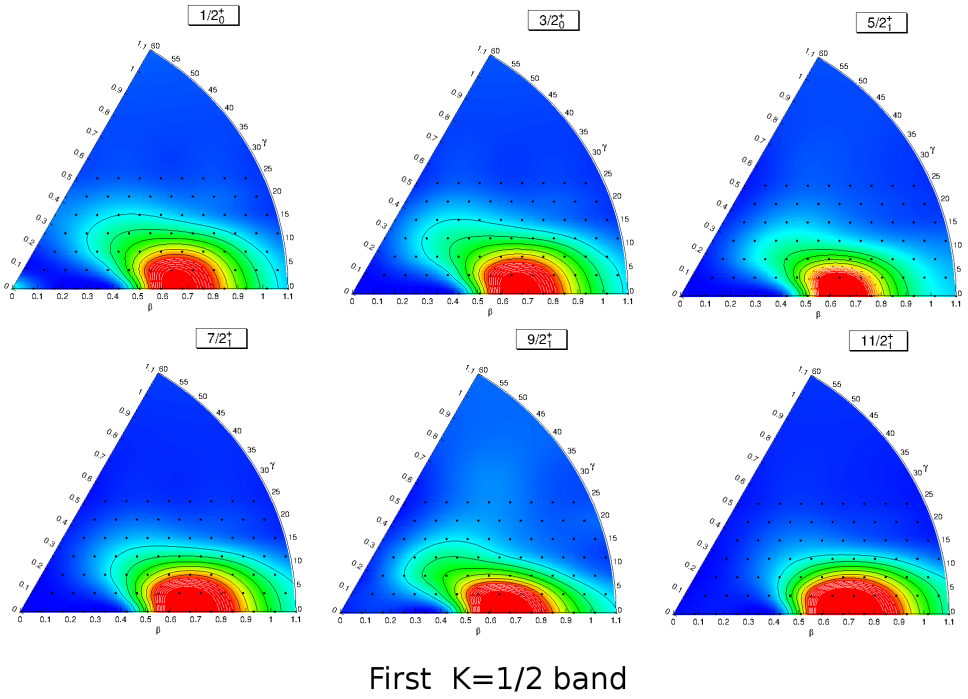

Figure 12.9: Collective w.f.s in the (β, γ) plane for the first $K = 1/2$ band.

core, and an intrinsic part, which describes the single-particle energies in the deformed potential. Due to the big deformation we expect to be in the strong coupling limit (where the angular momentum of the valence particle is strongly coupled to the motion of the core). In this limit $K = \Omega$ is a good quantum number which is clearly supported by results shown in table 12.1. We believe this purity, which has also been observed for even-even nuclei, is due to the low level density of this light nuclei. Therefore, in spite of the large triaxiality, mixing of states with different K requires a lot of energy.

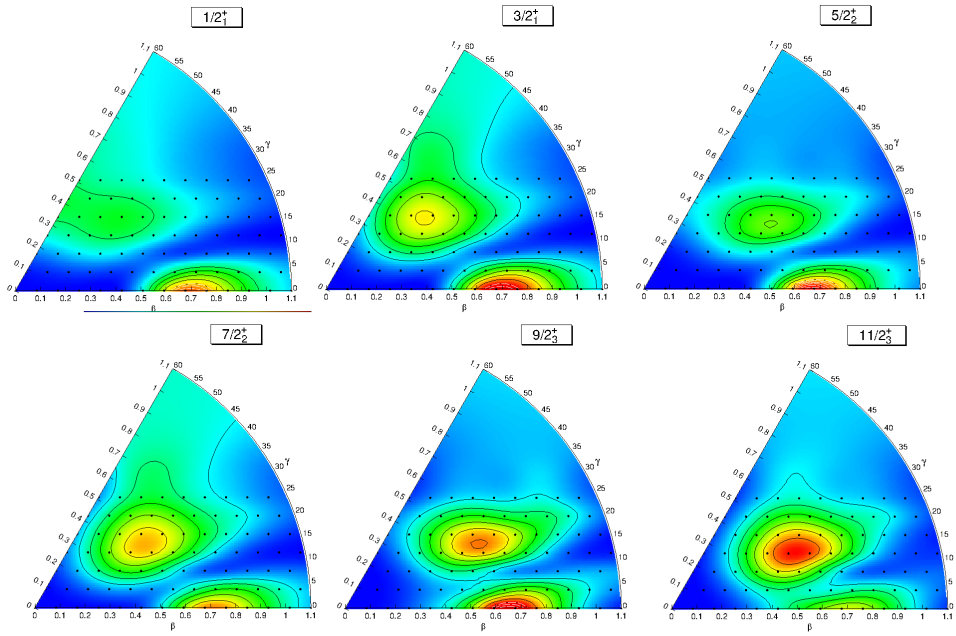

Figure 12.10: Collective w.f.s in the (β, γ) plane for the $K = 1/2\gamma-$band..

The energy in the strong coupling limit is given by [7]:

$$\begin{aligned} E^I_K &= \epsilon^i_k + A(I(I+1) - K^2) \quad K \neq 1/2 \\ E^I_K &= \epsilon^i_k + A(I(I+1) - \frac{1}{4} + \\ &+ a^i(I+1/2)(-1)^{I+1/2}) \quad K = 1/2 \end{aligned} \tag{12.10}$$

where ϵ^i_k are the quasi-particle energies,$A = \frac{1}{2\mathcal{I}}$ with $\mathcal{I}$ the moment of inertia

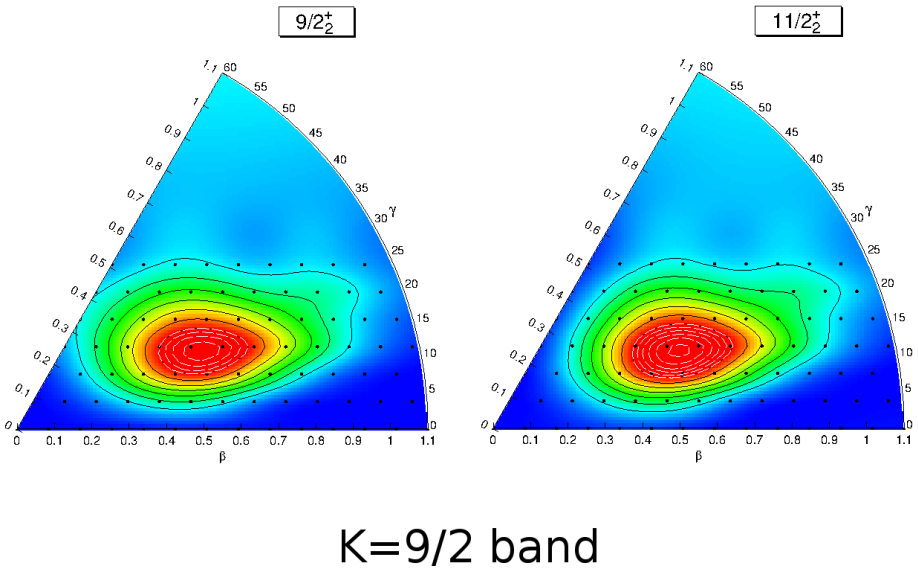

Figure 12.11: Collective w.f.s in the (β, γ) plane for the $K = 9/2$ band.

and a^i is the so-called decoupling factor:

$$\begin{aligned} a^i &= i\langle\Phi^i_{K=1/2}|j_+ e^{-i\pi j_x}|\Phi^i_{K=1/2}\rangle \\ &= |C^i_{nj}|^2(-1)^{j+\frac{1}{2}}(j+\frac{1}{2}) \end{aligned} \tag{12.11}$$

The C^i_{nj} are the coefficients of the decomposition of $\Phi^i_{K=1/2}$ into eigenstates of the total angular momentum $\hat{J}^2$; i.e. $|\Phi^i_{K=1/2}\rangle = \sum_{nj} C^i_{nj}|nj\Omega = K\rangle$. A fitting to this formula is shown in Fig 12.13 for theoretical and experimental results. The value of theoretical and experimental moment of inertia are very close (2.26 ± 0.03 and 2.45 ± 0.06 respectively). The first is a little smaller than the latter, giving a more stretched spectrum. This is also seen in even-even nuclei. However, this can be improved with the inclusion of the

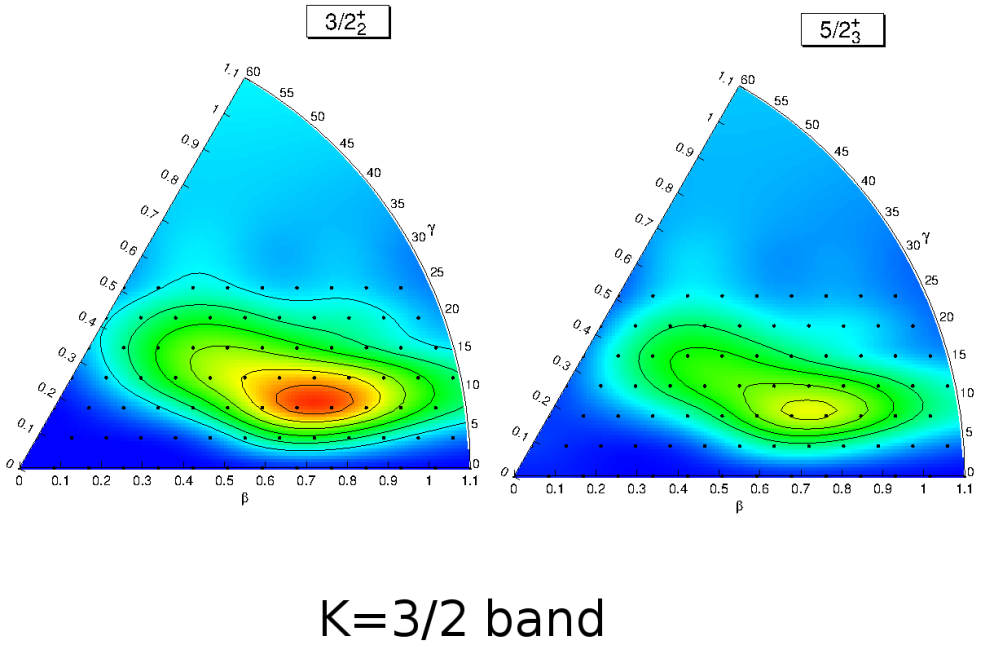

Figure 12.12: Collective w.f.s in the (β, γ) plane for the $K = 3/2$ band.

cranking term [4]. The w.f. shape 12.8 shows a "prolate" form with $\bar{\beta} \sim 0.51$.

The first excited band is interpreted as a particle in the [211 1/2] and, as we expected from Nilsson diagram and AMP-PESs, it is more deformed that the ground state band ($\bar{\beta} \sim 0.67$). Again is a pure K band, in this case $K = 1/2$. Using formula 12.10 and fitting the different parameters we obtain fig. 12.14. The inertial parameter is bigger than the one in the ground state band due to its bigger deformation. For the same reason mentioned above, the theoretical value is again a little smaller than the experimental one (2.75 ± 0.04 vs experimental 3.09 ± 0.06). The decoupling factor is quite small in the experimental being absent in the theoretical calculation. Note

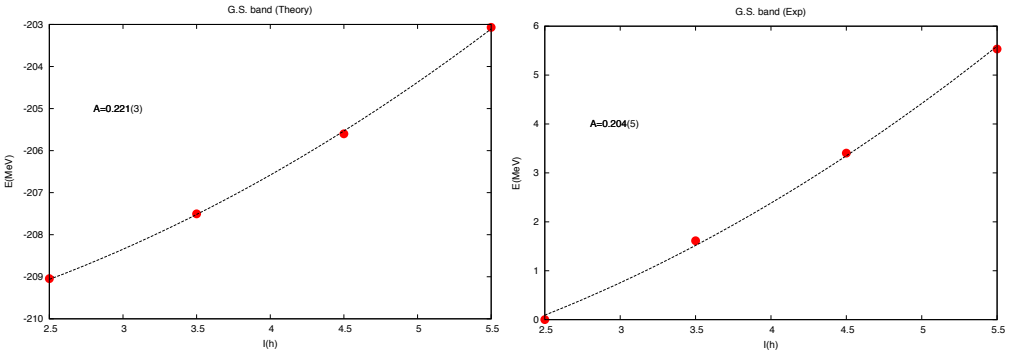

Figure 12.13: Fitting the ground band energy to equation 12.10 for theoretical and experimental results

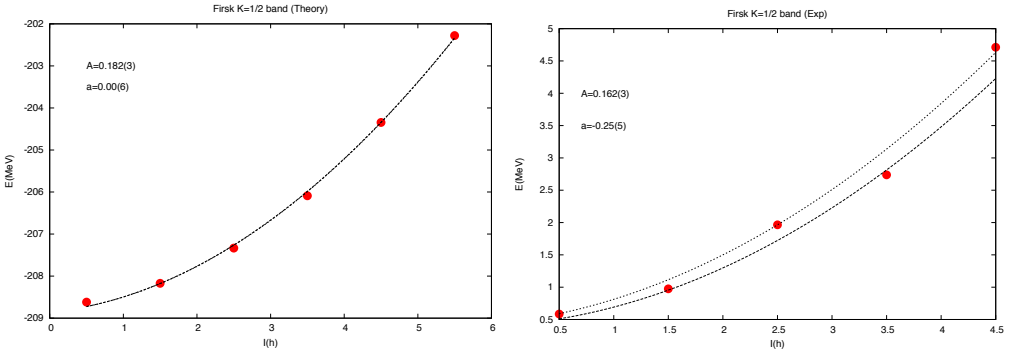

Figure 12.14: Fitting the first K=1/2 band energy to equation 12.10 for theoretical and experimental results

that, as seen in 12.11, the decoupling parameter is intimately related to the state of the odd nucleon in the spheroidal nucleus. A small change in its components modify the a^i value substantially.

The agreement of our data with experiment is very good, although the absence of the decoupling factor in our approach makes levels $1/2^+, 5/2^+$ quite deep and levels $3/2^+, 7/2^+$ too high in energy in comparison with experimental data.

The next positive band is also predominately $K = 1/2$ but it is more mixed

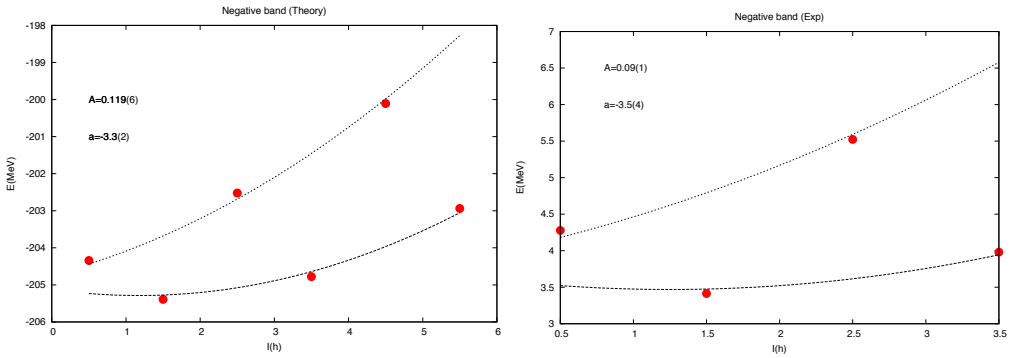

Figure 12.15: Fitting the negative parity band to equation 12.10 for theoretical and experimental results

than the previous ones, especially for states $I \geq 7/2$. We interpret this band as a $(K-2)_\gamma$ on the [202 5/2] state. This is supported by the electromagnetic properties (see section 12.4) The band-head is found at a higher energy than the experimental one. In [5] this state is interpreted as a mixture of two configurations; the $(K-2)_\gamma$ on the [202 5/2] state and a possible particle in the [200 1/2] orbit. In our PN-VAP approach we only take the quasiparticle state that minimizes the energy for each deformation. Thus, the absence of other configurations (such as this [200 1/2] state) results on a increased energy of this band. *Note that this does not happen in the first excited band, as its configuration is found at a "totally" different β, γ point than the fundamental one, and therefore both configurations are equally well described at PN-VAP level.

The fourth and fifth bands are pure $K = 9/2$ and $K = 3/2$. Because of their shapes and $\bar{\beta}$ deformations they can be interpreted as $\gamma-bands$ on the states mentioned above. The less deformed one, i.e., the $K = 9/2$, is interpreted as a $(K+2)_\gamma$ on the [202 5/2] state, also supported by the electromagnetic

properties, while the $K = 3/2$ as a $(K-2)_\gamma$ on the [211 1/2] Nilsson state. For the same reason mentioned above, these bands are found at a higher energy than expected.

Finally we notice a $13/2^+$ state only present in the experimental data. This is an aligned state in the "x" direction [8]. As we have not considered cranking here (and the corresponding treatment of the other two sextants) that state does not appear in the theoretical calculations. However, we tested this with a PNAMP-calculation (without β, γ mixing): i.e only K-mixing, including this cranking term and all three sextant and we found this state.

In the negative parity channel the ground band corresponds to filling the state [330 1/2] with a particle. As a consequence of the high value of the decoupling parameter the band is very distorted, being the state with $I = 3/2$ the lowest one. The strength of the decoupling parameter increases when levels with large single-particle angular momenta are involved, as in this case $J = 7/2$. Our value (-3.3) is similar to the experimental-fitted one (-3.5) as seen in figure 12.15. As in the positive parity channel, the fitting gives a higher moment of inertia for this band. Experimentally is 5.5 ± 0.6 and the theoretical result 4.1 ± 0.2, leading to a stretched spectrum. The first three states are very well described but the $5/2^-$ is already too high in energy. The state $7/2^-$ was identified either with a $11/2^-$ or a $7/2^-$ for a long time. Nilsson model predicts a $11/2^-$ state. However, due to a measured M1 transition to the first $7/2^-$, the $11/2^-$ was discarded. It is possible that we missed this state (as we missed the $13/2^+$) because of the absence of cranking and the two other sextants. However we also performed a PNAMP-

calculation in this negative parity channel (without configuration mixing) including cranking and three sextants and we do not find this state, so we discard this state as an aligned sate. Other explanations would be that this is a state described by a higher number of quasi-particle states , or maybe an incorrect M1 assignment for the transition to the fist $7/2^-$.

12.4 Magnetic properties

12.4.1 Electromagnetic transitions

Finally, in figure 12.16 the B(E2) and B(M1) values are shown. In general the experiment is well described, being the B(E2) values slightly overestimated. This is also seen in even-even nuclei and is due to the fact that we get too large deformation. We showed in this work that the addition of the cranking term reduces these values [9]. For transitions between states of the same K value we obtain:

$$B(E2, I_i \rightarrow I_f) = Q_0^2 \frac{5}{16\pi} |C_{K0K}^{I_i 2 I_f}|2 \tag{12.12}$$

In Fig 12.17 we represent with filled circles the BE2 transition normalized to the transition $7/2 \rightarrow 5/2$ for the ground state band and the first K=1/2 band. With empty boxes we represent the values according to eq 12.12. It is again clear that the particle plus rotor model provides a very good description for this two bands. Using this formula for the ground state band we can extract a value for the intrinsic quadrupole moment. We obtain values between $59e^2fm^2$ and $67e^2fm^2$. Using the experimental data available we obtain

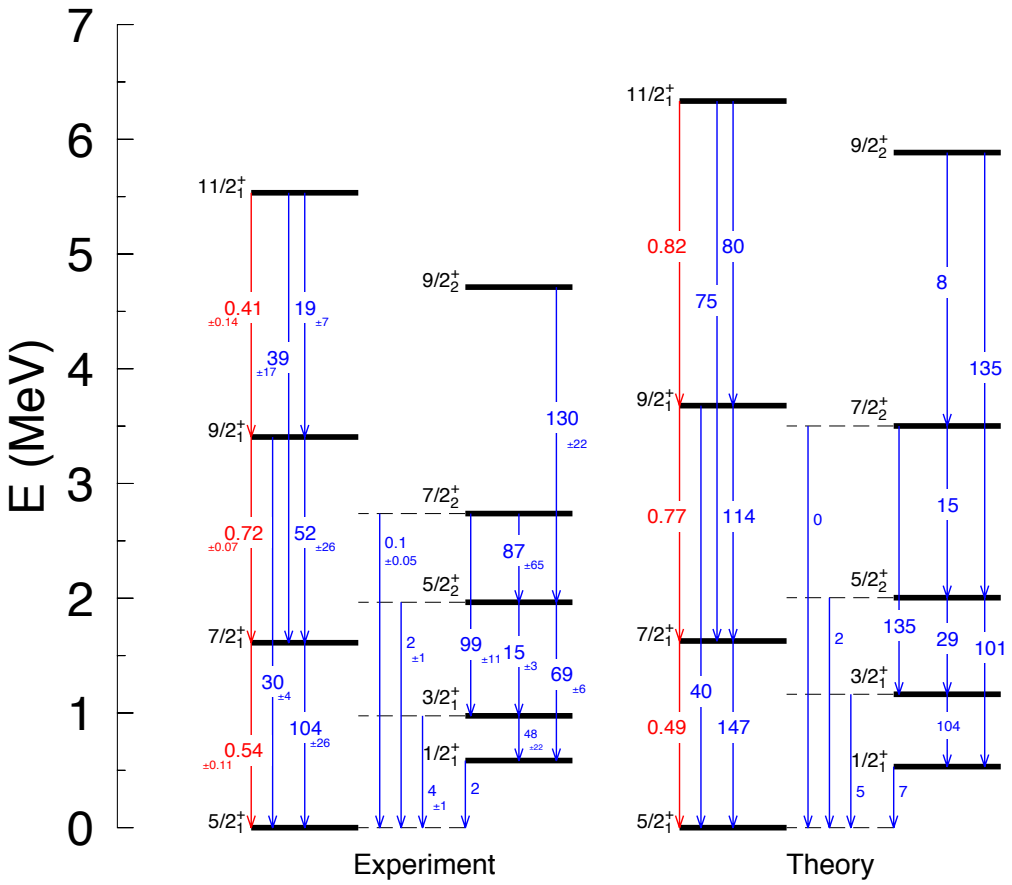

Figure 12.16: Experimental and theoretical values of transions inter and intra the two lowest bands

Figure 12.17: BE2 transition normalized to the transition $7/2 \rightarrow 5/2$ for the ground state band and the first K=1/2 band. With empty boxes we represent the values according to eq 12.12.

values between $40e^2fm^2$ and $55e^2fm^2$, but as the error in the measured values is too large, again smaller as in previous results.

For the first $K = 1/2$ band we obtain bigger values (more deformation), also in agreement with previous sections (around $68 - 73e^2fm^2$).

12.4.2 Quadrupole moment

The quadrupole moment is calculated as:

$$Q(I\sigma) = \sqrt{\frac{16\pi}{5}} \begin{pmatrix} I & I & I \\ I & 0 & -I \end{pmatrix} \langle \Psi^{N,I,\pi}_{M,\sigma} || \hat{M}^{elec}_{2} || \Psi^{N,I,\pi}_{M,\sigma} \rangle$$

where $\hat{M}^{elec}_{2\mu} = erY_{2\mu}(\Theta\phi)$ are the electrical quadrupole moment operators. For a pure $|K|$-band it takes the form:

$$Q(I,K) = Q_0 \frac{3K^2 - I(I+1)}{(I+1)(2I+3)} \tag{12.13}$$

with Q_0 the intrinsic moment macroscopic state. In Fig 12.18 we represent with filled circles the spectroscopic quadrupole moment normalized to a reference value. Each colour corresponds to one of the five different bands. The reference value is $I_{ref} = 5/2$, for the $K = 5/2$ band, $I_{ref} = 3/2$ for $K = 1/2$ and $K = 3/2$ bands and $I_{ref} = 9/2$ for $K = 9/2$ band. The empty boxes represent the values expected according to eq 12.13. On the top panel the values obtained in our calculation and on the bottom panel the shell model results with the USD interaction. In our pnvap-pnamp approach the ground band clearly follows the trend of the model. The first excited band also follows it, however the values of $I = 5/2, 9/2$ are a little lower than expected. This effect is seen clearer in the second $K = 1/2$ band. We notice also that the most deviated value is $I = 9/2$, which can be a consequence of more mixing between bands for this I-value. The last

two bands also reflect the $Q(I,K)$ behavior. In the shell model calculation a lot of mixing takes place for $I \geq 9/2$. Notice the oscillating pattern of $K = 1/2$ also takes place in the shell model calculation. The relation of the quadrupole moment of a band and a gamma vibration on that band can be also extracted from expression 12.13. For a $K = 1/2$ gamma band on a $K = 5/2$ band we should obtain $\frac{Q(I,K=5/2)}{Q(I,K=1/2)} = -\frac{75-2I(2I+2)}{3-2I(2I+2)}$, which gives $-1.25, -0.2, 0.25, 0.49$ for $I = 5/2, 7/2, 9/2, 11/2$ respectively. In our calculation we obtain $-1.31, -0.16, 0.37, 0.44$ which confirms our interpretation of this band as a gamma band. For a $K = 9/2$ band on a $K = 5/2$ band the relation is $\frac{Q(I,K=5/2)}{Q(I,K=9/2)} = -\frac{75-2I(2I+2)}{243-2I(2I+2)}$, giving $-0.17, -0.68$ for $I = 9/2, 11/2$ respectively. In our calculation the values are $-0.19, -0.74$, confirming also the interpretation of the fourth band as a gamma vibration on the ground band. Finally, for the fifth band, interpreted as a gamma-vibration on the first K=1/2 band, we shoul have the following relation: $\frac{Q(I,K=1/2)}{Q(I,K=3/2)} = -\frac{3-2I(2I+2)}{27-2I(2I+2)}$, giving $-1.00, 4.00$ for $I = 3/2, 5/2$ respectively. In our calculation the values are $-1.00, 3.82$, confirming again the interpretation given.

12.5 Summary

We have presented the first application of a GCM calculation with angular momentum projected triaxial PN-VAP blocked states. The light nucleus ^{25}Mg was used to illustrate the method. We showed the reliability of the method comparing our results with other models as well as with the experimental data available.

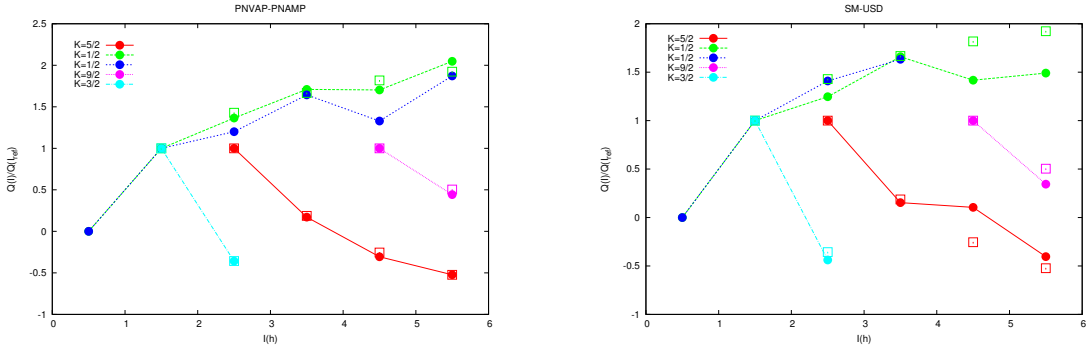

Figure 12.18: With filled circles the spectroscopic quadrupole moment normalized to a reference value. Each color corresponds to one of the five different bands. The reference value is $I_{ref} = 5/2$, for $K = 5/2$ band, $I_{ref} = 3/2$ for $K = 1/2$ and $K = 3/2$ bands and $I_{ref} = 9/2$ for $K = 9/2$ band. On the top panel the values in our calculation and on the bottom panel and in the shell model approach. Each color represent a different band. The empty boxes correspond to the values expected according to eq 12.13

We have shown the importance of the particle number projection before the minimization procedure in the pairing energy calculation, as well as in the blocked state determination.

The recovery of rotational invariance allows to describe the spectra of this nucleus satisfactorily. The inclusion of the cranking procedure may result in the compression of the slightly stretched spectra and in a reduction of the B(E2) transitions. Also,mixing other one quasi-particle states (or different number of quasi-particles) may lower the energy of the excited bands.

Bibliography

[1] M Anguiano, JL Egido, and LM Robledo. *Nuclear Physics A*, 696(3-4):467–493, 2001.

[2] http://www.nndc.bnl.gov.

[3] T. R. Rodríguez and J. L. Egido. *Phys.Rev. C*, 81:064323, 2010.

[4] Marta Borrajo, Tomás R. Rodríguez, and J. Luis Egido. *Physics Letters B*, 746:341 – 346, 2015.

[5] D. M. Headly et al. *Phys.Rev. C*, 38:1698, 1988.

[6] P. Ring and P. Schuck. *The nuclear many body problem*. Springer-Verlag, Berlin, 1980.

[7] Ben R. Mottelson Aage Bohr. *Nuclear Structure. Volume II: Nuclear Deformations*. World Scientific, 1998.

[8] J. Luis Egido, Marta Borrajo, and Tomás R. Rodríguez. *Phys. Rev. Lett.*, 116:052502, Feb 2016.

[9] M. Borrajo and J. L. Egido. *Acta Phys. Polon. Supp.*, 8(3):567–574, 2015.

Chapter 13

Conclusions

13.1 Summary of Thesis Achievements

Mean field approaches are a good starting point used to describe the nuclei structure. However, they are restricted to the description of global properties. The development of beyond mean field techniques allows to study properties such as nuclear spectroscopy and electromagnetic transitions. This work extends these theories in two directions. The first one is the inclusion of time reversal symmetry breaking states by means of the cranking procedure. The second is the extension of these approaches to the description of odd-A nuclei.

1. The addition of new degrees of freedom introduces different types of correlations which results not only in a good qualitative description, but also in a quantitative agreement with experimental data. In this

work we include time reversal symmetry breaking states adding a new generator coordinate; the cranking frequency, and preserving the nuclear deformations β, γ coordinates as well. The previous restriction of using only time reversal symmetry conserving states tended to favor those intrinsic states with no angular momentum content, leading to a stretched spectrum. The effect of including states with this new broken symmetry was first tested in the even-A nuclei of the Mg isotopic chain, where a noticeable compression of the spectrum was obtained, leading to an excellent agreement with experimental data.

The inclusion of cranking open also the possibility to describe new states which correspond to aligned configurations. In particular the recently measured 4^+ isomer of the ^{44}S nucleus was correctly predicted by our theory.

This new degree of freedom increases the CPU time substantially. We also propose in this work an approximation which reduces the computational effort. It consists on the reduction the number of wave functions used in the generator coordinate method by including only β deformation and cranking frequency as generator coordinates and using the self-consistent γ deformation. With this approximation not only the excitation energy of the 2^+ states were put close to the experimental ones but also the electromagnetic probabilities $B(E2)$ from the 0^+ to the 2^+ states were reduced, in agreement with experimental data.

2. The second development of this work consists on the application of this mechanism to odd-A nuclei. Up to now these developments had

taken place in even nuclei and it seemed natural to extend this to odd-even ones. We applied a self-consistent theory with exact blocking and particle number and angular momentum projection to study the ground properties of the odd an even isotopes of Mg. We obtain an outstanding description of binding energies, odd-even mass differences, mass radii and electromagnetic moments.

Not only ground state properties are well described in our approach. We performed a detailed study of the ^{31}Mg nucleus at the border of the N=20 inversion island where ground state properties and excited states, as well as transition probabilities were studied obtaining a good agreement with the current experimental data.

Finally, the most general configuration mixing approach was carried out in the ^{25}Mg nucleus where the β, γ deformations were used as generator coordinates. We obtained a quantitative agreement with the experimental data in the first bands of positive and negative parity as well as a qualitative agreement in the rest of the bands. These bands are identified by means of the collective wave functions and the transition rates, which are also in good agreement with the current measured values.

13.2 Future applications

The techniques developed in this work can be used to study other kind of systems such as;

1. Even-A systems with odd-N and odd-Z number. In these systems a rich study can be done due to the different possibilities in the blocking channels; i.e. we can obtain positive parity states by blocking both a proton and a neutron in the positive parity channel or in the negative parity one. Negative parity bands are obtained by blocking protons and neutrons in different parity channels.

2. The use of cranking in odd systems would remove the degeneration in the simplex channel, opening the possibility to find new states.

3. Use the cranking procedure to obtain a ore accurate spectrum an also find aligned states, as we did in the ^{44}S nucleus.

13.3 Future Work

Although the complexity of our approximations and the improvements done so far, future work in this field can be done. The first improvements are related to the increasing of the variational space in order to include more correlations:

1. Inclusion of *different* quasi-particle states for a *given* value of the generator coordinates to describe excited bands in odd-A nuclei.

2. Inclusion of a many quasi-particle states.

3. The rupture of spatial parity symmetry and the subsequent restoration would allow to describe octupole deformations.

The increasing of the variational space increments the computational effort substantially, so some improvements or approaches must be carried out.

1. Eliminate the linear dependent wave functions of the GCM before the calculation of the energy overlaps. This means calculating only the norm overlaps, then eliminate the wave functions which are linear dependent and use only the ones left in the final calculation.

2. Try to use as less points as we can for each of the generator coordinates. For example, if we are only interested in the ground band and its properties, the angular momentum potential energy surfaces (PES) provide a good reference, as we know that states with smaller energies are the ones which will be more important in the mixing.

Another improvement is related to the interaction used. The development of beyond mean field methods call for a new fit of the interaction (or even the inclusion or modification of some of the terms). Although some room was left for the extra binding appearing with the implementation of these methods, this seems not enough, as we clearly saw in the study of the Mg isotopic chain.

Chapter 14

Conclusiones

14.1 Resumen de los resultados obtenidos

Los métodos de campo medio son un buen punto de partida para describir la estructura nuclear. Sin embargo están restringidos a la descripción de propiedades globales de los núcleos. El desarrollo de las técnicas más allá del campo medio nos permite estudiar lo espectros nucleares así como las transiciones electromagnéticas y otras propiedades. Este trabajo ha desarrollado estas técnicas en dos direcciones. La primera es la incorporación de estados que rompen la invarianza bajo inversión temporal mediante el procedimiento de cranking. La segunda es la extensión de estos métodos a núcleos con un número impar de partículas.

1. La adición de nuevos grados de libertad introduce diferentes tipos de correlaciones que resultan no sólo en una buena descripción cualitativa

del núcleo, si no también en un buen acuerdo con los datos experimentales. En este trabajo incluimos estados que rompen la invarianza bajo inversión temporal mediante la incorporación de una nueva coordenada generadora; la frecuencia de cranking, manteniendo también como coordenadas las deformaciones nucleares β, γ. La restricción previa de usar sólo estados que mantienen la invarianza bajo inversión temporal favorecía aquellos estados intrínsecos sin contenido de momento angular dando lugar a un espectro alargado. El efecto de incorporar estos estados con la nueva simetría rota fue estudiado primero en los núcleos pares de la cadena isotópica de magnesio, donde se obtuvo una compresión notable del espectro, dando lugar a un excelente acuerdo con los datos experimentales. La incorporación del cranking abrió también la posibilidad a describir estados que corresponden a configuraciones alineadas. En particular el predijimos correctamente el recién medido estado 4^+ del núcleo exótico ^{44}S.

Este nuevo grado de libertad también aumenta de forma considerable el tiempo de CPU necesario. En este trabajo también hemos propuesto una aproximación que permite disminuir dicho tiempo de cálculo. Consiste en reducir el númer de funciones de onda usadas en el generador de coordinadas, incluyendo sólo la deformación β y la frecuencia de cranking como coordenadas generadoras y usando la deformación γ obtenida autoconsistentemente. Con esta aproximación no sólo la energía de excitación de los estados 2^+ se fuerno mejoradas, si no que las probabilidades de transición electromagnéticas entre los estados 0^+ y 2^+ fueron reducidas, de acuerdo con los datos medidos en la actualidad.

2. La segunda aportación de este trabajo consistió en la aplicación de este mecanismo a núcleos impares. Hasta ahora estos métodos tan sólo habían sido llevado a cabo en núcleos pares y parece natural extenderlo al resto de núcleos. Aplicamos nuestra teoría con bloqueo exacto y proyección a número de partículas y momento angular a los núcleos par e impar de la cadena isotópica de magnesio. Obtenemos un excepcional acuerdo en la descripción de las energías de ligadura, los radios de masa, la diferencia de energías par-impar y en los momentos electromagnéticos. No sólo las propiedades de los estados fundamenteales se describen bien con esta teoría. Hicimos también un estudio detallado del núcleo ^{31}Mg situado en el borde de la isla de inversión N=20, en el que tanto los estados fudamentales como los excitados fueron correctamente descritos así como las probabilidades de transición, obteniendo un buen acuerdo con los datos experimentales actuales.

Por último, llevamos a cabo el cálculo más general posible en el núcleo ^{25}Mg, donde las deformaciones β, γ fueron usadas como coordenadas generadoras. Obtuvimos un acuerdo cuantitativo con el experimento en las primeras bandas de cada paridad, así como una buena descripción cualitativa del resto de bandas. Nuestros resultados también fueron comparados con otros modelos teóricos.

14.2 Futuras aplicaciones

Las técnicas desarrolladas en este trabajo pueden ser usadas para estudiar otro tipo de sistemas como:

1. Sistemas con un número impar de protones y de neutrones. En estos sistemas podemos realizar un estudio muy rico debido a las diferentes posibilidades de bloqueo en los distintos canales. Por ejemplo, para obtener los estados de paridad positiva podemos bloquear un protón y un neutrón con paridad positiva o bien bloquear ambos con negativa. Las bandas negativas se obtienen bloqueando distintos canales de paridad para el protón y neutrón.

2. Usar el procedimiento de cranking en nćleos impares para romper la degeneración en el canal de bloqueo del simplex, abriendo la posibilidad a encontrar nuevos estados.

3. Usar el procedimiento de cranking también en núcleos impares para obtener un espectro más comprimido y buscar estados alineados tal y como hicimos en el núcleo ^{44}S

14.3 Trabajo futuro

A pesar de la complejidad de las aproximaciones, podeos implementar aún varias mejoras. Las primeras hacen referencia al aumento del espacio variacional para incluir más correlaciones:

1. Incorporación de *diferentes* estados de quasi-particle para un *determinado* valor del resto de coordenadas generadoras. Esto nos permitiría una mejor descripción de las bandas excitadas.

2. Incoporar estados de muchas quasi-partículas.

3. Romper la simetría de la paridad espacial y la subsiguiente restitución para describir deformaciones octupolares.

El incremento del espacio variacional aumenta el esfuerzo computacional sustancialmente, por lo que debemos realizar también mejoras en este sentido.

1. Eliminar la dependencia lineal de las funciones de onda del generador de coordenadas antes de calcular los solapes de la energía. Esto significa calcular sólo los solapes de la norma, elimiar aquellos linealmente dependientes y luego proceder con el cálculo completo.

2. Tratar de usar los menores puntos que podamos para cada una de las coordenadas generadoras. Por ejemplo, si sólo estamos interesados en calcular las propiedasdes de la banda funcdamental, podemos usar las superficies de energía proyectadas (PES) como referencia, ya que sabemos que sólo los estados con energías próximas al mínimo serán importante en la mezcla de configuraciones.

Otra mejoría está relacionada con la interacción usada. El desarrollo de los métodos más allá de campo medio hace necesario un reajuste de la interacción (o incluso incluir nuevos términos o modificar alguno de ellos). Aunque se

dejo algún espacio para la energía de ligadura extra que conlleva el uso de estas técnicas, hemos visto en este trabajo que no es suficiente.

Appendix A

Calculation of the norm overlap

In this appendix we derive the expression to calculate the Norm $\mathcal{N}^{NZ,I}_{KK'}(\vec{q},\vec{q}\,')$ between two projected states $|\Phi(\vec{q})^{NZ,IMK}\rangle = P^I_{MK}P^NP^Z|\Phi(\vec{q})\rangle$ with different values of $K,\vec{q}$. Our goal is to calculate:

$$\mathcal{N}^{NZ,I}_{KK'}(\vec{q},\vec{q}\,') \;=\; \langle\Phi(\vec{q})^{NZ,IMK}|\Phi(\vec{q}\,')^{NZ,IMK'}\rangle \tag{A.1}$$

As we saw in chapter 6, the main ingredient in the calculation is

$$n(\vec{q},\vec{q}\,',\Omega,\varphi_{l_\tau}) = \langle\Phi_\tau(\vec{q})|\hat{R}(\Omega)e^{i\varphi_{l_\tau}\hat{N}_\tau}|\Phi_\tau(\vec{q})\rangle \tag{A.2}$$

and then we use the following sequence to calculate A.1

$$\begin{array}{ccccc} n(\vec{q},\vec{q}\,',\Omega,\varphi_{l_\tau}) & \overset{\sum_{l_\tau=1}^{L} e^{-i\varphi_{l_\tau}N_\tau}}{\rightarrow} & n^\tau(\vec{q},\vec{q}\,',\Omega) & \overset{\prod_{\tau=Z,N}}{\rightarrow} & \\ & & n^{NZ}(\vec{q},\vec{q}\,') & \overset{\int d\Omega D^{J\star}_{KK'}(\Omega)}{\rightarrow} & \mathcal{N}^{NZ,I}_{KK'}(\vec{q},\vec{q}\,') \end{array} \tag{A.3}$$

A.1 Theoretical derivation

We will follow closely Ref [1, 2]. Our wave function is characterized by the Bogoliubov amplitudes U, V. As we saw this transformation can be decomposed in three independent transformations. The D transformation defines the canonical basis. In this basis the wave function is written:

$$|w\rangle = \Pi_k^M (u_\alpha + v_k a_k^\dagger a_{\bar{k}}^\dagger)|-\rangle \tag{A.4}$$

The elements u_k are defined positive. The matrices U, V have dimension $2M \times 2M$ .. The overlap between the $|w\rangle$ state and the transformed one is;

$$\begin{aligned} \langle w|\hat{R}(\Omega)e^{-i\varphi_{l_\tau}\hat{N}_\tau}|w\rangle &= \langle w|\hat{F}|w\rangle = \frac{(-1)^M}{\Pi_k^M (v_k)^2} pf(\mathbb{M}) \\ &= \frac{(-1)^M}{\Pi_k^M (v_k)^2} pf \begin{bmatrix} V^T U & V^T F^T V^\star \\ -V^\dagger F V & U^\dagger V^\star \end{bmatrix} \end{aligned} \tag{A.5}$$

where $pf(\mathbb{M})$ is the pfaffian of the matrix $\mathbb{M}$. In A.5 we have to omit the space which is not occupied, i.e.; those states with $v_k = 0$. This means U, V, F must be truncated to omit this space.

In the configuration mixing approach we have different vacuums. We can write;

$$|w\rangle = \frac{detC}{\Pi_{k=1}^M v_k} \beta_1 .. \beta_{2M}|-\rangle \qquad |w'\rangle = \frac{detC'}{\Pi_{k=1}^M v'_k} \beta'_1 .. \beta'_{2M}|-\rangle \tag{A.6}$$

with amplitudes (U, V) and U', V'. C is the matrix of the third transforma-

tion 3.7. The overlap in this case is:

$$\langle w|F|w'\rangle = (-1)^M \frac{detC^\star detC}{\Pi_k^M v_k v'_k} pf \begin{bmatrix} V^T U & V^T F^T V'^\star \\ -V'^\dagger F V & U'^\dagger V'^\star \end{bmatrix} \tag{A.7}$$

If we are dealing with an odd-N state;

$$|qw\rangle = c_q^\dagger |w\rangle = \sum_j q_j c_j^\dagger |w\rangle \tag{A.8}$$

the overlap results:

$$\langle wq|F|w'q'\rangle = (-1)^{M'} \frac{detC^\star detC}{\Pi_k^{M'} v_k v'_{k'}} pf \begin{bmatrix} V^T U & 0^\uparrow & V^T F^T q'^\uparrow & V^T F^T V'^\star \\ \vec{0} & 0 & -\vec{q}^\star F^T q'^\uparrow & \vec{q}^\star F^T V'^\star \\ -\vec{q}\,' F V & -\vec{q}\,' F q^{\star\uparrow} & 0 & 0^\uparrow \\ -V'^\dagger F V & -V'^\dagger F q^{\star\uparrow} & 0^\uparrow & U'^\dagger V'^\star \end{bmatrix} \tag{A.9}$$

Note $\vec{q}$ ($q^\uparrow$) is just the row (column) of the V amplitude of the Bogoliubov transformation which corresponds to the blocked state, this is $V_{k=q}$.

A.2 Structure of $\mathbb{M}$

Using the decomposition of the U, V amplitudes 3.7;

$$\begin{aligned} U &= D\bar{U}C \quad V = D\bar{V}C \\ U' &= D'\bar{U}'C' \quad V' = D'\bar{V}'C' \end{aligned} \tag{A.10}$$

We can write;

$$\begin{aligned}\mathbb{M} &= \begin{pmatrix} C^T\bar{V}^T\bar{U}C & C^T\bar{V}^T D^T F^T D'\bar{V}'C' \\ -C'^T\bar{V}'^T D'^T F D\bar{V}C & C'^T\bar{U}'^T\bar{V}'C' \end{pmatrix} \\ &= \begin{pmatrix} C^T\bar{V}^T\bar{U}C & C^T\bar{V}^T D^T F^T D'\bar{V}'C' \\ -C'^T\bar{V}'^T D'^T F D\bar{V}C & C'^T\bar{U}'^T\bar{V}'C' \end{pmatrix} \\ &= \begin{pmatrix} C^T\bar{V}^T\bar{U}C & C^T\bar{V}^T\bar{F}^T\bar{V}'C' \\ -C'^T\bar{V}'^T\bar{F}\bar{V}C & C'^T\bar{U}'^T\bar{V}'C' \end{pmatrix} \end{aligned} \tag{A.11}$$

with $\bar{F} = D'^T F D$. If we define the $4M \times 4M$ matrix;

$$\mathbb{C} = \begin{pmatrix} C & 0 \\ 0 & C' \end{pmatrix} \tag{A.12}$$

is straightforward to write:

$$\mathbb{M} = \mathbb{C}^T\bar{\mathbb{M}}\mathbb{C}' \tag{A.13}$$

where $\bar{\mathbb{M}}$ has the same form as A.7 but using $\bar{U}^{(\prime)}, \bar{V}^{(\prime)}, \bar{F}^{(\prime)}$ in stead of $U^{(\prime)}, V^{(\prime)}, F^{(\prime)}$. Given any matrix B and a skew-symmetric matrix A;

$$pf(B^T AB) = det(B)pf(A)$$

Using this property:

$$\begin{aligned} pf(\bar{\mathbb{M}}) &= pf(\mathbb{C}^T\mathbb{M}\mathbb{C}) = det(\mathbb{C})pf(\mathbb{M}) \\ &= det(C)det(C')pf(\mathbb{M}) \end{aligned}$$

As $det(C) = \pm 1, det(C') = \pm 1$ the difference between calculating the overlap using $\bar{U}^{(\prime)}, \bar{V}^{(\prime)}, \bar{F}^{(\prime)}$ and $U^{(\prime)}, V^{(\prime)}, F^{(\prime)}$ is only a global phase. Due to the simplicty of the former ones, we will use them in the folowing to study the different simplex blocks and the effect of blocking a state (odd-nuclei). Furthermore, matrices $\bar{U}, \bar{V}$ relate $\{\alpha\}$ and $\{a\}$ basis. From chapter 3 we know that these basis only differ to $\{\beta\}$ and $\{c\}$ ones by a unitary transformation between particle operators, which does not mix signature. Therefore the simplex-block properties remain unchanged.

$$\begin{bmatrix} \vec{\alpha} \\ \vec{\bar{\alpha}} \\ \vec{\alpha}^\dagger \\ \vec{\bar{\alpha}}^\dagger \end{bmatrix} = \mathbb{W} \begin{bmatrix} \vec{a} \\ \vec{\bar{a}} \\ \vec{a}^\dagger \\ \vec{\bar{a}}^\dagger \end{bmatrix} = \left[\begin{array}{c|c} \bar{U}^T & \bar{V}^T \\ \hline \bar{V}^T & \bar{U}^T \end{array}\right] \begin{bmatrix} \vec{a} \\ \vec{\bar{a}} \\ \vec{a}^\dagger \\ \vec{\bar{a}}^\dagger \end{bmatrix} \tag{A.14}$$

Using the U and V blocked structure;

$$\begin{bmatrix} \vec{\alpha} \\ \vec{\bar{\alpha}} \\ \vec{\alpha}^\dagger \\ \vec{\bar{\alpha}}^\dagger \end{bmatrix} = \left[\begin{array}{c|c|c|c} \bar{U}^{1,T} & \dots & \dots & \bar{V}^{1,T} \\ \hline \dots & \bar{U}^{2,T} & \bar{V}^{2,T} & \dots \\ \hline \dots & \bar{V}^{1,T} & \bar{U}^{1,T} & \dots \\ \hline \bar{U}^{2,T} & \dots & \dots & \bar{V}^{2,T} \end{array}\right] \begin{bmatrix} \vec{a} \\ \vec{\bar{a}} \\ \vec{a}^\dagger \\ \vec{\bar{a}}^\dagger \end{bmatrix} \tag{A.15}$$

Although $\bar{U}^1 = \bar{U}^2$ and $\bar{V}^1 = -\bar{V}^2$ we will keep indeces 1,2 in the following derivation, as it gives a clearer vision of the evolution of the different blocks, especially in odd systems.

A.2.1 Even system structure

As an example lets suppose the dimension is M=3. If the blocking number is equal to zero, then we have the same number of operators α_i and $\alpha_{\bar{i}}$ and relation A.15 becomes;

$$\begin{bmatrix} \alpha_1 \\ \alpha_2 \\ \alpha_3 \\ \alpha_{\bar{1}} \\ \alpha_{\bar{2}} \\ \alpha_{\bar{3}} \\ \alpha_1^\dagger \\ \alpha_2^\dagger \\ \alpha_3^\dagger \\ \alpha_{\bar{1}}^\dagger \\ \alpha_{\bar{2}}^\dagger \\ \alpha_{\bar{3}}^\dagger \end{bmatrix} = \left[\begin{array}{ccc|ccc|ccc|ccc} \bar{U}_1^1 & 0 & 0 & \dots & \dots & \dots & \dots & \dots & \dots & \bar{V}_1^1 & 0 & 0 \\ 0 & \bar{U}_2^1 & 0 & \dots & \dots & \dots & \dots & \dots & \dots & 0 & \bar{V}_2^1 & 0 \\ 0 & 0 & \bar{U}_3^1 & \dots & \dots & \dots & \dots & \dots & \dots & 0 & 0 & \bar{V}_3^1 \\ \hline \dots & \dots & \dots & \bar{U}_1^2 & 0 & 0 & \bar{V}_1^2 & 0 & 0 & \dots & \dots & \dots \\ \dots & \dots & \dots & 0 & \bar{U}_2^2 & 0 & 0 & \bar{V}_2^2 & 0 & \dots & \dots & \dots \\ \dots & \dots & \dots & 0 & 0 & \bar{U}_3^2 & 0 & 0 & \bar{V}_3^2 & \dots & \dots & \dots \\ \hline \dots & \dots & \dots & \bar{V}_1^1 & 0 & 0 & \bar{U}_1^1 & 0 & 0 & \dots & \dots & \dots \\ \dots & \dots & \dots & 0 & \bar{V}_2^1 & 0 & 0 & \bar{U}_2^1 & 0 & \dots & \dots & \dots \\ \dots & \dots & \dots & 0 & 0 & \bar{V}_3^1 & 0 & 0 & \bar{U}_3^1 & \dots & \dots & \dots \\ \hline \bar{V}_1^2 & 0 & 0 & \dots & \dots & \dots & \dots & \dots & \dots & \bar{U}_1^2 & 0 & 0 \\ 0 & \bar{V}_2^2 & 0 & \dots & \dots & \dots & \dots & \dots & \dots & 0 & \bar{U}_2^2 & 0 \\ 0 & 0 & \bar{V}_3^2 & \dots & \dots & \dots & \dots & \dots & \dots & 0 & 0 & \bar{U}_3^2 \end{array}\right] \begin{bmatrix} a_1 \\ a_2 \\ a_3 \\ a_{\bar{1}} \\ a_{\bar{2}} \\ a_{\bar{3}} \\ a_1^\dagger \\ a_2^\dagger \\ a_3^\dagger \\ a_{\bar{1}}^\dagger \\ a_{\bar{2}}^\dagger \\ a_{\bar{3}}^\dagger \end{bmatrix} \tag{A.16}$$

In general;

$$\alpha_i = \bar{U}_i^1 a_i + \bar{V}_i^1 a_{\bar{i}}^\dagger \qquad \alpha_{\bar{i}} = \bar{U}_i^2 a_{\bar{i}} + \bar{V}_i^2 a_i^\dagger \tag{A.17}$$

$$\alpha_i^\dagger = \bar{U}_i^1 a_i^\dagger + \bar{V}_i^1 a_{\bar{i}} \qquad \alpha_{\bar{i}}^\dagger = \bar{U}_i^2 a_{\bar{i}}^\dagger + \bar{V}_i^2 a_i \tag{A.18}$$

For example for operator number 1;

$$\alpha_1 = \bar{U}_1^1 a_1 + \bar{V}_1^1 a_{\bar{1}}^\dagger \quad \alpha_{\bar{1}} = \bar{U}_1^2 a_{\bar{1}} + \bar{V}_1^2 a_1^\dagger \tag{A.19}$$

$$\alpha_1^\dagger = \bar{U}_1^1 a_1^\dagger + \bar{V}_1^1 a_{\bar{1}} \quad \alpha_{\bar{1}}^\dagger = \bar{U}_1^2 a_{\bar{1}}^\dagger + \bar{V}_1^2 a_1 \tag{A.20}$$

A.2.2 Odd system: Blocked level

Now suposse we block level number 3. If the blocked level has positive signature we now have M-1 operators α_i and M+1 operators $\alpha_{\bar{i}}$.

$$\begin{bmatrix} \alpha_1 \\ \alpha_2 \\ \alpha_{\bar{1}} \\ \alpha_{\bar{2}} \\ \alpha_{\bar{3}} \\ \alpha_{\bar{4}} \\ \alpha_1^\dagger \\ \alpha_2^\dagger \\ \alpha_{\bar{1}}^\dagger \\ \alpha_{\bar{2}}^\dagger \\ \alpha_{\bar{3}}^\dagger \\ \alpha_{\bar{4}}^\dagger \end{bmatrix} = \left[\begin{array}{ccc|ccc|ccc|ccc} \bar{U}_1^1 & 0 & 0 & \dots & \dots & \dots & \dots & \dots & \dots & \bar{V}_1^1 & 0 & 0 \\ 0 & \bar{U}_2^1 & 0 & \dots & \dots & \dots & \dots & \dots & \dots & 0 & \bar{V}_2^1 & 0 \\ \hline \dots & \dots & \dots & \bar{U}_1^2 & 0 & 0 & \bar{V}_1^2 & 0 & 0 & \dots & \dots & \dots \\ \dots & \dots & \dots & 0 & \bar{U}_2^2 & 0 & 0 & \bar{V}_2^2 & 0 & \dots & \dots & \dots \\ \dots & \dots & \dots & 0 & 0 & 0 & 0 & 0 & 1 & \dots & \dots & \dots \\ \dots & \dots & \dots & 0 & 0 & 1 & 0 & 0 & 0 & \dots & \dots & \dots \\ \hline \dots & \dots & \dots & \bar{V}_1^1 & 0 & 0 & \bar{U}_1^1 & 0 & 0 & \dots & \dots & \dots \\ \dots & \dots & \dots & 0 & \bar{V}_2^1 & 0 & 0 & \bar{U}_2^1 & 0 & \dots & \dots & \dots \\ \hline \bar{V}_1^2 & 0 & 0 & \dots & \dots & \dots & \dots & \dots & \dots & \bar{U}_1^2 & 0 & 0 \\ 0 & \bar{V}_2^2 & 0 & \dots & \dots & \dots & \dots & \dots & \dots & 0 & \bar{U}_2^2 & 0 \\ 0 & 0 & 1 & \dots & \dots & \dots & \dots & \dots & \dots & 0 & 0 & 0 \\ 0 & 0 & 0 & \dots & \dots & \dots & \dots & \dots & \dots & 0 & 0 & 1 \end{array}\right] \begin{bmatrix} a_1 \\ a_2 \\ a_3 \\ a_{\bar{1}} \\ a_{\bar{2}} \\ a_{\bar{3}} \\ a_1^\dagger \\ a_2^\dagger \\ a_3^\dagger \\ a_{\bar{1}}^\dagger \\ a_{\bar{2}}^\dagger \\ a_{\bar{3}}^\dagger \end{bmatrix} \tag{A.21}$$

So for example for operator number 1 (non-blocked) the expression is the same as A.19-A.20 . The same is true for the non-blocked level 2. However,

te expression for 3 and 4 becomes;

$$\alpha_{\bar{3}} = a_3^\dagger \quad \alpha_{\bar{3}}^\dagger = a_3 \tag{A.22}$$

$$\alpha_{\bar{4}} = a_{\bar{3}} \quad \alpha_{\bar{4}}^\dagger = a_{\bar{3}}^\dagger \tag{A.23}$$

We know that for an occupied level "$\bar{q}$" $v_{\bar{q}} = 1$ and $u_q = 0$ (ie $\alpha_{\bar{q}} = a_q^\dagger$), and for an empty level $v_q = 0$ and $u_q = 1$. Therefore is clear that in the example above $\alpha_{\bar{3}}$ is occupied while $\alpha_{\bar{4}}$ is empty. In order to compute the norm overlap of expression A.9 we must exclude the empty levels. The way to do this is to "cut" the subspace belonging to $\alpha_{\bar{4}}$, and, for expression A.23, which in the canonical basis is the subspace of $a_{\bar{3}}$. This corresponds to a reduction of one column and one row in matrices $\bar{U}$ and $\bar{V}$.

Columns in matrices $\bar{U}$ and $\bar{V}$ correspond to different α, while rows correspond to different a [1] Matrix $\bar{U}^1$ remains equal. In $\bar{U}^2$ we eliminate the last column (corresponding to $\alpha_{\bar{4}}$), and last row (corresponding to $a_{\bar{3}}$) . In matrix $\bar{V}^1$ we exclude last row (corresponding to $a_{\bar{3}}$) and in $\bar{V}^2$ we exclude last column (corresponding to $\alpha_{\bar{4}}$). The transformation is;

[1] *Note that in expression A.14 we are using the transpose ones.

$$\left[\begin{array}{cc|cccc} \bar{U}_1^1 & 0 & \cdots & \cdots & \cdots & \cdots \\ 0 & \bar{U}_2^1 & \cdots & \cdots & \cdots & \cdots \\ 0 & 0 & \cdots & \cdots & \cdots & \cdots \\ \hline \cdots & \cdots & \bar{U}_1^2 & 0 & 0 & 0 \\ \cdots & \cdots & 0 & \bar{U}_2^2 & 0 & 0 \\ \cdots & \cdots & 0 & 0 & 0 & 1 \end{array}\right] \rightarrow \left[\begin{array}{cc|ccc} \bar{U}_1^1 & 0 & \cdots & \cdots & \cdots \\ 0 & \bar{U}_2^1 & \cdots & \cdots & \cdots \\ 0 & 0 & \cdots & \cdots & \cdots \\ \hline \cdots & \cdots & \bar{U}_1^2 & 0 & 0 \\ \cdots & \cdots & 0 & \bar{U}_2^2 & 0 \end{array}\right] \tag{A.24}$$

$$\left[\begin{array}{cc|cccc} \cdots & \cdots & \bar{V}_1^2 & 0 & 0 & 0 \\ \cdots & \cdots & 0 & \bar{V}_2^2 & 0 & 0 \\ \cdots & \cdots & 0 & 0 & 1 & 0 \\ \hline \bar{V}_1^1 & 0 & \cdots & \cdots & \cdots & \cdots \\ 0 & \bar{V}_2^1 & \cdots & \cdots & \cdots & \cdots \\ 0 & 0 & \cdots & \cdots & \cdots & \cdots \end{array}\right] \rightarrow \left[\begin{array}{cc|ccc} \cdots & \cdots & \bar{V}_1^2 & 0 & 0 \\ \cdots & \cdots & 0 & \bar{V}_2^2 & 0 \\ \cdots & \cdots & 0 & 0 & 1 \\ \hline \bar{V}_1^1 & 0 & \cdots & \cdots & \cdots \\ 0 & \bar{V}_2^1 & \cdots & \cdots & \cdots \end{array}\right] \tag{A.25}$$

In order to derivate future expressions we will define matrices $\tilde{U}$ and $\tilde{V}$ as;

$$\left[\begin{array}{cc|ccc} \bar{U}_1^1 & 0 & \cdots & \cdots & \cdots \\ 0 & \bar{U}_2^1 & \cdots & \cdots & \cdots \\ 0 & 0 & \cdots & \cdots & \cdots \\ \hline \cdots & \cdots & \bar{U}_1^2 & 0 & 0 \\ \cdots & \cdots & 0 & \bar{U}_2^2 & 0 \end{array}\right] = \left[\begin{array}{cc|ccc} & & \cdots & \cdots & \cdots \\ & \tilde{U}^1 & & & \\ & & \cdots & \cdots & \cdots \\ 0 & 0 & \cdots & \cdots & \cdots \\ \hline \cdots & \cdots & & & 0 \\ & \bar{U}^2 & & & \\ \cdots & \cdots & & & 0 \end{array}\right] \tag{A.26}$$

$$\left[\begin{array}{cc|ccc} \cdots & \cdots & \bar{V}_1^2 & 0 & 0 \\ \cdots & \cdots & 0 & \bar{V}_2^2 & 0 \\ \cdots & \cdots & 0 & 0 & 1 \\ \hline \bar{V}_1^1 & 0 & \cdots & \cdots & \cdots \\ 0 & \bar{V}_2^1 & \cdots & \cdots & \cdots \end{array}\right] = \left[\begin{array}{cc|ccc} \cdots & \cdots & & \tilde{V}^2 & 0 \\ \cdots & \cdots & & & 0 \\ \cdots & \cdots & 0 & 0 & 1 \\ \hline & \tilde{V}^1 & \cdots & \cdots & \cdots \\ & & \cdots & \cdots & \cdots \end{array}\right] \tag{A.27}$$

The $4M \times 4M$ transformation matrix $F = \hat{R}(\Omega)e^{i\varphi\hat{N}}$ (or $\bar{F}$) ,is resized accordingly; i.e. the rows and columns belonging to the subspace of $a_{\bar{3}}$ have to be omitted. Block number 1 belongs to subspace with positive signature $\{a_i\}$, and therefore remains unchanged, with dimension $2M \times 2M$. Block number 2 belongs to subspace with negative signature $\{a_{\bar{i}}\}$ and reduces to $2M-1 \times 2M-1$. Blocks 3 and 4 mix signatures. Their new dimensions are $2M \times 2M-1$ and $2M-1 \times 2M$ respectively.

$$\left[\begin{array}{c|c} \bar{F}^1 & \bar{F}^3 \\ \hline \bar{F}^4 & \bar{F}^2 \end{array}\right] \rightarrow \left[\begin{array}{c|c} \bar{F}^1 & \bar{F}^3 \\ \hline \bar{F}^4 & \bar{F}^2 \end{array}\right] = \left[\begin{array}{c|c|c} \tilde{F}^1 & \bar{F}_{q3}^{1\uparrow} & \tilde{F}^3 \\ \hline \vec{\bar{F}}_{3q}^1 & \bar{F}_{33}^1 & \vec{\bar{F}}_{3q}^3 \\ \hline \tilde{F}^4 & \bar{F}_{q3}^{4\uparrow} & \tilde{F}^2 \end{array}\right] \tag{A.28}$$

In A.28 we also defined $\tilde{F}$ in the same way we did for $\tilde{U}, \tilde{V}$. The blocked subspace of $\bar{F}$ is written with a $\rightarrow$ (as in $\vec{\bar{F}}_{3q}^1$) when is a row, and with an $\uparrow$ (as in $F_{q3}^{1\uparrow}$) when is a column. Now we are prepared to study the block properties on expression A.9. Note that as matrices U and V are real, and the matrix

is skew symmetric, the right botton box (U^TV) is equal to the transpose of the left top box (V^TU). In addition the right top box (V^TT^TV) is minus the transpose right bottom box (V^TT^TV). Therefore we have to study only the block properties of two of the boxes: U^TV and $-V^TFV$. Using A.26, A.27 and A.28:

$$V^TU = \left[\begin{array}{cc|ccc} \cdots & \cdots & & & \\ & & \tilde{V}^{1T}\tilde{U}^2 & & 0^{\uparrow} \\ \cdots & \cdots & & & \\ \hline & & \cdots & \cdots & \cdots \\ \tilde{V}^{2T}\tilde{U}^1 & & & & \\ & & \cdots & \cdots & \cdots \\ & & & & \\ \vec{0} & & \cdots & \cdots & \cdots \end{array}\right] \tag{A.29}$$

$$-V^TFV = \left[\begin{array}{cc|cc} & & & \\ -\tilde{V}^{1T}\tilde{F}^2\tilde{V}^2 & & -\tilde{V}^{1T}\tilde{F}^4\tilde{V}^2 & -\tilde{V}^{1T}\bar{F}^{4\uparrow}_{q3} \\ & & & \\ \hline & & & \\ -\tilde{V}^{2T}\tilde{F}^3\tilde{V}^1 & & -\tilde{V}^{2T}\tilde{F}^1\tilde{V}^2 & -\tilde{V}^{2T}\bar{F}^{1\uparrow}_{q3} \\ & & & \\ -\vec{\bar{F}}^3_{3q}\tilde{V}^1 & & -\vec{\bar{F}}^1_{3q}\tilde{V}^2 & -\bar{F}^1_{33} \end{array}\right] \tag{A.30}$$

Now we compare expressions A.29 and A.30 with A.9. Notice first that in expressions A.29 and A.30 the vector $\vec{q} = (0\ 0\ 0...1)$, because we are working with $\bar{U}, \bar{V}$ matrices in stead of U, V ones. We see we arrive at the correct form of matrix $\mathbb{M}$ (blocking the last state). [2]

[2]Note that the last row in expression A.30 can be move to he first row without changing the value of the Pfaffian

Bibliography

[1] GF Bertsch and LM Robledo. *Physical review letters*, 108(4):042505, 2012.

[2] C. González-Ballestero, L.M. Robledo, and G.F. Bertsch. *Computer Physics Communications*, 182(10):2213 – 2218, 2011.

Appendix B

Operator-Overlap

In this appendix we derive the expression of the expected value $\mathcal{O}^{NZ,I}_{KK'}(\vec{q},\vec{q}\,')$ of any operator $\hat{O}$ between two projected states $|\Phi(\vec{q})^{NZ,IMK}\rangle = P^I_{MK}P^NP^Z|\Phi(\vec{q})\rangle$ with different values of $K,\vec{q}$. Our goal is to calculate:

$$\mathcal{O}^{NZ,I}_{KK'}(\vec{q},\vec{q}\,') \;=\; \langle\Phi(\vec{q})^{NZ,IMK}|\hat{O}_{KK'}|\Phi(\vec{q}\,')^{NZ,IMK'}\rangle \tag{B.1}$$

As we saw in chapter 6, the main ingredient in the calculation is

$$o^{NZ}(\vec{q},\vec{q}\,',\Omega,\varphi_{l_Z},\varphi_{l_N}) = \frac{\langle\Phi(\vec{q})|\hat{O}\hat{R}(\Omega)e^{i\varphi_{l_\pi}\hat{N}_Z}e^{i\varphi_{l_N}\hat{N}_\nu}|\Phi(\vec{q}\,')\rangle}{\langle\Phi(\vec{q})|\hat{R}(\Omega)e^{i\varphi_{l_Z}\hat{N}_Z}e^{i\varphi_{l_N}\hat{N}_N}|\Phi(\vec{q}\,')\rangle} \tag{B.2}$$

and then use the following sequence to calculate B.1

$$\begin{array}{lll} o(\vec{q},\vec{q}\,',\Omega,\varphi_{l_Z},\varphi_{l_N}) & \overset{\sum_{l_Z=1}^{L}\sum_{l_N=1}^{L} y_{l_Z}y_{l_N}}{\rightarrow} & o(\vec{q},\vec{q}\,',\Omega) \overset{\times n^{NZ}(\vec{q},\vec{q}\,')}{\rightarrow} \\ & & O^{NZ}(\vec{q},\vec{q}\,',\Omega) \overset{\int d\Omega D^{J\star}_{KK'}(\Omega)}{\rightarrow} \mathcal{O}^{NZ,I}_{KK'}(\vec{q},\vec{q}\,') \end{array} \tag{B.3}$$

Expression $y_{l_Z} y_{l_N}$ in the sequence above was calculated in 6.92 of appendix A. In this chapter we are going to develop the tools to calculate B.2 (blue color).

B.1 Theoretical derivation

Lets define a transformation $\hat{F} \rightarrow F_{ij} = \langle i|\hat{F}|j\rangle$. This transformation must fulfill the following properties;

1. Maintains fermionic commutation rules

$$\hat{F}\{c_i^\dagger c_j\}\hat{F}^\dagger = \delta_{ij} \tag{B.4}$$

2. Is unitary

$$\hat{F}\hat{F}^\dagger = \hat{F}^\dagger\hat{F} = \mathbb{I} \tag{B.5}$$

3. Does not mix creation and anhilation operators

$$\begin{aligned} \hat{F}c_i^\dagger\hat{F}^\dagger &= \sum_j F_{ji}c_j^\dagger \\ \hat{F}c_i\hat{F}^\dagger &= \sum_j F_{ji}^\star c_j \end{aligned} \tag{B.6}$$

The transformation $\hat{R}(\Omega)e^{i\varphi_{l_\pi}\hat{N}_\pi}e^{i\varphi_{l_\nu}\hat{N}_\nu}$ on expression B.2 is an example of this transformation. The elements F_{ij} are easy to obtain. Moreover, the particle number projection part is independent of (i,j). If this i,j correspond

to isospin τ :

$$\begin{aligned} F_{ij} &= \langle i^\tau|\hat{R}(\Omega)e^{i\varphi_{l_\pi}\hat{N}_\pi}e^{i\varphi_{l_\nu}\hat{N}_\nu}|j^\tau\rangle = \langle -|c_i^\tau\hat{R}(\Omega)e^{i\varphi_{l_\pi}\hat{N}_\pi}e^{i\varphi_{l_\nu}\hat{N}_\nu}c_j^{\tau\dagger}|-\rangle \\ &= e^{i\varphi}\langle -|c_i^\tau\hat{R}(\Omega)c_j^{\tau\dagger}e^{i\varphi_{l_\tau}\hat{N}_\tau}|-\rangle = e^{i\varphi}\langle -|c_i^\tau\hat{R}(\Omega)c_j^{\tau\dagger}|-\rangle \\ &= e^{i\varphi}\langle i^\tau|\hat{R}(\Omega)|j^\tau\rangle \end{aligned} \tag{B.7}$$

So the operator $\hat{F}$ is written in a simple way;

$$\hat{F} = e^{i\varphi}\hat{R}(\Omega) \tag{B.8}$$

We know that state $|\Phi(\vec{q})\rangle$ is the vacuum of quasi-particle operators $\beta_k(\vec{q})$, and state $|\Phi(\vec{q}\,')\rangle$ is the vacuum of quasi-particle operators $\beta_k(\vec{q}\,')$, i.e;

$$\begin{aligned} \beta_k(\vec{q})|\Phi(\vec{q})\rangle = 0 \quad \forall k \\ \beta_k(\vec{q}\,')|\Phi(\vec{q}\,')\rangle = 0 \quad \forall k \end{aligned} \tag{B.9}$$

We can define the state $|\tilde{\Phi}(\vec{q}\,')\rangle$ as;

$$|\tilde{\Phi}(\vec{q}\,')\rangle = \hat{F}|\Phi(\vec{q}\,')\rangle \tag{B.10}$$

This state is vacuum of a different of operators $\tilde{\beta}_k(\vec{q}\,')$;

$$\tilde{\beta}_k(\vec{q}\,')|\tilde{\Phi}(\vec{q}\,')\rangle = 0 \quad \forall k \tag{B.11}$$

These new quasi-particle operators are related to the particle operators by the corresponding amplitudes $\tilde{U}(\vec{q}\,'), \tilde{V}(\vec{q}\,')$;

$$\begin{pmatrix} \tilde{\beta}(\vec{q}\,') \\ \\ \tilde{\beta}^{\dagger}(\vec{q}\,') \end{pmatrix} = \begin{pmatrix} \tilde{U}^{\dagger}(\vec{q}\,') & \tilde{V}^{\dagger}(\vec{q}\,') \\ \\ \tilde{V}^{T}(\vec{q}\,') & \tilde{U}^{T}(\vec{q}\,') \end{pmatrix} \begin{pmatrix} c \\ \\ c^{\dagger} \end{pmatrix} \tag{B.12}$$

The operator $\hat{O}$ is a product of creation and anhilation of any of the operators used up to now $\beta_k^{(\dagger)}(\vec{q}), \tilde{\beta}_k^{(\dagger)}(\vec{q}\,'), c_k^{(\dagger)}$. Being $a, b, c...$ any of these operators;

$$\hat{O} = abc...yz.. \tag{B.13}$$

With these definitions the calculation of B.2 reduces to;

$$\frac{\langle \Phi(\vec{q})|\hat{O}\hat{F}|\Phi(\vec{q}\,')\rangle}{\langle \Phi(\vec{q})|\hat{F}|\Phi(\vec{q}\,')\rangle} = \frac{\langle \Phi(\vec{q})|abc..xyz|\tilde{\Phi}(\vec{q}\,')\rangle}{\langle \Phi(\vec{q})|\tilde{\Phi}(\vec{q}\,')\rangle} \tag{B.14}$$

where we can apply the generalized Wick theorem. This theorem allows us to calculate the mean values of a product of operators $abc...$ between states with the same or different quasi-particle vacuum as a sum of the products of all possible two operators.

$$\frac{\langle \Phi(\vec{q})|abc..xyz|\tilde{\Phi}(\vec{q}\,')\rangle}{\langle \Phi(\vec{q})|\tilde{\Phi}(\vec{q}\,')\rangle} = [ab]...[yz] \pm [ac]...[yz] \pm ... \tag{B.15}$$

with

$$[ab] = \frac{\langle \Phi(\vec{q})|ab|\tilde{\Phi}(\vec{q}\,')\rangle}{\langle \Phi(\vec{q})|\tilde{\Phi}(\vec{q}\,')\rangle} = \frac{\langle \Phi(\vec{q})|ab\hat{F}|\Phi(\vec{q}\,')\rangle}{\langle \Phi(\vec{q})|\hat{F}|\Phi(\vec{q}\,')\rangle} \tag{B.16}$$

Many of the contractions of the expression above vanish. We are going to see which of them do not. First we consider those between quasi-particle operators $\beta(\vec{q})$, $\beta^\dagger(\vec{q})$, $\tilde{\beta}(\vec{q}\,')$, $\tilde{\beta}^\dagger(\vec{q}\,')$. In principle there are 16 possible combinations. However,

$$\langle\Phi(\vec{q})|\beta_i^\dagger(\vec{q}) = 0 \quad \tilde{\beta}_i(\vec{q}\,')|\tilde{\Phi}(\vec{q}')\rangle = 0 \tag{B.17}$$

so all combinations of the type $\beta^\dagger(\vec{q})\alpha$ y $\alpha\tilde{\beta}(\vec{q}\,')$ (where α is any operator) vanish. That leaves 9 combinations. 4 of them do not mix β with $\tilde{\beta}$ operators:

$$\beta(\vec{q})\beta^\dagger(\vec{q}), \beta(\vec{q})\beta(\vec{q}), \tilde{\beta}(\vec{q}\,')\tilde{\beta}^\dagger(\vec{q}\,'), \tilde{\beta}(\vec{q}\,')\beta(\vec{q}$$

The other five do;

$$\beta(\vec{q})\tilde{\beta}^\dagger(\vec{q}\,'), \tilde{\beta}(\vec{q}\,')\beta(\vec{q}), \tilde{\beta}(\vec{q}\,')\beta^\dagger(\vec{q}), \tilde{\beta}^\dagger(\vec{q}\,')\beta(\vec{q}), \tilde{\beta}^\dagger(\vec{q}\,')\beta^\dagger(\vec{q})$$

The first four are easier due to the fermionic character of the operators:

$$\begin{aligned} \beta_i(\vec{q})\beta_j^\dagger(\vec{q}) &= \delta_{ij} - \beta_j^\dagger(\vec{q})\beta_i(\vec{q}) \\ \tilde{\beta}_i(\vec{q}')\tilde{\beta}_j^\dagger(\vec{q}') &= \delta_{ij} - \tilde{\beta}_j^\dagger(\vec{q}')\tilde{\beta}_i(\vec{q}') \end{aligned} \tag{B.18}$$

and we can use;

$$\begin{aligned} \frac{\langle\Phi(\vec{q})|\beta_i(\vec{q})\beta_j^\dagger(\vec{q})|\tilde{\Phi}(\vec{q}')\rangle}{\langle\Phi(\vec{q})|\tilde{\Phi}(\vec{q}')\rangle} &= \frac{\langle\Phi(\vec{q})|\delta_{ij}|\tilde{\Phi}(\vec{q}')\rangle}{\langle\Phi(\vec{q})|\tilde{\Phi}(\vec{q}')\rangle} - \frac{\langle\Phi(\vec{q})|\beta_j^\dagger(\vec{q})\beta_i(\vec{q})|\tilde{\Phi}(\vec{q}')\rangle}{\langle\Phi(\vec{q})|\tilde{\Phi}(\vec{q}')\rangle} \\ &= \frac{\langle\Phi(\vec{q})|\delta_{ij}|\tilde{\Phi}(\vec{q}')\rangle}{\langle\Phi(\vec{q})|\tilde{\Phi}(\vec{q}')\rangle} \end{aligned} \tag{B.19}$$

In a compact notation, the contractions between operators $\beta(\vec{q})$:

$$\begin{aligned} & \langle\Phi(\vec{q})|\tilde{\Phi}(\vec{q}\,')\rangle^{-1} \begin{pmatrix} \langle\Phi(\vec{q})|\beta(\vec{q})\beta(\vec{q})|\tilde{\Phi}(\vec{q}\,')\rangle & \langle\Phi(\vec{q})|\beta(\vec{q})\beta^{\dagger}(\vec{q})|\tilde{\Phi}(\vec{q}\,')\rangle \\ \langle\Phi(\vec{q})|\beta^{\dagger}(\vec{q})\beta(\vec{q})|\tilde{\Phi}(\vec{q}\,')\rangle & \langle\Phi(\vec{q})|\beta^{\dagger}(\vec{q})\beta^{\dagger}(\vec{q})|\tilde{\Phi}(\vec{q}\,')\rangle \end{pmatrix} \\ = \; & \langle\Phi(\vec{q})|\tilde{\Phi}(\vec{q}\,')\rangle^{-1} \begin{pmatrix} \langle\Phi(\vec{q})|\beta(\vec{q})\beta(\vec{q})|\tilde{\Phi}(\vec{q}\,')\rangle & \mathbb{I} \\ 0 & 0 \end{pmatrix} \end{aligned} \tag{B.20}$$

A similar relation as B.19 for $\tilde{\beta}$ operators allows us to obtain:

$$\begin{aligned} & \langle\Phi(\vec{q})|\tilde{\Phi}(\vec{q}\,')\rangle^{-1} \begin{pmatrix} \langle\Phi(\vec{q})|\tilde{\beta}(\vec{q}\,')\tilde{\beta}(\vec{q}\,')|\tilde{\Phi}(\vec{q}\,')\rangle & \langle\Phi(\vec{q})|\tilde{\beta}(\vec{q}\,')\tilde{\beta}^{\dagger}(\vec{q}\,')|\tilde{\Phi}(\vec{q}\,')\rangle \\ \langle\Phi(\vec{q})|\tilde{\beta}^{\dagger}(\vec{q}\,')\tilde{\beta}(\vec{q}\,')|\tilde{\Phi}(\vec{q}\,')\rangle & \langle\Phi(\vec{q})|\tilde{\beta}^{\dagger}(\vec{q}\,')\tilde{\beta}^{\dagger}(\vec{q}\,')|\tilde{\Phi}(\vec{q}\,')\rangle \end{pmatrix} \\ = \; & \langle\Phi(\vec{q})|\tilde{\Phi}(\vec{q}\,')\rangle^{-1} \begin{pmatrix} 0 & \mathbb{I} \\ 0 & \langle\Phi(\vec{q})|\tilde{\beta}^{\dagger}(\vec{q}\,')\tilde{\beta}^{\dagger}(\vec{q}\,')|\tilde{\Phi}(\vec{q}\,')\rangle \end{pmatrix} \end{aligned} \tag{B.21}$$

For the mixed terms, we will see in Appendix () that only the one with $\tilde{\beta}$ operator on the right is necessary for the calculations. Therefore;

$$\begin{aligned} & \langle\Phi(\vec{q})|\tilde{\Phi}(\vec{q}\,')\rangle^{-1} \begin{pmatrix} \langle\Phi(\vec{q})|\beta(\vec{q})\tilde{\beta}(\vec{q}\,')|\tilde{\Phi}(\vec{q}\,')\rangle & \langle\Phi(\vec{q})|\beta(\vec{q})\tilde{\beta}^{\dagger}(\vec{q}\,')|\tilde{\Phi}(\vec{q}\,')\rangle \\ \langle\Phi(\vec{q})|\beta^{\dagger}(\vec{q})\tilde{\beta}(\vec{q}\,')|\tilde{\Phi}(\vec{q}\,')\rangle & \langle\Phi(\vec{q})|\beta^{\dagger}(\vec{q})\tilde{\beta}^{\dagger}(\vec{q}\,')|\tilde{\Phi}(\vec{q}\,')\rangle \end{pmatrix} \\ = \; & \langle\Phi(\vec{q})|\tilde{\Phi}(\vec{q}\,')\rangle^{-1} \begin{pmatrix} 0 & \langle\Phi(\vec{q})|\beta(\vec{q})\tilde{\beta}^{\dagger}(\vec{q}\,')|\tilde{\Phi}(\vec{q}\,')\rangle \\ 0 & 0 \end{pmatrix} \end{aligned} \tag{B.22}$$

B.2 $\mathbb{T}$ transformation matrix

On the expressions above we have two different vacuums on the left and on the side $\{\vec{q}\}, \{\vec{q}\,'\}$. These two basis can be related with matrix $\hat{\mathbb{T}}_{q\to q'}$;

$$|\Phi(\vec{q}\,')\rangle = \hat{\mathbb{T}}_{q\to q'}|\Phi(\vec{q})\rangle \tag{B.23}$$

Therefore $|\Phi(\vec{q})\rangle$ and $|\tilde{\Phi}(\vec{q}\,')\rangle$ are related by a double transformation $\mathbb{T}$ which is the action of operators F and $\hat{\mathbb{T}}_{q\to q'}$;

$$|\tilde{\Phi}(\vec{q}\,')\rangle = \hat{F}\hat{\mathbb{T}}_{q\to q'}|\Phi(\vec{q})\rangle = \mathbb{T}|\Phi(\vec{q})\rangle \tag{B.24}$$

With theses relations;

$$\begin{pmatrix} \beta(\vec{q}) \\ \\ \beta^{\dagger}(\vec{q}) \end{pmatrix} = \begin{pmatrix} T_{11} & T_{12} \\ \\ T_{21} & T_{22} \end{pmatrix} \begin{pmatrix} \tilde{\beta}(\vec{q}\,') \\ \\ \tilde{\beta}^{\dagger}(\vec{q}\,') \end{pmatrix} \tag{B.25}$$

and

$$\begin{pmatrix} \tilde{\beta}(\vec{q}\,') \\ \\ \tilde{\beta}^{\dagger}(\vec{q}\,') \end{pmatrix} = \mathbb{T} \begin{pmatrix} \beta(\vec{q}) \\ \\ \beta^{\dagger}(\vec{q}) \end{pmatrix} \mathbb{T}^{-1} \tag{B.26}$$

Both $\beta(\vec{q}), \tilde{\beta}(\vec{q}\,')$ are related to the particle basis $\{c, c^{\dagger}\}$ by $U(\vec{q}), V(\vec{q})$ and $\tilde{U}(\vec{q}\,'), \tilde{V}(\vec{q}\,')$ respectively. In addition the latter is related to $U(\vec{q}\,'), V(\vec{q}\,')$ through matrix $\hat{F}$. This allows us to write;

$$\begin{pmatrix} T_{11} & T_{12} \\ \\ T_{21} & T_{22} \end{pmatrix} = \begin{pmatrix} U^{\dagger}(\vec{q}) & V^{\dagger}(\vec{q}) \\ \\ V^{T}(\vec{q}) & U^{T}(\vec{q}) \end{pmatrix} \begin{pmatrix} F & 0 \\ \\ 0 & F^{\star} \end{pmatrix} \begin{pmatrix} U(\vec{q}\,') & V^{\star}(\vec{q}\,') \\ \\ V(\vec{q}\,') & U^{\star}(\vec{q}\,') \end{pmatrix} \tag{B.27}$$

With the definition;

$$[\hat{\mathbb{F}}] = \frac{\hat{F}}{\langle \Phi(\vec{q}) | \hat{F} | \Phi(\vec{q}\,') \rangle} \tag{B.28}$$

we can express the basic contractions (color blue on expressions B.20-B.22) as [1]

$$\begin{aligned}
\langle\Phi(\vec{q})|\beta_l(\vec{q})\beta_{l'}(\vec{q})[\hat{\mathbb{F}}]|\Phi(\vec{q}\,')\rangle &= -(T_{12}T_{22}^{-1})_{ll'} \\
\langle\Phi(\vec{q})|\tilde{\beta}_l^{\dagger}(\vec{q})\tilde{\beta}_{l'}^{\dagger}(\vec{q})[\hat{\mathbb{F}}]|\Phi(\vec{q}\,')\rangle &= -(T_{22}^{-1}T_{21})_{ll'} \\
\langle\Phi(\vec{q})|[\hat{\mathbb{F}}]\beta_l^{\dagger}(\vec{q})\beta_{l'}^{\dagger}(\vec{q})|\Phi(\vec{q}\,')\rangle &= -(T_{22}^{-1}T_{21})_{ll'}
\end{aligned} \tag{B.29}$$

B.3 Generalizaed density matrix and pairing tensors

If the operator is expressed using particle operators, it would be interesting to obtain also the generalized density matrix and pairing tensors:

$$\begin{aligned}
\rho_{ll'}^{10} &\equiv \langle\Phi(\vec{q})|c_{l'}^{\dagger}c_l[\hat{\mathbb{F}}]|\Phi(\vec{q}\,')\rangle \\
\kappa_{ll'}^{10} &\equiv \langle\Phi(\vec{q})|c_{l'}c_l[\hat{\mathbb{F}}]|\Phi(\vec{q}\,')\rangle \\
\kappa_{ll'}^{01} &\equiv \langle\Phi(\vec{q})|c_{l'}^{\dagger}c_l^{\dagger}[\hat{\mathbb{F}}]|\Phi(\vec{q}\,')\rangle
\end{aligned} \tag{B.30}$$

Using the relation between particle and quasi-particle operators:

$$\begin{aligned} c_l &= \sum_k U_{lk}(\vec{q})\beta_k(\vec{q}) + V^{\star}_{lk}(\vec{q})\beta^{\dagger}_k(\vec{q}) \\ &= \sum_k \tilde{U}_{lk}(\vec{q}')\tilde{\beta}_k(\vec{q}') + \tilde{V}^{\star}_{lk}(\vec{q}')\tilde{\beta}^{\dagger}_k(\vec{q}') \\ c^{\dagger}_l &= \sum_k U^{\star}_{lk}(\vec{q})\beta^{\dagger}_k(\vec{q}) + V_{lk}(\vec{q})\beta_k(\vec{q}) \\ &= \sum_k \tilde{U}^{\star}_{lk}(\vec{q}')\tilde{\beta}^{\dagger}_k(\vec{q}') + \tilde{V}_{lk}(\vec{q}')\tilde{\beta}_k(\vec{q}') \end{aligned} \tag{B.31}$$

and taking into account expressions B.20-B.22 and B.29;

$$\begin{aligned} \rho^{10}_{ll'} &= \sum_{kk'} \langle \Phi(\vec{q})|(U^{\star}_{l'k'}(\vec{q})\beta^{\dagger}_{k'}(\vec{q}) + V_{l'k'}(\vec{q})\beta_{k'}(\vec{q}))(\tilde{U}_{lk}(\vec{q}')\tilde{\beta}_k(\vec{q}') \\ &\quad + \tilde{V}^{\star}_{lk}(\vec{q}')\tilde{\beta}^{\dagger}_k(\vec{q}')[\hat{\mathcal{F}}]|\Phi(\vec{q}'))\rangle \\ &= \sum_{kk'} V_{l'k'}(\vec{q})\tilde{V}^{\star}_{lk}(\vec{q}')\langle \Phi(\vec{q})|\beta_{k'}(\vec{q})\tilde{\beta}^{\dagger}_k(\vec{q}')[\hat{\mathcal{F}}]|\Phi(\vec{q})\rangle \\ &= \sum_{kk'} V_{l'k'}(\vec{q})\tilde{V}^{\star}_{lk}(\vec{q}')[T^T_{22}]^{-1}_{k'k} \\ &= (V(\vec{q})[T^T_{22}]^{-1}\tilde{V}^{\dagger}(\vec{q}'))_{l'l} \\ &= (\tilde{V}^{\star}(\vec{q}')[T_{22}]^{-1}V^T(\vec{q}))_{ll'} \\ &= (FV^{\star}(\vec{q}')[T_{22}]^{-1}V^T(\vec{q}))_{ll'} \end{aligned} \tag{B.32}$$

$$\begin{aligned}
\kappa^{10}_{ll'} &= \sum_{kk'}\langle\Phi(\vec{q})|(U_{l'k'}(\vec{q})\beta_{k'}(\vec{q}) + V^{\star}_{l'k'}(\vec{q})\beta^{\dagger}_{k'}(\vec{q})(\tilde{U}_{lk}(\vec{q}')\tilde{\beta}_{k}(\vec{q}') \\
&\quad +\tilde{V}^{\star}_{lk}(\vec{q}')\tilde{\beta}^{\dagger}_{k}(\vec{q}'))[\hat{\mathcal{F}}]|\Phi(\vec{q}'))\rangle \\
&= \sum_{kk'} U_{l'k'}(\vec{q})\tilde{V}^{\star}_{lk}(\vec{q}')\langle\Phi(\vec{q})|\beta_{k'}\beta^{\dagger}_{k}[\hat{\mathcal{F}}]|\Phi(\vec{q})\rangle \\
&= \sum_{kk'} U_{l'k'}(\vec{q})\tilde{V}^{\star}_{lk}(\vec{q}')[T^{T}_{22}]^{-1}_{k'k} \\
&= (U(\vec{q})[T^{T}_{22}]^{-1}\tilde{V}^{\dagger}(\vec{q}'))_{l'l} \\
&= (\tilde{V}^{\star}(\vec{q}')[T_{22}]^{-1}U^{T}(\vec{q}))_{ll'} \\
&= (FV^{\star}(\vec{q}')[T_{22}]^{-1}U^{T}(\vec{q}))_{ll'} \qquad \text{(B.33)}
\end{aligned}$$

$$\begin{aligned}
\kappa^{01}_{ll'} &= \sum_{kk'}\langle\Phi(\vec{q})|(U^{\star}_{lk}(\vec{q})\beta^{\dagger}_{k}(\vec{q}) + V_{lk}(\vec{q})\beta_{k}(\vec{q})(\tilde{U}^{\star}_{l'k'}(\vec{q}')\tilde{\beta}^{\dagger}_{k'}(\vec{q}') \\
&\quad +\tilde{V}_{l'k'}(\vec{q}')\tilde{\beta}_{k'}(\vec{q}'))[\hat{\mathcal{F}}]|\Phi(\vec{q}'))\rangle \\
&= \sum_{kk'} V_{lk}(\vec{q})\tilde{U}^{\star}_{l'k'}(\vec{q}')\langle\Phi(\vec{q})|\beta_{k}(\vec{q})\tilde{\beta}^{\dagger}_{k'}(\vec{q}')[\hat{\mathcal{F}}]|\Phi(\vec{q})\rangle \\
&= \sum_{kk'} V_{l'k'}(\vec{q})\tilde{U}^{\star}_{lk}(\vec{q}')[T^{T}_{22}]^{-1}_{kk'} \\
&= (\tilde{U}^{\star}(\vec{q}')[T^{T}_{22}]^{-1}V^{T}(\vec{q}))_{ll'} \\
&= -(\tilde{U}^{\star}(\vec{q}')[T_{22}]^{-1}V^{T}(\vec{q}))_{ll'} \\
&= -(F^{\star}U^{\star}(\vec{q}')[T_{22}]^{-1}V^{T}(\vec{q}))_{ll'} \qquad \text{(B.34)}
\end{aligned}$$

Summarizing the expressions above we write the generalized density matrix and pairing tensors as;

$$\begin{aligned}
\rho^{10}_{ll'} &\equiv \langle\Phi(\vec{q})|c^{\dagger}_{l'}c_{l}[\hat{\mathbb{F}}]|\Phi(\vec{q}\,')\rangle = (FV^{\star}(\vec{q}\,')T^{-1}_{22}V^{T}(\vec{q}))_{ll'} \\
\kappa^{10}_{ll'} &\equiv \langle\Phi(\vec{q})|c_{l'}c_{l}[\hat{\mathbb{F}}]|\Phi(\vec{q}\,')\rangle = (FV^{\star}(\vec{q}\,')T^{-1}_{22}U^{T}(\vec{q}))_{ll'} \\
\kappa^{01}_{ll'} &\equiv \langle\Phi(\vec{q})|c^{\dagger}_{l'}c^{\dagger}_{l}[\hat{\mathbb{F}}]|\Phi(\vec{q}\,')\rangle = -(F^{\star}U^{\star}(\vec{q}\,')T^{-1}_{22}V^{T}(\vec{q}))_{ll'} \qquad \text{(B.35)}
\end{aligned}$$

B.4 Block structure of T_{22} and ρ, κ

B.4.1 T_{22} block structure

In this section we are going to study the block properties of matrix T_{22} defined in Appendix which is necessary to compute the density matrix and pairing tensors B.35. As these matrices do not mix isospin and parity we omit indeces $Z, N, +, -$ on the expressions for U, V.

Using B.27 and the expression for $\hat{F}$ B.8

$$T_{22} = e^{i\varphi} V^T(\vec{q}) \hat{R}(\Omega) V(\vec{q}\,')^\star + e^{i\varphi} U^T(\vec{q}) \hat{R}^\star(\Omega) U(\vec{q}\,')^\star \tag{B.36}$$

The rotation matrix $R(\Omega)$ mix signatures and thefore has four different blocks;

$$R(\Omega) = \begin{bmatrix} R^1(\Omega) & R^3(\Omega) \\ R^4(\Omega) & R^2(\Omega) \end{bmatrix} \tag{B.37}$$

Using the blocks of matrices U, V;

$$T_{22}(\vec{q}, \vec{q}\,', \Omega, \varphi) = \begin{bmatrix} T_{22}^1 & T_{22}^3 \\ T_{22}^4 & T_{22}^2 \end{bmatrix} \tag{B.38}$$

with

$$\begin{aligned}
T^1_{22}(\vec{q},\vec{q}\,',\Omega,\varphi) &= e^{i\varphi}V^{1T}(\vec{q})R^2(\Omega)V^{1\star}(\vec{q}\,') + e^{-i\varphi}U^{1T}(\vec{q})R^1(\Omega)U^{1\star}(\vec{q}\,') \\
T^2_{22}(\vec{q},\vec{q}\,',\Omega,\varphi) &= e^{i\varphi}V^{2T}(\vec{q})R^1(\Omega)V^{2\star}(\vec{q}\,') + e^{-i\varphi}U^{2T}(\vec{q})R^2(\Omega)U^{2\star}(\vec{q}\,') \\
T^3_{22}(\vec{q},\vec{q}\,',\Omega,\varphi) &= e^{i\varphi}V^{1T}(\vec{q})R^4(\Omega)V^{2\star}(\vec{q}\,') + e^{-i\varphi}U^{1T}(\vec{q})R^3(\Omega)U^{2\star}(\vec{q}\,') \\
T^4_{22}(\vec{q},\vec{q}\,',\Omega,\varphi) &= e^{i\varphi}V^{2T}(\vec{q})R^3(\Omega)V^{1\star}(\vec{q}\,') + e^{-i\varphi}U^{2T}(\vec{q})R^4(\Omega)U^{1\star}(\vec{q}\,')
\end{aligned} \tag{B.39}$$

In absence of blocking, all the blocks have the same dimension $M \times M$. If there is blocking the dimensions are;

$$\begin{aligned}
U^1, V^1 &\rightarrow (M \times M_1) = (M \times M - n_b) \\
U^2, V^2 &\rightarrow (M \times M_2) = (M \times M + n_b) \\
R^i(\Omega) &\rightarrow (M \times M) \quad \forall i = 1,2,3,4
\end{aligned} \tag{B.40}$$

so

$$\begin{aligned}
T^1_{22} &\rightarrow (M_1 \times M_1) = (M - n_b \times M - n_b) \\
T^2_{22} &\rightarrow (M_2 \times M_2) = (M + n_b \times M + n_b) \\
T^3_{22} &\rightarrow (M_1 \times M_2) = (M - n_b \times M + n_b) \\
T^4_{22} &\rightarrow (M_2 \times M_1) = (M + n_b \times M - n_b)
\end{aligned} \tag{B.41}$$

For example if we block a state with positive signature, $n_b > 0$ and the matrix

will be;

$$\left[\begin{array}{c|c} T^1_{22} & T^3_{22} \\ \hline T^4_{22} & T^2_{22} \end{array}\right] \tag{B.42}$$

B.4.2 ρ, κ block structure

In the following we derivate the block structure for the matrix density and pairing tensors. This matrices mix signatures and therefore have four blocks;

$$\begin{aligned} \rho^{10}(\vec{q},\vec{q}\,',\Omega,\varphi) &= \begin{bmatrix} (\rho^{10})^1 & (\rho^{10})^3 \\ (\rho^{10})^4 & (\rho^{10})^2 \end{bmatrix} \\ \kappa^{10}(\vec{q},\vec{q}\,',\Omega,\varphi) &= \begin{bmatrix} (\kappa^{10})^1 & (\kappa^{10})^3 \\ (\kappa^{10})^4 & (\kappa^{10})^2 \end{bmatrix} \\ \kappa^{01}(\vec{q},\vec{q}\,',\Omega,\varphi) &= \begin{bmatrix} (\kappa^{01})^1 & (\kappa^{01})^3 \\ (\kappa^{01})^4 & (\kappa^{01})^2 \end{bmatrix} \end{aligned} \tag{B.43}$$

Using B.35 and B.51 is simple to obtain;

$$
\begin{aligned}
(\rho^{10}(\vec{q},\vec{q}\,',\Omega,\varphi))^1 &= e^{i\varphi}(R^3V^{1\star}(\vec{q}\,')(T^3_{22})^{-1}V_2^T(\vec{q}) + R^1V^{2\star}(\vec{q}\,')(T^2_{22})^{-1}V_2^T(\vec{q})) \\
(\rho^{10}(\vec{q},\vec{q}\,',\Omega,\varphi))^2 &= e^{i\varphi}(R^2V^{1\star}(\vec{q}\,')(T^1_{22})^{-1}V_1^T(\vec{q}) + R^4V^{2\star}(\vec{q}\,')(T^4_{22})^{-1}V_1^T(\vec{q})) \\
(\rho^{10}(\vec{q},\vec{q}\,',\Omega,\varphi))^3 &= e^{i\varphi}(R^3V^{1\star}(\vec{q}\,')(T^1_{22})^{-1}V_1^T(\vec{q}) + R^1V^{2\star}(\vec{q}\,')(T^4_{22})^{-1}V_1^T(\vec{q})) \\
(\rho^{10}(\vec{q},\vec{q}\,',\Omega,\varphi))^4 &= e^{i\varphi}(R^2V^{1\star}(\vec{q}\,')(T^3_{22})^{-1}V_2^T(\vec{q}) + R^4V^{2\star}(\vec{q}\,')(T^2_{22})^{-1}V_2^T(\vec{q}))
\end{aligned}
$$

$$
\begin{aligned}
(\kappa^{10}(\vec{q},\vec{q}\,',\Omega,\varphi))^1 &= e^{i\varphi}(R^3V^{1\star}(\vec{q}\,')(T^1_{22})^{-1}U_1^T(\vec{q}) + R^1V^{2\star}(\vec{q}\,')(T^4_{22})^{-1}U_1^T(\vec{q})) \\
(\kappa^{10}(\vec{q},\vec{q}\,',\Omega,\varphi))^2 &= e^{i\varphi}(R^2V^{1\star}(\vec{q}\,')(T^3_{22})^{-1}U_2^T(\vec{q}) + R^4V^{2\star}(\vec{q}\,')(T^2_{22})^{-1}U_2^T(\vec{q})) \\
(\kappa^{10}(\vec{q},\vec{q}\,',\Omega,\varphi))^3 &= e^{i\varphi}(R^3V^{1\star}(\vec{q}\,')(T^3_{22})^{-1}U_2^T(\vec{q}) + R^1V^{2\star}(\vec{q}\,')(T^2_{22})^{-1}U_2^T(\vec{q})) \\
(\kappa^{10}(\vec{q},\vec{q}\,',\Omega,\varphi))^4 &= e^{i\varphi}(R^2V^{1\star}(\vec{q}\,')(T^1_{22})^{-1}U_1^T(\vec{q}) + R^4V^{2\star}(\vec{q}\,')(T^4_{22})^{-1}U_1^T(\vec{q}))
\end{aligned}
$$

$$
\begin{aligned}
(\kappa^{01}(\vec{q},\vec{q}\,',\Omega,\varphi))^1 &= -e^{-i\varphi}(R^1U^{1\star}(\vec{q}\,')(T^3_{22})^{-1}V_2^T(\vec{q}) + R^3U^{2\star}(\vec{q}\,')(T^2_{22})^{-1}V_2^T(\vec{q})) \\
(\kappa^{01}(\vec{q},\vec{q}\,',\Omega,\varphi))^2 &= -e^{-i\varphi}(R^4U^{1\star}(\vec{q}\,')(T^1_{22})^{-1}V_1^T(\vec{q}) + R^2U^{2\star}(\vec{q}\,')(T^4_{22})^{-1}V_1^T(\vec{q})) \\
(\kappa^{01}(\vec{q},\vec{q}\,',\Omega,\varphi))^3 &= -e^{-i\varphi}(R^1U^{1\star}(\vec{q}\,')(T^1_{22})^{-1}V_1^T(\vec{q}) + R^3U^{2\star}(\vec{q}\,')(T^4_{22})^{-1}V_1^T(\vec{q})) \\
(\kappa^{01}(\vec{q},\vec{q}\,',\Omega,\varphi))^4 &= -e^{-i\varphi}(R^4U^{1\star}(\vec{q}\,')(T^3_{22})^{-1}V_2^T(\vec{q}) + R^2U^{2\star}(\vec{q}\,')(T^2_{22})^{-1}V_2^T(\vec{q}))
\end{aligned}
$$

Evidently these are square matrices with dimensions $M \times M$. For example in the expression for $(\rho^{10})^1$:

$$
\begin{aligned}
(\rho^{10})^1 &\propto (R^3V^{1\star}(\vec{q}\,')(T^3_{22})^{-1}V_2^T(\vec{q}) + R^1V^{2\star}(\vec{q}\,')(T^2_{22})^{-1}V_2^T(\vec{q})) \\
[(M\times M)] &\to (M\times M)(M_1\times)(M_1\times M_2)(M_2\times M) \\
&+ (M\times M)(M\times M_2)(M_2\times M_2)(M_2\times M) \qquad \text{(B.44)}
\end{aligned}
$$

Invertibility of T_{22}

In order to obtain the density matrix and the pairing tensors we have to calculate the inverse of T_{22}. It is important to prove the determinant of this matrix is not zero in extreme cases (for example of empty levels). We take the Bogoliubov amplitudes of A.21 ; For simplicity to study the shape of this matrix we will use $\bar{U}, \bar{V}$.

$$
\begin{aligned}
T^1_{22} &= e^{i\varphi} \begin{bmatrix} & 0 \\ \tilde{V}^{T1} & \\ 0 & \end{bmatrix} R^2 \begin{bmatrix} & \tilde{V}^1 \\ & \\ 0 & 0 \end{bmatrix} + e^{-i\varphi} \begin{bmatrix} & 0 \\ \tilde{U}^{T1} & \\ 0 & \end{bmatrix} R^1 \begin{bmatrix} & \tilde{U}^1 \\ & \\ 0 & 0 \end{bmatrix} \\
&= \begin{bmatrix} e^{i\varphi}\tilde{V}^{T1} R^2 \tilde{V}^1 \\ \\ +e^{-i\varphi}\tilde{U}^{T1} R^1 \tilde{U}^1 \end{bmatrix}
\end{aligned} \tag{B.45}
$$

$$
\begin{aligned}
T_{22}^{2} &= e^{i\varphi}
\begin{bmatrix}
 & & 0 \\
\tilde{V}^{T2} & & \\
 & & 0 \\
 & & \\
0 & 0 & 1 \\
 & & \\
0 & 0 & 0
\end{bmatrix}
R^{1}
\begin{bmatrix}
 & & 0 & 0 \\
 & \tilde{V}^{2} & & \\
 & & 0 & 1 \\
 & & & \\
0 & 0 & 0 & 0
\end{bmatrix}
+ e^{-i\varphi}
\begin{bmatrix}
 & & 0 \\
\tilde{U}^{T2} & & \\
 & & 0 \\
 & & \\
0 & 0 & 0 \\
 & & \\
0 & 0 & 1
\end{bmatrix}
R^{2}
\begin{bmatrix}
 & & 0 & 0 \\
 & \tilde{U}^{2} & & \\
 & & 0 & 0 \\
 & & & \\
0 & 0 & 0 & 1
\end{bmatrix} \\
&= \begin{bmatrix}
e^{-i\varphi}\tilde{V}^{T1}R^{1}\tilde{V}^{T1} & 0 & 0 \\
+e^{-i\varphi}\tilde{U}^{T2}R^{2}\tilde{U}^{T2} & 0 & 0 \\
0 & 0 & e^{-i\varphi}R^{1}_{MM} \quad 0 \\
0 & 0 & 0 \quad e^{-i\varphi}R^{2}_{MM}
\end{bmatrix}
\end{aligned}
\tag{B.46}
$$

$$
\begin{aligned}
T^3_{22} &= e^{i\varphi}
\begin{bmatrix} & & 0 \\ \tilde{V}^{T1} & & \\ & & 0 \end{bmatrix}
R^4
\begin{bmatrix} & & 0 & 0 \\ \tilde{V}^2 & & & \\ & & 0 & 1 \\ & & & \\ 0 & 0 & 0 & 0 \end{bmatrix}
+ e^{-i\varphi}
\begin{bmatrix} & & 0 \\ \tilde{U}^{T1} & & \\ & & 0 \end{bmatrix}
R^3
\begin{bmatrix} & & 0 & 0 \\ \tilde{U}^2 & & & \\ & & 0 & 0 \\ & & & \\ 0 & 0 & 0 & 1 \end{bmatrix} \\
&= \begin{bmatrix} e^{i\varphi}\tilde{V}^{T1}R^4\tilde{V}^2 & 0 & 0 \\ \\ +e^{-i\varphi}\tilde{U}^{T1}R^3\tilde{U}^2 & 0 & 0 \end{bmatrix}
\end{aligned}
\tag{B.47}
$$

$$
\begin{aligned}
T_{22}^4 &= e^{i\varphi} \begin{bmatrix} & & 0 \\ \tilde{V}^{T2} & & \\ & & 0 \\ & & \\ 0 & 0 & 1 \\ & & \\ 0 & 0 & 0 \end{bmatrix} R^3 \begin{bmatrix} & \\ \tilde{V}^1 & \\ & \\ & \\ 0 & 0 \end{bmatrix} + e^{-i\varphi} \begin{bmatrix} & & 0 \\ \tilde{U}^{T2} & & \\ & & 0 \\ & & \\ 0 & 0 & 0 \\ & & \\ 0 & 0 & 1 \end{bmatrix} R^4 \begin{bmatrix} & \\ \tilde{U}^1 & \\ & \\ & \\ 0 & 0 \end{bmatrix} \\
&= \begin{bmatrix} e^{-i\varphi} \tilde{V}^{T2} R^3 \tilde{V}^1 & \\ & \\ +e^{-i\varphi} R^4 \tilde{U}^{T2} \tilde{U}^1 & \\ & \\ 0 & 0 \\ & \\ 0 & 0 \end{bmatrix}
\end{aligned} \tag{B.48}
$$

Finally, and using that $\tilde{U}^1 = \tilde{U}^2 = \tilde{U}$ and $\tilde{V}^1 = -\tilde{V}^2 = \tilde{V}$ the matrix takes the simple form;

$$T_{22} = \left[\begin{array}{cc|cc|cc} & & & & 0 & 0 \\ A & & B & & & \\ & & & & 0 & 0 \\ \hline & & & & 0 & 0 \\ C & & D & & & \\ & & & & 0 & 0 \\ \hline 0 & 0 & 0 & 0 & e^{i\varphi}R^1_{MM}(\Omega) & 0 \\ 0 & 0 & 0 & 0 & 0 & e^{-i\varphi}R^2_{MM}(\Omega) \end{array}\right] \tag{B.49}$$

where $R^{1,2}_{MM}(\Omega)$ is the matrix element of the rotation matrix which corresponds to the blocked state, which in this case is the last one (M).

$$\begin{aligned} A &= e^{i\varphi}\tilde{V}^T R^2(\Omega)\tilde{V} + e^{-i\varphi}\tilde{U}^T R^1(\Omega)\tilde{U} \\ D &= -e^{i\varphi}\tilde{V}^T R^1(\Omega)\tilde{V} + e^{-i\varphi}\tilde{U}^T R^2(\Omega)\tilde{U} \\ C &= -e^{i\varphi}\tilde{V}^T R^4(\Omega)\tilde{V} + e^{-i\varphi}\tilde{U}^T R^3(\Omega)\tilde{U} \\ D &= -e^{i\varphi}\tilde{V}^T R^3(\Omega)\tilde{V} + e^{-i\varphi}\tilde{U}^T R^4(\Omega)\tilde{U} \end{aligned} \tag{B.50}$$

Is clear that the determinant is just the same as the paired-system one multiplied by these $R^{1,2}_{MM}(\Omega)$ elements. As we have seen T_{22} is invertible. Its

inverse T_{22}^{-1} have also four signature blocks namely;

$$T_{22}^{-1}(\vec{q}, \vec{q}\,', \Omega, \varphi) = \begin{bmatrix} (T_{22}^{1})^{-1} & (T_{22}^{3})^{-1} \\ (T_{22}^{4})^{-1} & (T_{22}^{2})^{-1} \end{bmatrix} \tag{B.51}$$

A simple case: $\hat{R}(\Omega) = \mathbb{I}$

In case of no angular momentum projection, $\hat{R}^1(\Omega) = \hat{R}^1(\Omega) = \mathbb{I}$ and $\hat{R}^3(\Omega) = \hat{R}^4(\Omega) = 0$ so T_{22} takes the simple form:

$$T_{22} = \left[\begin{array}{cc|cc|cc} & & & & 0 & 0 \\ A & & 0 & & & \\ & & & & 0 & 0 \\ \hline & & & & 0 & 0 \\ 0 & & A & & & \\ & & & & 0 & 0 \\ \hline 0 & 0 & 0 & 0 & e^{i\varphi} & 0 \\ 0 & 0 & 0 & 0 & 0 & e^{-i\varphi} \end{array}\right] \tag{B.52}$$

With

$$A = e^{i\varphi}\tilde{V}^T\tilde{V} + e^{-i\varphi}\tilde{U}^T\tilde{U} \tag{B.53}$$

So the determinant is exactly the same as with the even system function; Matrix A is diagonal, with elements

$$A_i = e^{i\varphi}v_i^2 + e^{-i\varphi}u_i^2 \tag{B.54}$$

the determinant takes the simple form:

$$Det \quad T_{22} = det \quad (AA - BB) \tag{B.55}$$

and taking into account **??**

$$Det\ T_{22} = \prod_{i=1,M} (e^{i\varphi}v_i^2 + e^{-i\varphi}u_i^2)^2 \tag{B.56}$$

B.5 Summary

To summarize, to calculate expression B.2;

1. Express operator $\hat{O}$ as a product of any of the (quasi)-particle operators used B.13

2. Apply Wick theorem B.15.

3. Calculate the different contractions B.16 using relations B.29 and B.35

.

Bibliography

[1] Varshalovich, D. A., Moskalev, A. N.Khersonski, V. K. (1988) Quantum theory of angular momentum:irreducible tensors,spherical harmonics, vector coupling coefficients, 3nj symbols Singapore ; World Scientific Pub.,

Appendix C

GCM overlaps

In this appendix, with the use of the expressions obtain in appendix B, we calculate the mean value of the Hamiltonian between GCM wave functions, needed for the configuration mixing calculation. The goal is to calculate expression :

$$\begin{aligned} e^{NZ}(\vec{q},\vec{q}\,',\Omega) &= \frac{\langle\Phi(\vec{q})|\hat{H}\hat{R}(\Omega)\hat{P}^Z\hat{P}^N|\Phi(\vec{q}\,')\rangle}{\langle\Phi(\vec{q})|\hat{R}(\Omega)\hat{P}^Z\hat{P}^N|\Phi(\vec{q}\,')\rangle} \\ &= \sum_{l_Z=1}^{L}\sum_{l_N=1}^{L} y_{l_Z}y_{l_N}e(\vec{q},\vec{q}\,',\Omega,\varphi_{l_Z},\varphi_{l_N}) \end{aligned} \tag{C.1}$$

with

$$e(\vec{q},\vec{q}\,',\Omega,\varphi_{l_Z},\varphi_{l_N}) = \frac{\langle\Phi(\vec{q})|\hat{H}\hat{R}(\Omega)e^{i\varphi_{l_Z}\hat{N}_Z}e^{i\varphi_{l_N}\hat{N}_N}|\Phi(\vec{q}\,')\rangle}{\langle\Phi(\vec{q})|\hat{R}(\Omega)e^{i\varphi_{l_Z}\hat{N}_Z}e^{i\varphi_{l_N}\hat{N}_N}|\Phi(\vec{q}\,')\rangle} \tag{C.2}$$

This is, use the expressions in last chapter to the particular case in which $\hat{O} = \hat{H}$. The hamiltonian has one-body terms and two body terms. Lets

start with the easiest one; the one body term (Kinetic term).

C.0.1 Kinetic term

We separate this term into the proton and the neutron parts:

$$\hat{T}_{kin} = \sum_{k_1 k_2} t_{k_1 k_2} c^{\dagger}_{k_1} c_{k_2} = \sum_{k_1 k_2 \epsilon Z} t_{k_1 k_2} c^{\dagger}_{k_1} c_{k_2} + \sum_{k_1 k_2 \epsilon N} t_{k_1 k_2} c^{\dagger}_{k_1} c_{k_2} \tag{C.3}$$

Our goal is to calculate:

$$e^{NZ}_{kin}(\vec{q}, \vec{q}\,', \Omega) \;=\; \sum_{l_Z=1}^{L} \sum_{l_N=1}^{L} y_{l_Z} y_{l_N} e_{kin}(\vec{q}, \vec{q}\,', \Omega, \varphi_{l_Z}, \varphi_{l_N}) \tag{C.4}$$

with

$$e_{kin}(\vec{q}, \vec{q}\,', \Omega, \varphi_{l_Z}, \varphi_{l_N}) \;=\; \frac{\langle \Phi(\vec{q}) | \hat{T}_{kin} \hat{R}(\Omega) e^{i\varphi_{l_Z} \hat{N}_Z} e^{i\varphi_{l_N} \hat{N}_N} | \Phi(\vec{q}\,') \rangle}{\langle \Phi(\vec{q}) | \hat{R}(\Omega) e^{i\varphi_{l_Z} \hat{N}_Z} e^{i\varphi_{l_N} \hat{N}_N} | \Phi(\vec{q}\,') \rangle} \tag{C.5}$$

In order to lighter the expressions we will use $\vec{\alpha} = \vec{q}, \vec{q}\,', \Omega$.

$$
\begin{aligned}
e^{NZ}_{kin}(\vec{q},\Omega) &= \sum_{l_Z=1}^{L}\sum_{l_N=1}^{L} y_{l_Z}(\vec{\alpha},\varphi_{l_Z}) y_{l_N}(\vec{\alpha},\varphi_{l_N}) \\
&\times \left[\sum_{k_1k_2\epsilon Z} t_{k_1k_2} \frac{\langle\Phi_Z|c^\dagger_{k_1}c_{k_2}\hat{R}(\Omega)e^{i\varphi_{l_Z}\hat{N}_Z}|\Phi_Z\rangle\langle\Phi_N|\hat{R}(\Omega)e^{i\varphi_{l_N}\hat{N}_N}|\Phi_N\rangle}{\langle\Phi_Z|\hat{R}(\Omega)e^{i\varphi_{l_Z}\hat{N}_Z}|\Phi_Z\rangle\langle\Phi_N|\hat{R}(\Omega)e^{i\varphi_{l_N}\hat{N}_N}|\Phi_N\rangle} + Z\leftrightarrow N\right] \\
&= \sum_{l_Z=1}^{L}\sum_{l_N=1}^{L} y_{l_Z}(\vec{\alpha},\varphi_{l_Z}) y_{l_N}(\vec{\alpha},\varphi_{l_N}) \left[\sum_{k_1k_2\epsilon Z} t_{k_1k_2} \frac{\langle\Phi_Z|c^\dagger_{k_1}c_{k_2}\hat{R}(\Omega)e^{i\varphi_{l_Z}\hat{N}_Z}|\Phi_Z\rangle}{\langle\Phi_Z|\hat{R}(\Omega)e^{i\varphi_{l_Z}\hat{N}_Z}|\Phi_Z\rangle} + Z\leftrightarrow N\right] \\
&\overset{1}{=} \sum_{l_Z=1}^{L} y_{l_Z}(\vec{\alpha},\varphi_{l_Z}) \sum_{k_1k_2\epsilon Z} t_{k_1k_2} \frac{\langle\Phi_Z|c^\dagger_{k_1}c_{k_2}\hat{R}(\Omega)e^{i\varphi_{l_Z}\hat{N}_Z}|\Phi_Z\rangle}{\langle\Phi_Z|\hat{R}(\Omega)e^{i\varphi_{l_Z}\hat{N}_Z}|\Phi_Z\rangle} + Z\leftrightarrow N \\
&= \sum_{l_Z=1}^{L} y_{l_Z}(\vec{\alpha},\varphi_{l_Z}) \sum_{k_1k_2\epsilon Z} t_{k_1k_2} \langle\Phi_Z|c^\dagger_{k_1}c_{k_2}[\hat{\mathcal{M}}(\Omega,\varphi_{l_Z})]|\Phi_Z\rangle + Z\leftrightarrow N \\
&= \sum_{l_Z=1}^{L} y_{l_Z}(\vec{\alpha},\varphi_{l_Z}) \sum_{k_1k_2\epsilon Z} t_{k_1k_2} \frac{\langle\Phi_Z|c^\dagger_{k_1}c_{k_2}[\hat{\mathcal{M}}(\Omega,\varphi_{l_Z})]|\Phi_Z\rangle}{\langle\Phi_Z|\hat{R}(\Omega)e^{i\varphi_{l_Z}\hat{N}_Z}|\Phi_Z\rangle} + Z\leftrightarrow N \\
&= \sum_{l_Z=1}^{L} y_{l_Z}(\vec{\alpha},\varphi_{l_Z}) Tr(t\rho(q,\Omega,\varphi_{l_Z})) + \sum_{l_N=1}^{L} y_{l_N}(\vec{\alpha},\varphi_{l_N}) Tr(t\rho(\vec{\alpha},\varphi_{l_N})) \\
&= Tr[t\rho^{10,Z}(\vec{\alpha})] + Tr[t\rho^{10,N}(\vec{\alpha})] \qquad \text{(C.6)}
\end{aligned}
$$

where

$$
\rho^{10,\tau}(\vec{\alpha}) = \sum_{l_Z=1}^{L} y_{l_Z}(\vec{\alpha},\varphi_{l_Z})\rho(\vec{\alpha},\varphi_{l_Z}) \qquad \text{(C.7)}
$$

C.0.2 Two-body terms

The two body part is:

$$
\hat{V} = \sum_{k_1k_2k_3k_4} \bar{v}_{k_1k_2k_3k_4} c^\dagger_{k_1}c^\dagger_{k_2}c_{k_4}c_{k3} \qquad \text{(C.8)}
$$

As before our goal is to calculate;

$$e_{2b}^{NZ}(\vec{q},\vec{q}\,',\Omega) = \sum_{l_Z=1}^{L}\sum_{l_N=1}^{L} y_{l_Z} y_{l_N} e_{2b}(\vec{q},\vec{q}\,',\Omega,\varphi_{l_Z},\varphi_{l_N}) \tag{C.9}$$

with ;

$$e_{2b}(\vec{q},\vec{q}\,',\Omega,\varphi_{l_Z},\varphi_{l_N}) = \frac{\langle\Phi(\vec{q})|\hat{V}\hat{R}(\Omega)e^{i\varphi_{l_Z}\hat{N}_Z}e^{i\varphi_{l_N}\hat{N}_N}|\Phi(\vec{q}\,')\rangle}{\langle\Phi(\vec{q})|\hat{R}(\Omega)e^{i\varphi_{l_Z}\hat{N}_Z}e^{i\varphi_{l_N}\hat{N}_N}|\Phi(\vec{q}\,')\rangle} \tag{C.10}$$

Using the Wick theorem;

$$\begin{aligned} V(\vec{q},\Omega,\varphi_{l_Z},\varphi_{l_N}) &= \frac{1}{4}\sum_{k_1k_2k_3k_4}\bar{v}_{k_1k_2k_3k_4}\langle\Phi|\tilde{\Phi}\rangle^{-2}\{\langle\Phi|c_{k_1}^\dagger c_{k_3}|\tilde{\Phi}\rangle\langle\Phi|c_{k_2}^\dagger c_{k_4}|\tilde{\Phi}\rangle \\ &\quad -\langle\Phi|c_{k_1}^\dagger c_{k_4}|\tilde{\Phi}\rangle\langle\Phi|c_{k_2}^\dagger c_{k_3}|\tilde{\Phi}\rangle + \langle\Phi|c_{k_1}^\dagger c_{k_2}^\dagger|\tilde{\Phi}\rangle\langle\Phi|c_{k_4}c_{k_3}|\tilde{\Phi}\rangle\} \\ &= \frac{1}{2}\sum_{k_1k_2k_3k_4}\bar{v}_{k_1k_2k_3k_4}\langle\Phi|\tilde{\Phi}\rangle^{-2}\{\langle\Phi|c_{k_1}^\dagger c_{k_3}|\tilde{\Phi}\rangle\langle\Phi|c_{k_2}^\dagger c_{k_4}|\tilde{\Phi}\rangle \\ &\quad +\frac{1}{2}\langle\Phi|c_{k_1}^\dagger c_{k_2}^\dagger|\tilde{\Phi}\rangle\langle\Phi|c_{k_4}c_{k_3}|\tilde{\Phi}\rangle\} \end{aligned} \tag{C.11}$$

The first term is called Hartree-Fock. The second is the pairing term. We calculate them separately. We will use the following definitions, which are the generalization of 3.14 and 3.15 but using the generalized density and pairing tensors B.35:

$$\Gamma_{ll'}^{10,\tau\tau'}(\vec{\alpha},\varphi_{l_Z}) = \sum_{kk'}\bar{v}_{lkl'k'}\rho_{k'k}^{10}(\vec{\alpha},\varphi_{l_\tau}) \tag{C.12}$$

$$\Delta_{ll'}^{10,\tau}(\vec{\alpha},\varphi_{l_Z}) = \sum_{kk'}\bar{v}_{ll'kk'}\kappa_{kk'}^{10}(\vec{\alpha},\varphi_{l_\tau}) \tag{C.13}$$

Hartree-Fock terms

$$
\begin{aligned}
e^{ZN}_{V,HF}(\vec{\alpha}) &= \frac{1}{2}\sum_{l_Z=1}^{L}\sum_{l_N=1}^{L} y_{l_Z}(\vec{\alpha},\varphi_{l_Z})y_{l_N}(\vec{\alpha},\varphi_{l_N})\frac{\sum_{k_1k_2k_3k_4}\bar{v}_{k_1k_2k_3k_4}\{\langle\Phi|c^{\dagger}_{k_1}c_{k_3}|\tilde{\Phi}\rangle\langle\Phi|c^{\dagger}_{k_2}c_{k_4}|\tilde{\Phi}\rangle\}}{\langle\Phi|\tilde{\Phi}\rangle^2} \\
&= e^{Z}_{V,HF_1}(\vec{\alpha}) + e^{NZ}_{V,HF_2}(\vec{\alpha}) + e^{ZN}_{V,HF_3}(\vec{\alpha}) + e^{N}_{V,HF_4}(\vec{\alpha}) \qquad \text{(C.14)}
\end{aligned}
$$

In term 1; $k_1,k_2,k_3,k_4\epsilon\ Z$. In term 1; $k_1,k_2,k_3,k_4\ \epsilon\ N$.For term 3 $k_1,k_3\ \epsilon\ Z$ and $k_2,k_4\ \epsilon\ N$.For the last one $k_1,k_3\ \epsilon\ N$ and $k_2,k_4\ \epsilon\ Z$.

$$
\begin{aligned}
e^{Z}_{HF_1}(\vec{\alpha}) &= \frac{1}{2}\sum_{l_Z=1}^{L} y_{l_Z}(\vec{\alpha},\varphi_{l_Z})\sum_{l_N=1}^{L} y_{l_N}(\vec{\alpha},\varphi_{l_N})\sum_{k_1k_2k_3k_4\epsilon Z}\bar{v}_{k_1k_2k_3k_4} \\
&\times \frac{\langle\Phi_Z|c^{\dagger}_{k_1}c_{k_3}\hat{R}(\Omega)e^{i\varphi_{l_Z}\hat{N}_Z}|\Phi_Z\rangle\langle\Phi_N|\hat{R}(\Omega)e^{i\varphi_{l_N}\hat{N}_N}|\Phi_N\rangle}{\langle\Phi_Z|\hat{R}(\Omega)e^{i\varphi_{l_Z}\hat{N}_Z}|\Phi_Z\rangle\langle\Phi_N|\hat{R}(\Omega)e^{i\varphi_{l_N}\hat{N}_N}|\Phi_N\rangle} \\
&\times \frac{\langle\Phi_Z|c^{\dagger}_{k_2}c_{k_4}\hat{R}(\Omega)e^{i\varphi_{l_Z}\hat{N}_Z}|\Phi_Z\rangle\langle\Phi_N|\hat{R}(\Omega)e^{i\varphi_{l_N}\hat{N}_N}|\Phi_N\rangle}{\langle\Phi_Z|\hat{R}(\Omega)e^{i\varphi_{l_Z}\hat{N}_Z}|\Phi_Z\rangle\langle\Phi_N|\hat{R}(\Omega)e^{i\varphi_{l_N}\hat{N}_N}|\Phi_N\rangle} \\
&= \frac{1}{2}\sum_{l_Z=1}^{L} y_{l_Z}(\vec{\alpha},\varphi_{l_Z})\sum_{k_1k_2k_3k_4\epsilon Z}\bar{v}_{k_1k_2k_3k_4}\rho_{k_3k_1}(\vec{\alpha},\varphi_{l_Z})\rho_{k_4k_2}(\vec{\alpha},\varphi_{l_Z}) \\
&= \frac{1}{2}\sum_{l_Z=1}^{L} y_{l_Z}(\vec{\alpha},\varphi_{l_Z})\sum_{k_1k_2k_3k_4\epsilon Z}\bar{v}_{k_1k_2k_3k_4}\rho_{k_3k_1}(\vec{\alpha},\varphi_{l_Z})\rho_{k_4k_2}(\vec{\alpha},\varphi_{l_Z}) \\
&= \frac{1}{2}\sum_{l_Z=1}^{L} y_{l_Z}(\vec{\alpha},\varphi_{l_Z})\sum_{k_1k_3\epsilon Z}\Gamma^{10,Z,Z}_{k_3k_1}(\vec{\alpha},\varphi_{l_Z})\rho_{k_3k_1}(\vec{\alpha},\varphi_{l_Z}) \\
&= \frac{1}{2}\sum_{l_Z=1}^{L} y_{l_Z}(\vec{\alpha},\varphi_{l_Z})Tr\left\{\Gamma^{10,ZZ}(\vec{\alpha},\varphi_{l_Z})\rho^{10}(\vec{\alpha},\varphi_{l_Z})\right\} \qquad \text{(C.15)}
\end{aligned}
$$

The expression for $e^{Z}_{V,HF_2}(\vec{\alpha})$ is the same as (C.15) exchanging $Z \leftrightarrow N$. For term number three;

$$
\begin{aligned}
e^{ZN}_{V,HF_3}(\vec{\alpha}) &= \frac{1}{2}\sum_{l_Z=1}^{L} y_{l_Z}(\vec{\alpha},\varphi_{l_Z}) \sum_{l_N=1}^{L} y_{l_N}(\vec{\alpha},\varphi_{l_N}) \sum_{\substack{k_1,k_3\epsilon Z \\ k_2,k_4\epsilon N}} \bar{v}_{k_1k_2k_3k_4} \\
&\times \frac{\langle\Phi_Z|c^{\dagger}_{k_1}c_{k_3}\hat{R}(\Omega)e^{i\varphi_{l_Z}\hat{N}_Z}|\Phi_Z\rangle\langle\Phi_N|\hat{R}(\Omega)e^{i\varphi_{l_N}\hat{N}_N}|\Phi_N\rangle}{\langle\Phi_Z|\hat{R}(\Omega)e^{i\varphi_{l_Z}\hat{N}_Z}|\Phi_Z\rangle\langle\Phi_N|\hat{R}(\Omega)e^{i\varphi_{l_N}\hat{N}_N}|\Phi_N\rangle} \\
&\times \frac{\langle\Phi_N|c^{\dagger}_{k_2}c_{k_4}\hat{R}(\Omega)e^{i\varphi_{l_N}\hat{N}_N}|\Phi_N\rangle\langle\Phi_Z|\hat{R}(\Omega)e^{i\varphi_{l_Z}\hat{N}_Z}|\Phi_Z\rangle}{\langle\Phi_Z|\hat{R}(\Omega)e^{i\varphi_{l_Z}\hat{N}_Z}|\Phi_Z\rangle\langle\Phi_N|\hat{R}(\Omega)e^{i\varphi_{l_N}\hat{N}_N}|\Phi_N\rangle} \\
&= \frac{1}{2}\sum_{l_Z=1}^{L} y_{l_Z}(\vec{\alpha},\varphi_{l_Z}) \sum_{l_N=1}^{L} y_{l_N}(\vec{\alpha},\varphi_{l_N}) \sum_{\substack{k_1,k_3\epsilon Z \\ k_2,k_4\epsilon N}} \bar{v}_{k_1k_2k_3k_4}\rho_{k_3k_1}(\vec{\alpha},\varphi_{l_Z})\rho_{k_4k_2}(\vec{\alpha},\varphi_{l_N}) \\
&= \frac{1}{2}\sum_{l_Z=1}^{L} y_{l_Z}(\vec{\alpha},\varphi_{l_Z}) \sum_{l_N=1}^{L} y_{l_N}(\vec{\alpha},\varphi_{l_N}) \sum_{k_1k_3\epsilon Z} \Gamma^{10,Z,Z}_{k_3k_1}(\vec{\alpha},\varphi_{l_N})\rho_{k_3k_1}(\vec{\alpha},\varphi_{l_Z}) \\
&= \frac{1}{2}\sum_{l_N=1}^{L} y_{l_N}(\vec{\alpha},\varphi_{l_N}) \sum_{k_1k_3\epsilon Z} \Gamma^{10,ZN}_{k_3k_1}(\vec{\alpha},\varphi_{l_N})\rho^{10,Z}_{k_3k_1}(\vec{\alpha}) \\
&= \frac{1}{2}\sum_{l_N=1}^{L} y_{l_N}(\vec{\alpha},\varphi_{l_N}) Tr\left\{\Gamma^{10,Z,N}(\vec{\alpha},\varphi_{l_N})\rho^{10,Z}(\vec{\alpha})\right\} \qquad \text{(C.16)}
\end{aligned}
$$

and finally fourth term is obtained exchanging $Z \leftrightarrow N$ in (C.16) .

Pairing term

$$
\begin{aligned}
e^{NZ}_{V,EP}(\vec{q},\Omega) &= \frac{1}{4}\sum_{l_Z=1}^{L}\sum_{l_N=1}^{L} y_{l_Z}(\vec{\alpha},\varphi_{l_Z})y_{l_N}(\vec{\alpha},\varphi_{l_N}) \\
&\quad \frac{\sum_{k_1k_2k_3k_4}\bar{v}_{k_1k_2k_3k_4}\{\langle\Phi|c^{\dagger}_{k_1}c^{\dagger}_{k_2}|\tilde{\Phi}\rangle\langle\Phi|c_{k_4}c_{k_3}|\tilde{\Phi}\rangle\}}{\langle\Phi|\tilde{\Phi}\rangle^2} \\
&= e^{Z}_{V,EP_1}(\vec{q},\Omega) + e^{N}_{V,EP_2}(\vec{q},\Omega) \qquad \text{(C.17)}
\end{aligned}
$$

In the first one; $k_i \, \epsilon \, Z$ and in the second $k_i \, \epsilon \, N \; \forall \; i \, \epsilon \, 4$

$$
\begin{aligned}
e^{Z}_{V,EP_1}(\vec{\alpha}) &= \frac{1}{4}\sum_{l_Z=1}^{L} y_{l_Z}(\vec{\alpha},\varphi_{l_Z})\sum_{l_N=1}^{L} y_{l_N}(\vec{\alpha},\varphi_{l_N})\sum_{k_1k_2k_3k_4\epsilon Z}\bar{v}_{k_1k_2k_3k_4} \\
&\times \frac{\langle\Phi_Z|c^{\dagger}_{k_1}c^{\dagger}_{k_2}\hat{R}(\Omega)e^{i\varphi_{l_Z}\hat{N}_Z}|\Phi_Z\rangle\langle\Phi_N|\hat{R}(\Omega)e^{i\varphi_{l_N}\hat{N}_N}|\Phi_N\rangle}{\langle\Phi_Z|\hat{R}(\Omega)e^{i\varphi_{l_Z}\hat{N}_Z}|\Phi_Z\rangle\langle\Phi_N|\hat{R}(\Omega)e^{i\varphi_{l_N}\hat{N}_N}|\Phi_N\rangle} \\
&\times \frac{\langle\Phi_Z|c_{k_4}c_{k_3}\hat{R}(\Omega)e^{i\varphi_{l_Z}\hat{N}_Z}|\Phi_Z\rangle\langle\Phi_N|\hat{R}(\Omega)e^{i\varphi_{l_N}\hat{N}_N}|\Phi_N\rangle}{\langle\Phi_Z|\hat{R}(\Omega)e^{i\varphi_{l_Z}\hat{N}_Z}|\Phi_Z\rangle\langle\Phi_N|\hat{R}(\Omega)e^{i\varphi_{l_N}\hat{N}_N}|\Phi_N\rangle} \\
&= \frac{1}{4}\sum_{l_Z=1}^{L} y_{l_Z}(\vec{\alpha},\varphi_{l_Z})\sum_{k_1k_2k_3k_4\epsilon Z}\bar{v}_{k_1k_2k_3k_4}\kappa^{10}_{k_3k_4}(\vec{\alpha},\varphi_{l_Z})\kappa^{01}_{k_1k_2}(\vec{\alpha},\varphi_{l_Z}) \\
&= \frac{1}{2}\sum_{l_Z=1}^{L} y_{l_Z}(\vec{\alpha},\varphi_{l_Z})\sum_{k_1k_2\epsilon Z}\Delta^{10}_{k_1k_2}(\vec{\alpha},\varphi_{l_Z})\kappa^{01}_{k_1k_2}(\vec{\alpha},\varphi_{l_Z}) \\
&= -\frac{1}{2}\sum_{l_Z=1}^{L} y_{l_Z}(\vec{\alpha},\varphi_{l_Z})\sum_{k_1k_2\epsilon Z}\Delta^{10}_{k_1k_2}(\vec{\alpha},\varphi_{l_Z})\kappa^{01}_{k_2k_1}(\vec{\alpha},\varphi_{l_Z}) \\
&= -\frac{1}{2}\sum_{l_Z=1}^{L} y_{l_Z}(\vec{\alpha},\varphi_{l_Z})Tr\{\Delta^{10}(\vec{\alpha},\varphi_{l_Z})\kappa^{01}(\vec{\alpha},\varphi_{l_Z})\} \qquad \text{(C.18)}
\end{aligned}
$$

and the same expression for $e^{\pi}_{V,EP_2}(\vec{q},\Omega)$ exchanging $Z \leftrightarrow N$ in (C.18) .

Agradecimientos

En primer lugar me gustaría expresar mi agradecimiento a mi director de tesis Luis Egido, por haberme enseñado tanto sobre la Fsica, por dedicar tantas horas de su tiempo y paciencia, y muy especialmente por poner orden en mi desorden. Te agradezco que, hace ya cuatro cursos, me brindaras la oportunidad de hacer esta tesis contigo.

Me gustaría agradecer a las personas que han pertenecido a nuestro grupo de investigación y que comenzaron desarrollando los mt́odos en los que yo me he basado, en particular las aportaciones de Luis Miguel Robledo, Marta Anguiano y Tomás Rodríguez. A Tomás le quiero agradecer especialmente sus explicaciones y sus notas, así como su apoyo. Creo que todo hubiese sido mucho más complido sin él.

Me gustaría agradecer a mi compañera de despacho Nuria Vaquero su siempre predisposición a ayudar desde el primer día en que llegué, así como a Fangqi Chen con la que aprendí muchas cosas en nuestras discusiones.

Esta tesis también ha sido posible por varios profesores de la carrera, que de una forma u otra han contribuído a que yo eligiera y pudiera realizar este trabajo, especialmente a Alfredo Poves que fue mi profesor de Física Nuclear en la Licenciatura y por tanto con el que aprendí mis primeras cosas en esta rama. Me acuerdo también de mi profesor de Física de bachillerato Ángel, gracias al cual desarrollé mi interés en esta parte de la ciencia. También a mi tío Manuel, que aunque no consiguió que me dedicara a la Astrofísica, si contribuyó a que quisiera dedicarme a la investigación.

Quiero extender mi gratitud al personal administrativo del departamento así como de informática.

A Leni Bascones con quien, en mis dos veranos en el CSIC, aprendí por primera vez qué significa ser investigador.

También extiendo este agradecimiento a mi tutora en mi estancia en París Natalie Pillet, y al resto de amigos que allí conocí y que me hicieron la estancia muy agradable. Espeacialmente a Marc Verriere.

A mis amigos del doctorado Sergio, María, Diego, Guilherme y Victor. También a Javi por enseñarme a abrir la mente y mirar más allá de mi propio trabajo. También a Rubén muy especialmente por sus cafés y risas, así como por compartir su afición deportiva conmigo.

A mis amigos del máster Fran, David, Sergio, Irene, Samu, Vicky y a los de carrera Mónica, Juan, Mar, Julio y Adri.

A amigos y compis de atletismo que tantas veces han aguantado que les cuente los resultados que he iba obteniendo durante los entrenamientos...

A mi novio Juan Carlos, sobre todo por su paciencia en este última etapa, y muy especialmente a mis padres y a mi hermano, quienes siempre han estado en los buenos y malos momentos, y sin los cuales nada de esto no hubiera sido posible.